Universiteit Leiden
The Netherlands

Fundamental research on the voltammetry of polycrystalline gold

Yang, S.

Citation
Yang, S. (2024, April 9). *Fundamental research on the voltammetry of polycrystalline gold*. Retrieved from https://hdl.handle.net/1887/3731809

Version:	Publisher's Version
License:	Licence agreement concerning inclusion of doctoral thesis in the Institutional Repository of the University of Leiden
Downloaded from:	https://hdl.handle.net/1887/3731809

Note: To cite this publication please use the final published version (if applicable).

Fundamental Research on the Voltammetry of Polycrystalline Gold

Proefschrift

ter verkrijging van
de graad van doctor aan de Universiteit Leiden,
op gezag van rector magnificus prof.dr.ir. H. Bijl,
volgens besluit van het college voor promoties
te verdedigen op dinsdag 9 april 2024
klokke 13:45 uur

Shengxiang Yang
geboren te Yunnan, China
in 1990

Promotores

Dr. D. G. H. Hetterscheid
Prof. dr. M. T.M. Koper

Promotiecommissie:

Prof. dr. M. Ubbink
Prof. dr. E. Bouwman
Dr. R. V. Mom
Prof. dr. E. Pidko (Delft University of Technology, Netherlands)
Dr. A. A. Thevenon-Kozub (Utrecht University, Netherlands)

Table of Contents

Chapter 1 Introduction……...…...**02**

Chapter 2 Redefinition of the active species and mechanism of the oxygen evolution reaction on gold oxide……..**38**

Chpater 3 Evolution of amorphous metal oxide structures during catalysis…....**58**

Chpater 4 Exploring the excess free charge distribution under catalytic conditions using a quartz crystal microbalance methodology…….....**72**

Chapter 5 Summary……**98**

APPENDICES

Appendix I Supporting information for chapter 2……....**106**

Appendix II Supporting information for chapter 3……..….…**112**

Appendix III Supporting information for chapter 4……....**142**

Samenvatting…….…….…….…...….**158**

Summary in Chinese…….…….……**166**

Curriculum Vitae…….…….…….….**172**

List of publications…….…….…….….....**174**

Acknowledgments…….…….…….….**176**

现在是过去的未来，
Now is the future of the past,
也是未来的过去。
also the past of the future.
Voltammetry

1

Introduction

1.1 Voltammetry as the central technique in electrochemical analysis

Over the past century, the field of electroanalysis has experienced a remarkable evolution, with voltammetry emerging as its central technique. Voltammetry is an electrochemical technique that involves applying a potential that varies with time to a working electrode and measuring the resulting current flowing between the working and counter electrodes. (Fig.1)

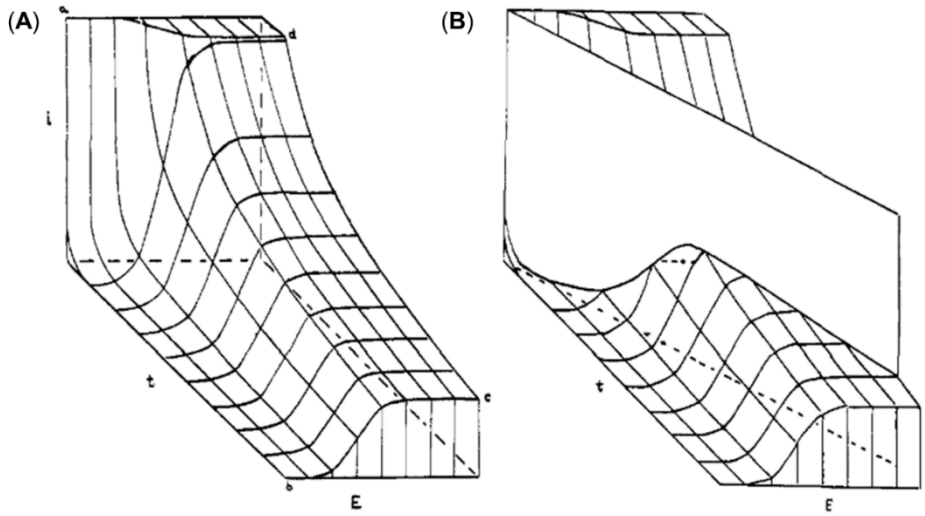

Fig. 1 The three-dimensional i-t-E surface for a Nernstian reaction. (**A**) The steady-state voltammogram corresponds to a cut parallel to the i-E plane. (**B**) another cut representing a linear potential sweep across this surface. Adapted from Reference [1].

In a relatively short period of just over 60 years, a diverse array of methods has been developed around voltammetry, specialized instruments have been designed and built, and a comprehensive theoretical and mathematical framework has been established.[2, 3] Since then voltammetry has become an essential technique in our current scientific research. It provides valuable information about the electrochemical properties and behavior of materials, which can have significant implications in fields such as materials science,[4-6] energy storage,[7-9] corrosion studies,[10-12] and sensor development.[13, 14]

A few specific examples of the importance of voltammetry on solid electrodes are given below:

(1). Electrode characterization

Voltammetry enables the determination of electrochemical parameters of the electrode materials, such as the electroactive surface area, charge transfer kinetics, and electrochemical stability.[15-17] These parameters are crucial for understanding the performance and behavior of electrodes in various applications.

(2). Material analysis

Voltammetry allows for the investigation of material properties and composition.[4-6] By studying the electrochemical behavior of an electrode, researchers can gain insights into the oxidation/reduction processes, interfacial reactions, and the surface reactivity of the material. This information is valuable for designing and optimizing electrode materials for energy storage devices such as batteries and supercapacitors.[9]

(3). Sensor development

Solid electrodes are often used in the development of electrochemical sensors. Voltammetry allows for the sensitive detection and quantification of analytes in various samples. By applying a potential to the electrode and measuring the resulting current response, it is possible to obtain information about the concentration, presence, or behavior of target analytes. This has applications in environmental monitoring, biomedical diagnostics, and industrial process control.[18]

(4). Corrosion studies

Voltammetry is used to study corrosion processes on electrode surfaces.[10-12] By monitoring the current response at different potentials, researchers can gain insights into the corrosion mechanisms, corrosion rates, and protective properties of coatings or inhibitors. This knowledge helps in the development of effective corrosion prevention strategies and the design of more corrosion-resistant materials.

(5). Energy conversion and storage

Solid electrodes play a crucial role in energy conversion and storage devices such as fuel cells, electrolyzes, and batteries.[7-9] Voltammetry allows for the investigation of electrochemical

reactions, charge/discharge processes, and performance characteristics of these electrodes, and thereby for the improvement of the efficiency, stability, and lifespan of energy storage systems.

In summary, voltammetry now becomes an indispensable tool for studying the electrochemical properties of materials, analyzing their behavior, and designing advanced technologies. It provides valuable information for materials characterization, sensor development, corrosion studies, and energy-related applications.

1.2 The history of Polarography — the forerunner of solid electrode voltammetry

Voltammetry originated in early 1922 when Heyrovsky initiated the measurement of current flow and drop time as a function of the potential at a dropping mercury electrode (DME).[19] The measurement wherein current-voltage curves on the DME were obtained were referred to as polarography.

On February 10 1922, Jaroslav Heyrovsky integrated a mirror galvanometer, a highly sensitive instrument, into the circuit. Through meticulous point-to-point measurements, he achieved a significant milestone by obtaining the first polarogram (Fig. 2). A few years later, Heyrovsky collaborated with Masuro Skikata (Fig. 3A) to develop an innovative instrument for the automatic recording of Cyclic Voltammetry (CV) curves, known as polarography (Fig. 3B). This pioneering work marked the advent of the first automated recording by an analytical instrument, signifying the onset of a new era in instrumental analysis.[20, 21]

At the time, mercury was widely regarded as the optimal electrode material for polarography.[22] The Dropping Mercury Electrode (DME) offered an easily renewable and atomically smooth surface, effectively mitigating issues related to electrode passivation and fouling. In addition, due to its high overpotential for the evolution of hydrogen, mercury exhibited a broad potential window, extending to negative potentials as low as −1.6 V vs. SCE.[23] This unique property made mercury the preferred material for the determination of electrochemically reducible analytes.

From the 1940s to the early 1960s, polarographic methods on mercury electrodes experienced a rapid growth along two parallel paths. On one side, numerous variations of the traditional dropping mercury electrode emerged, including the mercury streaming electrode, the

hanging drop mercury electrode, the static mercury drop electrode, the mercury film electrode, the mercury amalgam electrode, the mercury microelectrode, the chemically modified mercury electrode, the controlled growth mercury electrode, and the contractible mercury drop electrode.[24] These innovations expanded the versatility and applicability of mercury-based polarography. On the other side, various modifications to the basic polarographic method were developed, such as oscillopolarography, Kalousek's switcher, AC polarography, Tast polarography, normal pulse polarography, differential pulse polarography, square-wave voltammetry, cyclic voltammetry, anodic stripping voltammetry, adsorptive stripping voltammetry, convolution techniques, and elimination methods.[19, 24] These advancements aimed to enhance the sensitivity, selectivity, and speed of polarography experiments, especially in light of trace analysis. Due to the increasing awareness of the potential toxicity of mercury, the utilization of mercury in polarography gave rise to increasing concerns, particularly from the 1960s onward. As a result, the practice of polarography diminished. It is widely believed that the decline of polarography can be primarily attributed to the apprehension surrounding mercury toxicity.[22, 25] However, despite the limited use of these derived polarographic methods, they have played a vital role in providing invaluable insights and experiences that have contributed significantly to the advancement of the electrochemical methodology as a whole.

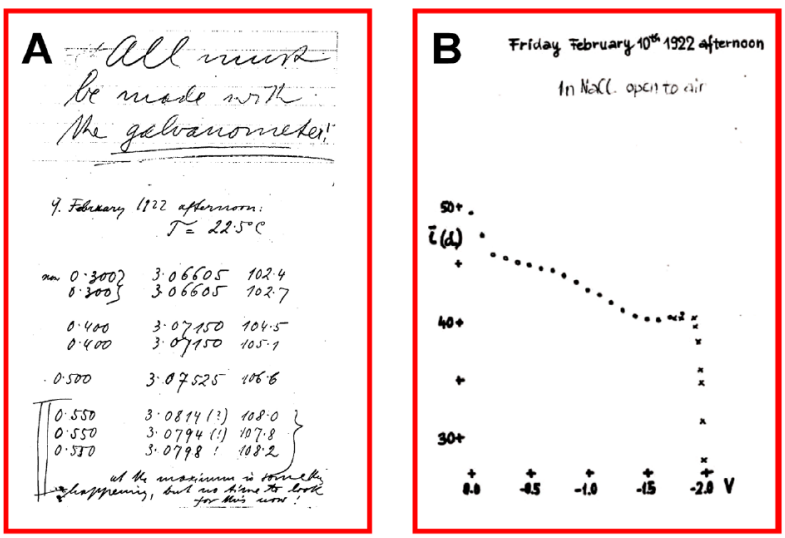

Fig.2 Image of two selected pages from Heyrovsky's laboratory notebook. Legend: (**A**) Protocol from February 9, 1922. On February 2, 1922, Heyrovsky conducted measurements of

electrocapillary curves in a 1 M NaCl solution exposed to air, but at the time did not realize what is going on at the maximum. (**B**) The first polarogram. Plot recorded on February 10, 1922. Adapted from Reference [22].

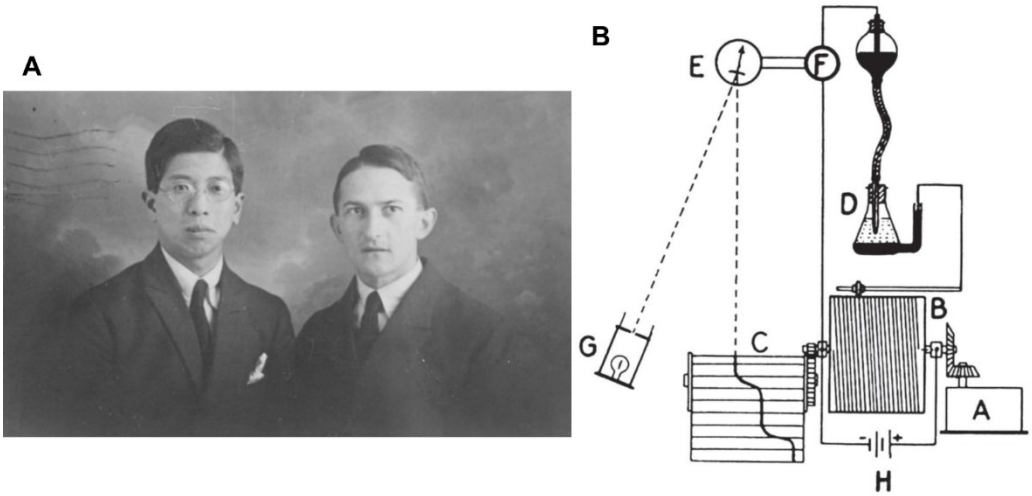

Fig.3 (**A**) Masuzo Shikata and Jaroslav Heyrovsky in London, December 12th 1923; (Adapted from Ref [19]). (**B**) Schematics of the Heyrovsky–Shikata photographic recording polarograph. Adapted from Reference [26].

1.3 The history of voltammetry on solid electrodes

The term "voltammetry" was officially adopted by the IUPAC Nomenclature Committee in the 1960s, but it was originally coined by Kolthoff and Laitinen in 1940 to describe voltage-controlled electrolytical methods.[27] Following this terminology, polarography was considered a specific form of voltammetry that utilized the Dropping Mercury Electrode (DME). When the mercury ceased to drop, the technique was no longer referred to as polarography, but rather as voltammetry with the Hanging Mercury Drop Electrode (HMDE). Since the 1960s, voltammetry techniques conducted at stationary and solid electrodes have gained popularity, gradually replacing the use of polarography with the DME.[2, 3]

The progress in voltammetry at solid electrodes was propelled by advancements in instrumentation.[2, 20] The use of operational amplifiers, initially based on vacuum tubes and later on transistors and integrated circuits, revolutionized the construction of electrochemical instruments.[20] In addition, the availability of Polaroid Land cameras and x-y recorders for

recording oscilloscope traces contributed to the field.[2] These developments facilitated the creation of more precise three-electrode static systems capable of accommodating various voltammetry modes such as lineal voltammetry, cyclic voltammetry, normal pulse voltammetry, differential pulse voltammetry, stripping voltammetry, etc.[28, 29] In addition, the advent of computers has had a profound impact on the advancement of instrumentation. In contemporary times, computer-controlled instrumentation is widely utilized, allowing for the implementation of various modifications of voltammetry using a single specialized apparatus.[2] Moreover, experiments can be automatically evaluated on a computer screen with the aid of suitable software that streamlines data analysis and enhances experimental efficiency.

Modern voltammetry techniques in combination with a rapid development of electrochemical instrumentation has largely encouraged electrochemists to step beyond trace metal determination and speciation, which had been the main application of polarography thus far, and to investigate more complex problems such as the corrosion of materials,[12, 30, 31] dissolution kinetics,[32, 33] structure-activity relationships of electrochemical processes,[34, 35] electrocatalysis,[36-38] kinetic studies of short-lived homogeneous reactions,[39, 40] and many other processes.

Since the 1960s, there has also been a growing research interest focused on the electrodes themselves. Electroanalytical chemists began delving into the physical chemistry of solid electrodes using voltammetry, and discussions aimed at designing and engineering modified electrodes emerged.[2] Initially, platinum, gold, and, to a lesser extent, silver were among the first solid electrodes studied as working electrodes.[12, 41] Subsequently, metals such as bismuth, nickel, palladium, rhodium, ruthenium, and indium, in various forms such as wires, plates, and disks, were also utilized for specific electroanalytical applications.[25] Following the initial surge of interest in solid noble metals, carbon-based electrodes gained rapid development due to their advantages such as a wider potential range, a more diverse surface chemistry, its chemical inertness, cost-effectiveness, and easy accessibility.[42-44] Simultaneously, in the mid-1970s, electrode modification techniques gained popularity with the aim of enhancing the sensitivity and selectivity of solid electrodes. Since then, various conductive materials have been explored for electrode modification purposes, including coatings composed of clays,[45] zeolites,[46]

inorganic crystals,[47] enzyme layers,[18] organic metals,[48] composites,[49] and nanomaterials.[50] These modified electrode materials have significantly advanced the development of various modern electrochemical sensors.

During the rapid development of voltammetry, significant discoveries have been made in electrochemical catalysts and energy storage materials. For instance, dimensionally stable anodes (DSA) were patented by Beer in the 1960s (in Britain) and 1970s (in the United States).[51] DSAs are coatings of a mixed ruthenium-titanium oxide (RTO), consisting of rutile RuO_2 and TiO_2 deposited on titanium. These coatings have found extensive use in industrial chlor-alkali and chlorate cells, leading to substantial energy savings due to their lower overpotentials at industrial current densities. The discovery of DSAs has been hailed as "one of the greatest technological breakthroughs of the past 50 years of electrochemistry".[52]

The first report on the nickel metal hydride battery (NiMH or Ni-MH) dates back to 1967.[53] In the 1970s, the advantage of using lithium metal for high-energy density storage systems was demonstrated through the assembly of primary lithium cells.[54, 55] During the same period, numerous inorganic compounds were found to react reversibly with alkali metals. These compounds, later identified as intercalation compounds, played a crucial role in the development of high-energy rechargeable lithium systems. The concept of electrochemical intercalation, fundamental to modern Li-ion batteries, was clearly defined in 1973.[56, 57]

Around the same time, the theoretical framework for pseudo-capacitance related to electrochemical supercapacitors was postulated by Conway and Gileadi.[58] Experimental observations revealed the rapid charge transfer processes of surface-bound species, such as underpotential deposition (UPD), adsorbed intermediates during electrolysis, and modified thin-film electrodes.[59] In 1971, Trasatti and his colleagues investigated the charge storage behavior of a ruthenium oxide thin film in sulfuric acid and discovered pseudo-capacitance in transition metal oxides for the first time. This discovery marked the beginning of research on electrochemical supercapacitor materials.[58, 60]

Overall, during this period, the thriving advancement of materials science across various fields has greatly ignited researchers' curiosity on the fundamental processes occurring at the solid-liquid interface.

1.4 The complexity and advantage of cyclic voltammetry on solid electrodes

In a conventional voltametric three-electrode setup, the electrode potential (E) is controlled between the working electrode (WE) and reference electrode (RE), while electrons flow between the counter electrode (CE) and the WE with the higher or lower electrochemical potential through the potentiostat, as depicted in Fig 4A. A voltammogram typically plots the resulting current (i) on the y-axis and the applied potential (E vs. the RE) on the x-axis. There are two primary processes depicted in the figures: one is the Faradaic process involving electron transfer (Fig. 4B) and the other is a non-Faradaic process without any electron transfer (Fig. 4C). In the absence of an electrochemical reaction, the electron flow cannot pass through the electrode-solution interface, resulting in a CV without any Faradaic current indicative of redox reactions (Fig. 4C). At a given potential, there will exist a charge on the metal electrode, q^M, and a charge in the solution, q^S. The charge on the metal, q^M, represents an excess or deficiency of electrons and resides in a very thin layer (0.1 Å) on the metal surface.[61, 62] The charge in solution, q^S , is made up of an excess of either cations or anions in the vicinity of the electrode surface. At all times, $q^M = - q^S$.[61] When E is scanned positively (the green line in Fig. 4B), the number of electrons decreases at the working electrode, resulting in a deficiency of electrons on the surface and a corresponding net positive surface charge. Conversely, when E is scanned negatively (the red line in Fig. 4B), the number of electrons increases, leading to an excess of electrons on the surface and a corresponding net negative surface charge. These positive or negative surface charges attract counterions to the electrode surface through electrostatic interactions. This process of physisorption is referred to as a non-Faradaic process, as illustrated in Fig. 4C.

In addition to non-Faradaic processes, there are also Faradaic processes that involve electron transfer between the working electrode and a reactant. Let us consider the electrochemical reaction of a species A from the solution, which has molecular orbitals (MO) including the highest occupied MO (HOMO) and the lowest unoccupied MO (LUMO). If the

Fermi level of the electrode is positioned higher than the HOMO but lower than the LUMO, no electron transfer occurs between the electrode and species A. However, by increasing E positively, a thermodynamic driving force is created, causing the energy level of metal electrons to gradually decrease until it becomes lower than the energy of the HOMO. At this point, a favorable condition is established for electrons to flow from species A to the electrode, resulting in the oxidation of species A ($A \rightarrow A^{+} + e^{-}$). Conversely, if we decrease E negatively, the energy level of electrons gradually increases and becomes higher than the LUMO. In this scenario, electrons flow from the electrode to species A, leading to the reduction of species A ($A + e^{-} \rightarrow A^{-}$). The redox equilibrium of species A is described by the Nernst equation (eq 1). This equation establishes a relationship between the potential of an electrochemical cell (E), the standard potential of species A (E°), and the relative activities of the oxidized (Ox) and reduced (Red) forms of the analyte at equilibrium. The Nernst equation is expressed as follows:

$$E = E^{\circ} + \frac{RT}{nF} ln \frac{(Ox)}{(Red)} \quad (1)$$

Where R is the universal gas constant, T represents the temperature in Kelvin, n is the number of electrons involved in the redox reaction, and F is Faraday's constant.

To gain a better understanding of the relationship between the resulting current and the potential change in a cyclic voltammogram, let us consider the example of the reduction of ferrocenium (Fc^{+}) to ferrocene (Fc) (Fc=[Fe(Cp_2)]; Cp = cyclopentadienyl). Fig. 5H illustrates a typical cyclic voltammogram for a solution of Fc^{+} undergoing a reversible one-electron reduction to Fc. The Nernst equation for the reaction $Fc^{+} + e^{-} \rightleftharpoons Fc$ can be represented as follows:

$$E = E^{\circ} + \frac{RT}{nF} ln \frac{[Fc^{+}]}{[Fc]} \quad (2)$$

Changes in the applied potential at the electrode-liquid interface affect the equilibrium ratio of Fc+ and Fc, as determined by the Nernst equation. However, a different behavior emerges in the solution, where the Fc+:Fc ratio is governed by diffusion kinetics. Specifically, as the applied potential becomes sufficiently negative, the oxidized species (Fc+) present will undergo reduction at the electrode surface. This reduction leads to a diminishing concentration

of Fc^+ near the electrode, as illustrated in the concentration-distance profiles depicted in Fig. 5(A-G). This phenomenon is mirrored in the voltammogram by a peak in the current (i_p), succeeded by a decline in the current flow as the potential is further scanned negatively. Consequently, a concentration gradient is established, necessitating the transport of the oxidized species from the bulk solution to the electrode surface to enable additional current to flow.

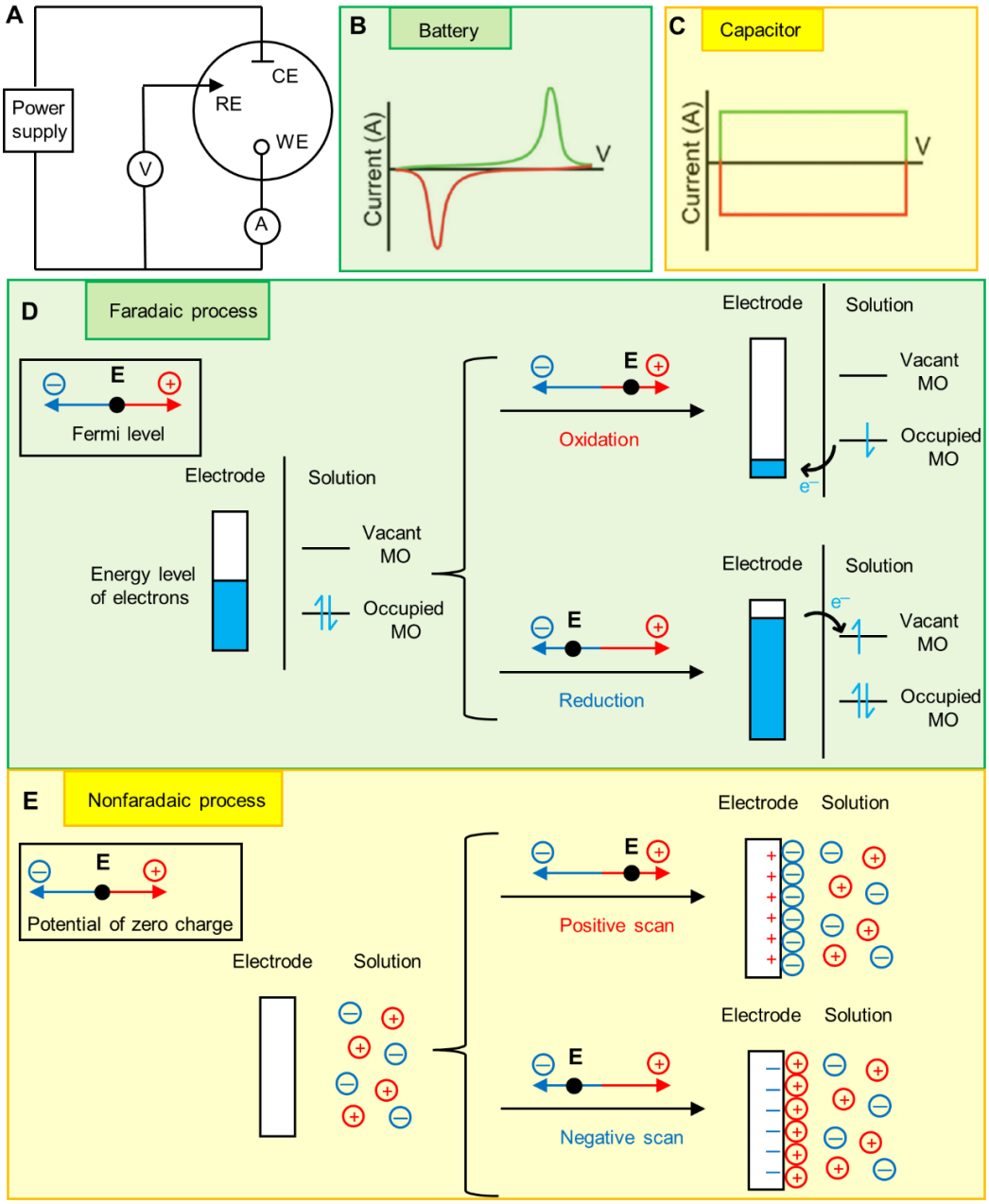

Fig.4 Cyclic voltammetry (CV) measurements. (**A**) Schematic of a typical three electrode electrochemical set up with the appropriate symbols used for Working Electrode (WE, O), Counter Electrode (CE, ⊥) and Reference Electrode (RE, arrow). (**B**) Representative CV illustrating electron transfer within a battery system. (**C**) Exemplary CV depicting for a physical capacitor behavior devoid of electron transfer. (**D**) Representation of Faradaic oxidation and reduction process of species (chemical processes with electrons transfer) in solutions with the change of applied potential of electrode. The molecular orbitals (MO) of species shown are the highest occupied MO and the lowest vacant MO. (**E**) Representation of a Non-faradaic process driven by electrostatic forces arising from extra positive and negative charges at the surface. B and C adapted from Reference [63].

In cyclic voltammetry, the speed of a redox reaction is governed by the sweep rate (ν, mV s^{-1}). Taking into account the difference in kinetic limitations, the current response to the sweep rate (ν) depends on whether the redox reaction is diffusion-controlled or surface-controlled.[64, 65] If a redox reaction is controlled by the semi-infinite diffusion process, the current response varies with $\nu^{1/2}$(eq 3) (Fig. 6A).[5, 64] Diffusion controlled redox reactions encompass a wide range homogeneous electrochemical catalytic processes, and voltammograms prove accurate kinetic information to investigating their kinetics.

$$I_{(V)} = a\nu^{1/2} \quad (3)$$

$$I_{(V)} = a\nu \quad (4)$$

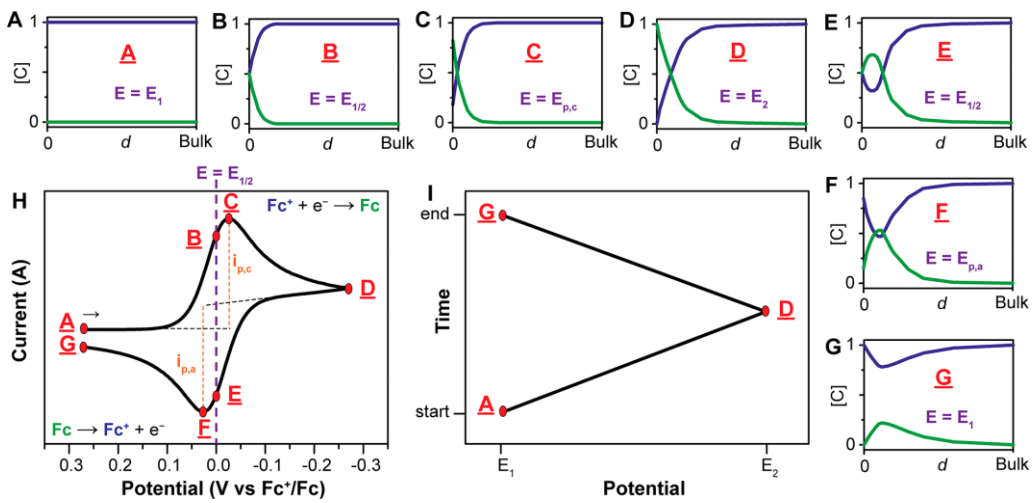

Fig. 5 (**A−G**): Concentration profiles (mM) for Fc^+ (blue) and Fc (green) as a function of the distance from the electrode (d, from the electrode surface to the bulk solution, e.g. 0.5 mm) at various points during the voltammogram. (**H**): Voltammogram of the reversible reduction of a 1 mM Fc^+ solution to Fc, at a scan rate of 100 mV s^{-1}. (**I**): Applied potential as a function of time for a generic cyclic voltammetry experiment, with the initial, switching, and end potentials represented (A, D, and G, respectively). Adapted from Reference [5].

If a redox reaction is limited by a surface reaction wherein diffusion does not play a role, the current would vary directly with ν (eq 4) (Fig. 6B).[64, 66] Such surface redox reactions are referred to as pseudocapacitance, which was introduced in the early 1960s to describe surface Faradaic process such as underpotential deposition and hydrogen adsorption.[58] It was later extended to energy storage in the early 1970s when researchers observed that thin films of hydrous RuO_2 cycled in an acidic electrolyte exhibited cyclic voltammograms resembling those of capacitors, while single-crystal RuO_2 did not exhibit such behavior.[60] Since then, more and more examples of pseudocapacitance behavior have been identified including (1) redox reactions (2), intercalation of cations (3), doping and de-doping in conductive polymers (4) and underpotential deposition of metals (Fig. 7).[63] Especially the discovery of surface redox reactions has opened up a new world of opportunities to enhance the specific capacitance of various energy storage systems.

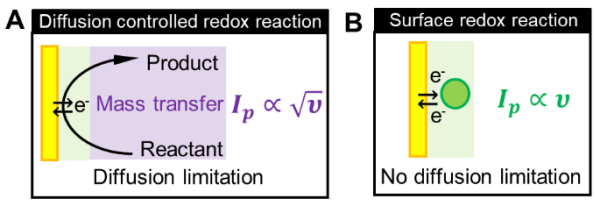

Fig. 6 (**A**) Schematic representation of a diffusion controlled redox reaction and its electrochemical response in which the peak current (I_p) varies with the square root of the scan rate ($\sqrt{v}$). (**B**) Schematic representation of surface redox reaction and its electrochemical response that shows the peak current (I_p) varies with the scan rate (v).

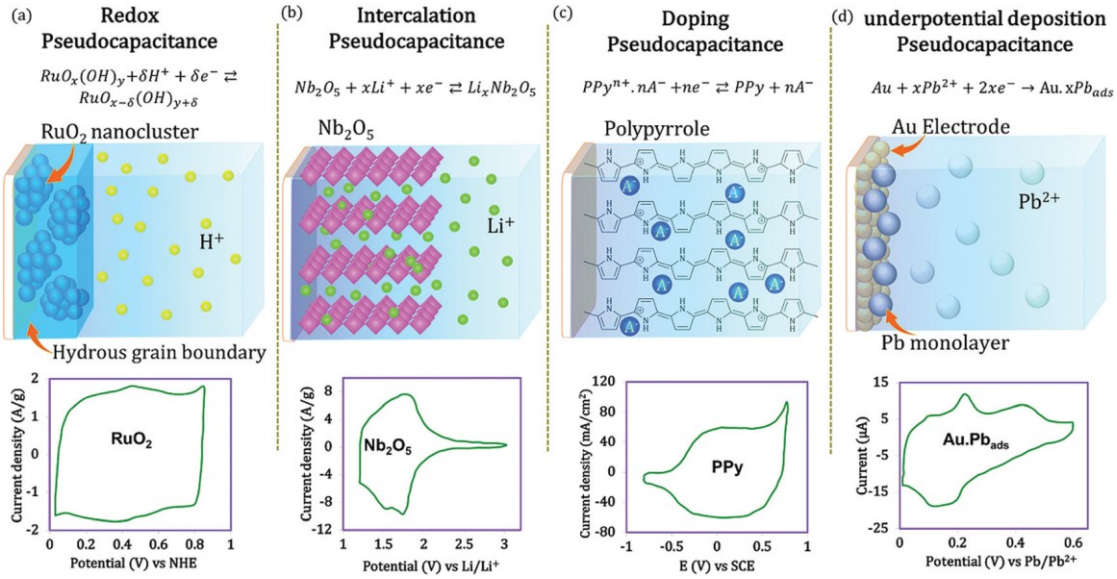

Fig.7 Different types of redox mechanisms that give rise to pseudocapacitance. (**a**) Redox pseudocapacitance, as in $RuO_2 \cdot xH_2O$. (**b**) Intercalation pseudocapacitance, as in Nb_2O_5. (**c**) Doping pseudocapacitance, as in polypyrrole and (**d**) underpotential deposition based pseudocapacitance, as in the deposition of lead on the surface of a gold electrode. Adapted from Reference [63].

The complexity of a redox reaction is also reflected in the electron transfer mechanism. For an electrochemical reaction, especially a multielectron reaction process, the reaction process involves various intermediates. Let us consider the oxygen reduction reaction (ORR) as an example. The ORR process involves different oxygenated intermediates, such as OH^-, HO_2^-, O_2^{2-} and O_2^-. On basis of whether oxygen directly adsorbs on the catalyst, the ORR process can be simply separated into a surface-dependent inner-sphere electron transfer mechanism and a surface-independent outer-sphere electron transfer mechanism.[67] In the inner-sphere reactions, O_2 binds to the electrode surface and the electrons are transferred directly from the material surface to the specifically adsorbed intermediates, as shown in Fig. 8a. In this case, the ORR kinetics are mainly governed by the binding energies between oxygenated intermediates and the catalyst.[68] In outer-sphere reactions, no chemisorption of oxygen takes place, and the ORR must involve electron tunneling across the solvent layer, which separates the oxygenated intermediates from the electrode surface, as shown in Fig. 8b. While numerous

in situ spectroscopic techniques can aid confirming the presence of intermediates, the question of whether these species remain in solution or undergo adsorption onto the electrode surface remains a subject of ongoing debate.[69]

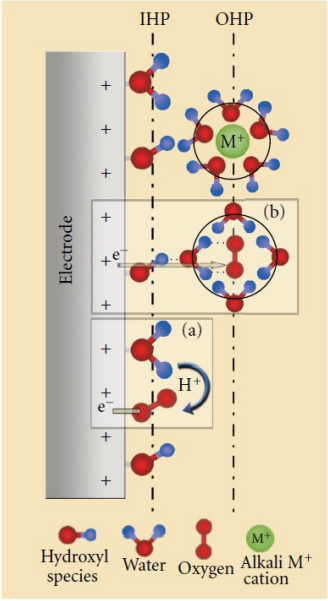

Fig. 8 Schematic illustration of the double-layer structure during the oxygen reduction reaction (ORR) in alkaline media. Insets illustrate inner-sphere (a) and outer-sphere (b) electron transfer processes. Adapted from Reference [70].

The complexity of voltammetry stems from the coexistence of various species at the electrode-solution interface, each exhibiting complex non-Faradaic and/or Faradaic processes. The measured E-I relationship in voltammetry represents a combination of all these processes, involving intricate theories. However, despite its complexity, voltammetry at solid electrodes has rapidly become one of the most widely used electrochemical methods, primarily due to significant advancements in the chemical analysis.[20] A key advantage of solid electrode voltammetry is its seamless integration with other techniques, facilitating the development of diverse in situ methods, such as steady-state mass transfer study at rotating electrodes,[71, 72] in situ spectroscopic methods,[73, 74] scanning electrochemical microscopy,[75] in situ mass spectrometry,[36] in situ quartz crystal microbalance techniques,[76, 77] in situ atomic force

microscopy,[78] et. al. These integrated approaches provide invaluable insights into the complex microscopic phenomena taking place at the electrode-interface.

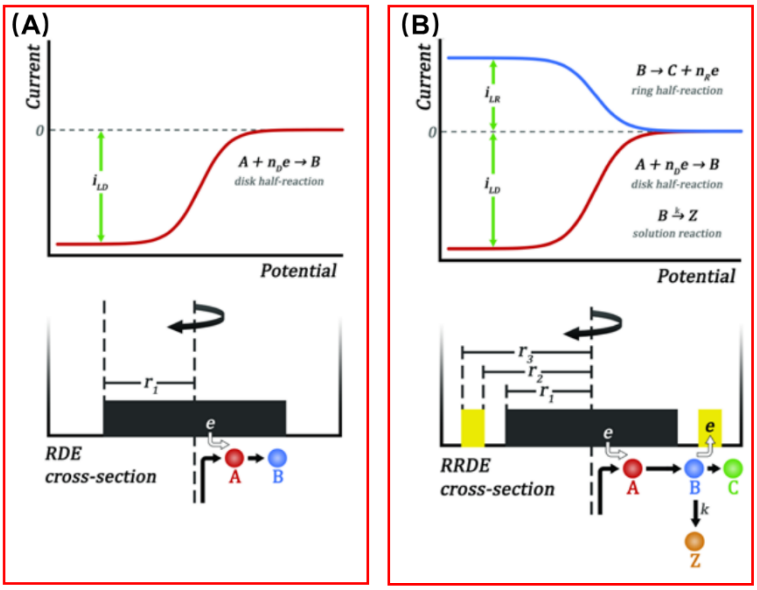

Fig. 9 (**A**) Steady-state mass transport at the Rotating Disk Electrode (RDE) conveys material from the bulk solution towards the disk. The Levich equation predicts the limiting current (i_{LD}) observed as species A is reduced to B. (**B**) Mass transport at the Rotating Ring-Disk Electrode (RRDE) first conveys species A from the bulk solution to the disk electrode where it is reduced to B. The species B is swept to the ring electrode and detected as an anodic current as it is oxidized to C. In some systems, as B transits from the disk to the ring, it may undergo a competing side reaction in solution, lowering the observed ring current. The RRDE may be used to probe the kinetics of such side reactions. Adapted from Reference [72].

One of the most important advances in solid electrode voltammetry is the investigation of the hydrodynamic behavior of a reaction at the interface by performing voltammetry with a rotating disk electrode (RDE). The RDE methodology was first introduced by Levich and his colleagues.[72] When the potential of the RDE is maintained at (or swept to) a sufficiently negative value, the cathodic current is limited solely by the rate of mass transport of species A to the disk surface in presence of a proficient catalyst (Fig. 9A). Under these conditions, an expression for the limiting current (i_{LD}), known as the Levich equation, can be written as follows:

$$i_{LD} = 0.62 n_D F (\pi r_1^2) C_A^* D_A^{2/3} \nu^{-1/6} \omega^{1/2} \quad (3)$$

Where F is the Faraday constant, r_1 is the radius of the disk electrode, C_A^* is the concentration of the electroactive species A in the bulk solution, D_A is the diffusion coefficient of the electroactive species, ν is the kinematic viscosity of the solution, and ω is the angular rotation rate of the disk electrode. Levich's development of the rotating disk electrode (RDE) was highly significant as it offered an experimentally reproducible and mathematically well-defined method for electrochemists to precisely control the rate at which an electroactive species reaches the electrode surface. This technique has been instrumental in advancing our understanding of mass transport phenomena and reaction kinetics at solid electrode interfaces.[79, 80]

Additional important hydrodynamic voltammetry technique involves using a rotating ring-disk electrode (RRDE), which is very similar to a RDE.[72] The main difference is that the RRDE includes a second working electrode in the form of a ring surrounding the central disk of the first working electrode. In the RRDE experiment, the convection-diffusion mass transport can carry a portion of the products generated at the disk electrode to the ring electrode, as illustrated in Fig. 9B. For instance, in the case of a species A being reduced to B at the disk electrode ($A + n_D e^- \rightarrow B$), the limiting cathodic current at the disk is given by the Levich equation (Eq. 3). An anodic half-reaction may be used to detect B as it arrives at the ring electrode ($B \rightarrow C + n_R e^-$). The anodic limiting current at the ring electrode (i_{LR}) can be expressed in terms of the cathodic limiting current at the disk electrode (i_{LD}) as follows:

$$i_{LR} = -i_{LD} (n_R / n_D) N_{max} \quad (4)$$

Where N_{max} is the maximum theoretical collection efficiency, which is a unitless value indicating the fraction of material from the disk that is theoretically expected to arrive at the ring.[40] This value of N_{max} is influenced by the geometric characteristics, such as the shape and size, of the ring and disk electrodes. As long as the electron transfer kinetics are suitably rapid and concentration-dependent, the collection efficiency is primarily governed by the geometric factors of the electrodes, regardless of the specific electrochemical reactions taking place. The key point is that N_{max} is determined solely by the physical dimensions of the electrodes and is

not influenced by the electrochemical processes themselves. The ring-disk geometry provides a distinctive approach to investigate the behavior of unstable catalytic intermediates, enabling in situ monitoring as a direct function of the applied reaction conditions.

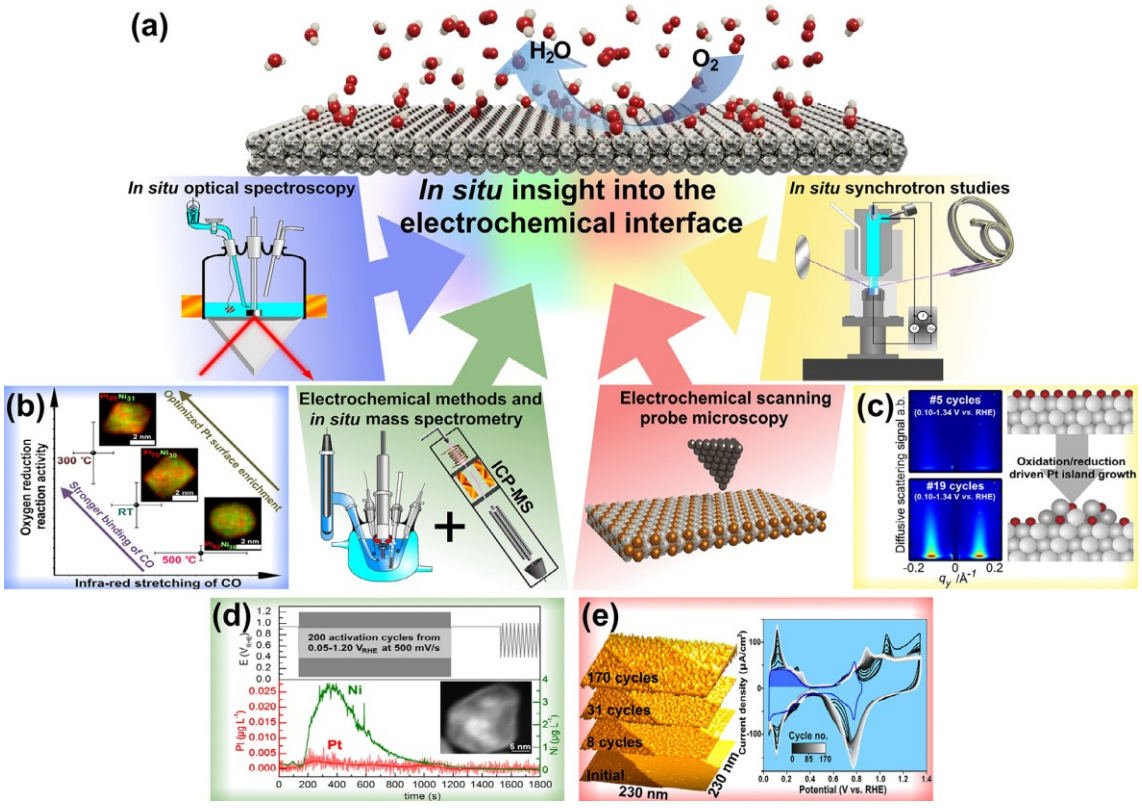

Fig. 10 Selection of in situ characterization of the electrochemical interface of relevance for the ORR: (**a**) Schematic representation of a selection of techniques that provide an in situ insight into ORR electrocatalysts: in situ optical spectroscopy, electrochemical methods combined with mass spectrometry, electrochemical scanning probe microscopy and in situ X-ray characterization techniques. (**b**) Correlation of CO stretching from in situ FTIR with the ORR activity of Pt-Ni nanoparticles. (**c**) Pt(111) oxidation and catalyst roughening probed by in situ GI-XRD. (**d**) Electrochemical flow cell combined with ICP-MS monitoring the Pt/Ni dissolution during dealloying of Pt-Ni nanoparticles. (**e**) In situ STM images and CVs of a Pt(111) electrode surface during oxidation-reduction cycles. Adapted from Reference [81].

Another important advantage of solid electrode voltammetry is the ability to trace formed intermediates of electrochemical reactions in situ and identify the active phase of catalysts at a

particular applied potential by combining it with various techniques. To date, there are numerous advanced in situ electrochemical characterization techniques that enable probing the electrode-interface at the atomic and molecular level, as depicted in Fig. 10. These techniques include in situ spectroscopy,[73, 74] in situ mass spectrometry,[36] scanning probe microscopy,[75, 78] in situ synchrotron studies,[81] and in situ quartz crystal microbalance (QCM).[76, 77] The integration of these in situ electrochemical techniques is pivotal in yielding valuable insights into the intricate relationships between a material's structure and its reactivity, as well as the underlying mechanisms of reactions.

In the context of this thesis, our focus will primarily be on elucidating the principles of the electrochemical quartz crystal microbalance (EQCM) to illustrate the seamless synergy between voltammetry and quartz crystal microbalance (QCM) technology. The potential usefulness of QCM as a mass sensor was first demonstrated by Sauerbrey in 1959. The technique relies on acoustic wave devices based on piezoelectric resonators whose frequency responses are related to the mass change per unit area at the QCM surface.[82] According to the Sauerbrey equation (Eq. 5), a mass change (Δm) at the surface induces a shift in the resonance frequency (Δf) of the QCM, enabling the detection of sub-monolayer weight changes, as illustrated in the Fig. 11.[83]

$$\Delta m = -C_m \Delta f \quad (5)$$

Where C_m is the proportionality constant that depends only on the properties and dimensions of the quartz crystal resonator.

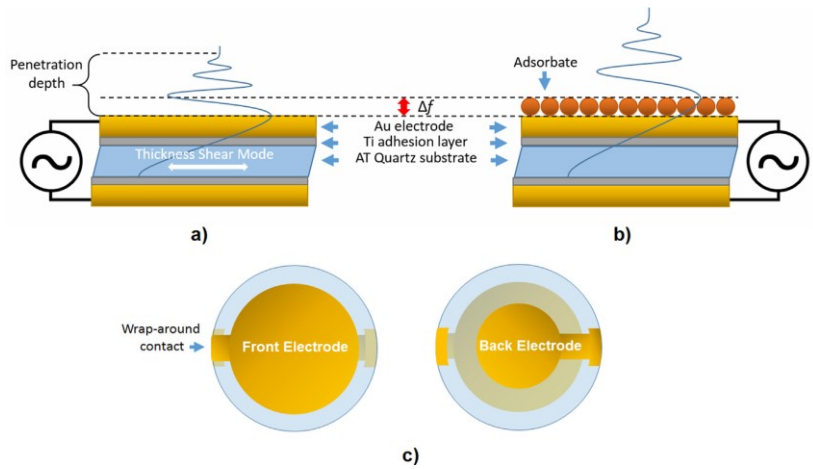

Fig. 11 Schematic cross-section of a quartz crystal showing thickness sheer oscillation overlaid with the fundamental resonance wave (**a**), the change in oscillation resonance frequency (△f) when a rigid mass adsorbs to the surface (**b**) and front and back view of a quartz crystal with wrap-around electrode typically used for liquid measurements (**c**). Adapted from Reference [83].

The applicability of the QCM was extended to liquid based systems by Nomura and Okuhara in their publication in 1982, sparking the development of the EQCM for the field of interfacial electrochemistry.[84] Initially, QCMs were mainly used as thin film deposition monitors to control the film thickness. However the combination of electrochemistry and QCM operation has opened up new insights into interfacial electrochemical processes.[85, 86]

For a long time, directly uncovering whether a reaction process is homogenous or heterogenous has been a challenge.[39, 85] Although spectroscopic evidence can confirm the existence of different types of intermediates at the electrode interface, it remained unclear whether the formed intermediates remained in solution or in an adsorbed state on the catalyst.[69] The EQCM technique allows for the in situ measurement of mass changes occurring at the electrode as the applied potential is scanned during a CV experiment. For a homogenous reaction process, the mass response shows no significant change during different CV cycles, whereas an experiment in which a heterogeneous deposit is formed, the mass response shows a significant increase with the number of CV cycles or time in an amperometry experiment, as shown in Fig. 12. This capability of EQCM offers valuable information to distinguish between homogeneous and heterogeneous electrochemical processes at the electrode interface. However, for an extended period, any alteration in the oscillation resonance frequency of EQCM was often simplistically attributed solely to electrochemical deposition on the surface.[87] Nevertheless, numerous researchers have discovered that the calculated mass change derived from frequency changes can exceed the theoretically expected maximum amount of electrochemical deposition in electrolyte solutions,[76, 88] The underlying reasons for this phenomenon are believed to be associated with variations in solution viscosity and density resulting from shifts in the applied potential.[89] The precise quantification of these effects remains elusive, consequently constraining the accuracy of EQCM measurements.

While measuring potential (E) and current (I) might seem straightforward, confirming the precise factors responsible for the alterations in the E-I relationship in voltammetry is challenging. Fortunately, the development of in situ electrochemical methods has allowed us to gradually unveil the rich and mysterious information hidden within the voltammogram. These advanced techniques provide valuable insights into the intricate processes occurring at the electrode-interface, shedding light on the underlying mechanisms and revealing the intricate dynamics of electrochemical reactions. As a result, the voltammetry technique has become even more powerful and informative, playing a pivotal role in advancing our understanding of electrochemical processes and catalysis in various applications.

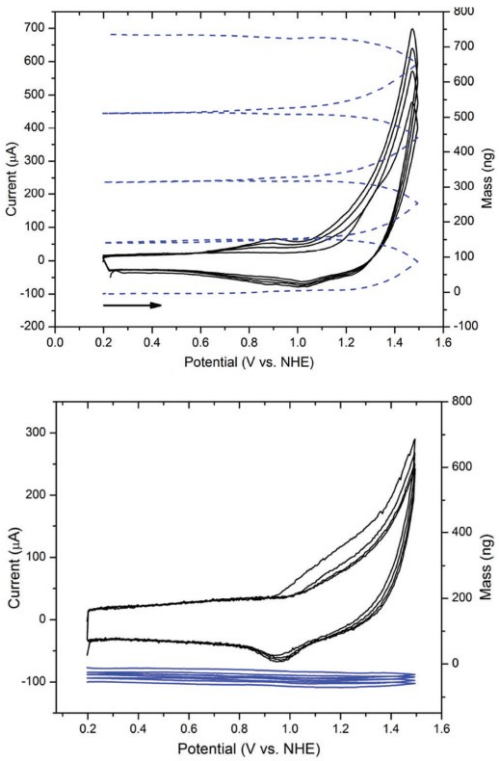

Fig. 12 Difference in the EQCM response of a deposition formed from the precursor $[Ir(Cp^*)(OH_2)_3]SO_4$ (top) and formation of a homogeneous catalyst from the precursor $[Ir(Cp^*)(pyalc)(CF_3COO)]$ (bottom).† The currents are depicted in black and the mass trace in blue. Cp*=pentamethylcyclopentadienyl; pyalc = 2-(2′-pyridyl)-2-propanolate. Adapted from Reference [85].

1.5 Remaining challenges in Voltammetry

Although the progress of in situ techniques has certainly enriched our comprehension of electrochemical processes, the fundamental challenges of understanding Faradaic and non-Faradaic currents in voltammetry persist within the broader context of energy convection systems. This thesis will concentrate on addressing the two most important fundamental questions in the realm of voltammetry.

The question one: *What is the relation between the applied potential and the surface charge, and the structure of both the surface and surface-liquid interface?*

The relation between the applied potential and surface charge

In an electrochemical reaction, the electrode potential serves as the driving force for the electrochemical process.[62] As the net surface excess charge changes through the potentiostat during positive or negative scanning of the potential, the electrochemical potential of the electrons on the working electrode either increase or decrease accordingly. The change in potential leads to a redistribution of ions, resulting in the formation of an electric double layer (EDL) at the interface between the electrode and the surrounding solution.[61] The EDL formation is an example of a non-Faradaic process, as shown in Fig. 4C.

A crucial concept in understanding the excess charge and potential effects at the electrode interface is the potential of zero charge (PZC). The PZC is defined as the potential at which no net excess charge exists on the electrode surface, but it is essential to recognize that the PZC is significantly influenced by the surface characteristics and material properties of the electrode.[90-92] Initial insights into the concept of excess charge and the PZC were obtained from measurements of the surface tension at mercury-electrolyte interfaces, as depicted in Fig. 13A.[93] In these surface tension measurements, the liquid mercury electrode provides a clean and well-defined surface structure, and a wide potential range where only non-Faradaic processes occur. The PZC is identified as the potential at which the surface tension is maximal (Fig. 13B).[93] However, conducting such surface tension measurement is not feasible at solid materials.

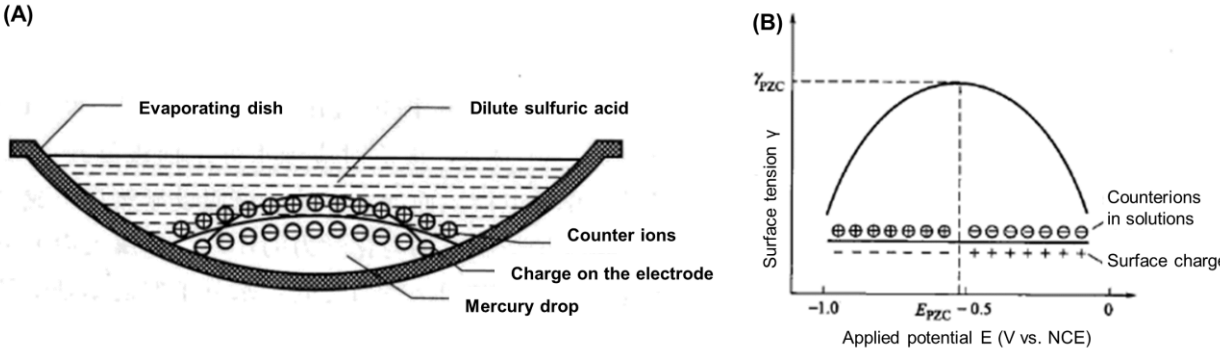

Fig. 13 (**A**) The surface leveling phenomenon when a double layer is formed on the surface of a mercury drop. The figure illustrates the scenario with a negatively charged surface. (**B**) Electrocapillary curve of the dropping mercury electrode (DME), where E_{PZC} is the potential of zero charge, and γ_{PZC} is the surface tension at the E_{PZC}. Adapted from Reference [94].

Variations in the surface excess charge will induce a redistribution of ions, resulting in the non-Faradaic currents that can be observed in a CV. Electrochemical capacitance measurements calculated from the current responses in a voltammogram have played a crucial role in understanding the electrochemical interface structure on the electrode surface, particularly for solid electrodes. For example, in a voltammetry measurement, a differential capacitance (C) is determined using the following equation:

$$C = \frac{I}{\nu \times S} \quad (6)$$

where I is the current (A), ν is the scan rate (V/s) and S is the electrode surface (m^2). Based on the research of the differential capacitance, the classical model for EDL known as the Gouy-Chapman-Stern (GCS) model was developed and show in Fig. 14.[95, 96] In the GCS model, the total capacitance of the electric double layer (C_{GCS}) can be divided into two components: the inner layer or Helmholz capacitance (C_H) and the diffuse layer or Gouy-Chapman capacitance (C_{GC}):

$$\frac{1}{C_{GCS}} = \frac{1}{C_H} + \frac{1}{C_{GC}} \quad (7)$$

In a measurement to determine the non-Faradaic current, there is a key premise that the current observed in the voltammogram should be entirely attributed to non-Faradaic currents.

Non-Faradaic currents are electrostatic in nature and result from the adsorption or desorption of ions from the electrolyte solution onto the electrode surface without any involvement of electron transfer processes.

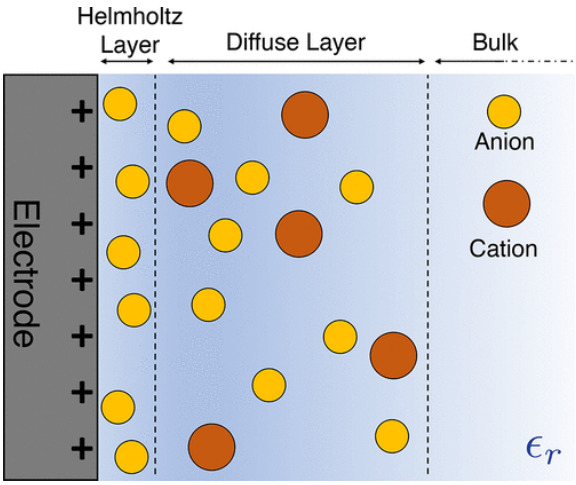

Fig. 14 Schematic representation of the electrical double layer at a planar electrode according to the GCS model. Anions are displayed in yellow, and cations are in orange. They are immersed in a dielectric continuum of relative permittivity ϵ_r. Adapted from Reference [96].

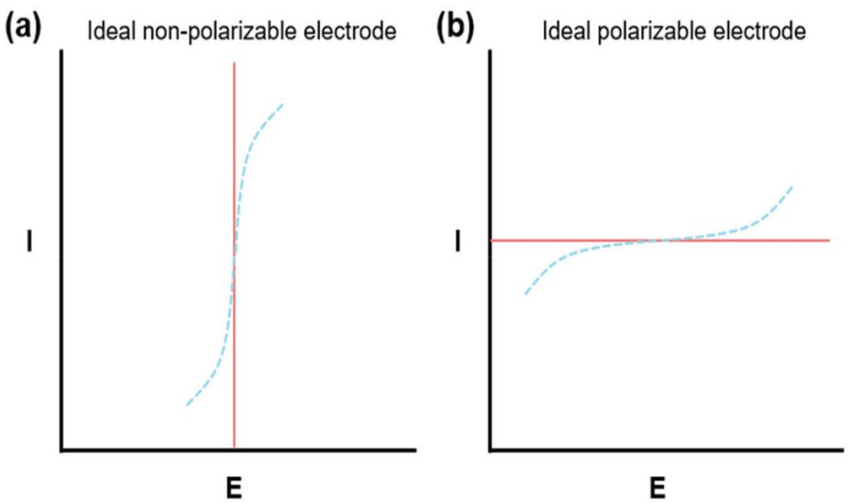

Fig. 15 Polarization behaviors of (**a**) an ideal non-polarizable electrode and (**b**) an ideal polarizable electrode (red lines). Blue dotted lines indicate that the practical electrode deviates from the ideal situation beyond a certain current or potential range. Adapted from Reference [97].

Polarization is defined as "*the divergence of the electrode (or cell) potential (E) from its equilibrium value (E_{eq}) for a cell or electrode possessing a distinct equilibrium potential*" , according to the dictionary of electrochemistry.[98] In the context of voltammetry, the process can be considered as a potentiostatic polarization, i.e. driven by the potentiostat. Fig. 4B and C illustrates two ideal current responses that an electrode may have when the applied potential is changed.

An electrode that exhibits no charge transfer across the electrode-solution interface during polarization is referred to as an ideal polarized electrode (as indicated in the red line of the Fig. 15b). Its behavior is analogous to that of a capacitor (Fig. 4C). Under this scenario, where the capacitance remains constant, the current response maintains constant, resulting in the manifestation of a rectangular shape of the CV, governed by the relationship wherein the current is directly proportional to the scan rate (Eq. 8).

$$I = C \times \nu \quad (8)$$

Moreover, a consistent current flows until a sufficient amount of charge (q) has accumulated to be balanced on the charge of the electrode surface, following the equation (Eq. 9).

$$\frac{\mathrm{d}q}{\mathrm{d}E} = C \quad (9)$$

In reality, a solid electrode is more complex, both in terms of physical and chemical characteristics of the electrode surface, including the crystallographic orientation, surface defects, surface roughness, the presence of adsorbed species, and any modifications or coatings.[61, 99] When the potential changes, various chemical processes, including electron transfer from the electrode structure to electrolytes and solvents in the solutions, can alter the current response in the potential region of polarization.

The concept of an ideal non-polarized electrode is therefore a hypothetical one, representing an electrode where a Faradaic current can flow freely without any change in potential from its equilibrium value. In this scenario, where there is no diffusion, the electrode reaction is considered to be infinitely fast, resulting in an infinite current density (as indicated

in the red line of the Fig. 15a). However, this ideal situation is not achievable in reality. When the potential continues to change, the surface concentration of the reactant must decrease, leading to an decreased flux of electrons towards the surface. Eventually, depletion effects of reactant come into play, and an infinite current response for an ideal non-polarization process becomes impossible. In practical terms, no electrode can be truly non-polarizable, as there will always be some limitations and factors that influence the electrochemical processes at the electrode-solution interface. The actual behavior of a solid electrode lies somewhere between the ideal polarized and ideal non-polarizable scenarios (as indicated by the blue dots in the Fig. 15).[97]

One of the challenges in electrochemical measurements is the difficulty of separating the non-Faradaic current arising from the electric double layer (EDL) from the Faradaic current caused by reactions that involve charge transfer. When a redox reaction occurs, the resulting Faradaic currents will be entangled with the non-Faradaic current of the EDL. As a result, it becomes challenging to precisely determine the exact potential of zero charge (PZC) and how the excess charge that has accumulated on the electrode surface changes, as the real EDL capacitance is unknown. Over time, researchers have developed more complex physicochemical models by considering various factors in addition to the classical Gouy-Chapman-Stern (GCS) model.[96] These factors include the field-dependent orientation of water molecules, the discreteness of adsorbed ions, and quantum effects of metal electrons.[61, 95, 100] However, attempts to obtain perfect or even satisfactory fits of the capacitance by adjusting multiple factors can easily lead to overfitting, if the model becomes too complex, and thereby loses any predictive accuracy in the process. To allow for sufficient experimental data to calibrate these models on, it is essential to perform precise experiments that directly trace the change of the excess charge on the electrode surface without being influenced by chemisorption or chemical reactions.

Discovering novel in situ techniques or exploring the potential applications of existing in situ methods that allow for the direct observation and measurement of changes in the excess charge on the electrode surface, that is separated from any current contributions from chemisorption processes or redox reactions, is of utmost importance. Such methodologies

would provide valuable insights into the intricate question "*What is the relation between the applied potential and surface charge?*" Accordingly, this thesis tackles precisely such an exploration of existing methods. These advancements would significantly enhance our understanding of complex electrochemical processes and pave the way for more accurate modeling and interpretation of electrochemical data.

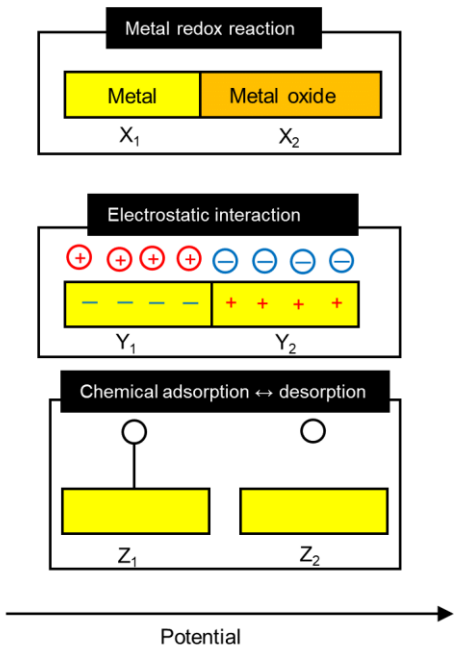

Fig. 16 Schematic representation illustrating three potential electrochemical processes occurring when the potential changes on a metal electrode. X_1 and X_2 depict alterations in the electrode surface between metal and metal oxide with changes in the applied potential. Y_1 and Y_2 correspond to positive and negative excess charges, respectively, attracting counterions electrostatically. Z_1 and Z_2 signify the chemical adsorption and desorption process of ions, respectively.

The structure of the surface and surface-liquid interface

The difficulties in comprehending the solid-liquid interface structure, where the solid electrode interfaces with the solution, arise not only from the interplay between Faradaic and non-Faradaic currents but also from the structural alterations occurring on the electrode due to

the presence of chemisorbed electrolytes, solvents, and even concurrent corrosion or passivation processes.[35, 101, 102] All these processes are influenced by changes in potential.

In a voltammogram, a solid electrode can undergo oxidation and reduction processes, resulting in different regions based on the metal region (X_1) and metal oxide region (X_2), as depicted in Fig. 16. Within both the metal region and the metal oxide region, there coexist different electrostatic interactions (represented as Y_1 and Y_2) and various chemical adsorption and desorption phenomena (represented as Z_1 and Z_2). Concerning the interface structure at the metal region (X_1), a significant challenge arises in quantification of the ion distribution at the solid – liquid interface. This task is complicated by the difficulty of discerning between non-Faradaic and Faradaic currents in CVs. To address this, the key lies in discovering a direct analytical method capable of identifying the surface charge density, which plays a direct role in governing the ion distribution at the interface.

In the realm of the interface structure, another challenge is the accurate identification of the oxide structure in the oxide region (X_2). The structure of the metal oxide can be highly diverse depending on the specific environment and continuously changes under different electrochemical conditions.[102] These structural variations contribute significantly to the overall complexity of comprehending the electrochemical interface structure.

The question two: *How does the structure of the solid-liquid interface affect catalytic activity?*

Due to climate change and depleting petroleum supplies, the development of energy conversion technologies, such as fuel cells,[103, 104] water electrolysis,[39, 105] batteries and pseudocapacitors,[7, 58, 63] and CO_2 to fuel conversion,[106, 107] has become increasingly important. The efficiency of these energy conversion systems is largely determined by catalytic processes involving oxygen, namely the oxygen evolution reaction (OER) and the oxygen reduction reaction (ORR), which are known to be sluggish reaction that limit the performance of electrolyzes and fuel cells respectively.[108, 109] Reversibility refers the ability of a chemical reaction to proceed in both the forward and reverse directions under the same conditions. A reversible reaction implies that when the potential is changed in one direction, the reaction

proceeds, and when the potential is reversed, the reaction goes backward. Reversible reactions allow the system to efficiently convert between chemical and electrical energy with minimal losses. Fig. 16 illustrates the half-cell reactions and steady-state polarization curves for the hydrogen evolution reaction (HER) and hydrogen oxidation reaction (HOR) as well as the ORR and OER. It is evident that the catalytic reactions involving oxygen are far more irreversible than hydrogen catalysis, as achieving desirable reaction rates for OER and ORR requires significant overpotentials, even in presence of the best-performing electrocatalysts.[110]

Decades of research on the ORR and OER have not fully elucidated what makes a good catalyst. One significant discovery from computational chemistry community is that the optimal binding strength of oxygen-containing species is crucial for high electrocatalytic performance, aligning with the Sabatier principle, a primary paradigm of heterogeneous catalysis. Rossmeisl, Norskov and others have found that the adsorption energies of these intermediates follow a linear scaling relationship.[111, 112] While computational chemistry provides valuable insights, contradictions often arise between theoretical predictions and electrochemical experiments. Some solid materials with weak oxygen binding energy exhibit excellent oxygen catalysis under specific conditions, while scaling relations would predict low activities.[67, 80, 113] Gold, for instance, known for its inertness, binds oxygen relatively weakly. It indeed demonstrates poor activity for OER and ORR in acidic solutions, yet becomes an excellent catalyst for these reactions in alkaline solutions.[70]

The intricacy of electrocatalytic activity cannot be exclusively attributed to the individual properties of the material, but rather emerges from the combined characteristics of the entire interface environment. This includes the electrode material, the solvent and electrolyte present in the solution, and the structure of the solid-liquid interface. Each of these interactions can affect the electrode surface, thereby exerting a profound influence on the course of the reaction process. Traditional electrochemical theories, like the empirical Butler-Volmer theory, offer limited insights into how the precise solid-liquid interface structure affects the catalytic performance of the electrode in real environments.[108] It is therefore crucial to undertake fundamental investigations to understand how the structure of the solid – liquid interface of catalytic materials influence the catalytic performance. The success of such investigations is

fundamentally rooted in a profound understanding of the interfacial structure, as sought in the first research question. Given the dynamic changes in the catalyst structure during catalytic processes, a genuine representation of the surface structure of the catalyst remains elusive. Similarly, identifying which interactions at the surface-liquid interface hold significance remains a challenge. The existing models, although built upon simple principles predicting scaling relations, are limited in their capacity to elucidate strategies to circumvent these relations. The lack of clear insights into structure - activity correlations underscores the necessity for more comprehensive research, spanning fields such as electrochemistry and materials science, conducted under conditions that mirror real-world scenarios.

Our aim is to gain a profound understanding of the intricate interplay between electrode materials and the complex electrolytic environment within the context of electrocatalytic reactions. This holistic perspective is crucial for uncovering the underlying mechanisms, establishing correlations, and ultimately bridging the knowledge gap that hinders the development of efficient and effective catalytic processes.

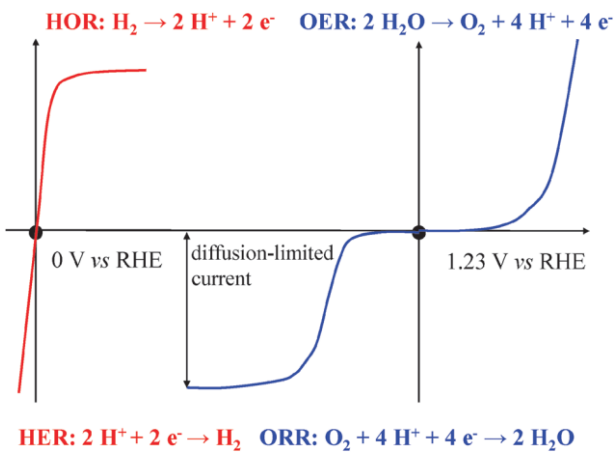

Fig. 16 The polarization curves for two pairs of the key energy-related electrochemical reactions and their overall reaction equations. Red and blue curves refer to the hydrogen-involving and oxygen-involving reactions, respectively. The lines are not drawn to scale. Adapted from Reference [109].

1.6 Structure of the thesis

In this thesis, our attention will be directed towards addressing the two fundamental questions outlined in section 1.5, i.e. *What is the relation between the applied potential and surface charge, and the structure of both the surface and surface-liquid interface?* and *How does the structure of the solid-liquid interface affect catalytic activity?*

To address the two research questions, we conducted an in depth investigation using CV techniques on gold in solutions of varying pH, employing a range of different in situ characterization techniques, such as in situ Surface–Enhanced Raman Spectroscopy (SERS), rotating disk electrode (RDE) techniques, rotating ring-disk electrode (RRDE) techniques, and electrochemical quartz crystal microbalance (EQCM) measurements. Gold, being the noblest metal, is exceptionally well-suited material to carry out such studies and has historically played a pivotal role in pioneering fundamental breakthroughs. Notably, gold's unique properties, including its status as the noblest metal and minimal strength of chemisorption of electrolytes onto its surface, have been well-established.[114-116] These attributes significantly simplify the complexity of the interface structure when using gold as the material of choice.

Our study concentrated on the two core remaining challenges outlined in section 1.5, beginning with a comprehensive investigation into the interface structure within the metal region (X_1) and the oxide region (X_2), respectively. Drawing from the outcomes of these investigations, we formulated various theoretical frameworks to elucidate how the interface structure evolves as a function of various stimuli. Building upon the insights garnered from the first research question regarding the interfacial structure, we were able to comprehend the pH-dependent nature of the oxygen reduction reaction (ORR) and oxygen evolution reaction (OER) activities, as well as the structural alterations accompanying these catalytic processes.

In **Chapter 2**, an in-depth exploration was undertaken to investigate the phenomenon of "peak separation behavior" observed in CVs during gold oxide reduction. The phenomenon involves a scenario where the reduction peak of gold oxide appears singular in an acidic solution, but splits into two peaks in neutral and alkaline solutions. Historically, a conventional model, known as the hydrous oxide model, was utilized to explain this behavior. This model attributed the two reduction peaks to the reduction processes of the inner-monolayer and the outer hydrous layer of the metal oxide surfaces, respectively. Despite its extensive use, the hydrous oxide

model has its limitations, leading to inconsistencies. The central objective of this chapter was to rigorously investigate the inconsistencies intrinsic to the conventional model concerning inner and outer oxide films.

Through rigorous analysis, we initially identified a significant error in the convention hydrous oxide model: On several occasions the a peak that should be attributed to the O_2 reduction reaction on gold was misinterpreted as an oxide reduction peak, particularly in alkaline environments. Additionally, we unveiled the existence of two distinct pH-dependent oxides. The α oxide predominantly manifests in low-pH environments, while the β oxide prevails in high-pH environment. Further study revealed that the two oxides are pivotal for the oxygen evolution reaction (OER) and lead to different OER pathways. This oxide classification was pinpointed by systematic tracing of gold oxide's reduction behavior and conducting in situ surface-enhanced Raman spectroscopy (SERS). This novel discovery of two pH-dependent oxides enabled us to establish a more precise and accurate correlation between the observed reduction peaks and the underlying oxide structures.

By thoroughly exploring the intricacies of the oxide reduction peaks across the entire pH window, we not only challenged the established hydrous oxide model but also revealed the presence of two pH-dependent oxides and their significance in the OER process. The utilization of advanced in situ analytical technique — SERS — played a crucial role in unraveling the complex oxide structure and forming a deeper understanding of the underlying oxide reduction mechanisms.

In **Chapter 3**, we explored the intriguing "non-Nernstian behavior" characterized by anomalous potential shifts in the oxide reduction peaks of CVs. Although this phenomenon had been noted in various literature reports, it was commonly attributed to solution complexity, with the underlying cause remaining enigmatic. Our study was aimed to uncover the true origin of this behavior.

Our investigation commenced by establishing a direct correlation between the potential shift of the gold oxide reduction peaks and the presence of Au^{3+} cations within oxide layer. Remarkably, this discovery not only unveiled the underlying mechanism for variations in oxide

structure across different solution environments but also elucidated why the oxide structure evolves during catalytic processes. The crucial factor lies in binding of formed Au^{3+} cations to the gold oxide.

Our exploration was facilitated by employing advanced in situ techniques, including RRDE and EQCM. These tools enabled us to probe deeply into the intricacies of the amorphous oxide structure within realistic catalytic environments. This pivotal discovery not only demystified the elusive nature of the amorphous oxide structure but also offered a dynamic perspective, providing insight into the evolving oxide structure. Furthermore, our findings highlighted the interface changes driven by electrostatic interactions involving surface gold cations, influencing the complex oxygen evolution reaction at the dynamic oxide interface.

The adept application of sophisticated methodologies like RRDE and EQCM allowed us to unravel intricacies that were previously obscured, fostering a more clear understanding of the intricate interplay among oxide structures, electrostatic interactions, and catalytic reactions at the oxide interface.

In **Chapter 4**, our focus was dedicated to unraveling the intricate current response behaviors within the electrochemical double layer region. This current encompasses both Faradaic current, involving electron transfer, and non-Faradaic current, arising from electrostatic interactions. For an extended duration, accurately identifying and quantifying these two currents has posed limitations on our understanding of the surface charge, a factor that directly influences the strength of the interfacial electric field.

Our investigation was centered on deciphering the connection between the current response in cyclic voltammetry (CV) and the frequency response observed by quartz crystal microbalance (QCM) measurements. A primary objective was to establish a quantitative framework for determination of the surface charge, even in the presence of complexities introduced by chemisorption and even the electrocatalytic oxygen reduction process.

Through our research, we devised a direct in situ method for both identifying and quantifying the surface charge. This innovative approach marked a significant advancement in our ability to unravel the interplay between the surface charges and the chemistry occurring at

the interface. Moreover, this method enabled us to directly observe the dynamic changes in the surface charge during the catalytic oxygen reduction reaction (ORR).

By systematically investigating the current response, we have not only enriched our understanding of the dynamics within the electrochemical double layer but also developed a potent toolkit for assessing surface charge variations across diverse electrochemical conditions. This achievement offers a novel perspective to examine the relation between the surface charge and the interface structure on gold, paving the way for more nuanced insights into catalytic reactions, such as ORR, and their underlying mechanisms.

Throughout this thesis, a series of foundational insights regarding electrochemical signals have been uncovered through discovered by a comprehensive integration of detailed CV behavior investigations and various in situ techniques applied to gold electrodes. These newfound insights provide a fresh standpoint, simplifying the comprehension of complex interface environments.

References

1. Reinmuth, W. H., *Analytical Chemistry* **1960,** *32* (11), 1509-1512.
2. Bard, A. K.; Zoski, C. G., *Analytical Chemistry* **2000,** *72* (9), 346A-352A.
3. Budnikov, G. K.; Shirokova, V. I., *Journal of Analytical Chemistry* **2009,** *64* (12), 1279-1288.
4. Augustyn, V.; Simon, P.; Dunn, B., *Energy & Environmental Science* **2014,** *7* (5).
5. Elgrishi, N.; Rountree, K. J.; McCarthy, B. D.; Rountree, E. S.; Eisenhart, T. T.; Dempsey, J. L., *Journal of Chemical Education* **2018,** *95* (2), 197-206.
6. Rountree, E. S.; McCarthy, B. D.; Eisenhart, T. T.; Dempsey, J. L., *Inorg Chem* **2014,** *53* (19), 9983-10002.
7. Simon, P.; Gogotsi, Y.; Dunn, B., *Science* **2014,** *343* (6176), 1210-1211.
8. Brousse, T.; Bélanger, D.; Long, J. W., *Journal of The Electrochemical Society* **2015,** *162* (5), A5185-A5189.
9. Pu, X.; Zhao, D.; Fu, C.; Chen, Z.; Cao, S.; Wang, C.; Cao, Y., *Angew Chem Int Ed Engl* **2021,** *60* (39), 21310-21318.
10. Macdonald, D. D.; Qiu, J., *Journal of Solid State Electrochemistry* **2020,** *24* (11-12), 2663-2677.
11. Mansfeld, F., *Journal of Solid State Electrochemistry* **2008,** *13* (4), 515-520.
12. Conway, B. E., *Prog. Surf. Sci.* **1995,** *49* (4), 331-452.
13. Diaz-Cruz, J. M.; Serrano, N.; Perez-Rafols, C.; Arino, C.; Esteban, M., *J Solid State Electrochem* **2020,** *24* (11-12), 2653-2661.
14. Lubert, K.-H.; Kalcher, K., *Electroanalysis* **2010,** *22* (17-18), 1937-1946.
15. Guin, S. K.; Ambolikar, A. S.; Das, S.; Poswal, A. K., *Electroanalysis* **2020,** *32* (7), 1629-1641.
16. Nong, H. N.; Falling, L. J.; Bergmann, A.; Klingenhof, M.; Tran, H. P.; Spori, C.; Mom, R.; Timoshenko, J.; Zichittella, G.; Knop-Gericke, A.; Piccinin, S.; Perez-Ramirez, J.; Cuenya, B. R.; Schlogl, R.; Strasser, P.; Teschner, D.; Jones, T. E., *Nature* **2020,** *587* (7834), 408-413.
17. Kolb, D. M., *Prog. Surf. Sci.* **1996,** *51* (2), 109-173.
18. Sarma, A. K.; Vatsyayan, P.; Goswami, P.; Minteer, S. D., *Biosens Bioelectron* **2009,** *24* (8), 2313-22.
19. Heyrovský, M., *Journal of Solid State Electrochemistry* **2010,** *15* (7-8), 1799-1803.
20. Bard, A. J., *Journal of Chemical Education* **2007,** *84* (4), 644.
21. Smutok, O.; Katz, E., *Journal of Solid State Electrochemistry* **2023**.
22. Hájková, A.; Vyskočil, V.; Barek, J.; Němcová, V. In *The current role of polarography in the light of the coming 90th anniversary of its discovery (a reflection)*, 2011.
23. Heyrovský, M., Catalytic Hydrogen Evolution at Mercury Electrodes from Solutions of Peptides and Proteins. In *Perspectives in Bioanalysis*, Paleček, E.; Scheller, F.; Wang, J., Eds. Elsevier: 2005; Vol. 1, pp 657-687.
24. Barek, J.; Zima, J., *Electroanalysis* **2003,** *15* (5-6), 467-472.
25. Senturk, Z., *Crit Rev Anal Chem* **2022**, 1-12.
26. Heyrovský, J.; Shikata, M., *Recueil des Travaux Chimiques des Pays-Bas* **1925,** *44* (6), 496-498.
27. Kolthoff, I. M.; Laitinen, H. A., *Science* **1940,** *92* (2381), 152-154.
28. Scholz, F., *Journal of Solid State Electrochemistry* **2010,** *15* (7-8), 1509-1521.
29. Colburn, A. W.; Levey, K. J.; O'Hare, D.; Macpherson, J. V., *Phys Chem Chem Phys* **2021,** *23* (14), 8100-8117.
30. Kolotyrkin, Y. M.; Losev, V. V.; Chemodanov, A. N., *Materials Chemistry and Physics* **1988,** *19* (1), 1-95.
31. Yi, Y.; Weinberg, G.; Prenzel, M.; Greiner, M.; Heumann, S.; Becker, S.; Schlögl, R., *Catalysis Today* **2017,** *295*, 32-40.
32. Grdeń, M.; Łukaszewski, M.; Jerkiewicz, G.; Czerwiński, A., *Electrochim. Acta* **2008,** *53* (26), 7583-7598.
33. Cherevko, S.; Topalov, A. A.; Zeradjanin, A. R.; Katsounaros, I.; Mayrhofer, K. J. J., *RSC Adv.* **2013,** *3* (37).
34. Luo, M.; Koper, M. T. M., *Nat. Catal.* **2022,** *5* (7), 615-623.
35. Chen, X.; McCrum, I. T.; Schwarz, K. A.; Janik, M. J.; Koper, M. T. M., *Angew Chem Int Ed Engl* **2017,** *56* (47), 15025-15029.
36. Gorlin, M.; Ferreira de Araujo, J.; Schmies, H.; Bernsmeier, D.; Dresp, S.; Gliech, M.; Jusys, Z.; Chernev, P.; Kraehnert, R.; Dau, H.; Strasser, P., *J Am Chem Soc* **2017,** *139* (5), 2070-2082.
37. Gorlin, M.; Halldin Stenlid, J.; Koroidov, S.; Wang, H. Y.; Borner, M.; Shipilin, M.; Kalinko, A.; Murzin, V.; Safonova, O. V.; Nachtegaal, M.; Uheida, A.; Dutta, J.; Bauer, M.; Nilsson, A.; Diaz-Morales, O., *Nat Commun* **2020,** *11* (1), 6181.
38. Trzesniewski, B. J.; Diaz-Morales, O.; Vermaas, D. A.; Longo, A.; Bras, W.; Koper, M. T.; Smith, W. A., *J. Am. Chem. Soc.* **2015,** *137* (48), 15112-21.
39. Costentin, C.; Dridi, H.; Saveant, J. M., *J Am Chem Soc* **2015,** *137* (42), 13535-44.
40. Langerman, M.; Hetterscheid, D. G. H., *Angew Chem Int Ed Engl* **2019,** *58* (37), 12974-12978.
41. Laurence D. Burke, L. D. B., Electrochemistry of hydrous oxide films. *Modern Aspects of Electrochemistry* 1986 pp 169-189.
42. Miller, F. J.; Zittel, H. E., *Analytical Chemistry* **1963,** *35* (12), 1866-&.

43. Zittel, H. E.; Miller, F. J., *Analytical Chemistry* **1965,** *37* (2), 200-&.
44. Yoshimori, T.; Arakawa, M.; Takeuchi, T., *Talanta* **1965,** *12* (2), 147-152.
45. Tonelli, D.; Scavetta, E.; Giorgetti, M., *Anal Bioanal Chem* **2013,** *405* (2-3), 603-14.
46. Walcarius, A., *Chemistry of Materials* **2001,** *13* (10), 3351-3372.
47. Alves, W. A.; Matos, I. O.; Takahashi, P. M.; Bastos, E. L.; Martinho, H.; Ferreira, J. G.; Silva, C. C.; de Almeida Santos, R. H.; Paduan-Filho, A.; Da Costa Ferreira, A. M., *European Journal of Inorganic Chemistry* **2009,** *2009* (15), 2219-2228.
48. Royzen, M.; Wilson, J. J.; Lippard, S. J., *J Inorg Biochem* **2013,** *118*, 162-70.
49. Eftekhari, A., *Journal of Power Sources* **2017,** *343*, 395-411.
50. Goodridge, F.; King, C. J. H.; Wright, A. R., *Electrochim. Acta* **1977,** *22* (4), 347-352.
51. Karlsson, R. K.; Cornell, A., *Chem Rev* **2016,** *116* (5), 2982-3028.
52. Trasatti, S., *Electrochim. Acta* **2000,** *45* (15), 2377-2385.
53. McHenry, E. J., *Electrochemical Technology* **1967,** *5* (5-6), 275-&.
54. Ikeda, H.; Saito, T.; Tamura, H., *Cleveland Section of the Electrochemical Society* **1975**, 384.
55. Tarascon, J. M.; Armand, M., *Nature* **2001,** *414* (6861), 359-367.
56. Steele, B., *Ed. W. van Gool, North Holland, Amsterdam* **1973**, 103.
57. Van Gool, W., **1973**.
58. Fleischmann, S.; Mitchell, J. B.; Wang, R.; Zhan, C.; Jiang, D.-e.; Presser, V.; Augustyn, V., *Chemical Reviews* **2020,** *120* (14), 6738-6782.
59. Scholz, F.; Leiva, E. P. M., *ChemElectroChem* **2018,** *5* (6), 849-854.
60. Trasatti, S.; Buzzanca, G., *Journal of Electroanalytical Chemistry and Interfacial Electrochemistry* **1971,** *29* (2), A1-A5.
61. Lu-Lu Zhang, C.-K. L., Jun Huang, *Journal of Electrochemistry* **2022,** *28* (2), 2108471.
62. Boettcher, S. W.; Oener, S. Z.; Lonergan, M. C.; Surendranath, Y.; Ardo, S.; Brozek, C.; Kempler, P. A., *ACS Energy Letters* **2020,** *6* (1), 261-266.
63. Noori, A.; El-Kady, M. F.; Rahmanifar, M. S.; Kaner, R. B.; Mousavi, M. F., *Chem Soc Rev* **2019,** *48* (5), 1272-1341.
64. Costentin, C.; Porter, T. R.; Saveant, J. M., *ACS Appl Mater Interfaces* **2017,** *9* (10), 8649-8658.
65. Yang, X.; Rogach, A. L., *Advanced Energy Materials* **2019,** *9* (25).
66. Simon, P.; Gogotsi, Y., *Nature Materials* **2008,** *7* (11), 845-854.
67. Ramaswamy, N.; Mukerjee, S., *The Journal of Physical Chemistry C* **2011,** *115* (36), 18015-18026.
68. Viswanathan, V.; Hansen, H. A.; Rossmeisl, J.; Norskov, J. K., *J Phys Chem Lett* **2012,** *3* (20), 2948-51.
69. Strobl, J. R.; Scherson, D., *The Journal of Physical Chemistry C* **2021,** *125* (25), 13862-13870.
70. Ramaswamy, N.; Mukerjee, S., *Advances in Physical Chemistry* **2012,** *2012*, 1-17.
71. Vesztergom, S.; Ujvári, M.; Láng, G. G., *Electrochem. commun.* **2011,** *13* (4), 378-381.
72. Dalton, F., *Electrochemical Society Interface* **2016,** *25* (3), 50-59.
73. Yang, S.; Hetterscheid, D. G. H., *ACS Catal.* **2020,** *10* (21), 12582-12589.
74. Jin, L.; Seifitokaldani, A., *Catalysts* **2020,** *10* (5), 481.
75. Wahab, O. J.; Kang, M.; Unwin, P. R., *Current Opinion in Electrochemistry* **2020,** *22*, 120-128.
76. Kautek, W.; Sahre, M.; Soares, D. M., *Ber. Bunsenges. Phys. Chem.* **1995,** *99* (4), 667-676.
77. Tsai, W. Y.; Taberna, P. L.; Simon, P., *J Am Chem Soc* **2014,** *136* (24), 8722-8.
78. Patel, A. N.; Collignon, M. G.; O'Connell, M. A.; Hung, W. O.; McKelvey, K.; Macpherson, J. V.; Unwin, P. R., *J Am Chem Soc* **2012,** *134* (49), 20117-30.
79. Mei, D.; He, Z. D.; Zheng, Y. L.; Jiang, D. C.; Chen, Y. X., *Phys Chem Chem Phys* **2014,** *16* (27), 13762-73.
80. Prieto, A.; Hern$\diamond$ndez, J.; Herrero, E.; Feliu, J. M., *Journal of Solid State Electrochemistry* **2003,** *7* (9), 599-606.
81. Escudero-Escribano, M.; Jensen, K. D.; Jensen, A. W., *Current Opinion in Electrochemistry* **2018,** *8*, 135-146.
82. Sauerbrey, G., *Zeitschrift Fur Physik* **1959,** *155* (2), 206-222.
83. Horst, R. J.; Katzourakis, A.; Mei, B. T.; de Beer, S., *HardwareX* **2022,** *12*, e00374.
84. Buttry, D. A.; Ward, M. D., *Chemical Reviews* **1992,** *92* (6), 1355-1379.
85. Schley, N. D.; Blakemore, J. D.; Subbaiyan, N. K.; Incarvito, C. D.; D'Souza, F.; Crabtree, R. H.; Brudvig, G. W., *J Am Chem Soc* **2011,** *133* (27), 10473-81.
86. Hetterscheid, D. G. H., *Chem Commun (Camb)* **2017,** *53* (77), 10622-10631.
87. Hillman, A. R., *Journal of Solid State Electrochemistry* **2011,** *15* (7-8), 1647-1660.
88. Gordon, J. S.; Johnson, D. C., *Journal of Electroanalytical Chemistry* **1994,** *365* (1), 267-274.
89. Hubkowska, K.; Łukaszewski, M.; Czerwiński, A., Quartz crystal nanobalance measurements in electrocatalysis. In *Encyclopedia of Interfacial Chemistry*, Wandelt, K., Ed. Elsevier: Oxford, 2018; pp 402-412.
90. Le, J.; Iannuzzi, M.; Cuesta, A.; Cheng, J., *Phys Rev Lett* **2017,** *119* (1), 016801.
91. Frumkin, A. N.; Petrii, O. A., *Electrochim. Acta* **1975,** *20* (5), 347-359.
92. Chen, J.; Nie, L.; Yao, S., *Journal of Electroanalytical Chemistry* **1996,** *414* (1), 53-59.

93. Payne, R., Double Layer at the Mercury-Solution Interface. In *Progress in Surface and Membrane Science*, Danielli, J. F.; Rosenberg, M. D.; Cadenhead, D. A., Eds. Elsevier: 1973; Vol. 6, pp 51-123.
94. Hamann, C. H.; Hamnett, A.; Vielstich, W., *Electrochemistry*. 2nd completely rev. and updated ed. ed.; Weinheim : Wiley: 2007.
95. Schmickler, W., *Chemical Reviews* **1996,** *96* (8), 3177-3200.
96. Jeanmairet, G.; Rotenberg, B.; Salanne, M., *Chem Rev* **2022,** *122* (12), 10860-10898.
97. Xiao, Y.; Xu, R.; Yan, C.; Huang, J. Q.; Zhang, Q.; Ouyang, M., *Advanced Functional Materials* **2021,** *32* (13).
98. Bard, A. J.; Inzelt, G.; Scholz, F., *Electrochemical dictionary*. Springer: 2012.
99. Song, J.; Wei, C.; Huang, Z. F.; Liu, C.; Zeng, L.; Wang, X.; Xu, Z. J., *Chem. Soc. Rev.* **2020,** *49* (7), 2196-2214.
100. Huang, J., *JACS Au* **2023,** *3* (2), 550-564.
101. Cherevko, S.; Zeradjanin, A. R.; Keeley, G. P.; Mayrhofer, K. J. J., *Journal of The Electrochemical Society* **2014,** *161* (12), H822-H830.
102. Ding, H.; Liu, H.; Chu, W.; Wu, C.; Xie, Y., *Chem. Rev.* **2021,** *121* (21), 13174-13212.
103. Yuan, C.; Wu, H. B.; Xie, Y.; Lou, X. W., *Angew. Chem. Int. Ed. Engl.* **2014,** *53* (6), 1488-504.
104. Stamenkovic, V. R.; Strmcnik, D.; Lopes, P. P.; Markovic, N. M., *Nat Mater* **2016,** *16* (1), 57-69.
105. Chen, X.; Aschaffenburg, D. J.; Cuk, T., *Nat. Catal.* **2019,** *2* (9), 820-827.
106. Deng, B.; Huang, M.; Zhao, X.; Mou, S.; Dong, F., *ACS Catalysis* **2021,** *12* (1), 331-362.
107. Dunwell, M.; Luc, W.; Yan, Y.; Jiao, F.; Xu, B., *ACS Catalysis* **2018,** *8* (9), 8121-8129.
108. Koper, M. T. M., *Chem. Sci.* **2013,** *4* (7), 2710-2723.
109. Jiao, Y.; Zheng, Y.; Jaroniec, M.; Qiao, S. Z., *Chem Soc Rev* **2015,** *44* (8), 2060-86.
110. Zeradjanin, A. R., *Current Opinion in Electrochemistry* **2018,** *9*, 214-223.
111. Man, I. C.; Su, H. Y.; Calle-Vallejo, F.; Hansen, H. A.; Martínez, J. I.; Inoglu, N. G.; Kitchin, J.; Jaramillo, T. F.; Nørskov, J. K.; Rossmeisl, J., *ChemCatChem* **2011,** *3* (7), 1159-1165.
112. Rossmeisl, J.; Logadottir, A.; Nørskov, J. K., *Chemical Physics* **2005,** *319* (1-3), 178-184.
113. Blizanac, B. B.; Ross, P. N.; Markovic, N. M., *Electrochim. Acta* **2007,** *52* (6), 2264-2271.
114. Peuckert, M.; Coenen, F. P.; Bonzel, H. P., *Surf. Sci.* **1984,** *141* (2-3), 515-532.
115. Burke, L. D.; Nugent, P. F., *Gold Bull.* **1997,** *30* (2), 43-53.
116. Weiher, N.; Willneff, E. A.; Figulla-Kroschel, C.; Jansen, M.; Schroeder, S. L. M., *Solid State Commun.* **2003,** *125* (6), 317-322.

一个简单误判引发的蝴蝶效应。

The butterfly effect triggered by a simple misjudgment.

2

Redefinition of the active species and mechanism of the oxygen evolution reaction on gold oxide

Abstract

Accurately identifying the active species of catalytic materials and understanding how they catalyze the oxygen evolution reaction (OER) are critical for the development of energy storage technologies. In this contribution we identify two pH-dependent active oxides by mapping the reduction behavior of gold oxide and by in situ surface-enhanced Raman spectroscopy. It was found that α oxide# is preferentially formed in an acidic solution whereas β oxide, $Au(OH)_3$, is preferably formed in an alkaline solution. In line with the presence of two different surface structures on gold, there are two OER mechanisms: one wherein water splitting occurs via proton-coupled electron transfer (PCET) steps mediated by α oxide, and a mechanism wherein electron and proton transfer are decoupled, and is mediated by a deprotonated form of $Au(OH)_3$. This identification of pH-dependent oxides offers a different perspective in our understanding of the OER mechanism on metal oxides in a full pH scale range.

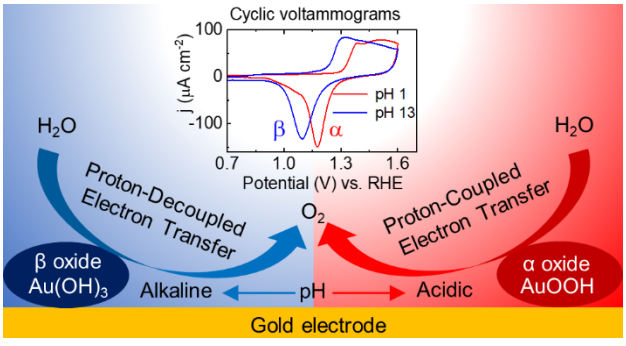

 # Note: In Chapter 2, we previously suggested that α oxide *could be AuOOH according to some literature. However, upon further examination, we've found that attributing AuOOH to α oxide is not reasonable, as it fails to account for various behaviors of α oxide. Consequently, we have reverted to the more conventional structure of gold oxide (Au_2O_3) in the subsequent chapters.*

This chapter was published as a research article: S. Yang, D. G. H. Hetterscheid*, *ACS Catal.* **10**, 12582-12589 (2020).

2.1 Introduction

More than two hundred and thirty years ago the first water electrolysis experiment was carried out by evolving hydrogen and oxygen separately at two gold electrodes.[1, 2] At present, water splitting is considered as an ideal solution to the world's renewable energy storage problem.[3-5] Using sunlight to split water into hydrogen and oxygen allows for the conversion of solar energy to chemical energy. This energy can be converted back to electricity in a fuel cell. It is widely accepted that one of the key bottlenecks in the overall water splitting reaction is the slow kinetics of the catalytic water oxidation reaction taking place at the anode.

Metal oxides are considered the best and most stable electrocatalysts for water oxidation.[3, 6, 7] In general oxidation mechanisms of noble metals involve three stages: (a) 2-dimensional (2D) electrodeposition of OH and O species on the metal surface; (b) quasi-3D surface reconstruction and place-exchange between the OH or O species and surface metal atoms; (c) growth or thickening of the oxide film.[8] Further development of the oxide film formation includes thin oxide films by stages (a) & (b) and thick hydrous oxide films by extension of oxide growth beyond the monolayer lavel.[9] Those mechanistic models are not only crucial for guiding catalyst design,[10, 11] but also for our understanding of the oxygen evolution reaction (OER) mechanism on metal oxides.[6, 12]

The initial quasi-3D metal oxide formation proceeding via reconstruction and place-exchange was identified not only on the basis of electrochemical behavior,[8, 13] but was also directly observed by atomic-resolution scanning tunneling microscopy and surface structure analyses.[14, 15] However, those in-situ observations and surface analysis techniques become less useful in the discussion of thicker oxide film formation, because these metal oxide layers are typically highly disordered.[16] Despite the lack of an effective detection of the surface structure of thicker oxide films, a concept of so-called hydrous oxide films involving thicker oxide formation was put forward on the basis of the observation that separate reduction peaks can be observed upon reduction of the metal oxide.[8, 9] In those reports the separation of the metal oxide reduction peaks was assumed to correspond to reduction of the inner-monolayer and the outer-hydrous layer of the metal oxide surfaces, respectively.

In this article we return to gold, the electrode material originally used two hundred and thirty years ago, and demonstrate that the model of inner and outer hydrous oxide films is incorrect. We identify that different active species, whose formations are pH dependent, play a role by combining the observed reduction behavior of gold oxide and in situ surface-enhanced Raman spectroscopy. Identification of this pH-dependent oxide is critical in order to fully understand the OER mechanism.

A typical and conventional OER mechanism on a metal oxide surface involves four proton-coupled electron transfer (PCET) steps at the oxide-electrolyte interface.[7, 17] The PCET-OER mechanism emphasizes the importance of optimizing the binding strength of reaction intermediates on surfaces to get high OER activities, which allows one to make OER activity predictions according to electronic structure parameters of the metal oxide.[4, 18] However the PCET-OER mechanism is not necessarily correct in all cases. OER activities that depend on the pH on the reversible hydrogen electrode (RHE) scale have been observed for various metal oxides in alkaline environment,[19-21] indicating that the OER process follows electron transfer steps that are not coupled to proton transfer on those metal oxides. The origin of pH-dependent OER mechanisms on the RHE scale has been revealed in recent years. For example, high-index facets of polycrystalline surfaces on oriented RuO_2 surfaces,[22] deprotonation of Ni-based catalysts,[23] and the covalence of metal-oxygen bonds in perovskites [21] can cause pH-dependent OER activity on the RHE scale. Moreover, many other explanations regarding OER mechanisms are only consistent in a relatively narrow pH range.[6, 21, 23] Although the difference in OER activity in acidic and alkaline solution is often related with the acid–base characteristics of the surface,[17, 24] lack of a clear explanation for these so-called “acid–base characteristics” limits our understanding of water splitting in a full pH range. In this manuscript we show that the mechanism wherein OER occurs on gold depends strongly on the surface structure of gold oxide, and that proton and electron transfer are coupled under acidic conditions, whereas these are decoupled during the OER at alkaline conditions.

2.2. Experimental section

2.2.1 General.

All glassware was thoroughly cleaned to remove impurities by overnight submersion in an aqueous 0.5 M H_2SO_4 solution mixing with 6.3 mM $KMnO_4$, followed by removal of excess $KMnO_4$ on the glassware in diluted H_2SO_4 and H_2O_2. The glassware was subsequently rinsed five times and boiled two times in Millipore MilliQ water (resistivity = 18.2 MΩ cm). Prior to electrochemical experiment, the glassware was boiled once in MilliQ water. Alumina suspensions (1.0, 0.3, and 0.05 μm) were obtained from Buehler. Electrolyte solutions were prepared with Suprapur® (Merck) reagents and MilliQ water. pH measurements were done using a Hanna Instruments HI 4222 pH meter which was calibrated using IUPAC standard buffers.

2.2.2. Electrochemical measurements.

All electrochemical measurements were conducted with an Autolab PGSTAT 12, 204 and 128N potentiostats in combination with Autolab NOVA software and carried out in conventional single compartment three-electrode glass cells at around 25 °C. A PEEK encapsulated gold electrode (A = 0.0314 cm^2, Metrohm) was used as working electrode, and a gold wire was the counter electrode, while a reversible hydrogen electrode (RHE) was employed as the reference electrode. Before every experiment the working electrode (the PEEK encapsulated gold) was manually polished for 2 minutes with 1.0, 0.3, and then 0.05 μm alumina suspensions on Buehler cloth polishing pads, followed by sonication in MilliQ water for 10 minutes. At the same time, the counter electrode (the gold wire) was flame annealed and rinsed with MilliQ water. The reference electrode (RHE) consisted of a Pt wire was connected via a Luggin capillary and continuously bubbled with H_2 gas during measuring.

The concentration of electrolyte solution was kept at 0.1 M for different pH solutions from pH 1-13 were obtained by mixing 0.1 M H_2SO_4, NaOH and Na_2SO_4. Unless stated otherwise, pH 1-13 represent solutions with fixed pH value comprising H_2SO_4, NaOH or Na_2SO_4 in this article. Dissolved oxygen in solution was removed prior to measurements by aeration with argon (purity grade 5.0) for at least 30 min. Argon was kept flowing above the solution during experiments. The onset potential of OER is acquired by intersection of tangents between the baseline and the rising current in the positive scan of Cyclic voltammograms, as shown in Fig.

S1.[25] Tafel analysis was done at steady state conditions and was used to understand OER reaction mechanism (see Fig. S10a&b).[26]

2.2.3 In situ surface enhanced Raman spectroscopy (SERS).

In situ surface enhanced Raman spectroscopy (SERS) was performed with a confocal Raman microscope (LabRamHR, Horiba Yobin Yvon) with an Olympus 50 × microscope objective, which was not immersed in the electrolyte, into a 5 µm spot on the electrode surface, which has been documented previously.[6, 27, 28] Backscattered light was filtered by a 633 nm edge filter, directed to the spectrograph and to the detector. With this configuration, a resolution of 1.2 cm^{-1} was obtained.[29] The electrochemical SERS experiments were made with an Ivium potentiostat/galvanostat (IviumStat). Figure S2 shows a schematic diagram of the electrochemical setup for in situ surface-enhanced Raman spectroscopic measurements. Each SERS was acquired with the accumulation of 100 scans with 1 s collection time.

A roughened gold surface was used as the working electrode. The working electrode was mechanically polished to a mirror finish using alumina with different grain size to 0.05 µm, rinsed with MilliQ water and sonicated for 15 min to remove all residuals of mechanical polishing. Then the gold electrode was electrochemically roughened by 25 oxidation-reduction cycles (ORC) in a 0.1M solution of KCl. The ORC were performed between -0.30 and 1.20 V vs. the saturated calomel electrode (SCE), which were held for 30 s and 1.3 s, respectively. A brownish surface was formed after roughening gold by this method.[6, 30] The quality of Au roughing can be visualized by a comparison of the current of the CV before and after Au roughing, as shown in Fig. S3. SERS spectra were recorded at 1 V vs RHE and set as the background signal and subtracted from further measurements in the same solution. Different backgrounds were set for solutions of different pH (H_2SO_4, Na_2SO_4, NaOH). All data were processed using Origin Pro 9.1.

2.3. Results and discussion

2.3.1 Inconsistencies in conventional models for the electrochemical redox behavior of gold.

In a typical cyclic voltammogram of gold (Fig.1a), the most notable oxide formation response in the positive sweep is an extended plateau rather than sharp peaks, independent of the applied pH. Formation of this plateau is attributed to the increased energy required to generate additional oxide by gradual changes in the hysteresis of the oxidation potential between Au and Au-OH species in the oxide layer.[31] It is therefore difficult to investigate the gold oxidation chemistry through this continuous oxidation process in the positive sweep. The behavior of gold in the negative sweep is more indicative of the processes taking place at its surface. Only one reduction peak can be detected in acidic solution, while the reduction peak splits into two separated peaks upon increasing the pH. Stable gold oxide with a +III oxidation state can be formed by the reaction ($2\mathrm{Au} + 3H_2\mathrm{O} \rightarrow Au_2O_3 + 6H^+ + 6e^-, E^O = 1.46\ V$), which is illustrated by the Pourbaix diagram of gold. Gold oxide with a +IV oxidation state can only be formed at a very high electric field by the reaction ($2\mathrm{Au} + 4H_2\mathrm{O} \rightarrow 2\mathrm{Au}O_2 + 8H^+ + 8e^-, E^O = 4.14\ V$).[32, 33] Consequently, Au(III) is the only oxidation state of gold present in the gold oxide layers as was shown by ex situ X-ray photoelectron spectroscopy (XPS)[34] and in situ extended X-ray absorption fine-structure (EXAFS) studies.[35] Because only one oxidation state (the trivalent) is involved, the presence of more than one reduction peak cannot be explained by different oxidation states of gold.

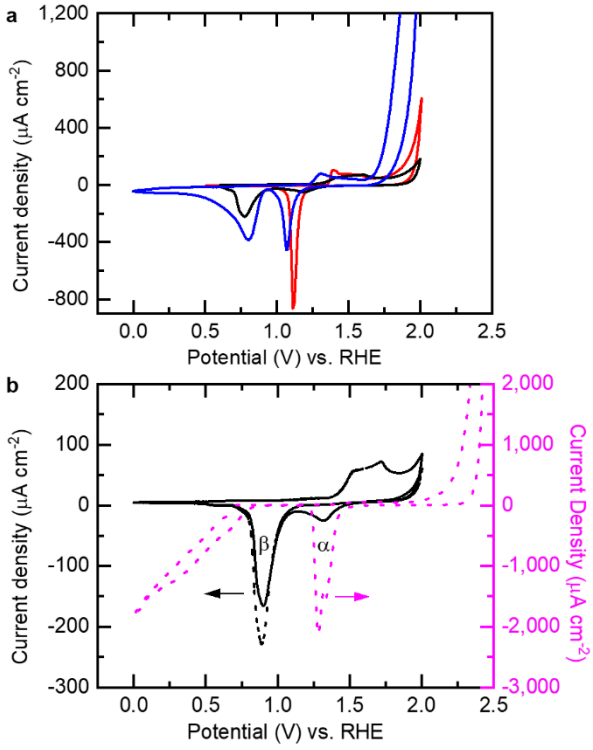

Figure 1. Electrochemical redox behavior of gold. **a**, Cyclic voltammograms (CVs) of gold between 0-2 V vs. RHE at 50 mV/s in Ar-saturated 0.1 M H_2SO_4 (red line), Na_2SO_4 (black line) and NaOH (blue line). **b**. CVs of gold vs. RHE in Ar-saturated 0.1 M Na_2SO_4 solution. Scan range of CVs: 0-2 V (black line); 0-2.7 V (pink dotted line); Black dotted line: gold was first oxidized between 1.6-1.8 V vs. RHE for 200 s, prior to recording the CV between 0-2 V vs. RHE in fresh 0.1 M Na_2SO_4 solution.

On the basis of the "separated reduction peaks" that can be observed for gold, the concept of hydrous oxide films was put forward last century.[9, 36, 37] The two main gold oxide reduction peaks have historically been assigned to a compact inner monolayer oxide and a hydrous outer layer oxide. In acidic solution the hydrous outer oxide layer was suggested to be thin enough so that its reduction peak overlaps with the reduction peak of compact inner oxides. At higher pH the thicker hydrous outer oxide layer was proposed to cause the reduction peak to split into two peaks (Fig. 1a).[31] The trivalent oxidation state of gold in all oxide forms has been regarded as consistent with the inner- and outer-layer oxide model.

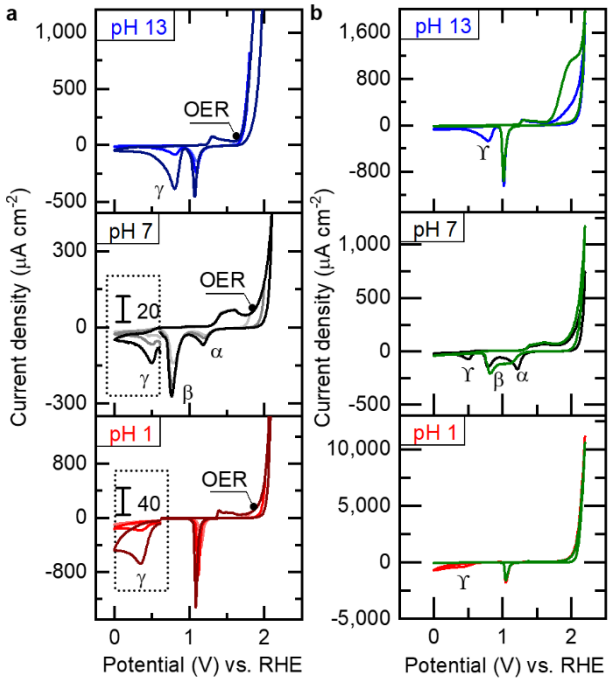

Figure 2. Recognition of the γ peak being associated with oxygen reduction. **a**, Cyclic voltammograms (CVs) of gold vs. RHE at 50 mV/s with change of scan range in Ar-saturated solution; The γ peaks are amplified (by different multiples) to clearly show their position; **b**, CVs on a gold rotating disk electrode (RDE) at 0 rpm between 0-2.2 V vs. RHE in Ar-saturated pH 1 (red line), pH 7 (black line), and pH 13 (blue line). Green line: CVs of RDE with 3000 rpm at those different pH solutions.

However, there are major problems with the inner- and outer-hydrous oxide model. In a CV of gold at neutral pH (Black line in Fig.1b), the relatively positive reduction peak corresponds to the inner monolayer of oxide, named as α oxide, and another relatively negative reduction peak is assigned to the outer hydrous oxide, named as β oxide. According to the mechanism of hydrous oxide film formation, the α peak cannot disappear because it represents the inner structure of the oxide layers. However, only the β peak, i.e. no α peak, can be detected on an oxidized gold electrode, which is oxidized at 1.6-1.8 V vs. RHE in advance (Black dotted line in Fig.1b). Moreover, when the upper limit of the positive scan is extended from 2.0 to 2.7 V (Pink dotted line Fig. 1b) the α peak increases to a huge reduction peak; this is not at all in

line with the hydrous oxide film model, where the α peak should not change in magnitude because it supposed to correspond to an inner monolayer.

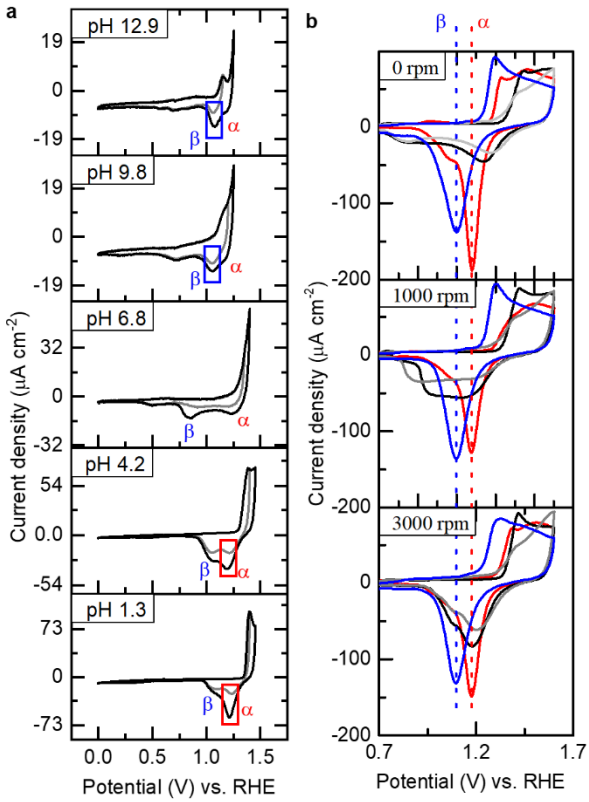

Figure 3. Identification of active gold oxides. **a**, Cyclic voltammograms (CVs) of gold in different Ar-saturated pH solutions at 50 mV/s. The upper limit of CV is kept to the range of potentials where gold oxidation occurs. **b**, CVs of of gold (RDE) between 0-1.6 V vs. RHE at rotation rates with different Ar-saturated 0.1 M electrolytes: H_2SO_4 (red line), Na_2SO_4 (black line), $NaClO_4$ (grey line), NaOH (blue line). The exact change of the potential value as a function of the rotation speed is shown in Fig. S4.

Figure 2a shows the change of CVs for gold with the increase of the upper vertex potential in acidic, neutral and alkaline solution. A new reduction peak appears once the upper limit of the voltammetry experiment was set above the onset potential of the oxygen evolution reaction (OER). In order to further identify the γ peak, the electrochemistry of gold was recorded in acidic, neutral and alkaline solution with a rotating disk electrode (RDE), as shown in Fig. 2b. It is clearly shown that the γ peak disappears upon rotation, while the reduction peaks of gold

oxide do not significantly change once O_2 is removed at a high rotation rate. This implies that the γ peak is the result of reduction of O_2. Note that the γ peak in alkaline solutions is often misinterpreted as a β peak of gold oxide reduction in the literature,[31, 37, 38] which makes the discussion of the redox chemistry of gold much more complex.

In order to eliminate the interference of O_2, CVs of gold were measured as a function of pH by keeping the upper limit of CV at the potentials at which gold oxidation begins while still below the onset potential of OER (Fig.3a). Both the α and β peaks were detected in all solutions irrespective of the pH. The CVs in alkaline solution revealed that β oxide is formed first while the applied potential is kept well below the reduction potential of α oxide; this is contrary to the past hydrous oxides films model wherein the inner α oxide must form first. Furthermore, a larger α peak was found in an acidic solution, while the β peak was significantly larger under alkaline conditions. This implies that α and β oxides are two relatively independent forms of gold oxide, whose formation is dependent on the pH. A similar result is obtained when the solution was changed from a Na_2SO_4 solution to a $NaClO_4$ solution, which means there is little influence of the electrolyte (Fig. S5).

2.3.2 Redefinition of the active gold oxides.

The initial stage of gold oxidation has been extensively discussed in the past.[8, 13] Hydroxide ion under alkaline conditions and water under acidic conditions, first chemisorb on gold to form $Au\text{-}OH_{ads}$. The $Au\text{-}OH_{ads}$ would continue to convert to $Au(OH)_3$ by place exchange reactions between Au and OH^-. The initial gold oxide $Au(OH)_3$ formation is in good agreement with DFT-based computational studies of the surface thermodynamics of electrochemistry of gold.[6] Since $Au(OH)_3$ relies on place exchange reactions between Au and OH^-, $Au(OH)_3$ formation should be enhanced with increasing the pH. From a comparison of CVs at different pH (Fig. 3a), the β peak therefore most likely corresponds to reduction of $Au(OH)_3$. Actually, gold(III) precipitations in alkaline media have been shown to correspond to $Au(OH)_3$ but not $Au_2O_3{\cdot}nH_2O$ according to XRD, TEM, Au Mössbauer spectroscopy, X-ray absorption spectroscopy (XAS) and thermogravimetry /differential thermal analysis (TGA/DTA) studies.[39]

It is interesting to note that the reduction potential difference of α and β oxide is roughly 0.13 ± 0.01 V in both acid and alkaline solutions, but becomes more than 0.4 V in neutral conditions (0.42V at pH 6.8). Therefore RDE experiments were conducted with varying rotation rates (Fig. 3b). At 0 rpm there is a minor positive shift of the α potential and a clear negative shift of the β peak in neutral solution compared to both acidic and alkaline media, irrespective of whether Na_2SO_4 or $NaClO_4$ was used as an electrolyte. The potential shifts of the α and β peaks in neutral media can be avoided upon increasing the rotation rates of the gold electrode. At 3000 rpm, it is clearly shown that the peak positions of α and β oxide in neutral solution coincide with the peak position of α in acid and the position of β in base. An effect of the scan rate on the peak position of the reduction peaks was investigated (Fig. S6). Both oxide reduction peaks show only a minor negative potential shift with increase of the scan rate. Their currents are linearly dependent on the scan rate, which is fully consistent with the characteristics of an irreversible oxide reduction process on the gold surface.

In situ surface enhanced Raman spectroscopy (SERS) was measured to further identify the structure of α and β oxide. The potential-dependent vibrational spectra in 0.1 M H_2SO_4, Na_2SO_4 and NaOH solution are shown in Fig. 4b-d. The observed broad frequency bands at 530-565 cm^{-1} are characteristic of the ν(Au-O) vibration, which can be detected when the applied potential is set above 1.35 V in H_2SO_4 1.45 V in Na_2SO_4, and 1.2 V in NaOH., These oxidation potentials are also consistent with the potential where gold oxidation occurs in LSV measurements (Fig. 4a). The ν(Au-O) vibration may point to oxide formation, though the band is especially broad and its frequency is easily influenced, by e.g. absorption of the electrolyte.

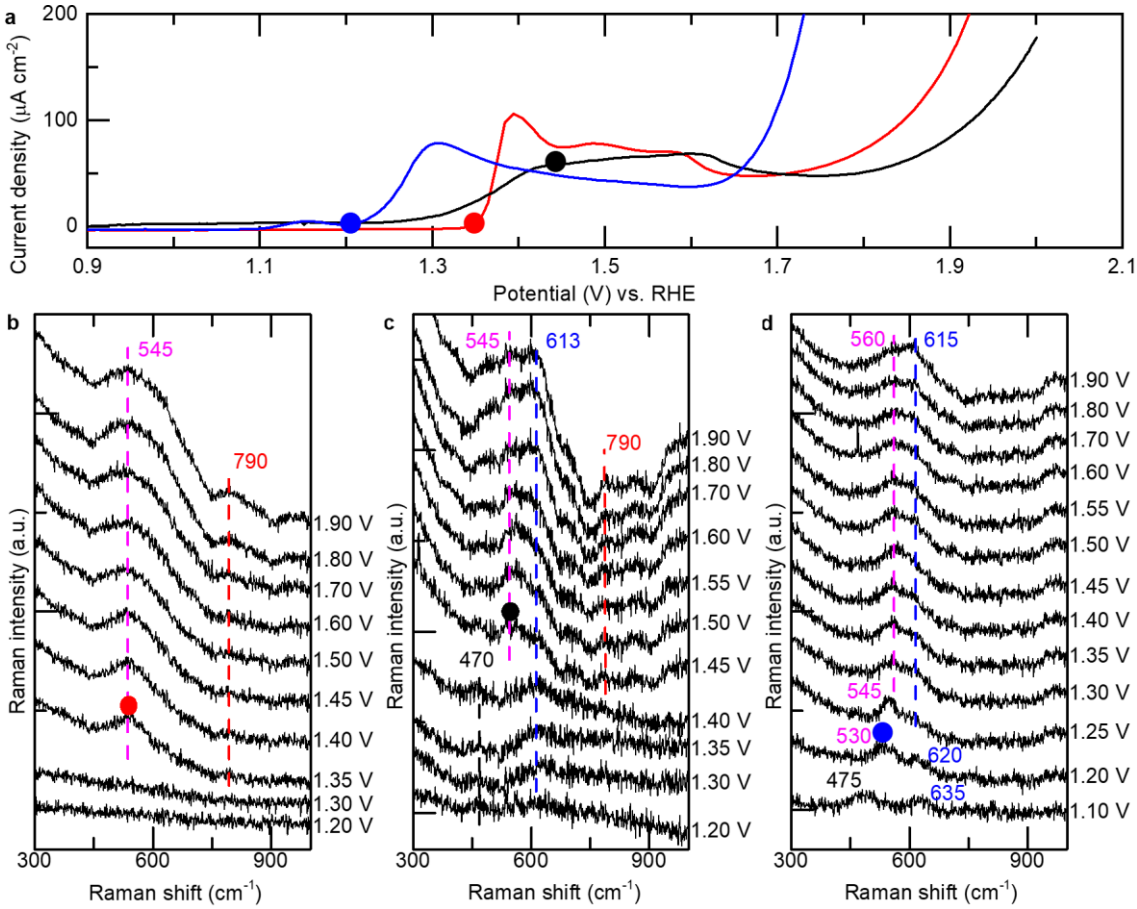

Figure 4. In situ Surface Enhanced Raman Spectroscopy (SERS) of gold oxidation. **a**, Linear sweep voltammetry (LSV) for electrocatalytic water oxidation from 0.9 V to 2 V vs. RHE at 50 mV/s on gold electrode in Ar saturated 0.1 M H_2SO_4 (red line), Na_2SO_4 (black line) and NaOH (blue line) solution. **b-d**, SERS of gold oxidation in 0.1 M H_2SO_4 (b), Na_2SO_4 (c) and NaOH (d), respectively. Oxidation potentials were recorded on the RHE scale. Solid circles represent the points where the ν(Au-O) vibration becomes visible in 0.1 M H_2SO_4 (red circle), Na_2SO_4 (black circle) and NaOH (blue circle) solutions.(Fig. S7), and/or the applied potential.[40] The wide Raman bands are most likely due to different coordination geometries and hydration states of the gold surface.[41]

The normal surface electro-oxidation of noble metals includes two steps: (i) initial deposition of O or OH species; (ii) ”oxide film” formation by place exchange with the surface metal atoms and adsorbed oxygen species along with further electron transfer.[8] These two steps

cannot be clear-cut distinguished. A band around 470-475 cm^{-1} is assigned to the reversible adsorbed OH^- (Fig. 4c-d). The ν(Au-OH^-) occurs around 400-450 cm^{-1} in 1 M KOH according to literature and shifts to higher frequencies at more positive potentials.[41] A significant frequency change from ν(Au-OH^-) at 475 cm^{-1} at 1.1 V to higher ν(Au-O), 530-560 cm^{-1}, with more positive potential in NaOH indicates a change in the oxide formation process from step (i) to step (ii). This is explained by yielding a strong ionic component to the Au-O bond energy in the process of place exchange between gold and oxygen since these gold atoms would get a more positive formal oxidation state.[41] According to the Raman spectrum of bulk-phase solid $Au(OH)_3$, the ν(Au-OH) vibration of $Au(OH)_3$ should be observed at 635 cm^{-1}.[41] Interestingly, the ν(Au-OH) vibration of $Au(OH)_3$ at 635 cm^{-1} first occurs at 1.1 V in NaOH and has a minor shift to 613 cm^{-1} with higher oxidation potentials (Fig. 4d). Note that ν(Au-OH) vibration at 613 cm^{-1} also can be observed in a Na_2SO_4 solution (Fig. 4c). This is consistent with the occurrence of the β peak in CVs of gold (Fig.3) caused by the reduction of $Au(OH)_3$.

In addition, the absence of an α peak in the CV in an NaOH solution (Fig.3a) is fully in line with the absence of a signal around 800 cm^{-1} in SERS experiments (Fig. 4d). Therefore, we assume the Raman signals recorded at approximately 820 cm^{-1} in perchloric media and at 790 cm^{-1} in sulfuric media is related to α oxide (Figure S7).

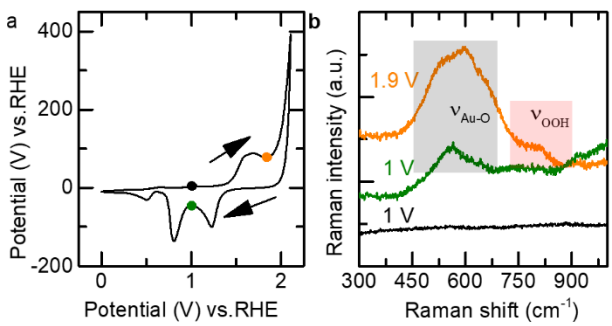

Figure 5 Reversibility of SERS of gold oxidation in 0.1 M Na_2SO_4. **a**, CV of gold electrode at 50 mV/s. **b**, SERS of gold oxidation in a positive scan and negative scan of CV.

In previous studies this band was found at values between 810 and 827 cm^{-1} in perchloric media.[6, 40, 42] A minor shift of 3-4 cm^{-1} was observed upon substitution of H_2O for D_2O.[40, 42] A significant shift of 74-77 cm^{-1} was observed upon substitution of $H_2{}^{16}O$ for $H_2{}^{18}O$ in previous

isotope studies.[6] Furthermore, the assignment of bands around 820 cm^{-1} to other forms of oxygen associated with Au (e.g. superoxo, oxo, and hydroxy) was excluded based on a series of DFT calculation.[27, 42] Therefore the signals in the range of 810 ± 20 cm^{-1} must be assigned to O-OH stretching. The O-OH stretching appears simultaneously with the appearance of ν(Au-O) of gold oxide in a H_2O_2 decomposition experiment on gold nanoparticles.[42] Tian and co-workers therefore claimed that the peak around 800 cm^{-1} must be assigned to an O-O stretch of an H-containing reaction intermediate, and not simply to an O-O stretch of peroxide. Interestingly two independent research groups (Bell and Koper) have claimed that the vibrational signal around 800 cm^{-1} was observed at least 0.4 V less positive than the onset of water oxidation in their in situ SERS experiments.[6, 40] However, according to DFT calculations of *OOH on gold and other metal oxides surface, the *OOH intermediate is the highest energy intermediate and should rapidly decompose into O_2.[7, 43] An explanation is that peroxidic species may exist within the oxide layer in acidic solution, which probably somehow related to a highly non-ordered structure.[19] However this still cannot explain the lack of an *OOH SERS signal in a low oxidation potential range at alkaline solution. Thus far these Raman signals have not been investigated in a full pH range. Koper and co-workers have put forward a more stable oxyhydroxide (AuOOH) formation mechanism in acidic solution on basis of DFT calculations. The oxyhydroxide is proposed an important role in the OER process. We therefore do consider the possibility that α oxide may predominantly be an oxyhydroxide, which structure may include *OOH species within oxide layer. In order to further confirm the relationship between α oxide and ν(OOH), an in situ SERS reversibility experiment was carried out in neutral solution (Fig. 5), where the collection time of SERS signals were increased from 1 second to 10 seconds to trace the change of SERS. Here, ν(Au-O) in the range of 500-620 cm^{-1} and ν(OOH) at 790 cm^{-1} can be detected once increase potential from 1 V to 1.9 V. When the potential is decreased from 1.9 V to 1 V the ν(OOH) will disappear, while some of the ν(Au-O) signal remains. At this potential of 1 V only β oxide can exist while α oxide is reduced. This confirms that the signal around 800 cm^{-1} does not simply represent surface-bound hydroperoxide species as an intermediate of OER, yet somehow must be related to the existence of α oxide .

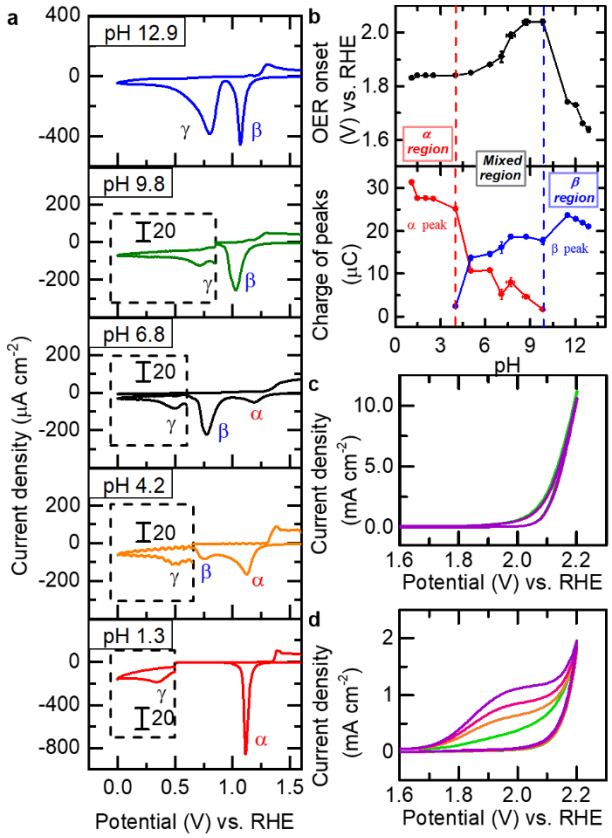

Figure 6. pH-dependent oxide formation and OER activity on gold. **a**, CVs of gold electrode showing the reduction peaks at 50 mV/s in different Ar-saturated pH solutions. Note that the scan range is 0-2V vs. RHE. The γ peaks are amplified (by different multiples) to clearly show their position. The oxidative areas in the 1.5-2 V range of these CVs, showing the OER, are shown in Fig. S8. **b**, The onset potential of OER (top) and the integrated charges of the α and β oxide reduction peaks at 50 mV/s in Ar-saturated solutions is plotted as a function of pH. The error bars represent the standard deviation of three measurements. **c-d**, CVs of gold (RDE) at 50 mV/s in Ar-saturated 0.1 M H_2SO_4 (c) or NaOH (d) solution at different rotation rates: 0 rpm (green line); 100 rpm (orange line); 1000 rpm (pink line) ; 3000 rpm (violet line); scan range is 0-2.2 V vs. RHE.

2.3.3 Two OER mechanisms leaded by two gold oxides.

Our results show that the structure of gold oxide is strongly dependent on the pH of the solution: α oxide, is preferentially formed in an acidic solution; β oxide, $Au(OH)_3$, is

preferentially formed in an alkaline solution (Fig. 6a). As with the surface structure of gold oxide, the mechanism of OER is also affected by the solution pH. The OER activity increases with decreasing pH in the low-pH region and with increasing pH in the high-pH region (Fig. S8). Very similar results have been obtained by Stahl and coworkers who revealed that different cobalt based active species exist at different pH values and have investigated the OER mechanism in a full pH region.[26] Although such pH dependent species may exist on more metal based catalysts, the lack of a clear understanding of the mechanism of pH dependent active species limits the development of better OER catalysts in case of several more metal based systems.

Figure 6b shows the OER onset potential and the integrated charges of the α and β oxide reduction peaks in a full pH window. The pH environment can be divided into three different regions: 1) The α region (pH lower than 4) in acidic solution; 2) The mixed region (pH from 4 to 10) in neutral solution; and 3) The β region (pH higher than 10) in alkaline solution. In the α region, α oxide is the only oxide that can exist in a stable form. In this window the OER onset potential is fixed at 1.84 V vs. RHE. This pH-independent OER activity on the RHE scale in the α region implies that the OER process at α oxide proceeds via four proton-coupled electron transfer (PCET) steps. In the mixed region, both α oxide and β oxide exist on the electrode surface. The amount of the two oxides changes with the pH of the solution in this region. The amount of α oxide decreases while the amount of β oxide increase with the increase of the pH. Interestingly, the OER onset potential also increases with pH. This shows that β oxide is less active for the OER than α oxide in this pH window. The OER activity level therefore strongly relies on the existence of α oxide in this mixed oxide region. In the β region at high pH values, only β oxide is present at the electrode surface. In this pH window the OER onset potential gradually decrease with an increase of the pH. This means that the OER must be pH dependent when catalyzed by β oxide, which implies that some of the proton and electron transfer steps are decoupled in the OER process in the high pH region For a reaction, the proton transfer step (PT) and electron transfer step (ET) will decouple if one of their activation energies is smaller than the activation energy of the PCET process.[17].

In order further evaluate the relationship between OER activity and the existence of oxides, a series of Tafel plots are obtained for these different pH regimes (Fig. S9, Table S1) In the α region, all Tafel plots overlap with Tafel slopes that are around 120 mV/decade. This further confirms that OER at α oxide proceeds via a pH independent process. In the mixed region the Tafel slopes are up to around 160-190 mV/decade, which is in agreement with a lower OER activity in this pH window. However the Tafel plots of β oxide appear initially at different potential regions and show that the evolution of oxygen starts earlier once the solution pH increases in β region. This is fully in line with a pH dependent OER process. Moreover, lower Tafel slopes (60-70 mV/decade) are found in the β region, which implies the decoupled OER process has a higher efficiency for oxygen evolution compared to the PCET OER process on α oxide.

The effect of solution pH on the proton affinity and electron affinity of the catalyst or reactant has been discussed during recent years.[17, 19, 44] According to acid-base characteristics of a catalyst on the surface, some catalysts have a proton affinity, which is equal to the (surface) pK_a of acid dissociation constant. If a solution pH is higher than the (surface) pK_a of a catalyst, deprotonation can occur to form a negatively charged surface leading to a decoupled electron-proton process, as shown in Fig.7. A very similar deprotonation process was observed recently in case of the water oxidation reaction at n-$SrTiO_3$.[45]

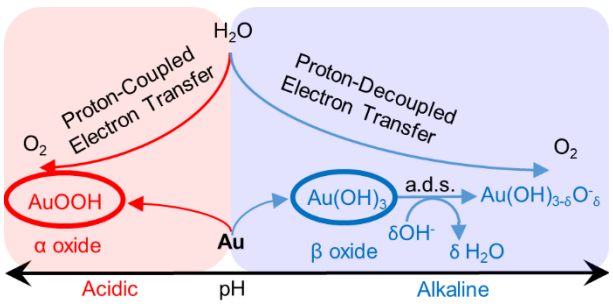

Figure 7. Proposed mechanism for electrocatalytic water oxidation on gold. In high pH region, the rate-limited step of oxygen evolution is deprotonation of $Au(OH)_3$ involving a decoupled proton transfer step.

This concept of surface deprotonation has been confirmed by thermodynamic explanations,[17] simple kinetic models,[46] and experiments.[19, 23] β oxide-$Au(OH)_3$ is also called

auric acid, and with a formula of H_3AuO_3, it is easy to speculate the existence of the (surface) pK_a of $Au(OH)_3$. Here, we do consider the influence of the acid-base characteristics of $Au(OH)_3$ ($\mathrm{Au}(OH)_3 + \sigma OH^- \rightleftharpoons \mathrm{Au}(OH)_{3-\sigma}O_\sigma^- + \sigma H_2\mathrm{O}$) to the OER process in a high pH region.

The deprotonation process of β oxide can be illustrated by rotating disk experiments (Fig. 6c-d): showing no significant changes in the OER activity at pH 1 (Fig. 6c), while the OER activity in pH 13 massively increases with an increase of the rotation rate (Fig. 6d). This indicates that the mass transport of OH^- is not a determining factor for the PCET-OER process at α oxide, but is rate limiting for the uncoupled OER process on β oxide. Note that OH^- will likely act as a proton accepter in the deprotonation process occurring at β oxide, which explains why mass transport of OH^- is part of the rate determining step in the proton-decoupled electron transfer process. However, we cannot rule out that part of our observations are due to hydroxide becoming a substrate instead of water at the more alkaline conditions.[47, 48]

2.4. Conclusions

In summary, we have reassigned the α and β reduction peaks of gold to two independent oxides on the basis of our electrochemical and in situ Raman data. It was found that α oxide is preferentially formed in in a low-pH region, and β oxide-$Au(OH)_3$ in a high-pH region. Our studies further revealed that there are two OER mechanisms taking place on a gold oxide surfaces: i.e., water splitting to O_2 through proton-coupled electron transfer (PCET) steps on α oxide; and via a path wherein proton and electron transfer are decoupled on β oxide-$Au(OH)_3$. We believe that our findings are not restricted to gold, and offer different insights in how OER occurs at metal oxides.

2.5 Associated content

Supporting information.

Figures S1-S9 and Table S1 are included in the supporting information. This material is available free of charge via the Internet at http://pubs.acs.org.

2.6 Acknowledgments

This work was supported from the China Scholarship Council (award number 201706420073).

2.7 References

1. Paets van Troostwijk, A.; Deiman, J. R., *Ann. Phys.* **1790,** *2*, 130-141.
2. De Levie, R., *J. Electroanal. Chem.* **1999,** *476* (1), 92-93.
3. McCrory, C. C.; Jung, S.; Peters, J. C.; Jaramillo, T. F., *J. Am. Chem. Soc.* **2013,** *135* (45), 16977-87.
4. Suntivich, J.; May, K. J.; Gasteiger, H. A.; Goodenough, J. B.; Shao-Horn, Y., *Science* **2011,** *334* (6061), 1383-1385.
5. Browne, M. P.; Sofer, Z.; Pumera, M., *En. Envir. Sci.* **2019,** *12* (1), 41-58.
6. Diaz-Morales, O.; Calle-Vallejo, F.; de Munck, C.; Koper, M. T. M., *Chem. Sci.* **2013,** *4* (6), 2334-2343.
7. Rossmeisl, J.; Qu, Z. W.; Zhu, H.; Kroes, G. J.; Nørskov, J. K., *J. Electroanal. Chem.* **2007,** *607* (1-2), 83-89.
8. Conway, B. E., *Prog. Surf. Sci.* **1995,** *49* (4), 331-452.
9. Burke, L. D.; Lyons, M. E. G., Electrochemistry of Hydrous Oxide Films. In *Modern Aspects of Electrochemistry* White, R. E.; Bockris, J. O. M.; Conway, B. E., Eds. Springer: New York, 1986 Vol. 18, pp 169-189.
10. Bond, G. C.; Thompson, D. T., *Catal. Rev.* **1999,** *41* (3-4), 319-388.
11. Haruta, M., *Chemphyschem* **2007,** *8* (13), 1911-3.
12. Juodkazis, K.; Juodkazytė, J.; Juodienė, T.; Šukienė, V.; Savickaja, I., *Electrochim. Acta* **2006,** *51* (27), 6159-6164.
13. Tremiliosi-Filho, G.; Dall'Antonia, L. H.; Jerkiewicz, G., *J. Electroanal. Chem.* **2005,** *578* (1), 1-8.
14. Gao, X.; Hamelin, A.; Weaver, M. J., *Phys. Rev. B* **1991,** *44* (19), 10983-10986.
15. Lipkowski, J.; Ross, P. N., *Structure of Electrified Interfaces*. Wiley-VCH: New York, 1993; Vol. 2.
16. Weiher, N. Combined in situ and ex situ studies of an electrochemical interface: investigation of anodic oxide layers on gold. Freie Universitaet, Berlin, 2003.
17. Koper, M. T. M., *Chem. Sci.* **2013,** *4* (7), 2710-2723.
18. Frydendal, R.; Busch, M.; Halck, N. B.; Paoli, E. A.; Krtil, P.; Chorkendorff, I.; Rossmeisl, J., *ChemCatChem* **2015,** *7* (1), 149-154.
19. Diaz-Morales, O.; Ferrus-Suspedra, D.; Koper, M. T. M., *Chem. Sci.* **2016,** *7* (4), 2639-2645.
20. Giordano, L.; Han, B.; Risch, M.; Hong, W. T.; Rao, R. R.; Stoerzinger, K. A.; Shao-Horn, Y., *Catal. Today* **2016,** *262*, 2-10.
21. Grimaud, A.; Diaz-Morales, O.; Han, B.; Hong, W. T.; Lee, Y. L.; Giordano, L.; Stoerzinger, K. A.; Koper, M. T. M.; Shao-Horn, Y., *Nat. Chem.* **2017,** *9* (5), 457-465.
22. Stoerzinger, K. A.; Rao, R. R.; Wang, X. R.; Hong, W. T.; Rouleau, C. M.; Shao-Horn, Y., *Chem* **2017,** *2* (5), 668-675.
23. Trzesniewski, B. J.; Diaz-Morales, O.; Vermaas, D. A.; Longo, A.; Bras, W.; Koper, M. T.; Smith, W. A., *J. Am. Chem. Soc.* **2015,** *137* (48), 15112-21.
24. Kuo, D. Y.; Kawasaki, J. K.; Nelson, J. N.; Kloppenburg, J.; Hautier, G.; Shen, K. M.; Schlom, D. G.; Suntivich, J., *J. Am. Chem. Soc.* **2017,** *139* (9), 3473-3479.
25. Huang, Z.-F.; Wang, J.; Peng, Y.; Jung, C.-Y.; Fisher, A.; Wang, X., *Adv. Energy Mater.* **2017,** *7* (23).
26. Gerken, J. B.; McAlpin, J. G.; Chen, J. Y.; Rigsby, M. L.; Casey, W. H.; Britt, R. D.; Stahl, S. S., *J. Am. Chem. Soc.* **2011,** *133* (36), 14431-42.
27. Diaz-Morales, O.; Hersbach, T. J. P.; Hetterscheid, D. G. H.; Reek, J. N. H.; Koper, M. T. M., *J. Am. Chem. Soc.* **2014,** *136* (29), 10432-10439.
28. de Ruiter, J. M.; Purchase, R. L.; Monti, A.; van der Ham, C. J. M.; Gullo, M. P.; Joya, K. S.; D'Angelantonio, M.; Barbieri, A.; Hetterscheid, D. G. H.; de Groot, H. J. M.; Buda, F., *ACS Catal.* **2016,** *6* (11), 7340-7349.
29. Lai, S. C. S.; Kleyn, S. E. F.; Rosca, V.; Koper, M. T. M., *J. Phys. Chem. C* **2008,** *112* (48), 19080-19087.
30. Gao, P.; Gosztola, D.; Leung, L. W. H.; Weaver, M. J., *J. Electroanal. Chem.* **1987,** *233* (1-2), 211-222.
31. Burke, L. D.; Nugent, P. F., *Gold Bull.* **1997,** *30* (2), 43-53.
32. Pourbaix, M., *Atlas of Electrochemical Euilibria in Aueous Solution*. National Association of Corrosion Engineers: Houston, TX, 1974; Vol. 2nd edn, p 644.
33. Burke, L. D.; Buckley, D. T.; Morrissey, J. A., *Analyst* **1994,** *119* (5), 841-845.
34. Peuckert, M.; Coenen, F. P.; Bonzel, H. P., *Surf. Sci.* **1984,** *141* (2-3), 515-532.
35. Weiher, N.; Willneff, E. A.; Figulla-Kroschel, C.; Jansen, M.; Schroeder, S. L. M., *Solid State Commun.* **2003,** *125* (6), 317-322.
36. Lohrengel, M. M.; Schultze, J. W., *Electrochim. Acta* **1976,** *21* (11), 957-965.
37. Burke, L. D.; McRann, M., *J. Electroanal. Chem. Interf. Electrochem.* **1981,** *125* (2), 387-399.
38. Doyle, R. L.; Lyons, M. E. G., *J. Solid State Electrochem.* **2014,** *18* (12), 3271-3286.
39. Kawamoto, D.; Ando, H.; Ohashi, H.; Kobayashi, Y.; Honma, T.; Ishida, T.; Tokunaga, M.; Okaue, Y.; Utsunomiya, S.; Yokoyama, T., *Bull. Chem. Soc. Jpn.* **2016,** *89* (11), 1385-1390.
40. Yeo, B. S.; Klaus, S. L.; Ross, P. N.; Mathies, R. A.; Bell, A. T., *Chemphyschem* **2010,** *11* (9), 1854-7.

41. Desilvestro, J.; Weaver, M. J., *J. Electroanal. Chem.* **1986,** *209* (2), 377-386.
42. Liu, K.; Chen, T.; He, S.; Robbins, J. P.; Podkolzin, S. G.; Tian, F., *Angew. Chem. Int. Ed. Engl.* **2017,** *56* (42), 12952-12957.
43. Rossmeisl, J.; Logadottir, A.; Nørskov, J. K., *Chem. Phys.* **2005,** *319* (1-3), 178-184.
44. Kwon, Y.; Lai, S. C.; Rodriguez, P.; Koper, M. T., *J. Am. Chem. Soc.* **2011,** *133* (18), 6914-7.
45. Chen, X.; Aschaffenburg, D. J.; Cuk, T., *Nat. Catal.* **2019,** *2* (9), 820-827.
46. Koper, M. T. M., *Top. Catal.* **2015,** *58* (18-20), 1153-1158.
47. Kafizas, A.; Ma, Y.; Pastor, E.; Pendlebury, S. R.; Mesa, C.; Francàs, L.; Le Formal, F.; Noor, N.; Ling, M.; Sotelo-Vazquez, C.; Carmalt, C. J.; Parkin, I. P.; Durrant, J. R., *ACS Catal.* **2017,** *7* (7), 4896-4903.
48. Imanishi, A.; Okamura, T.; Ohashi, N.; Nakamura, R.; Nakato, Y., *J. Am. Chem. Soc.* **2007,** *129* (37), 11569-11578.

Geocentrism
Heliocentrism
关键， The key is,
不在于他们在哪， not where they are,
而在于他们如何存在。 but how they exist.

3

Evolution of amorphous metal oxide structures during catalysis

Abstract

Amorphous metal oxide surfaces play a key role in electrocatalysis. Yet at present we know very little about the atomic structure of these amorphous metal oxide surfaces and the precise phenomena occurring at the liquid solid interface of these materials. Here we show that under oxidative conditions Au^{3+} cations are constantly being formed within amorphous gold oxide, and that these are the main cause for previously not understood phenomena such as non-Nernstian potential shifts. The Au^{3+} cations play a crucial role in the chemistry of gold oxide, where these form bonds with nucleophiles present within the amorphous gold oxide layer and the electrolyte solution, thereby dominating the interactions at the solid-liquid interface. Moreover we show that these exposed cationic sites play a crucial role not only in the structure of the solid-liquid interface but also actively take part in the catalytic water oxidation reaction.

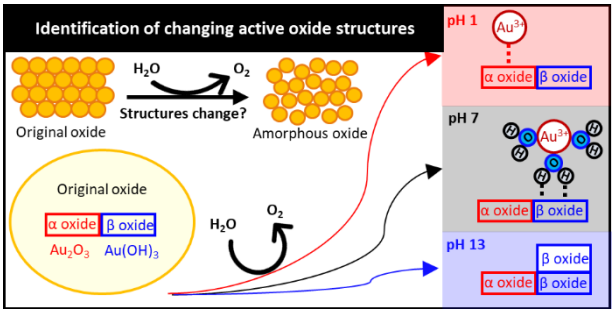

Keywords: Oxygen Evolution Reaction, Amorphous Gold Oxide, Non-Nernstian Shifts, Solid-Liquid Interface Structure, Gold Cation Interactions

3.1 Introduction

Metal oxide catalysts display a remarkable activity for a wide plethora of chemical reactions.[1-4] Despite the large interest in these catalytic materials by the scientific community, it remains a major challenge to accurately describe the real surface structure of metal oxides under realistic catalytic conditions. At present, our understanding of the metal oxide structure on the atomic–scale mainly relies on ex situ spectroscopy techniques in vacuum,[5-7] and computations on well-defined and highly symmetric metal surfaces. However, the corrosion and reconstruction of the metal oxide surface during catalysis results in the formation of amorphous structures, that are largely different than the original well–defined crystalline materials studied in vacuum and by computations.[7-10] Until now, the fundamental origins of the self–reconstruction processes occurring at these oxides during catalysis are not understood, and the active sites in these amorphous catalysts have rarely been discussed. These limitations are not only due to the lack of suitable in situ techniques to capture the complete phase transformation, but also due to a lack of a sound electrochemical theory that describes the phenomena occurring at the liquid–solid interface precisely.[7, 11] One of these ill-understood phenomena is the relationship between the peak potentials and pH under realistic conditions.

The potential where an electrochemical reaction ($Oxidant + ne^- \rightleftharpoons Reductant$) may occur can be described by the Nernst equation. This equation is written as $E = E^0 - \frac{RT}{nF} ln \frac{[reductant]}{[oxidant]}$, and defines a quantitative relationship between the measured potential (E) and the standard potential (E^0) as a function of the activities of all participating chemical species. The Nernst equation dictates that the reduction potential of a metal oxide ($M_2O_x + 2xH^+ + 2xe^- \rightarrow 2M + xH_2O$) should not change as a function of pH, with respect to the potential of the reversible hydrogen electrode ($RHE: 2H^+ + 2e^- \rightleftharpoons H_2$). The potential difference between the redox reaction and the RHE electrode should remain the same (it should follow Nernstian behavior) as both these redox reactions have the same 1:1 ratio of electrons and protons involved. However, anomalous potential shifts, i.e. “non–Nernstian behavior” are often encountered in many oxide reduction processes. Moreover, these anomalous shifts are extensively observed in many relevant electrochemical reactions such as the evolution and

reduction of oxygen,[12-14] the evolution, the oxidation of hydrogen,[15, 16] the oxidation of methanol, [17, 18] and the CO_2 reduction reaction.[19, 20] Thus far the non–Nernstian behavior of both metal oxide reduction and the aforementioned electrocatalytic reactions is rarely systematically studied. Moreover, many explanations for Non-Nernstian behavior of oxide reduction given in the past are vague (see the supplementary materials, section S1 for a brief literature overview) [11, 21]. In studies concerning catalytic reactions at metal oxide layers, it has often been assumed that the surface structure of the catalyst remains unchanged during the catalytic reaction. It is well known that this is not the case[2, 7].

In this manuscript we show that the non-Nernstian behavior of gold oxide reduction peak is intimately linked to the precise and ill-understood events that occur at the oxide surface. Gold is the noblest metal and – as so often demonstrated for new fundamental breakthroughs such as the exploration of metals' inert properties[22] and investigations into the structures of electrified interfacial water[23, 24] – the most appropriate metal for the oxide reduction studies targeted in this manuscript. It has been firmly established that the +III oxidation state is the only relevant oxidation state in gold oxide chemistry [25, 26] and the chemisorption of electrolytes on gold is weak.[27] The effect of oxidation state changes and electrolyte co–adsorption on non-Nernstian shifts therefore can be largely excluded. Employing gold electrodes, we show that non-Nernstian shifts are actually caused by the reduction of charge imbalanced Au^{3+} species. It is these Au^{3+} species that are dominating the interactions between the metal oxide surface and the electrolyte at the solid-liquid interface. In addition, these Au^{3+} species play a critical role in the oxygen evolution reaction. In general, our findings shed significant light on the atom–atom interactions taking place at the solid–liquid interface, and the reconstruction processes taking place at gold oxides during the oxygen evolution reaction.

3.2 Experimental results

The initial stages of the formation of gold oxidation during an oxidation reaction are associated with the sequential formation of sub–lattices of O and OH.[11] The O and OH chemisorb on gold to form stable Au_2O_3 (α–type) and $Au(OH)_3$ (β–type) monolayers, respectively. The existence of Au–O bonds in case of α oxide and Au–OH bonds in case of β oxide have been established previously by in situ Surface–Enhanced Raman Spectroscopy

(SERS).[8] At early stages of oxide formation, the reduction peak potentials of the formed α (E_α) and β (E_β) oxides follow the Nernst equation (fig. S1). In other words, E_α (1.23 V) and E_β (1.1 V) (see Fig. 1A) are independent of the pH providing that upper limit of the CV (E_+) is kept at an oxidation potential below 1.45 V vs RHE. However, non–Nernstian shifts can be observed when E_+ is systematically varied at higher potentials (Fig. 1A). When E_+ is set to a higher potential, E_α shifts negatively with higher E_+ in both acidic and neutral conditions (pH ≤ 10). In addition, E_α is pH dependent so that the E_α vs pH plot shows an increasing slope versus the RHE scale (Fig. 1B). A different behavior was observed in case of E_β (Fig. 1C). When E_+ is set below the onset potential of the oxygen evolution reaction (E_{OER}), E_β initially shifts negatively with increasing E_+ in the pH range of 4–10. The closer the pH of the solution is to 7, the larger the shift is that can be observed. However, these large negative shifts of E_β do not occur when E_+ is set above E_{OER}. (fig. S6) Interestingly, in alkaline solutions, E_β shows no potential shifts if E_+ is chosen below E_{OER} but moves gradually negative when E_+ is set above E_{OER} (Fig. 2C). These oxides reduction peaks show non–Nernstian behavior consistently and show only small deviations with the scan rate (0.01 to 0.5 V/s) (fig. S2). This indicates that the non–Nernstian behavior is not caused by kinetic effects, and cannot be explained by local pH effects (see fig. S2). Moreover, these non–Nernstian shifts of the α and β peaks do not depend on the cation (Li^+, Na^+, K^+, Cs^+) (see fig. S3) or the anion (SO_4^{2-} and ClO_4^-)[8] present in the electrolyte. We therefore can also exclude electrolyte adsorption playing a role.

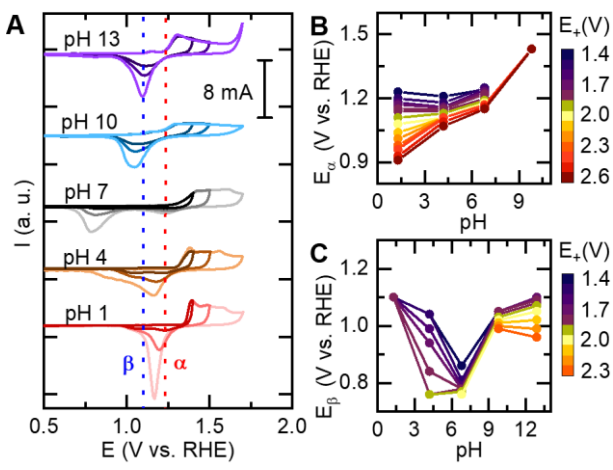

Fig. 1 The reduction of gold oxide follows non–Nernstian behavior. (**A**) CVs of gold in electrolyte solutions of different pH at 50 mV/s. 1.23 V (Red dash lines) and 1.1 V (Blue dash lines) represent the reduction peak potentials of α and β oxide at their initial formation stages, respectively (see fig. S1). (**B**) The potential of the α peak plotted as a function of pH and E_+. (**C**) The potential of the β peak plotted as a function of pH and E_+. Potentials are plotted versus RHE, i.e. a horizontal line would represent a Nernstian shift in B and C.

The release of gold cations during the oxide reduction process in acidic solutions has been reported previously in rotating ring–disk electrode (RRDE) experiment [28] and inductively coupled plasma mass spectrometry (ICP–MS) in a scanning flow cells (SFC).[29] As the +III oxidation state is the only relevant oxidation state in gold oxide chemistry (*22, 23*), we assume Au^{3+} is detected, but that we cannot fully rule out larger aggregates. Motivated by these observations, we investigated whether the existence of Au^{3+} ions which charge is not balanced due to a lack of neighboring oxide atoms cause the non–Nernstian shifts observed in these RRDE experiments (Fig. 2A). In an acidic solution, no Au^{3+} could be detected in the reverse scan in the E_+ range of 1.3 to 1.45 V, even though both α and β oxide are already formed at these potentials (Fig. 2B). When E_+ is set above 1.5 V, more and more Au^{3+} can be detected on the ring simultaneously with reduction of α oxide at the disk. Under conditions where Au^{3+} could be detected, the α peak shows a non–Nernstian shift (Fig. 2B). In an alkaline solution, the release of Au^{3+} also can be observed in case of β oxide, providing that E_+ is set at a higher potential than 1.9 V. Also these latter conditions trigger a negative non–Nernstian shift of the β peak (Fig. 2C). The α peak in acidic media and the β peak in alkaline solutions follow the same trend: If there is a non–Nernstian potential shift, this is always accompanied by the detection of gold cations on the RRDE ring.

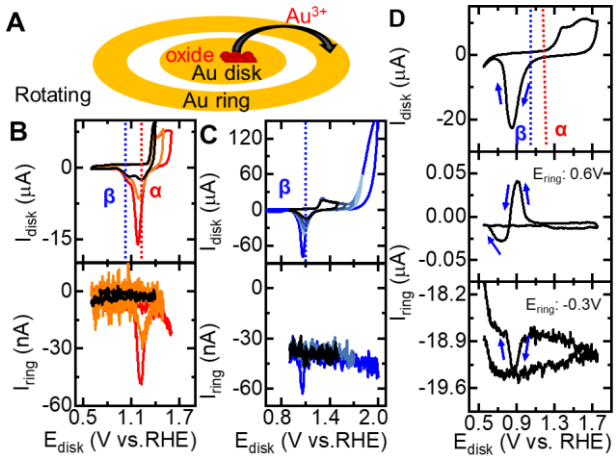

Fig.2 Au^{3+} release during gold oxide reduction. (**A**) Schematic of a rotating ring–disk electrode (RRDE) used to detect Au^{3+} that is released from the gold oxide disk and detected at the ring. (**B–D**) RRDE measurements of gold at 50 mV/s and 1600 rpm. The red and blue dashed lines represent the reduction peak potential of initial formation stage of α and β oxide, respectively. (**B**) The electrolyte is 0.1 M $HClO_4$, and E_{ring} is set at 0.6 V. (**C**) The electrolyte is 0.1 M NaOH, and E_{ring} is set at 0.9 V. (**D**) The electrolyte is 0.1 M $NaClO_4$, and E_{ring} was set at 0.6 V (middle) and –0.3 V (bottom), respectively. Different colors represent various CVs at different upper limit potentials.

When the potential of the gold ring (E_{ring}) is kept at 0.6 V in a neutral solution, initially an unusual positive current was observed on the ring, while the negative current signal that can be expected for Au^{3+} reduction was observed on the ring only after most of the β oxide is reduced at the disk (see middle part of Fig. 2D). When we match the lower potential limit ($E_{–}$) of the CV experiment with E_{β}, the negative current on the ring will emerge in the following positive scan (fig. S4A–D). This points to a delayed reduction response that is preceded by unknown oxidation process. Interestingly, the typical negative current of Au^{3+} reduction without the presence of any positive current can be observed immediately when E_{ring} is set below 0 V (see lower part of Fig. 2D).

All these observations illustrate that the observed non–Nernstian behavior is accompanied by the presence of Au^{3+} in solutions of all pH, and independent of whether α or β oxide is involved.

The mass change of the gold surface was investigated during CV experiments by characterizing the frequency response using a electrochemical quartz crystal microbalance (EQCM), whose oscillation frequency is inversely proportional to the change of mass on its surface (Fig. 3A).[30] These mass changes of the oxide reduction reaction do not only include the removal of lattice oxygen atoms, but also involve effects of the rigid double layer when bound water and electrolyte is dissociated.[31-33] While the mass changes very well fit to the amount of lattice oxygen atoms present in the oxide under conditions where no Au^{3+} is present, these mass changes become significantly larger in experiments with high E_+ where a lot of Au^{3+} is formed (fig. S8). This means that significantly more water and electrolyte molecules are bound when Au^{3+} is present at the electrode interface, and that one can use EQCM as a diagnostic tool to monitor Au^{3+} removal from the electrolyte surface. An onset potential of mass loss (E_ψ) appears during the oxide reduction process and can be correlated to E_α and E_β in solutions of different pH, shown in Fig 3B–D. When the two oxides show no non–Nernstian behavior in an acidic solution (E_+<1.5 V), the mass loss was observed only after the two oxides have been completely reduced (Fig. 3B). Once E_+ is set above 1.5 V, E_ψ immediately changes to the same potential as E_α and shifts negatively with E_α when E_+ is increased further. However, the shift of E_ψ will stop when E_+ >2.1 V while the shift of E_α continues so that the two potentials gradually separate for E_+ set in the range of 2.1 to 2.6 V. The separation between E_α and E_ψ also appears in the same range (2.1 to 2.6 V) in neutral solutions (Fig. 3C). When E_+ is lower than 1.9 V at neutral conditions, E_ψ only appears in the first half of the β peak but shows no relationship with the α peak even though a shift of the α peak can be observed. The correlation between E_ψ and E_β gradually turns into a correlation between E_ψ and E_α in a potential region from 1.9 V to 2.1 V (see fig. S6). In an alkaline solution (Fig. 3D), the correlation between E_ψ and E_β is more consistent. When E_+ is set below 1.7 V, E_ψ and E_β were found at 1.13V, and 1.10 V, respectively. When E_+ is set above 2 V, E_β and E_ψ will shift simultaneously with a constant potential difference of $E_\psi - E_\beta = 0.04$ V. Overall, the E_ψ shift shows a direct relationships with the non–Nernstian behavior of the α and/or β peaks, which have been correlated to the release of Au^{3+} by our RRDE experiments.

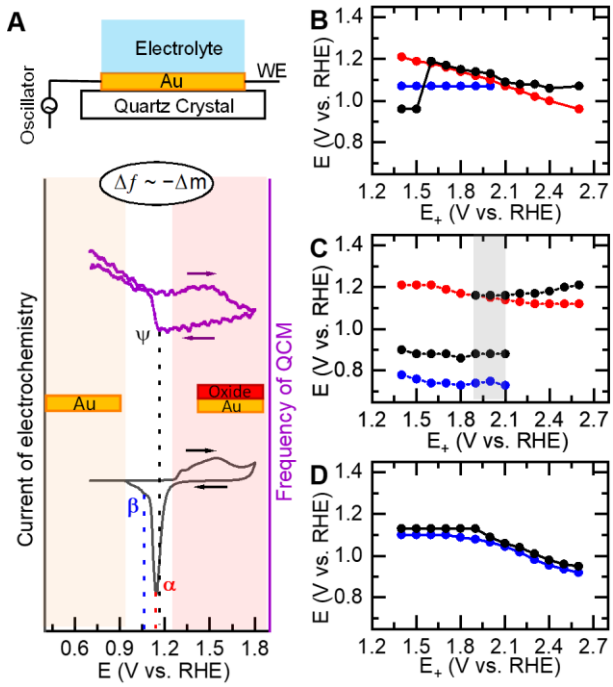

Fig. 3 The onset potential of surface mass loss during the gold oxides reduction process. (**A**) Schematic of the electrochemical quartz crystal microbalance (EQCM) used to detect the surface mass change. Show are the current (in black) and the frequency change (in purple) as function of the applied potential during an EQCM CV experiment. (**B–D**) E_α (red line), E_β (blue line) and the onset potential of mass loss (E_ψ, black line) as a function of E_+ in 0.1 M $HClO_4$ (**B**), $NaClO_4$ (**C**) and NaOH (**D**) (More details are shown in fig. S5–7).

3.3 The relationship between non–Nernstian behavior and the surface structure

Gold exhibits a strong covalent bonding character due to a relatively small 6s–5d energy gap and therefore enhanced s–d hybridization.[34] Two initial stable covalent oxides are formed by chemisorption of O and OH on gold, i.e. Au_2O_3 (α oxide) and $Au(OH)_3$ (β oxide).The Nernst equations of both α oxide ($Au_2O_3 + 6H^+ + 6e^- \rightarrow 2Au + 3H_2O$) and β oxide ($Au(OH)_3 + 3H^+ + 3e^- \rightarrow Au + 3H_2O$) dictate that the corresponding reduction potentials should not change with the pH of the solution on the RHE scale, illustrated in fig. S9. It is essential that the reaction stoichiometry is correct when the equilibrium potential of a redox half–reaction is calculated by applying the Nernst equation. At high electric fields, insulating gold oxide growth occurs via the "Mott–Cabrera" mechanism, where formed gold cations

($Au \leftrightharpoons Au^{3+} + 3e^-$) are injected into the oxide and migrate from the oxide layer into oxide–solution interface.[35] The electronic structure of such initial covalent oxides is expected to change dramatically when the amount of ionic gold ions increases within these oxide layers.

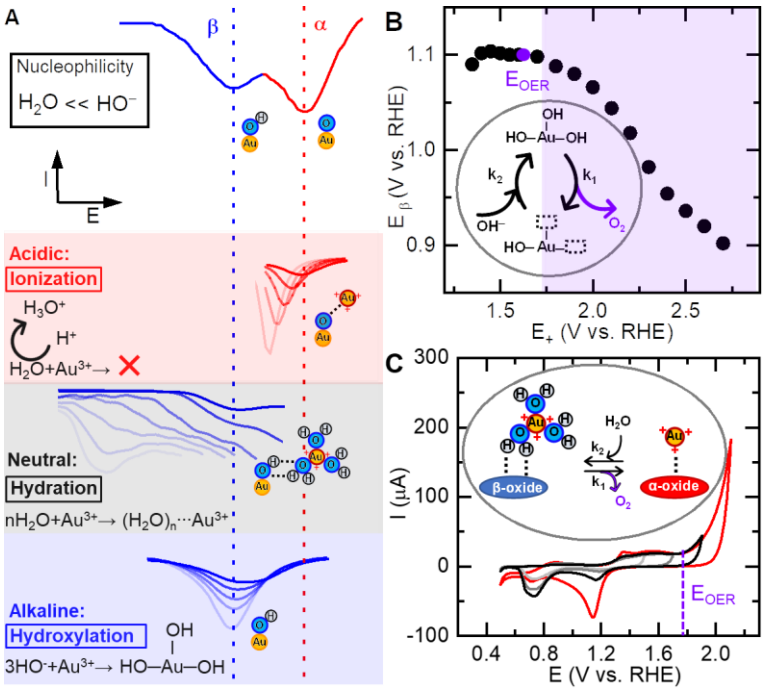

Fig.4 Ionization, Hydration and Hydroxylation of gold cation within gold as a function of pH. (A) Non–Nernstian responses for ionic bonding of Au^{3+} on α oxide (light red region); Non–Nernstian responses for hydrogen bonding of hydrous Au^{3+} on β oxide (light grey region); and Nernstian responses for covalent bonds of hydroxylated Au^{3+} on β oxide (light blue region). The red and blue dashed lines represent the reduction potential of initial formed thin α oxide (Au_2O_3) and β oxide ($Au(OH)_3$), respectively. The red and blue line represent the α and β reduction peak in CVs, respectively and their color changes (from dark to light) reflect the peak change with the increase of E_+ in different pH solutions. (**B**) The change of E_β at pH 13 when E_+ is set below and above E_{OER}. (**Insert B**) Proposed mechanism of mutual transformation of ionized Au^{3+} and hydroxylated Au^{3+} within $Au(OH)_3$ in the OER process in an alkaline solution. (**C**) The change of CVs in pH 7 when E_+ is set below and above E_{OER}. (**Insert C**) Proposed mechanism of mutual transformation between ionized Au^{3+} and hydrous Au^{3+} within α and β oxide in the OER process in a neutral solution.

Now the formation of Au^{3+} ions has been firmly established, one can discuss the potential effects of its presence on the chemistry at the gold oxide – liquid interface. The characteristic of Au^{3+} is a lack of electrons, and consequently its structure will strongly depend on the availability of good nucleophiles present in solution. As observed, the variations in metal cations and anions present in electrolytes have minimal impact on the gold oxide reduction process (Fig. S3). This suggests that highly hydrated metal cations and anions exhibit relatively uniform behavior at the gold oxide-liquid interface. Therefore, the two main types of nucleophiles present in an aqueous solution are H_2O in acidic and neutral solutions, and OH^- in an alkaline solution. Their nucleophilicity is strongly pH dependent with $H_2O << HO^-$. Since the nucleophilicity of H_2O in strong acidic solutions is very poor as the existence of hydronium anions, Au^{3+} will predominantly adsorb on the exposed oxygen sites of Au_2O_3. These oxygen sites can act as Lewis base sites to form ionic bonds with Au^{3+}. These ionic bonds of $Au_2O_3 \cdots Au^{3+}$(ionized Au^{3+}) would then stabilize α oxide resulting in the negative shift of the α peak. The formation of these ionic bonds takes time, and if the scan rate is fast enough (50 mV/s to 10 V/s), the non–Nernstian behavior of the α peak will disappear and instead a reversible free Au^{3+} reduction peak appears at 1.31 V vs RHE, illustrated in (fig. S10). The reversible reduction of free Au^{3+} has been reported previously at high temperature (365 K) and at high $HClO_4$ concentrations .[36] The ionic bonds of ionized Au^{3+} rely on the balance of electrostatic forces between the Au^{3+} ions and oxygen sites. Consequently, every oxide reduction step results in cleavage of these ionic bonds, which explains why the onset of Au^{3+} release from α oxide is coincidental with the onset of the reduction of α oxide observed in our RRDE experiment (fig. S11A).

When the pH of the electrolyte solution increases to neutral conditions, the nucleophilicity of water increases. Therefore, Au^{3+} is expected to form interaction with water molecules, rather than the exposed oxygen sites of Au_2O_3, and will form hydration shells (hydrous Au^{3+}). Such a hydration shell can also easily stabilize β oxide–$Au(OH)_3$ through hydrogen bonding interactions that cause an obvious potential shift of the β peak. The competition between ionized Au^{3+} and hydrous Au^{3+} can be monitored by the change of the two reduction peaks (α and β) in a pH range between 4 and 7 (fig. S12). The non–Nernstian behavior of the α and β oxide

reduction peaks will disappear when the rotation rate of the RDE experiments is set at 3000 rpm. This is in agreement with an efficient removal of Au^{3+} upon rotation, as it is merely attached via weak non covalent interactions (fig. S13A–B).

Formation of Au^{3+} bound to the electrode surface via ionic or hydration shell interactions can be observed by Non–Nernstian shifts of E_α and E_β and can be traced by the EQCM signal E_ψ (Fig. 3). (see the supplementary materials, section S3) There the presence of E_ψ does not directly relate to removal of a particular metal oxide, but rather to the presence of Au^{3+} on the oxide surface, both in case of α and β oxide. It is important to note that the EQCM can only detect mass changes at the surface and is not affected by the reduction of free Au^{3+} ions in solution. Therefore, the separation of E_α and E_ψ can be used to estimate to what extend Au^{3+} is bound to the electrode surface, or whether the gold ion has become fully solvated (see the supplementary materials, section S4). When E_+ is set above 2.1 V, E_α and E_ψ separate. This indicates that binding of Au^{3+} to the surface has become saturated and more free Au^{3+} unable to bind to the Au_2O_3 surface has escaped from the rigid interface into the diffusion layer. More specifically, taking into account the precise moment when E_ψ and E_α deviate, the amount of Au^{3+} within α oxide can be quantitatively evaluated on basis of the slope of the α oxide reduction peak in E–pH diagrams. (see the supplementary materials, section S5) With the increase of E_+, the α oxide is changing from a covalent oxide (Au_2O_3) to a covalent–ionic oxide ($Au_2O_3 \cdots xAu^{3+}$), where x represents the amount of Au^{3+} forming ionic bonds per α oxide site. Based on the increasing slope of the E–vs–pH plots (Fig. 1B), x increases from 0 to 0.4 before OER starts and quickly reaches saturation (x~0.9) at 2.1 V during the OER process (table S1). In other words, we have now largely turned the Non–Nernstian behavior of the oxide reduction reaction into a Nernstian one by including the correct amount of Au^{3+} in the reaction stoichiometry.

When the pH of the solution is further increased to alkaline conditions, the main nucleophile present in solution is OH^- rather than H_2O. OH^- can form more stable covalent bonds with Au^{3+} (hydroxylated Au^{3+}). The bonding interaction between Au^{3+} and OH^- will produce new β oxide layers on top of the initially formed β oxide. The hydroxylation process

thereby ensures the uniformity and electrical neutrality of the β oxide, which therefore shows Nernstian behavior as E_β does not shift with pH.

3.4 The relationship between non–Nernstian behavior and reconstruction of the metal oxide during the OER

Although ionized Au^{3+}, hydrous Au^{3+} and hydroxylated Au^{3+} are the preferred structures in acidic, neutral and alkaline solution, respectively, as shown in Fig. 4A. These surface structures inevitably turn to ionic Au^{3+} at high rates of the oxygen evolution reaction (Fig. S5-7). It was previously reported the O_2 is produced from lattice-oxygen atoms [37] and that the oxygen evolution on $Au(OH)_3$ follows a Proton–Decoupled Electron Transfer process at alkaline conditions.[8] Fig. 4B shows the two main steps needed to form O_2 in an alkaline solution: (1) Formation of O_2 by lattice exchange between Au–OH covalent bonds leaving exposed sites on Au; (2) regeneration of $Au(OH)_3$ by coordination of hydroxide to the exposed sites on Au. The overall process must involve a delicate balance between these two reaction steps with the independent reaction rate constants k_1 and k_2. At low oxidation potentials, where $k_1 < k_2$, $Au(OH)_3$ retains its uniformity and electrical neutrality. Under these conditions, Au^{3+} release from $Au(OH)_3$ is not observed. Further increasing E_+ must result in $k_1 > k_2$. Under these conditions, Au^{3+} release from $Au(OH)_3$ becomes apparent. This ionization process likely takes place only on the outer layer of $Au(OH)_3$. This is in line with the RRDE experiments in alkaline solutions, where Au^{3+} release is observed only when the scanning potential approaches E_β where the outer layer of $Au(OH)_3$ is reduced (fig. S11B). A similar delicate balance exists between hydrous Au^{3+} and ionized Au^{3+} in neutral conditions (Fig. 4C). When $k_1 < k_2$, stable hydration shells of Au^{3+} are present within the β oxide even if E_+ is set slightly above E_{OER}. At higher oxidation potentials, where $k_1 > k_2$ and the free sites generated by elimination of O_2 are only sparsely replenished, ionized Au^{3+} on α oxide becomes the dominant surface structure. Since these non–covalent bonds are relatively weak, the mutual transformation between ionized Au^{3+} and hydrous Au^{3+} can be effected by rotation rates and rinsing of the electrode (see the supplementary materials, section S6).

3.5 Conclusions

We have confirmed that the non–Nernstian behavior of the electrochemical reactions and the precise reaction steps occurring on the electrode surface are intimately linked. More specifically, the non–Nernstian behavior of the gold oxide reduction reaction is due to charge imbalanced Au^{3+} present in the gold oxide layers that is being reduced in a reaction wherein no protons are involved. These Au^{3+} ions play a pivotal role in the surface chemistry of gold oxide and the chemical processes occurring that the solid-liquid interface. At the solid–liquid interface Au^{3+} is stabilized by ionic interactions with the gold oxide surface at acid conditions, via hydration shells under neutral conditions and upon hydroxide binding at alkaline conditions. Equilibria between these binding modes of Au^{3+} play a critical role in the OER mechanism wherein Au^{3+} is continuously formed by evolution of dioxygen from lattice oxides, and is continuously quenched upon replenishment by water or hydroxide. We believe that this chemistry may not be restricted to gold and will also occur on other metal oxides during many relevant electrocatalytic reactions. Overall, this work provides a new perspective on how the structure of amorphous oxides changes during a catalytic process, which is seen as one of the most challenging scientific questions for a long time.

3.6 Experimental procedures

Resource availability

Lead contact Further information and requests for resources should be directed to and will be fulfilled by the corresponding author, Dennis G. H. Hetterscheid (d.g.h.hetterscheid@chem.leidenuniv.nl).

Materials availability: This study did not generate new unique reagents.

Data and code availability

All data needed to evaluate the conclusions in the paper are present in the paper or the supplemental information. Full experimental procedures are provided in the supplemental information.

3.7 Acknowledgements

This work was supported from the China Scholarship Council (award number 201706420073).

3.8 References

1. Yuan, C.; Wu, H. B.; Xie, Y.; Lou, X. W., *Angew. Chem. Int. Ed. Engl.* **2014,** *53* (6), 1488-504.
2. Song, J.; Wei, C.; Huang, Z. F.; Liu, C.; Zeng, L.; Wang, X.; Xu, Z. J., *Chem. Soc. Rev.* **2020,** *49* (7), 2196-2214.
3. McCrory, C. C.; Jung, S.; Peters, J. C.; Jaramillo, T. F., *J. Am. Chem. Soc.* **2013,** *135* (45), 16977-87.
4. Hwang, J.; Rao, R. R.; Giordano, L.; Katayama, Y.; Yu, Y.; Shao-Horn, Y., *Science* **2017,** *358* (6364), 751-756.
5. Cheng, X.; Fabbri, E.; Nachtegaal, M.; Castelli, I. E.; El Kazzi, M.; Haumont, R.; Marzari, N.; Schmidt, T. J., *Chem. Mater.* **2015,** *27* (22), 7662-7672.
6. Wang, J.; Gao, Y.; Kong, H.; Kim, J.; Choi, S.; Ciucci, F.; Hao, Y.; Yang, S.; Shao, Z.; Lim, J., *Chem. Soc. Rev.* **2020,** *49* (24), 9154-9196.
7. Ding, H.; Liu, H.; Chu, W.; Wu, C.; Xie, Y., *Chem. Rev.* **2021,** *121* (21), 13174-13212.
8. Yang, S.; Hetterscheid, D. G. H., *ACS Catal.* **2020,** *10* (21), 12582-12589.
9. Gerken, J. B.; McAlpin, J. G.; Chen, J. Y.; Rigsby, M. L.; Casey, W. H.; Britt, R. D.; Stahl, S. S., *J. Am. Chem. Soc.* **2011,** *133* (36), 14431-42.
10. Bergmann, A.; Jones, T. E.; Moreno, E. M.; Teschner, D.; Chernev, P.; Gliech, M.; Reier, T.; Dau, H.; Strasser, P., *Nat. Catal.* **2018,** *1* (9), 711-719.
11. Conway, B. E., *Prog. Surf. Sci.* **1995,** *49* (4), 331-452.
12. Rao, R. R.; Huang, B.; Katayama, Y.; Hwang, J.; Kawaguchi, T.; Lunger, J. R.; Peng, J.; Zhang, Y.; Morinaga, A.; Zhou, H.; You, H.; Shao-Horn, Y., *J. Phys. Chem. C* **2021,** *125* (15), 8195-8207.
13. Beall, C. E.; Fabbri, E.; Schmidt, T. J., *ACS Catal.* **2021,** *11* (5), 3094-3114.
14. Takashima, T.; Hashimoto, K.; Nakamura, R., *J. Am. Chem. Soc.* **2012,** *134* (3), 1519-1527.
15. Subbaraman, R.; Tripkovic, D.; Strmcnik, D.; Chang, K.-C.; Uchimura, M.; Paulikas, A. P.; Stamenkovic, V.; Markovic, N. M., *Science* **2011,** *334* (6060), 1256-1260.
16. Zhang, B.; Zhang, B.; Zhao, G.; Wang, J.; Liu, D.; Chen, Y.; Xia, L.; Gao, M.; Liu, Y.; Sun, W.; Pan, H., *Nat. Commun.* **2022,** *13* (1), 5894.
17. Strmcnik, D.; Kodama, K.; van der Vliet, D.; Greeley, J.; Stamenkovic, V. R.; Marković, N. M., *Nat. Chem.* **2009,** *1* (6), 466-472.
18. Xu, C.; Tian, Z.; Shen, P.; Jiang, S. P., *Electrochim. Acta* **2008,** *53* (5), 2610-2618.
19. Chen, Y.; Li, C. W.; Kanan, M. W., *J. Am. Chem. Soc.* **2012,** *134* (49), 19969-19972.
20. Gu, J.; Héroguel, F.; Luterbacher, J.; Hu, X., *Angew. Chem. Int. Ed.* **2018,** *57* (11), 2943-2947.
21. Laurence D. Burke, L. D. B., Electrochemistry of hydrous oxide films. *Modern Aspects of Electrochemistry* 1986 pp 169-189.
22. Hammer, B.; Norskov, J. K., *Nature* **1995,** *376* (6537), 238-240.
23. Li, C. Y.; Le, J. B.; Wang, Y. H.; Chen, S.; Yang, Z. L.; Li, J. F.; Cheng, J.; Tian, Z. Q., *Nat Mater* **2019,** *18* (7), 697-701.
24. Saavedra, J.; Doan, H. A.; Pursell, C. J.; Grabow, L. C.; Chandler, B. D., *Science* **2014,** *345* (6204), 1599-1602.
25. Peuckert, M.; Coenen, F. P.; Bonzel, H. P., *Surf. Sci.* **1984,** *141* (2-3), 515-532.
26. Weiher, N.; Willneff, E. A.; Figulla-Kroschel, C.; Jansen, M.; Schroeder, S. L. M., *Solid State Commun.* **2003,** *125* (6), 317-322.
27. Burke, L. D.; Nugent, P. F., *Gold Bull.* **1997,** *30* (2), 43-53.
28. Vesztergom, S.; Ujvári, M.; Láng, G. G., *Electrochem. commun.* **2011,** *13* (4), 378-381.
29. Cherevko, S.; Topalov, A. A.; Zeradjanin, A. R.; Katsounaros, I.; Mayrhofer, K. J. J., *RSC Adv.* **2013,** *3* (37).
30. Hubkowska, K.; Łukaszewski, M.; Czerwiński, A., Quartz crystal nanobalance measurements in electrocatalysis. In *Encyclopedia of Interfacial Chemistry*, Wandelt, K., Ed. Elsevier: Oxford, 2018; pp 402-412.
31. Watanabe, M.; Uchida, H.; Ikeda, N., *J. electroanal. chem.* **1995,** *380* (1), 255-260.
32. Daikhin, L.; Gileadi, E.; Tsionsky, V.; Urbakh, M.; Zilberman, G., *Electrochim. Acta* **2000,** *45* (22), 3615-3621.
33. Kautek, W.; Sahre, M.; Soares, D. M., *Ber. Bunsenges. Phys. Chem.* **1995,** *99* (4), 667-676.
34. Wang, L. S., *Phys. Chem. Chem. Phys.* **2010,** *12* (31), 8694-705.
35. Cabrera, N.; Mott, N. F., *Rep. Prog. Phys.* **1948,** *12*, 163-184.
36. Angersteinkozlowska, H.; Conway, B. E.; Tellefsen, K.; Barnett, B., *Electrochim. Acta* **1989,** *34* (8), 1045-1056.
37. Grimaud, A.; Diaz-Morales, O.; Han, B.; Hong, W. T.; Lee, Y. L.; Giordano, L.; Stoerzinger, K. A.; Koper, M. T. M.; Shao-Horn, Y., *Nat. Chem.* **2017,** *9* (5), 457-465.

Forms of
Electric Charge
Energy Conversion
Energy Storage
复杂背后的本质是简单。
The essence behind complexity is simplicity.

4

Exploring the excess free charge distribution under catalytic conditions using a quartz crystal microbalance methodology

Abstract

Understanding the distribution of the excess free charge at electrified interfaces is pivotal for the development of various energy conversion systems, such as electrolysers and fuel cells, and energy storage systems including electrical double layer capacitors, pseudocapacitors and batteries. Nonetheless, measuring the excess free charge on a solid material directly is challenging. This study introduces the utilization of an electrochemical quartz crystal microbalance (EQCM) as an innovative approach to discern and quantify the electrode excess free charge. The EQCM exploits the oscillation frequency of a quartz crystal as a sensitive indicator of mass changes on a gold electrode. By capitalizing on the frequency response of the quartz crystal to the electrostatic attraction of free charges, this method may provide a means to identify the potential regions where a positive and a negative excess charge exist, respectively. Our study reveals the presence of a potential region where no frequency changes can be detected by EQCM, while an increase in $-\Delta f$ occurs on both sides of this region. Under the assumption that the $-\Delta f$ reflects the complete formation of excess charge, our EQCM methodology allows for identification and quantification of the excess charge even during the catalytic oxygen reduction reaction. Through a comparison of the frequency response recorded by the EQCM and the capacitance recorded by cyclic voltammetry, we can estimate the amount of excess free charge and the Faradaic charge in the entire pH scale. Furthermore, by examining the correlation between the excess free charge and the frequency response, we have constructed excess free charge distribution diagrams for both Ar and O_2 saturated solutions.These diagrams aim to visually depict how the excess charge may fluctuate at specific pH levels and applied potentials before and during catalysis.

4.1 Introduction

When an electrode is immerged into an electrolyte solution and a potential is applied, an excess free charge (either positive or negative) will emerge on the electrode surface and attract ions with an opposite charge. The precise structure of this electrified interface plays a crucial role in various energy-conversion systems such as chemical energy conversion systems (e.g. water splitting, fuel cells), and electrochemical energy storage devices (e.g. electrical double layer capacitors, pseudocapacitors, batteries).[1-6] The presence of a potential of zero charge (PZC) is a defining characteristic of the interfaces of all these systems, representing the potential at which no excess charge exists on the electrode surface.[7-9] Initial insights into the excess free charge and the PZC were gained from measurements of the surface tension at the mercury-electrolyte interface, where the PZC is pinpointed as the potential corresponding to the maximal surface tension on an electrocapillary curve.[2, 10] Surface tension measurements were deemed as a direct approach for detecting the excess free charge on liquid metal surfaces.[11] However, extending such surface tension measurements to a solid material remains impossible. Drawing motivation from the successful identification of the PZC at mercury, which divides the electrified interface into two areas with opposing excess free charges, several indirect techniques have been developed to determine the PZC in solid materials. These methodologies encompass differential capacitance measurements,[10, 12] the CO charge displacement method,[13, 14] laser-induced temperature-jump methods,[15, 16] probe molecules techniques,[17, 18] spectroscopy methodologies,[19, 20] and computational approaches.[1, 5, 7] However, all these indirect techniques become inapplicable in determination of the PZC when specific adsorption reactions accompanied with charge transfer occur simultaneously— an occurrence widespread in solid materials.[21]

Exclusion of such chemisorption effects are for example important in the determination of the PZC with the minimum differential capacity approach, wherein it is assumed that the PZC is located there where the capacitance is minimal. Here any Faradaic current resulting from chemisorption reactions will directly disrupt the calculation of the differential capacity that relies on non-Faradaic current measurements. Increasingly intricate physical-chemical models have been integrated into the classical Couy-Chapman-Stern (GCS) model, that for example

include the field-dependent arrangement of water molecules, the discrete nature of adsorbed ions, and the quantum behavior of metals.[2, 22, 23] Consequently, it is often possible to achieve a perfect fit for many capacitance profiles, by simply adjusting the model parameters. It is however imperative to corroborate these assumptions through precise experimental investigations.

Other indirect methods to measure the PZC also exhibit limitations in determining the PZC in the presence of chemisorption reactions taking place. Determination of the PZC by laser-induced temperature-jump methods relies on monitoring of the orientation of interfacial water. However, this approach is ill-suited for situations involving chemisorption, as chemisorbed species hinder the reorientation of such water molecules.[15, 16] Probe molecule approaches, in which catalytic reactions are monitored that are sensitive to electrolyte accumulation, are sometimes employed to determine the PZC. Yet these methods are problematic given that the introduction of a chemical reagent that reacts with the electrode surface, and alters the electrochemical driving force for the forward chemical reaction during the analysis. This makes it challenging to accurately determine the PZC.[17, 18] While spectroscopic methods can offer valuable insights into the type of ions that are present and how these interact with the electrode interface, determination of the PZC remains highly challenging, given that spectral changes might not always directly correlate with variations in the excess free charge. Moreover, extracting meaningful information from obtained spectra often requires advanced data analysis and modeling techniques.[19, 21]

It is crucial to highlight that the excess free charge density, rather than the electrode potential, directly governs the strength of the interfacial electric field.[24, 25] This electric field in turn influences the energy of the bonds formed between the electrode surface and adsorbates.[24] Specifically the orientation of interfacial water,[5, 26, 27] and the hydration state of ions at the interface,[28, 29] strongly depend on the excess free charge density. Therefore determining the excess free charge is important for understanding the reaction pathways and energetics occurring at the solid-liquid interface of electrodes.[30-32] Due to the absence of an appropriate in situ method to quantify the excess free charge density, most research in this area has focused on identification of the PZC rather than exact measurements of the excess charge to monitor

the excess free charge distribution.[7, 19, 24] Thus far it has remained particularly challenging to pinpoint how the charge distribution occurs at the electrode surface when specific adsorption reactions comes into play. This particularly holds when electrochemical reactions occur simultaneously with the buildup of excess charge as is typical in real environments. Under such conditions very little is known on how the excess free charge changes as a function of the applied potential. This question is the source of contentious issues within energy conversion systems, such as the extensive discussions on the role of electrolytes and solvents in electrocatalytic processes in chemical energy conversion[33-35] as well as the intricate charge storage mechanisms in the field of electrochemical energy storage.[36-38]

Motivated by the necessity for a direct method to measure the excess free charge within practical electrochemical environments, we introduce the application of an electrochemical quartz crystal microbalance (EQCM) to identify and quantify the electrode charge. The proposed EQCM method may offer a means to identify the electrode charge, thereby allowing one to shed light on the intricate interplay between the excess free charge and electrochemical processes.

4.2 Experimental results

4.2.1 Direct determination of excess free charge on EQCM

EQCM is a sensitive technique that relies on an oscillating piece of quartz which frequency of oscillation relates to the mass of the piece of quartz. In the EQCM configuration, an ultrathin gold layer – on top of the piece of quartz – functions as a working electrode (Fig. 1). During electrochemical measurements frequency alterations triggered by mass changes at the electrode surface can be detected. In principle, these frequency changes can be converted to mass changes via the Sauerbrey equation: $\Delta m = C_f \cdot (-\Delta f)$.[39, 40] At the liquid – solid interface, alterations in frequency may not only originate from actual changes in mass of the solid electrode, but also in fluctuations of the density or viscosity of the electrolyte in the near vicinity of the electrode.[41-43]

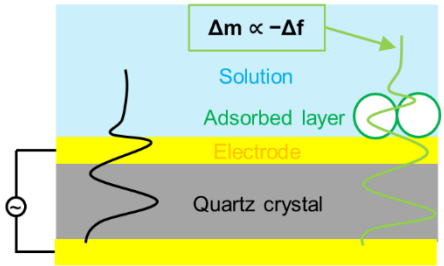

Fig. 1 EQCM setup illustrating the measurement of adsorbed molecule mass by tracking the resonant frequency change of a quartz crystal.

Initially, EQCM was primarily employed to detect Faradaic electrochemical deposition and striping processes.[39, 44] However, consistent frequency responses were even found in the regions of the electrochemical double layer (EDL) where Faradaic processes were absent.[45-47] For example, the Aurbach group investigated the effect of a range of different electrolytes on the frequency response in a series of EQCM measurements.[46] They calculated the amount of the adsorbed ions (ΔΓ) from the frequency response in EQCM measurements. It was found that ΔΓ is sensitive to the type of cations and increases as the scanning potential decreases providing that the applied potential is set below the PZC. Yet ΔΓ is sensitive to the type of anions and increases as the scanning potential increases when the applied potential is set higher than the PZC. These observations clearly show that EQCM can be used to detect the accumulation of ions at different potential regions. We have also assessed the frequency response by varying cations and anions on the gold electrode in pH 3 solutions (Fig.2). The results distinctly indicate that the frequency change is responsive to the types of cations in a low potential range (Fig. 2A) and to the types of anions in a high potential range (Fig. 2B). Our findings on gold align with the EQCM experiments on nonporous carbon conducted by Aurbach group. These observations validate that the frequency response is indeed induced by the electrostatic adsorption of different ions, driven by the excess charge on the surface. Despite the many studies have explored in-situ monitoring of changes in the electrochemical double layer structure through EQCM,[42, 45, 46] there remains a notable gap in our understanding of the distribution of ions at the solid liquid interface in a real environment. Although it has been shown that the frequency changes relate with the excess free charge, we

still do not exactly know which precise phenomenon is responsible for the frequency change. For example, an increase of excess free charge may lead to an increase of the viscosity of solution and/or concentration of the electrolyte near or at the electrode surface, and a combination of all these effects may be picked up by the EQCM experiment. Solving this knowledge gap is further complicated given that the chemical society still knows very little about the precise chemical processes occurring at the electrode interface, and how these are affected by subtle changes in electrolyte composition and pH changes.. For instance, the specific location where ion chemisorption occurs, the precise nature of the chemisorption processes, and how chemisorption reactions vary with alterations in the solution environment including the type and concentration of electrolyte types and the pH have not been identified for most electrode surfaces.. In this study, we have further investigated the direct resonant frequency response of the quartz crystal that results from the electrostatic interaction of the excess free charge in relation to the pH, and the counterions that are present in solution in case of a gold electrode.

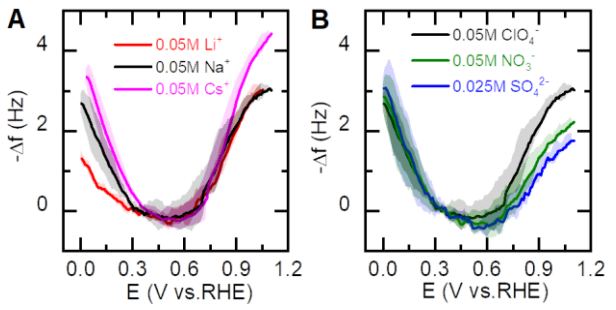

Fig. 2 the frequency change (-Δf) of EQCM on the gold electrode with change of types of ions at pH 3 solutions. (A) The frequency change (-Δf) at electrolytes with different cations. Anions is 0.05 M ClO_4^-. (B) The frequency change (-Δf) at electrolytes with different anions. Cations is 0.05 M Na^+. The shaded areas represent the range of frequency variations at every electrolyte during positive and negative scans in the three experiments.

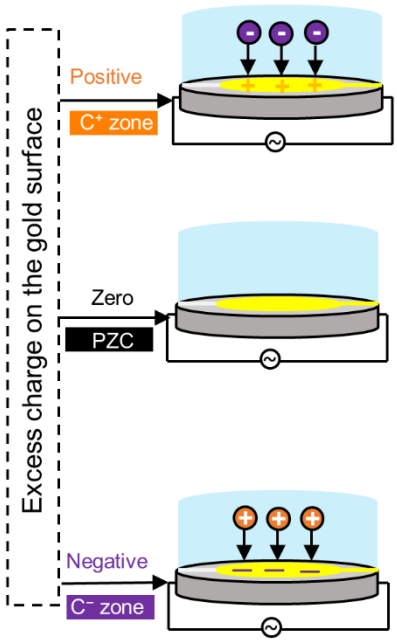

Fig. 3 Three proposed models depicting excess charge variations with a changing applied potential. When the surface possesses a positive charge, the quantity of the adsorbed anions corresponds to this positive excess charge. The associated potential region is termed the "C^+ zone". When the excess free charge remains at zero, no ions are electrostatically attracted, resulting in a potential of zero charge referred to as the "PZC". Conversely, when surface bears a negative charge, the amount of attracted cations corresponds to the negative excess charge. The corresponding potential region is labeled as "C^- zone".

In a hypothetical EQCM experiment there are three possible responses and related potential regions that one may expect to encounter (Fig. 3). The C^+ zone, the PZC, and C^- zone represent the potential regions, where a positive excess charge, zero excess charge and a negative excess charge exist, respectively. In order to establish a direct linear relationship between the excess charge and the frequency response, it is essential to first identify the correct C^+ and C^- zones.

As previous reports indicate, the chemisorption of anions frequently occur within the anticipated potential range where the PZC is expected.[20, 48, 49] Additionally, the potential region wherein the chemisorption of anions occurs is sensitive to various factors such as the electrolyte

type and concentration, as well as the pH. Cyclic voltammetry (CV) experiments on gold reveal two redox waves, which presence merely depends on the pH (Fig. 4B). One redox wave (X) is mostly visible in acidic solutions, while the other redox wave (Y) is most prevalent in more alkaline conditions. It is important to note at the position where the X or Y redox waves can be observed no significant frequency changes were observed in EQCM measurements. Instead a significant increase in $-\Delta f$ can be observed both at more positive and more negative potentials from the X and Y redox couples, as illustrated in Fig. 4A and Fig. S11.

Based on the QCM result, we can make a estimation of the potential region for the C^- and C^+ zones, respectively. To explore the correlation between excess free charge and the frequency response of the EQCM, we calculated the integrated charge of a CV (ΔQ) and the corresponding negative frequency change ($-\Delta f$) within the C^+ zone, in 0.1 M $HClO_4$, where the C^+ zone is most pronounced (Fig. 4D). This analysis distinctly reveals a proportional linear relationship without an intercept between ΔQ and $-\Delta f$, signifying that $-\Delta f$ directly corresponds to changes in the excess free charge in the C^+ zone. Additionally, in the C^- zone in 0.1 M NaOH, an inversely proportional relationship without an intercept between ΔQ and $-\Delta f$ was observed, indicating that $-\Delta f$ directly corresponds to changes of the excess charge in the C^- zone as well. (Fig. 4C) Furthermore, we have calculated ΔQ at different potential windows and found that the linear relationship between ΔQ and $-\Delta f$ is disrupted at a potential where the redox couples X and Y can be observed (Fig. S4).

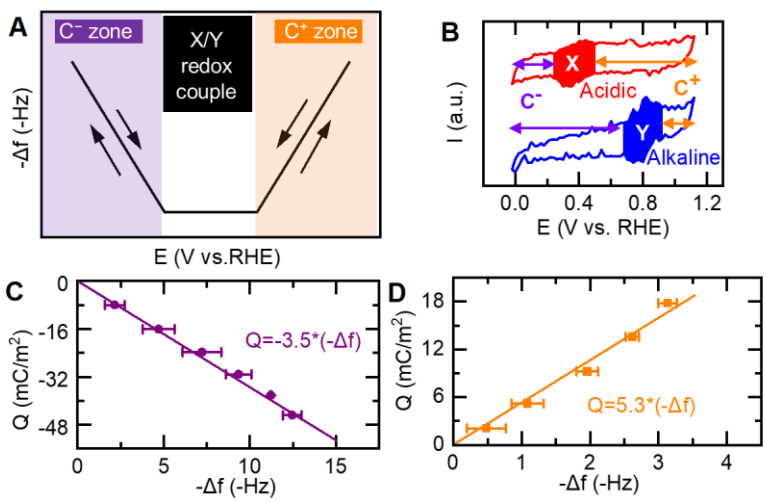

Fig. 4 Detection of the surface excess charge through electrochemical quartz crystal microbalance (EQCM) measurements. (A) Frequency response of the EQCM at various potential regions: $-\Delta f$ increases as the potential decreases in the C^- zone, but increases as the potential increases in the C^+ zone. Notably, there is a potential region where the X/Y redox reactions occur, effectively maintaining $-\Delta f$ at a minimum value. (**B**) Linear correlation of the frequency response and the integrated charge in the C^+ potential region in 0.1 M $HClO_4$. (**C**) Cyclic voltammograms (CVs) of gold in different Ar-saturated pH solutions at a scan rate of 50 mV/s. The C^+ and C^- zones denote the potential regions where a positive and negative surface excess charge is present, respectively. X and Y represent the regions where redox reactions occur in acidic (pH 3) and alkaline (pH 10) solutions, respectively. (**D**) Linear correlation of the frequency response and the integrated charge in the C^- potential region in 0.1 M NaOH.

In case of an ideal electrified interface, the capacitance (C) is constant irrespective of the scan rate. The change of the non-Faradaic charge (ΔQ) is related to the potential drop (ΔE) and C, and can be expressed as $\Delta Q = C \times \Delta E$.[4] Consequently, ΔQ remains independent of ν, even though the current (I) is proportional to ν ($I = C \times \nu$) while C remains constant.[38] To further confirm the direct relationship between the frequency change and the accumulation of the excess free charge, we investigated $-\Delta f$ at varying scan rates (ν) (Fig. S1). These experiments show that $-\Delta f$ is not affected by ν in both the C^+ and C^- zones, which fully in agreement with the expected behavior of a non-Faradaic process.

The classical GCS model divides the total capacitance of the electric double layer (C_{GCS}) into Helmholz capacitance (C_H) and the diffuse layer capacitance (C_{GC}):[10, 12]

$$\frac{1}{C_{GCS}} = \frac{1}{C_H} + \frac{1}{C_{GC}}$$

In this simplistic equation, C_H is assumed to remain constant, and C_{GC} is expected to decrease with lower electrolyte concentration.[50] Consequently, it is anticipated that the total capacitance will decrease at a lower electrolyte concentration. This decrease in electrolyte concentration directly leads to a decrease in the excess charge that is attracted to the surface in

line with the equation $\Delta Q = C \times \Delta E$. If the frequency change is indeed linked to the excess free charge, a diminishing $-\Delta f$ should logically manifest when the electrolyte concentration is lowered. To validate this hypothesis, we examined the impact of the electrolyte concentration on the frequency changes in the C^+ zone (Fig. S2A) and in the C^- zone (Fig. S2B). Indeed $-\Delta f$ diminishes in both zones when the electrolyte concentration is decreased from 0.1 M to 0.05 M. The diminished $-\Delta f$ observed in a more diluted solution further solidifies the direct relationship between the frequency change and excess charge on the gold surface.

4.2.2 Chemisorption of anions at the electrode surface

Under conditions that are thermodynamically favorable, solvated ions can undergo partial dehydration and engage in bonding interactions with the electrode surface. This phenomenon, termed partial charge transfer, can lead to the formation of partially charged chemisorbates.[51] This behavior has been observed primarily with anions on metallic surfaces due to their weakly bound solvation shells.[21] The two redox waves, denoted as X and Y, have previously been associated with chemical adsorption/desorption phenomena.[49, 52] (Fig. 5A). For instance, the X wave is linked to the chemisorption of anions such as perchlorate, sulfate and nitrate, while the Y wave involves the chemisorption of hydroxide. To understand these phenomena better, we examined the oxidation peak potentials (E_{X+}) and (E_{Y+}) (Fig. 5B) as well as the reduction peak potentials (E_{X-}) and(E_{Y-}) (Fig. 5C) in relation to the pH. This revealed that E_{X+} (0.31 V vs. NHE) and E_{X-} (0.19 V vs. NHE) are pH−independent on the NHE reference scale when the pH is below 8. On the other hand, E_{Y+} ($0.82\,V - 0.059\,V/pH\ vs. NHE$) and E_{Y-} ($0.77V - 0.059\,V/pH\ vs. NHE$) exhibit a pH−dependent shift of − 59 mV/pH in the pH range of 8 – 13.

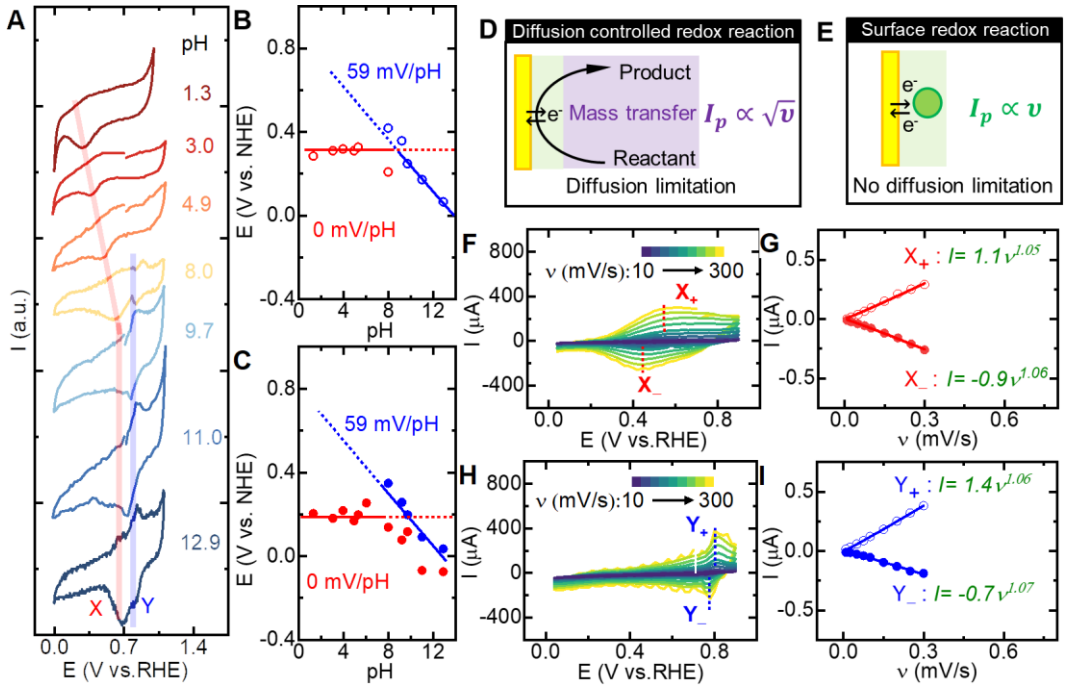

Fig. 5 X and Y redox peaks in the electrochemical double layer (EDL) region. (A) Cyclic voltammograms (CVs) of gold in Ar-saturated pH solutions (0.1 M ClO_4^-) at 50 mV/s. (**B**) Pourbaix diagram illustrating the X^+ (E_{X+}) and Y^+ (E_{Y+}) oxidation peaks during the positive scan of the CVs (Data from Fig. 5A). (**C**) Pourbaix diagram showcasing the X^- (E_{X-}) and Y^- (E_{Y-}) reduction peaks during the negative scan of the CVs (Data from Fig. 5A). (**D**) Schematic representation of a diffusion controlled redox reaction and its electrochemical response displaying the relationship between the peak current (I_p) and the square root of the scan rate ($\sqrt{\upsilon}$). (**E**) Schematic representation of a surface redox reaction and its electrochemical response demonstrating the relationship between the peak current (I_p) and the scan rate (υ). **(F)** CVs of gold in Ar-saturated 0.1 M $NaClO_4$ (pH 4) solutions at varying scan rates ranging from 10 to 300 mV/s. (**G**) Relationship between the scan rate and the X^+ and X^- peak currents in pH 4. (**H**) CVs of gold in Ar-saturated 0.1 M $NaClO_4$ (pH 10) solutions at varying scan rates ranging from 10 to 300 mV/s. (**I**) Relationship between the scan rate on the Y^+ and Y^- peak currents in pH 10.

The peak potentials associated with anion chemical adsorption and desorption (X redox couples) depend on the electrolyte concentration and the specific type of anion present (see S1

for details). Similar shifts in potential due to anion−dependent chemisorption (such as ClO_4^-, NO_3^-, or SO_4^{2-}) have been directly observed on the Au(111) surface using various in situ spectroscopy techniques, including surface-enhanced infrared absorption spectroscopy (SEIRAS), subtractive normalized interfacial Fourier transform IR spectroscopy (SNIFTIRS), IR reflection-absorption spectroscopy (IRAS).[20, 48, 49] Despite their relatively low surface coverage (less than 20%), the spectra clearly demonstrate that the bands corresponding to adsorbed anions (ClO_4^-, NO_3^-, and SO_4^{2-}) shift as the potential becomes more positive within the potential range where the X redox couple is active on Au(111). This direct evidence supports the notion that the X redox peaks are associated with direct anion binding to the gold surface.

As anticipated, the chemisorption of hydroxide is pH−dependent and shifts with a factor of $-0.059 \times pH$ in the Pourbaix diagram (Fig. 5B-C). While the detection of hydroxide absorption is typically easier in alkaline solutions,[52, 53] it can even be observed at pH 3 when the anion concentration is significatly reduced to 0.01M (Fig. S6 and S8). The Pourbaix diagram illustrates that the chemisorption potential of perchlorate shifts towards the chemisorption potential of hydroxide when the pH increases (Fig. 5B and C). The slope of E_{ClO4^-} ultimately changes from 0 mV/pH to −59 mV/pH once the pH surpasses 8, and the perchlorate and hydroxide chemisorption features closely overlap (Fig. 5 and Fig. S5-8). This change indicates a shift in anion chemisorption from an electron transfer (ET) process within the pH range of 1-8 to a proton−coupled electron transfer (PCET) process when the pH exceeds 8. This may suggest that co-chemisorption of perchlorate and hydroxide may occur within the pH range of 8-13, given their closely aligned equilibrium potential.

In the context of a redox reaction, the current response to an applied sweep rate (ν) hinges on whether the redox reaction process is governed by diffusion or surface phenomena.[54, 55] When a redox reaction is controlled by diffusion, the current response varies with the square root of the scan rate ($I_{(V)} = a\nu^{1/2}$) (Fig. 5D).[54, 56] Conversely, if a redox reaction is primarily constrained by surface reactions and not influenced by diffusion, the current exhibits a direct linear relationship with the scan rate ($I_{(V)} = a\nu$) (Fig. 5E).[38, 54] Since the concentrations of Na^+ and ClO_4^- are roughly the same at 0.1 M, both at pH 4 and at pH 10, these specific pH values were selected to examine the correlation between the peak currents (I) and the scan rate (ν), as

depicted in Fig. 5F and H. The data in Fig. 5G and 5I unmistakably indicate that the current responses I_X and I_Y are directly proportional to the sweep rates for both the negative and positive scans. Since both features associated with perchlorate and hydroxide chemisorption follow a relationship of $I_{(V)} = av$, it can be inferred that both processes are governed by surface-controlled reactions devoid of diffusion involvement. Such surface-controlled redox reactions are commonly referred to as pseudocapacitance due to their proportionality to the scan rate, resembling the behavior of a physical capacitor. However, unlike traditional capacitors, these process involve Faradaic currents, as they stem from the occurrence of redox reactions.[38, 54] Notably, these redox reactions involving anions (X) and hydroxide (Y) are not diffusion controlled, suggesting that the anions are already present at the interface, or in case of Y involve the solvent (water).

In the potential region where the X (acidic conditions) and Y (alkaline conditions) redox waves are observed, $-\Delta f$ is unaffected by ΔQ (Fig. S3 and S4). This finding suggests that the excess free charge may remain relatively constant during these redox reactions, even as the potential changes. While the classical GCS model clearly elucidates the behavior of excess charge on the surface in the absence of chemisorption, it remains unclear how excess charge evolves when chemisorption occurs. It is worth noting that detecting excess charge changes in the presence of chemisorption has been considered a challenging task.[8] EQCM may offer a promising perspective for observing how the excess charge changes in a real-world environment. In the electrochemical double layer (EDL) potential region, EQCM exhibits a pronounced frequency response when there is no chemisorption and a minimum frequency response when chemisorption is occurring. The Kautek group examined the frequency changes on the gold electrode using EQCM in 0.5 M KOH. They observed a minimum frequency response in the potential region that is associated with OH^- chemisorption but noted a significant frequency response both above and below this region.[42] Furthermore, they compared the frequency and mass difference at various potential regions, to study diverse electrochemical processes such as the specific adsorption of hydroxide, and structural changes in the double layer potential region. The Kautek group proposed double layer models involving the outer and inner Helmholz layers, based on the frequency responses on the gold surface observed by

EQCM measurements. They suggested that within the outer Helmholtz layer, fully solvated anions or cations exhibit electrostatic attraction/repulsion, which can be detectable through frequency changes on the EQCM in the EDL region. However, within the inner Helmholtz layer, where specific anions are adsorbed, the formation of neutral ion pairs with the metal surface may lead to practically no observable electrostatic attraction/repulsion.

The EQCM measurements demonstrate that $-\Delta f$ remains at a minimum, with no significant frequency changes occurring in the potential regions where the surface-controlled chemisorption reactions transpire, as illustrated in the X zone in Fig. 6A and B, and the Y zone in Fig. 6C. EQCM measurements enable the identification of the C^+ zone, C^- zone and PRMF across the entire pH scale, as illustrated in Fig. 6D. Jun Cheng's group reported state-of-the-art ab initio molecular dynamics simulations of electrified Pt(111)/water interfaces.[5] Their research revealed the existence of water chemisorption when the metal surface transitions from a negative to a positive charge. This chemisorbed water alters the surface coverage, subsequently increasing the differential capacitance, resulting in a bell-shaped differential capacitance curve. We speculate that a similar chemisorption behavior may also occur with anions in case of the gold electrodes of study when the excess free charge shifts from negative to positive. Here these chemisorbed species may form neutral ion pairs within the Helmholtz layer act to offset the potential change.[42] This may explain why no significant excess charge is built up in the region where these surface redox reactions occur, and therefore results in an apparent potential region where minimum frequency changes occur(PRMF) that is situated between the C^+ and C^- zones.

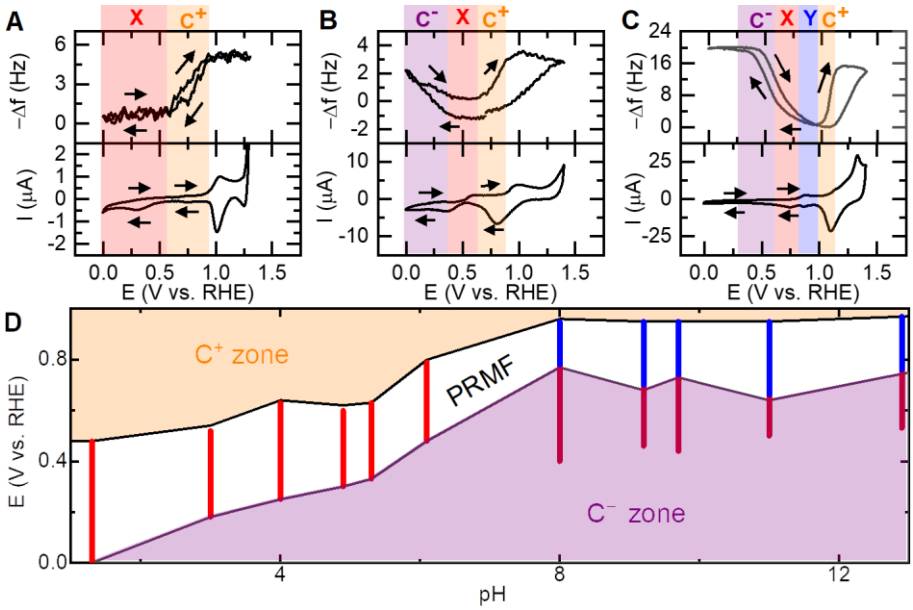

Fig. 6 Surface excess charge detection in different Ar-saturated pH solutions. (A-B) EQCM measurements on gold in 0.1M $HClO_4$ (**A**), $NaClO_4$ (**B**) and NaOH (**C**). The upper part displays the frequency response as a function of potential, while the lower part illustrates the CV. The scan rate is set at 50 mV/s in the EQCM measurements. The X and Y regions indicate the potential regions where the X and Y redox couples can be identified in a CV, respectively. C^+ signifies the potential region of positive excess charge, whereas C^- represents the potential region of negative excess charge. (**D**) Potential regions of C^+ and C^- observed across varying pH solutions. The red and blue lines depict the potential regions where the X and Y redox reactions are present, respectively, under Ar-saturated conditions. There is a potential region of minimum frequency (PRMF) between C^+ and C^- zones.

4.2.3 The electrified interface in the presence of oxygen

While discussions on electrochemical double layer (EDL) structure at electrode interfaces have persisted over a century,[23, 57, 58] the in situ visualization of the actual distribution of cations and anions at the solid-liquid interface during a catalytic process has remained elusive.[23, 59] Taking into account the linear correlation between $-\Delta f$ and ΔQ, and the hypothesis by Kautek

grouppoint to a potential region between C^+ and C^- where chemisorption occurs where frequency changes cannot be observed by EQCM, we can speculate what the charge distribution diagram at the solid-liquid interface would look like. While there may undoubtedly be more complex electrochemical processes at play at and near the PRMF, and we cannot dismiss the possibility that these other electrochemical processes also affect the excess free excess free charge and may not be detected by EQCM, in the following discussion we have assumed that the effect of such processes would be minimal. Under the assumption that $-\Delta f$ changes directly correlate with the excess charge, we can probe the EDL structure during catalytic processes. Since the oxygen reduction reaction (ORR) occurs within the PRMF region, we employed our EQCM methodology to detect the surface excess charge both under an inert atmosphere and during the catalytic ORR process.

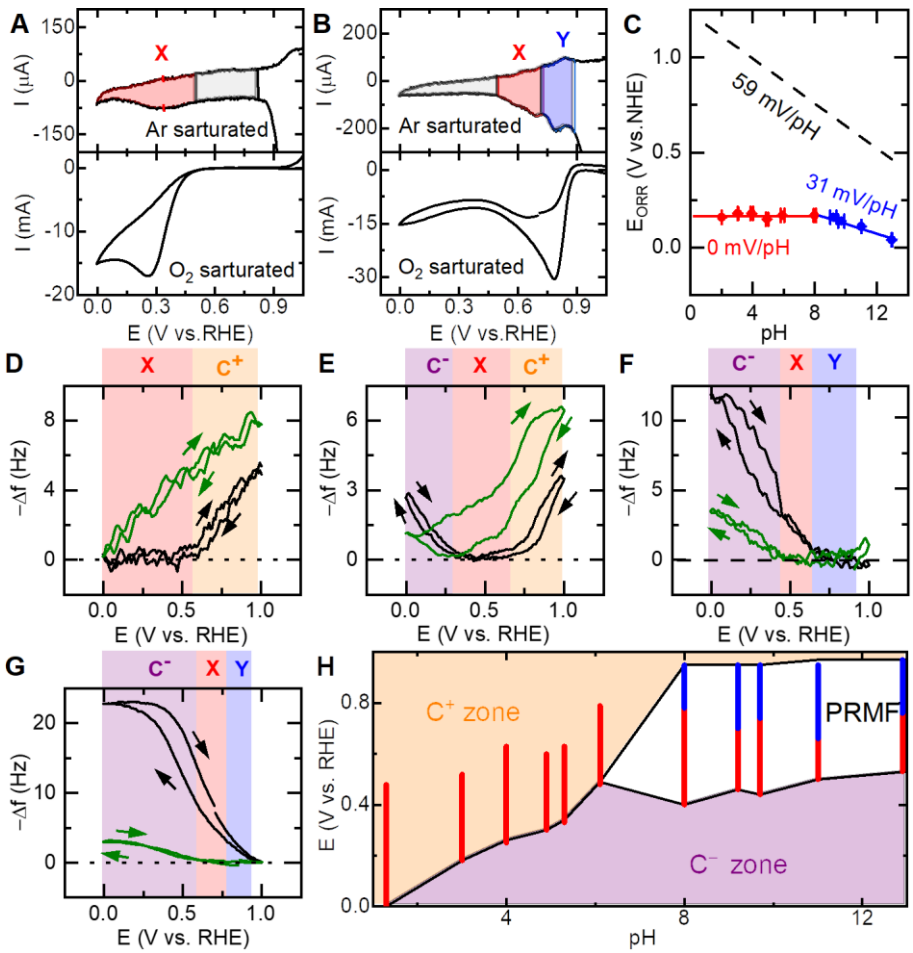

Fig. 7 Surface excess charge detection in the presence of oxygen reduction reaction in different pH solutions. (**A**) CVs of gold in Ar-saturated (top) and O_2-saturated (bottom) 0.1 M $HClO_4$ at 50 mV/s. (**B**) CVs of gold in Ar-saturated (top) and O_2-saturated (bottom) 0.1 M NaOH at 50 mV/s. **(C)** Pourbaix diagram illustrating the peak potential of oxygen reduction reaction (E_{ORR}) across the entire pH scale. (**D-G**) The EQCM frequency response in Ar-saturated (black line) and O_2-saturated (green line) conditions across different pH solutions: pH 1 (**D**), pH 4 (**E**), pH 10 (**F**), pH 13 (**G**). The X and Y zones indicate the potential regions where the X and Y redox couples are identifiable in a CV under Ar—saturated conditions. C^+ signifies the potential region of positive excess charge, while C^- represents the potential region of negative excess charge. (**H**) Potential regions of C^+ and C^- observed across varying pH solutions. The red and blue lines represent the potential regions where the X and Y redox reactions can be observed under Ar-saturated conditions, respectively.

Under saturated O_2 conditions, the potential region of the ORR consistently aligns with the potential regions where the X and Y redox reactions can be observed in the absence of O_2, as depicted in Fig. 7A and B. Given that the peak potential of the ORR, denoted as E_{ORR}, remains constant regardless of variations in the oxygen quantity, E_{ORR} apparently is not affected by kinetic factors, and therefore considered to be an interesting descriptor to monitor (Fig. S10). By recording E_{ORR} across different pH values and constructing a corresponding Pourbaix diagram (Fig. 7C), distinct E_{ORR} slopes (vs. NHE) become apparent. For pH levels lower than 8, E_{ORR} does not shift on the NHE reference scale. However, E_{ORR} displays a decrement of −31mV/pH once the pH surpasses 8. This dual E_{ORR} slope pattern in the Pourbaix diagram suggests that the rate−determining step of the electrochemical ORR process involves only electron transfer steps ($O_2 + e^- \rightleftarrows O_2^-$) within the pH range of 1-8, whereas it transitions to a two—electron and one−proton process ($O_2 + H^+ + 2e^- \rightleftarrows HO_2^-$) when the pH exceeds 8.

Gold, characterized by a weak oxygen binding energy, experiences a pronounced reduction in ORR overpotential when transitioning from acidic to alkaline solutions, a phenomenon akin to other materials exhibiting weak oxygen binding energies.[60] In terms of whether oxygen directly adsorb onto the catalyst, the ORR process can be conceptually divided into a surface-dependent inner-sphere electron transfer mechanism and a surface-independent

outer-sphere electron transfer mechanism.[61] Materials with low oxygen binding energies, including Au,[62] Ag,[63] carbon materials[64] and several oxides,[65] have been proposed to reduce O_2 through an outer-sphere electron transfer process. Within this context, it has been hypothesized that chemisorbed anions function as outer-sphere bridges between the O_2 and the Au surface, thereby stabilizing catalytic intermediates in alkaline solutions.[60, 62, 66] However, the outer-sphere electron transfer mechanism alone does not comprehensively explain the two distinct trends in ORR activities exhibited by these systems, occurring both below and above pH 8.

We conducted a comparatively analysis of the frequency response as a function of the applied potential using EQCM in both Ar−saturated and O_2−saturated solutions (Fig. 7D-G). When the pH of the solution is below 8, a notable difference is observed when comparing the conditions under saturated Ar and O_2. Specifically, the PRMF width diminishes, and the onset potential of C^+ zone, denoted as onset C^+ undergoes a negative potential shift under saturated O_2. (Fig. 7D and E). In instances where the pH is 1, the onset C^+ shifts from 0.55 V vs. RHE under Ar to 0 V vs. RHE under O_2 (Fig. 7D). Similarly, at pH 4, the onset C^+ transition occurs from 0.67 V vs. RHE under Ar to 0.3 V vs. RHE under O_2 (Fig. 7E). Moreover, EQCM analysis in presence of oxygen shows that the onset potential of the ORR falls within the C^+ region when the pH is below 8 (Fig. S11A and B).

Conversely, when the pH of the solution exceeds 8, a noticeable disparity of potential regions emerges in the PRMF and the C^- zone comparing saturated Ar and O_2. Notably, under O_2 −saturated conditions, the PRMF consistently maintains its presence, even as the Faradaic current associated with catalytic O_2 reduction increases by a factor of 150 when compared to the current under Ar conditions (Fig. S11C and D). Moreover, its width expands in conjunction with the negatively shifted onset potential of the C^- zone, recognized as onset C^- (Fig. 7F and G).

Assuming that the variables resulting from the ORR reaction process, such as pH fluctuations and the quantities of reactants and products, have a minimal impact on the EQCM signal, the identification of the PRMF, C^+ and C^- zones within O_2− saturated solutions becomes straightforward, as depicted in Fig. 7H. Any distinction can be easily observed when comparing conditions under O_2 (Fig. 7H) with that under Ar (Fig. 6D). Notably, when the pH is below 8,

the width of PRMF diminishes, and onset C^+ shifts negatively. Conversely, the width of PRMF expands, and the onset C^- shifts negatively when the pH exceeds 8. This notable change in the PRMF under O_2−saturated conditions could potentially imply that the presence of O_2 leads to the detachment of perchlorate from the electrode surface, while hydroxide remains bound.

In essence, the precise identification of the PRMF, C^+ and C^- zones reveals how the excess free charge may change under catalytic ORR conditions under the assumption that $-\Delta f$ changes directly correlate with the excess charge.

4.2.4 Charge distribution at electrified interfaces

The essence of the electrified interface lies in comprehending the distribution of the excess free charge. Assuming that Δf gives us the full picture regarding the surface excess charge, the processes occuring at the gold surface can be devided in a Faradaic process involving surface redox reactions in the PRMF, and non-Faradaic processes that occur in the C^- and C^+ zones. To assess these two processes, we examined the differential capacitances at varying pH, as depicted in Fig. 8A. Beyond the potential range of the surface redox reactions (X and Y zones), a differential capacitance of approximately 18 μF/cm^2 is observed. However, within the X and/or Y redox regions, the presence of charge transfer from chemical adsorption/desorption enhances the differential capacitance, resulting in a bell-shaped curve with a maximum capacitance of 50 μF/cm^2. The bell-shaped differential capacitance arises from the chemisorption of perchlorate (X region) and hydroxide (Y region) on gold. The chemical adsorption/desorption of perchlorate within the pH rang of 1-8 (Fig. 8B) and hydroxide within pH 8-13 (Fig. 8C) constitute two distinct surface redox reactions. We speculate that these surface reactions apparently impede the buildup of excess charge, resulting in the appearance of a PRMF where $-\Delta f$ remains minimal in EQCM experiments. This may suggest that excess charge is established and augmented only after the completion of chemical adsorption (during a positive scan) or desorption (during a negative scan) (Fig. 8D).

To analyze the net Faradaic charge distribution of surface redox reactions existing in the PRMF, we sum the integrated charge of adsorption during positive and desorption during negative scan in a CV experiment (Section S3 (2) and Fig.S12). For the non-Faradaic regions

(i.e. the C^+ and C^- zones), we can calculate the accumulated excess charge (ΔQ) using the potential difference (ΔE) between the onset potential of the non-Faradaic region to the calculated potential point, as well as the known capacitance (C_{Ar}) from a cyclic voltammogram (Fig. 8A). The formula for calculating ΔQ is $\Delta Q = \frac{C_{Ar} \times \Delta E}{A}$, where A is the electrode surface area (section S3(3)). By plotting the calculated Faradaic charge in the PRMF area and the excess charge in the non-Faradaic zones as a function of the applied potential, we can construct excess free charge distribution diagrams that are based on our assumption that Δf relates directly to the surface excess charge. (Fig. 8E-F).

Determination of the distribution of excess charge during a catalytic process where significant catalytic currents can be observed, has been unprecedented due to the lack of appropriate methods. Our EQCM methodology allows for the exploration of the excess charge by monitoring the frequency response during the catalytic oxygen reduction process. While it is not feasible to measure the excess charge directly from current under catalytic conditions, we managed to estimate the capacitance within O_2-saturated solutions by utilizing the relationship between the frequency changes and the excess free charge. Based on the linear relationship between the frequency changes observed by EQCM to the excess free charge, we speculate that the slope of these frequency changes as a function of the potential change is linked to capacitance through the equation $C = \frac{Q}{\Delta E} \propto \frac{-\Delta f}{\Delta E}$ (Fig. S13). Assuming that the reactants and products in a catalytic process do not significantly influence the frequency of the EQCM, we can obtain the difference in capacitance between an O_2 and an Ar atmosphere, which can be related using a corrective coefficient (K). This coefficient is calculated as the ratio of $\frac{-\Delta f}{\Delta E}$ under O_2 to the that recorded under Ar and is expressed as $K = \frac{(\frac{-\Delta f}{\Delta E})_{O_2}}{(\frac{-\Delta f}{\Delta E})_{Ar}} = \frac{C_{O_2}}{C_{Ar}}$.

By comparing the frequency response under O_2 and under Ar, it becomes clear that K correlates linearly with E within the C^- zone, while K is unaffected by E in the C^+ zone (Fig. S13). This disparity is due to $(\frac{-\Delta f}{\Delta E})_{O_2}$ not being fully linear in contrast to $(\frac{-\Delta f}{\Delta E})_{Ar}$. The observed disparity can likely be attributed to the occurrence of the ORR, which takes place prominently in the PRMF and C^- zone but is less prevalent in the C^+ zone. Since K remains constant at 0.8

in the C^+ zone (Fig. S13C), we assume the excess charge in the C^+ zone under O_2 saturated conditions using the equation $\Delta Q_{O_2} == \frac{0.8\, C_{Ar} \times \Delta E}{A}$. The determination of capacitance in the C^- zone under O_2 conditions can be determined, and relies on the corrective coefficient K expressed as $C_{O_2} = K \times C_{Ar}$, wherein K was found emperically to change with $K = 0.18 - 0.24 \times E$ (More details in Fig. S13 and section S4). Consequently, we can estimate the excess charge in the C^- and C^+ zones, respectively, thereby unveiling a qualitative excess charge distribution diagram under saturated O_2 conditions as well. (Fig. 8G) Assuming excess free charge is reflected by the frequency changes of EQCM, the diagram visually demonstrates how the excess charge may fluctuate as a function of pH and the applied potential before and during catalysis.

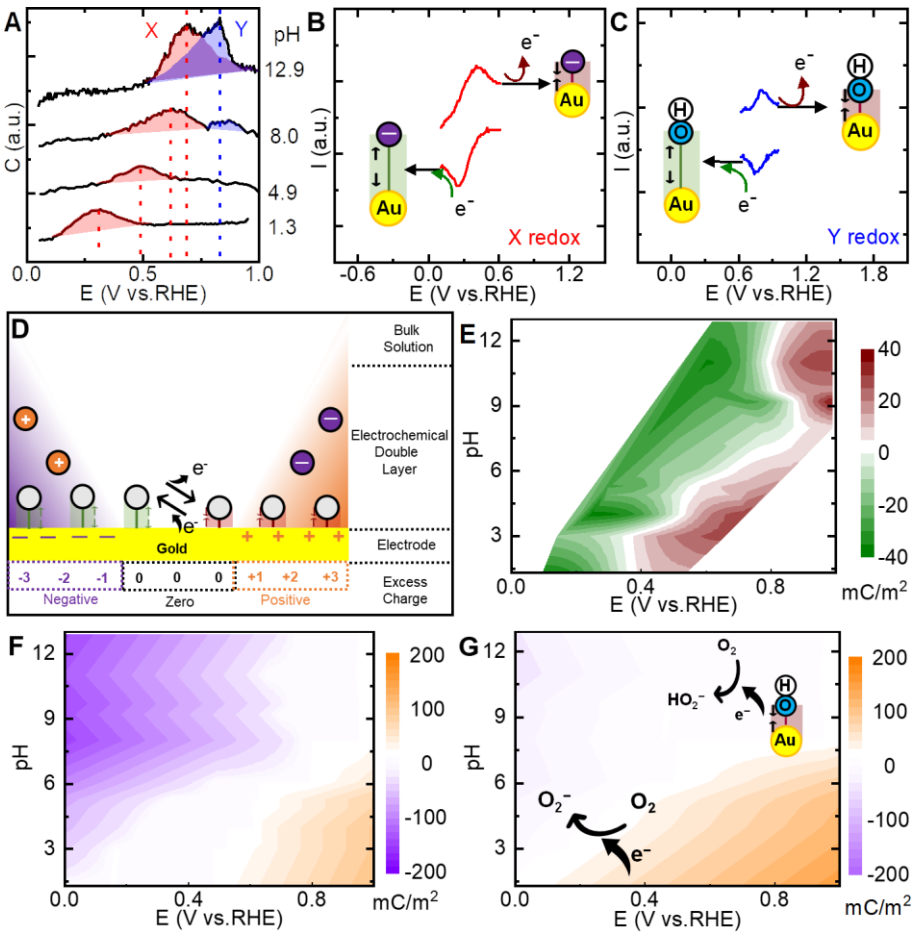

Fig. 8 Proposed charge distribution diagram on the gold surface in a full pH scale. (**A**) Average differential capacitances (C) calculated by cyclic voltammetry as a function of pH, with a potential range of 0 – 1 V vs. RHE and scan rate of 0.05 V/s. The pH of the solutions is adjusted using a mixture of 0.1 M $HClO_4$, $NaClO_4$ and NaOH. (More calculation details are shown in Section S3(1)). The red X and blue Y regions illustrate the contribution of ClO_4^- and OH^- surface redox reactions to the increase in the capacitance of gold. (**B**) Proposed X redox reaction (ClO_4^- chemical adsorption/desorption) on the gold surface. The red line represents a segment of the CV involving the X redox reaction. (**C**) Proposed Y redox reaction (OH^- chemical adsorption/desorption) on the gold surface. The blue line represents a segment of the CV involving the Y redox reaction. (**D**) Proposed structure of the electric double layer (EDL) on gold. The surface excess charge changes from negative (purple) to neutral and positive (orange) as the applied potential increases. Dark green and dark red boxes represent the chemical desorption and adsorption on the surface, respectively. (**E**) Distribution diagram of the net Faradaic charge for specific adsorption/desorption involving electron transfer in an Ar-saturated environment. The net charge of the surface redox reactions is the sum of integrated charges from both the positive and negative scans. (More details are shown in Section S3(2) and Fig.S12). (**F**) Surface excess charge distribution diagram on gold as a function of the pH under an Ar—saturated solution, within the potential region of 0 — 1 V vs. RHE. Purple, white, and orange colors represent three distinct excess charge states of the gold surface: negative, neutral, and positive, respectively. The details of mathematical model of excess charge under saturated Ar conditions are provided in Section S2(3). (**G**) Surface excess charge distribution diagram on gold as a function of pH in O_2-saturated solutions, within the potential region of 0-1 V vs. RHE. Purple, white, and orange colors represent three distinct excess charge states of the gold surface: negative, neutral, and positive, respectively. Further details of the mathematical model of excess charge under saturated O_2 conditions are discussed in Section S4.

4.3 Conclusion

In summary, our study presents a methodology for exploring the excess free charge by EQCM. Through the analysis of three distinct frequency responses of a quartz crystal, we have

successfully identified the potential regions where significant excess charge builds up on the electrode, i.e. a positive excess charge concentrated in the C^+ zone and a negative excess charge localized in the C^- zone. Additionally, we pinpointed an apparent potential region of where frequency changes cannot be detected by EQCM (PRMF), and where surface redox reactions involving Faradaic charge transfer are occurring. This EQCM method appears to be very versatile even during the electrocatalytic ORR. Moreover, our comprehensive EQCM and CV analysis has allowed us to create informative excess free charge distribution diagrams. These insights not only allow us to enhance our understanding of the interface environment in various materials, but also lay the groundwork for future investigations into tracking the real excess free charge dynamics during diverse chemical processes. Since the principles underlying a $-\Delta f$ response as a function of $\Delta Q$are not understood, and the precise reason for the absence of a frequency response in the PRMF remains unknown, it is worthwhile to conduct further investigations into these precise phenomena. This can be achieved through a comparative analysis of different in situ methods and the application of more detailed mathematical models.

4.4 References

1. Jeanmairet, G.; Rotenberg, B.; Salanne, M., *Chem Rev* **2022,** *122* (12), 10860-10898.
2. Schmickler, W., *Chemical Reviews* **1996,** *96* (8), 3177-3200.
3. Lin, S.; Chen, X.; Wang, Z. L., *Chem Rev* **2022,** *122* (5), 5209-5232.
4. Noori, A.; El-Kady, M. F.; Rahmanifar, M. S.; Kaner, R. B.; Mousavi, M. F., *Chem Soc Rev* **2019,** *48* (5), 1272-1341.
5. Le, J.-B.; Fan, Q.-Y.; Li, J.-Q.; Cheng, J., *Science Advances* **2020,** *6* (41), eabb1219.
6. Velasco-Velez, J.-J.; Wu, C. H.; Pascal, T. A.; Wan, L. F.; Guo, J.; Prendergast, D.; Salmeron, M., *Science* **2014,** *346* (6211), 831-834.
7. Le, J.; Iannuzzi, M.; Cuesta, A.; Cheng, J., *Phys Rev Lett* **2017,** *119* (1), 016801.
8. Frumkin, A. N.; Petrii, O. A., *Electrochim. Acta* **1975,** *20* (5), 347-359.
9. Chen, J.; Nie, L.; Yao, S., *Journal of Electroanalytical Chemistry* **1996,** *414* (1), 53-59.
10. Ojha, K.; Doblhoff-Dier, K.; Koper, M. T. M., *Proc Natl Acad Sci U S A* **2022,** *119* (3).
11. Payne, R., Double Layer at the Mercury-Solution Interface. In *Progress in Surface and Membrane Science*, Danielli, J. F.; Rosenberg, M. D.; Cadenhead, D. A., Eds. Elsevier: 1973; Vol. 6, pp 51-123.
12. Doblhoff-Dier, K.; Koper, M. T. M., *The Journal of Physical Chemistry C* **2021,** *125* (30), 16664-16673.
13. Rizo, R.; Sitta, E.; Herrero, E.; Climent, V.; Feliu, J. M., *Electrochim. Acta* **2015,** *162*, 138-145.
14. Weaver, M. J., *Langmuir* **1998,** *14* (14), 3932-3936.
15. Sarabia, F. J.; Sebastián, P.; Climent, V.; Feliu, J. M., *Journal of Electroanalytical Chemistry* **2020,** *872*.
16. Climent, V.; Coles, B. A.; Compton, R. G., *The Journal of Physical Chemistry B* **2002,** *106* (20), 5258-5265.
17. Ryu, J.; Surendranath, Y., *J Am Chem Soc* **2019,** *141* (39), 15524-15531.
18. Martínez-Hincapié, R.; Climent, V.; Feliu, J. M., *Electrochemistry Communications* **2018,** *88*, 43-46.
19. Xu, P.; von Rueden, A. D.; Schimmenti, R.; Mavrikakis, M.; Suntivich, J., *Nat Mater* **2023**.
20. Marinković, N. S.; Calvente, J. J.; Kloss, A.; Kováčová, Z.; Ronald Fawcett, W., *Journal of Electroanalytical Chemistry* **1999,** *467* (1), 325-334.
21. Magnussen, O. M., *Chemical Reviews* **2002,** *102* (3), 679-725.
22. Lu-Lu Zhang, C.-K. L., Jun Huang, *Journal of Electrochemistry* **2022,** *28* (2), 2108471.
23. Huang, J., *JACS Au* **2023,** *3* (2), 550-564.
24. Wang, X.; Kuang, Y.; Le, J.-B., *Current Opinion in Electrochemistry* **2023,** *40*.
25. Zhang, M.-K.; Cai, J.; Chen, Y.-X., *Current Opinion in Electrochemistry* **2022,** *36*.
26. Li, C. Y.; Le, J. B.; Wang, Y. H.; Chen, S.; Yang, Z. L.; Li, J. F.; Cheng, J.; Tian, Z. Q., *Nat Mater* **2019,** *18* (7), 697-701.
27. Li, X. Y.; Jin, X. F.; Yang, X. H.; Wang, X.; Le, J. B.; Cheng, J., *J Chem Phys* **2023,** *158* (8), 084701.
28. Le, J. B.; Chen, A.; Li, L.; Xiong, J. F.; Lan, J.; Liu, Y. P.; Iannuzzi, M.; Cheng, J., *JACS Au* **2021,** *1* (5), 569-577.
29. Tian, Z.-Q.; Ren, B.; Chen, Y.-X.; Zou, S.-Z.; Mao, B.-W., *Journal of the Chemical Society, Faraday Transactions* **1996,** *92* (20), 3829-3838.
30. Monteiro, M. C. O.; Dattila, F.; Hagedoorn, B.; García-Muelas, R.; López, N.; Koper, M. T. M., *Nat. Catal.* **2021,** *4* (8), 654-662.
31. Shah, A. H.; Zhang, Z.; Huang, Z.; Wang, S.; Zhong, G.; Wan, C.; Alexandrova, A. N.; Huang, Y.; Duan, X., *Nat. Catal.* **2022,** *5* (10), 923-933.
32. Gu, J.; Liu, S.; Ni, W.; Ren, W.; Haussener, S.; Hu, X., *Nat. Catal.* **2022,** *5* (4), 268-276.
33. Strmcnik, D.; Kodama, K.; van der Vliet, D.; Greeley, J.; Stamenkovic, V. R.; Marković, N. M., *Nat. Chem.* **2009,** *1* (6), 466-472.
34. Luo, M.; Koper, M. T. M., *Nat. Catal.* **2022,** *5* (7), 615-623.
35. Tang, B. Y.; Bisbey, R. P.; Lodaya, K. M.; Toh, W. L.; Surendranath, Y., *Nat. Catal.* **2023,** *6* (4), 339-350.
36. Simon, P.; Gogotsi, Y.; Dunn, B., *Science* **2014,** *343* (6176), 1210-1211.
37. Brousse, T.; Bélanger, D.; Long, J. W., *Journal of The Electrochemical Society* **2015,** *162* (5), A5185-A5189.
38. Simon, P.; Gogotsi, Y., *Nature Materials* **2008,** *7* (11), 845-854.
39. Hubkowska, K.; Łukaszewski, M.; Czerwiński, A., Quartz crystal nanobalance measurements in electrocatalysis. In *Encyclopedia of Interfacial Chemistry*, Wandelt, K., Ed. Elsevier: Oxford, 2018; pp 402-412.
40. Boer, D. D.; Siberie, Q.; Siegler, M. A.; Ferber, T. H.; Moritz, D. C.; Hofmann, J. P.; Hetterscheid, D. G. H., *ACS Catal.* **2022,** *12* (8), 4597-4607.
41. Daikhin, L.; Gileadi, E.; Tsionsky, V.; Urbakh, M.; Zilberman, G., *Electrochim. Acta* **2000,** *45* (22), 3615-3621.
42. Kautek, W.; Sahre, M.; Soares, D. M., *Ber. Bunsenges. Phys. Chem.* **1995,** *99* (4), 667-676.
43. Watanabe, M.; Uchida, H.; Ikeda, N., *J. electroanal. chem.* **1995,** *380* (1), 255-260.
44. Hetterscheid, D. G. H., *Chem Commun (Camb)* **2017,** *53* (77), 10622-10631.
45. Tsai, W. Y.; Taberna, P. L.; Simon, P., *J Am Chem Soc* **2014,** *136* (24), 8722-8.
46. Levi, M. D.; Sigalov, S.; Salitra, G.; Elazari, R.; Aurbach, D., *J Phys Chem Lett* **2011,** *2* (2), 120-4.

47. Levi, M. D.; Levy, N.; Sigalov, S.; Salitra, G.; Aurbach, D.; Maier, J., *Journal of the American Chemical Society* **2010,** *132* (38), 13220-13222.
48. Edens, G. J.; Gao, X.; Weaver, M. J., *Journal of Electroanalytical Chemistry* **1994,** *375* (1), 357-366.
49. Zhumaev, U. E.; Lai, A. S.; Pobelov, I. V.; Kuzume, A.; Rudnev, A. V.; Wandlowski, T., *Electrochim. Acta* **2014,** *146*, 112-118.
50. Garlyyev, B.; Xue, S.; Watzele, S.; Scieszka, D.; Bandarenka, A. S., *J Phys Chem Lett* **2018,** *9* (8), 1927-1930.
51. Schmickler, W.; Guidelli, R., *Electrochim. Acta* **2014,** *127*, 489-505.
52. Štrbac, S.; Adžić, R. R., *Journal of Electroanalytical Chemistry* **1996,** *403* (1), 169-181.
53. Prieto, A.; Hern$\diamond$ndez, J.; Herrero, E.; Feliu, J. M., *Journal of Solid State Electrochemistry* **2003,** *7* (9), 599-606.
54. Costentin, C.; Porter, T. R.; Saveant, J. M., *ACS Appl Mater Interfaces* **2017,** *9* (10), 8649-8658.
55. Yang, X.; Rogach, A. L., *Advanced Energy Materials* **2019,** *9* (25).
56. Elgrishi, N.; Rountree, K. J.; McCarthy, B. D.; Rountree, E. S.; Eisenhart, T. T.; Dempsey, J. L., *Journal of Chemical Education* **2018,** *95* (2), 197-206.
57. Doblhoff-Dier, K.; Koper, M. T. M., *Current Opinion in Electrochemistry* **2023**.
58. Pajkossy, T.; Kolb, D. M., *Electrochemistry Communications* **2003,** *5* (4), 283-285.
59. Damaskin, B. B.; Petrii, O. A., *Journal of Solid State Electrochemistry* **2011,** *15* (7-8), 1317-1334.
60. Ramaswamy, N.; Mukerjee, S., *Advances in Physical Chemistry* **2012,** *2012*, 1-17.
61. Ramaswamy, N.; Mukerjee, S., *The Journal of Physical Chemistry C* **2011,** *115* (36), 18015-18026.
62. Ignaczak, A.; Santos, E.; Schmickler, W., *Current Opinion in Electrochemistry* **2019,** *14*, 180-185.
63. Blizanac, B. B.; Ross, P. N.; Markovic, N. M., *Electrochim. Acta* **2007,** *52* (6), 2264-2271.
64. Yang, H. H.; McCreery, R. L., *Journal of The Electrochemical Society* **2000,** *147* (9), 3420.
65. Shao, M.; Chang, Q.; Dodelet, J. P.; Chenitz, R., *Chem Rev* **2016,** *116* (6), 3594-657.
66. Duan, Z.; Henkelman, G., *ACS Catalysis* **2019,** *9* (6), 5567-5573.

The Legend of Murloc

The Mystery of a Million Stars

The Lost Heart of the Electric Grove

Perplexities of the Identification Center

Anecdotes from the Scapegoat Farm

Chasing the Invisible Man

5

Summary

Since the application of voltammetry techniques have been expanded from its original use with mercury electrodes to a wide range of solid materials, modern voltammetry has evolved into an indispensable technique. It offers valuable insights into the electrochemical properties and behavior of materials, and therefore has had a big impact in various field like materials science, energy storage, corrosion studies, and sensor development. In a voltammogram, the correct interpretation of the current response is exceptionally crucial when the applied potential is changed by the potentiostat, but not always easy to unravel. Historically, gold was the focal point in some of the earliest discussions in electrochemical surface science, notably in the studies of Frumkin, Butler, Browden and Rideal, which took place simultaneously with initial research on mercury.[1] The knowledge gained by the interpretation of the electrochemical behavior of gold has had a profound impact on many modern scientific fields.[1-3]

In this thesis we investigated the relationship between the type of oxide and the oxygen evolution reaction (OER) activity by combining *in situ* Raman and voltammetry measurements (**Chapter 2**). We explored the behavior of the oxide reduction peaks using Rotating Ring-Disk Electrode (RRDE) and Electrochemical Quartz Crystal Microbalance (EQCM), thereby uncovering important details of the structural reconstruction of gold oxides (**Chapter 3**). Additionally, we evaluated the distribution of surface charges in the presence of chemical adsorption events and even in the oxygen reduction reaction (ORR) catalytic process using EQCM (**Chapter 4**). In this Chapter, the primary objective is to summarize the findings described in this thesis, and share some insights from our findings.

The separated reduction waves observed for gold oxides indicate the reduction of distinct types of oxide, rather than reductions of the so-called inner and outer oxide layers.

The experimental exploration of oxide formation in electrochemistry can be traced back to the 1930s. The introduction of the “charge-curve” method, initially employed by Bowden and Rideal[4] for measuring the double layer capacitance at Hg, independently saw applications to the study of electrochemical processes at Pt and Au by Frumkin *et.al.* and by Butler *et. al.*

in the early 1930s.[1, 5] A significant stride was taken in the 1960s by Will and Knorr,[6] who advanced our understanding of electrochemical surface processes at noble metals through the use of potentiostats. This method, an extension of the potential-sweep approach (i.e. voltammetry) already employed in polarography at DME, offered a new avenue for exploring interfacial processes at noble metals. The adoption of controlled-potential techniques, facilitated by electrochemical instrumentation, grants a level of control that is crucial for studying anodic oxide film formation at metals — an advantage not easily achieved through the examination of oxide film formation from the gas phase or with controlled current methods.

In the exploration of the oxide layer formation and reduction, electrochemists have made connections between different reduction waves and distinct oxide layers. This line of thought traces back to Shibata's findings on the reduction of thick-film Pt oxide reduction, where he discerned between the quasi-2d oxide film (α state) and the thick (β) oxide during a potential sweep towards negative potentials.[7, 8] Shibata proposed that the thick (β) oxide would be situated between the bulk metal and a layer of newly deposited metal atoms on the exterior of the remaining β oxide, arising from the reduction of the α state oxide.

Burke and Roche, however, introduced an alternative model known as the hydrous oxide model.[2, 9] According to the Burke model, a thick metal oxide comprises an inner monolayer (compact and anhydrous) and an outer oxide layer (dispersed and hydrous). In the hydrous oxide model, the inner oxide layer is reduced first before the outer oxide layers. Although these papers lacked any direct experimental evidence linking the oxide layers with the reduction peaks, these paved the way for further research, encompassing a broader range of materials to probe their various oxide layers by tracing reduction peaks.[10, 11] As a direct consequence, voltametric data have been mistakenly regarded as a convenient means to distinguish between the inner anhydrous oxide layer and the outer hydrous oxide layer.[2]

In **chapter 2**, our exploration delved into analysis of the reduction peaks of gold oxide across the entire pH scale, revealing a significant flaw in the existing hydrous oxide model. First of all the O_2 reduction peak has been frequently misconstrued as an oxide reduction peak in the common literature, leading to severe misinterpretations in the analysis of oxide layer

structure. While it is evident that gold oxides possess inner and outer components, the critical question that thus far has not been answered is whether electrochemical reduction of these inner and outer components is responsible for the observation of multiple gold oxide reduction waves observed in the voltammogram.

We therefore conducted a more in-depth investigation into the reduction chemistry of gold oxide, employing a combination of cyclic voltammetry and surface-enhanced Raman spectroscopy. Ultimately, we confirmed the presence of two distinct types of oxides (α oxide and β oxide). This oxide classification was pinpointed by systematic tracing of the gold oxide reduction behavior and by conducting *in situ* surface-enhanced Raman spectroscopy (SERS). In addition, we investigated the relationship between the OER activity and in relation to the type of oxide present and found that the two oxides are both pivotal for the OER, yet lead to different OER pathways. Thereby, this discovery significantly contributed to our understanding of why the OER activity on gold varies considerably as a function of pH.

The anomalous potential shifts that are observed in in case of the gold oxide reduction waves are not caused by mysterious ion effects from the electrolyte; Instead, these accurately reflect the way gold oxides undergo self-reconstruction processes.

Presently, our comprehension of the metal oxide structure on the atomic–scale mainly relies on *ex situ* spectroscopic techniques in vacuum,[12-14] and computations on well-defined and highly symmetrical metal surfaces. However, during catalysis, the corrosion and reconstruction of the metal oxide surface give rise to the formation of amorphous structures. These amorphous structures significantly differ from the original well–defined crystalline materials studied in vacuum and by computations.[14-17] At present the scientific community knows very little about the atomic structure of real metal oxide catalysts, especially at the solid liquid interface where electrocatalysis occurs. Therefore how the structure of amorphous oxides changes during a catalytic process is seen as one of the most challenging scientific questions .[14]

In **Chapter 2**, we corrected the traditional hydrous model, which mistakenly regarded different gold oxide reduction peaks as the reduction process from distinct oxide layers. The

disruption of that model has prompted us to reconsider the true underlying reasons behind the non-Nernstian behavior , i.e. abnormal potential shift, of the gold oxide reduction waves. This is crucial because many interpretations of non-Nernstian behavior on oxides in the past were built upon misinterpretations related to the hydrous model. For these reasons, we present our findings in **Chapter 3**.

In Chapter 3, we explored the intriguing "non-Nernstian behavior" characterized by anomalous potential shifts in the oxide reduction peaks of CVs. Our exploration was facilitated by employing advanced *in situ* techniques, including Rotating Ring-Disk Electrode (RRDE) and Electrochemical Quartz Crystal Microbalance (EQCM). These tools enabled us to probe deeply into the intricacies of the amorphous oxide structure within realistic catalytic environments.For instance, we could pinpoint the moment of Au^{3+} detection in the oxide reduction process by observing the reduction current of Au^{3+} on the ring during an RRDE experiment. By investigating the moment of mass loss on EQCM, we gained insights into the role of these Au^{3+} ions in stabilizing the interface between oxides and solutions. In the end, the data from various techniques interconnected, revealing that Au^{3+} cations play a crucial role in the chemistry of gold oxide. They form bonds with nucleophiles present within the amorphous gold oxide layer and the electrolyte solution, thereby dominating the interactions at the solid-liquid interface.

In this study we introduce an important connection between the non-covalent states of metals (ionic and hydrous metal cations) within covalent oxides and the dynamic evolution of oxide structures by tracing the non-Nernstian behaviors of gold oxide reduction. This newfound connection lies the basis for a more accurate understanding of the electrochemical behavior of oxides. This shows that is possible to trace structural changes caused by metal ions within amorphous metal oxides by investigating the Non-Nernstian behavior of such oxides. It serves as a reminder that understanding the manner in which metals are bound within the metal oxide (ionic bond, covalent bond or hydrogen bond) is crucial for comprehending the dynamic behavior of such metal oxides under realistic operating conditions.

Exploring the surface charge distribution during chemical adsorption/desorption and catalytic processes is possible by employing EQCM.

Inspired by the work in the preceding two Chapters (which focused on the potential range where oxides exist in voltammetry), the focus of chapter 4 lies with the relatively negative potential ranges where no oxides are present—specifically, the electrochemical double layer potential range. Here a new investigation was built from the ground up to understand the electrochemical behavior at the double layer region on gold. Thus, **Chapter 4** came into being.

Our original comprehension of the electric double layer structure at interface comes from surface tension measurements on mercury, where the potential of zero charge (PZC) is pinpointed as the potential corresponding to the maximal surface tension on an electrocapillary curve.[18] Variations in the surface excess charge will induce a redistribution of ions, resulting in the non-Faradaic currents that can be observed in a CV. Because there is a correlation between excess charge and non-Faradaic current, it allows us to investigate excess charge by current response without surface tension measurements. The correlation is crucial for solid electrode, as surface tension measurements are impossible on solid materials. Thus electrochemical capacitance measurements calculated from the current responses in a voltammogram have played a crucial role in understanding the electrochemical interface structure on the electrode surface, particularly for solid electrodes.

However the presence of Faradaic current resulting from the chemical adsorption/desorption of ions poses a challenge to the accuracy of capacitance measurements, given that chemical processes frequently occurs at solid electrodes. While numerous modified GCS models discuss the double layer structure by incorporating adsorption/desorption involving electron transfer, it must be emphasized that we still lack a precise understanding of how excess charge is built up exactly in the presence of chemical adsorption/desorption.

The use of the EQCM may allow for new insights into our understanding of electrochemical interfaces. The potential use of QCM as a mass sensor was first demonstrated by Sauerbrey in 1959. Nomura and Okuhara extended the applicability of QCM to liquid

based systems in their 1982 publication, initiating the development of EQCM for the field of interfacial electrochemistry.[19] Initially, QCMs were predominantly utilized as monitors for thin film deposition to control the film thickness. The initial application of EQCM measurements is rooted in the existence of a correlation between Faradaic charge involving electrochemical deposition and the mass change. However, increasing research has revealed that EQCM can also detect the electrostatic attraction of both ions and cations.[20, 21] These efforts have inspired our investigation into the distribution of excess charge on the gold surface. This was primarily accomplished through the combination of voltammetry and EQCM measurements.

In **Chapter 4**, we introduce the utilization of EQCM as an innovative approach to discern and quantify the electrode excess free charge. The EQCM exploits the oscillation frequency of a quartz crystal as a sensitive indicator of mass changes on a gold electrode. By capitalizing on the frequency response of the quartz crystal to the electrostatic attraction of free charges, this method may provide a means to identify the potential regions where a positive and a negative excess charge exist, respectively. Through a comparison of the frequency response recorded by the EQCM and the capacitance recorded by cyclic voltammetry, we can estimated the amount of excess free charge and the Faradaic charge in the entire pH scale. Furthermore, by examining the correlation between the excess free charge and the frequency response, we have constructed excess free charge distribution diagrams for both Ar and O_2 saturated solutions.These diagrams aim to visually depict how the excess charge may fluctuate at specific pH levels and applied potentials before and during catalysis.

The experimental results are exciting because through this study, we not only gained insights into the distribution of surface charges (excess charges and bound charges) in the presence of chemical adsorption without interference from Faradaic currents but also surprisingly discovered that this method of testing excess charge distribution may still be possible even during the oxygen reduction process.

Our discoveries in this thesis underscore the need for further in-depth research. Firstly, the Burke model involving different oxide layers was proposed based on the oxide reduction behaviors of various Nobel metals. **Chapter 2** reveals inaccuracies in applying the Burke

model to gold, necessitating an examination of its applicability to other metals. Secondly, the relatively limited influence of electrolyte ions on the gold oxide reduction behavior opens avenues to explore the relationship between Non-Nernstian behaviors and oxide structure changes (**Chapter 3**). Investigating the role of electrolyte ions in Non-Nernstian behaviors for more complex metal oxides poses an intriguing question on how metal cations from oxide play a role. Thirdly, our work indicates significant differences of interface environments for oxygen evolution/reduction on gold. Consequently, understanding these electrode structural changes becomes crucial for explaining the high overpotential of these reactions (**Chapter2-4**). Lastly, **Chapter 4** demonstrates that EQCM may be used to explore excess free charge on gold during ORR. This raises the intriguing possibility of investigating excess free charge on various materials and in different electrochemical reaction processes.

Besides, these three Chapters we mentioned earlier inspired us to reconsider more complex questions about how we comprehend the connection between applied potential and current in voltammetry. For example, how do we interpret changes in the shapes of redox peaks over different time scales, such as measurement time? How do we precisely identify the spatial distribution of active species in different homogeneous and heterogeneous processes in voltammetry? And Why do we sometime observe an imbalance between oxidation and reduction charges in voltammetry?

References

1. Conway, B. E., *Prog. Surf. Sci.* **1995,** *49* (4), 331-452.
2. Laurence D. Burke, L. D. B., Electrochemistry of hydrous oxide films. *Modern Aspects of Electrochemistry* 1986 pp 169-189.
3. Bard, A. K.; Zoski, C. G., *Analytical Chemistry* **2000,** *72* (9), 346A-352A.
4. Bowden, F. P.; Lowry, T. M., *Proceedings of the Royal Society of London. Series A, Containing Papers of a Mathematical and Physical Character* **1929,** *125* (798), 446-462.
5. Butler, J. A. V.; Armstrong, G.; Kendall, J., *Proceedings of the Royal Society of London. Series A, Containing Papers of a Mathematical and Physical Character* **1932,** *137* (833), 604-621.
6. Will, F. G.; Knorr, C. A., *Zeitschrift Fur Elektrochemie* **1960,** *64* (2), 258-269.
7. Shibata, S., *Electrochim. Acta* **1977,** *22* (2), 175-179.
8. James, S. D., *Journal of the Electrochemical Society* **1969,** *116* (12), 1681-&.
9. Burke, L. D.; McRann, M., *Journal of Electroanalytical Chemistry and Interfacial Electrochemistry* **1981,** *125* (2), 387-399.
10. Baten, S. M. A.; Taylor, A. G.; Wilde, C. P., *Electrochim. Acta* **2008,** *53* (23), 6829-6834.
11. Doyle, R. L.; Lyons, M. E. G., *Journal of The Electrochemical Society* **2013,** *160* (2), H142-H154.
12. Cheng, X.; Fabbri, E.; Nachtegaal, M.; Castelli, I. E.; El Kazzi, M.; Haumont, R.; Marzari, N.; Schmidt, T. J., *Chem. Mater.* **2015,** *27* (22), 7662-7672.
13. Wang, J.; Gao, Y.; Kong, H.; Kim, J.; Choi, S.; Ciucci, F.; Hao, Y.; Yang, S.; Shao, Z.; Lim, J., *Chem. Soc. Rev.* **2020,** *49* (24), 9154-9196.

14. Ding, H.; Liu, H.; Chu, W.; Wu, C.; Xie, Y., *Chem. Rev.* **2021,** *121* (21), 13174-13212.
15. Yang, S.; Hetterscheid, D. G. H., *ACS Catal.* **2020,** *10* (21), 12582-12589.
16. Gerken, J. B.; McAlpin, J. G.; Chen, J. Y.; Rigsby, M. L.; Casey, W. H.; Britt, R. D.; Stahl, S. S., *J. Am. Chem. Soc.* **2011,** *133* (36), 14431-42.
17. Bergmann, A.; Jones, T. E.; Moreno, E. M.; Teschner, D.; Chernev, P.; Gliech, M.; Reier, T.; Dau, H.; Strasser, P., *Nat. Catal.* **2018,** *1* (9), 711-719.
18. Hamann, C. H.; Hamnett, A.; Vielstich, W., *Electrochemistry*. 2nd completely rev. and updated ed. ed.; Weinheim : Wiley: 2007.
19. Buttry, D. A.; Ward, M. D., *Chemical Reviews* **1992,** *92* (6), 1355-1379.
20. Levi, M. D.; Salitra, G.; Levy, N.; Aurbach, D.; Maier, J., *Nat Mater* **2009,** *8* (11), 872-5.
21. Levi, M. D.; Sigalov, S.; Salitra, G.; Elazari, R.; Aurbach, D., *J Phys Chem Lett* **2011,** *2* (2), 120-4.

一个简单误判引发的蝴蝶效应。

The butterfly effect triggered by a simple misjudgment.

I

Supporting Information for Chapter 2

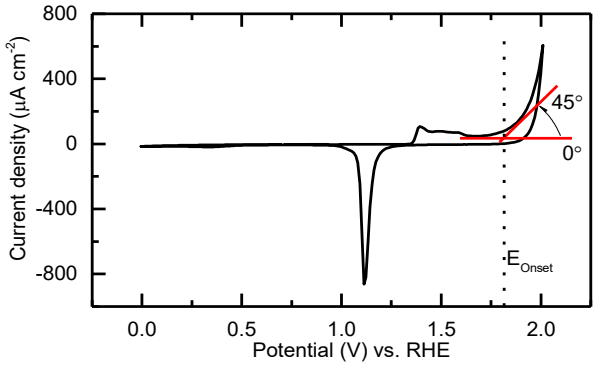

Fig. S1 The onset potential of OER is acquired by intersection of tangents between the baseline (horizontal line) and the rising current in the positive scan of cyclic voltammograms.[1] The angle between two intersection was fixed at 45°.

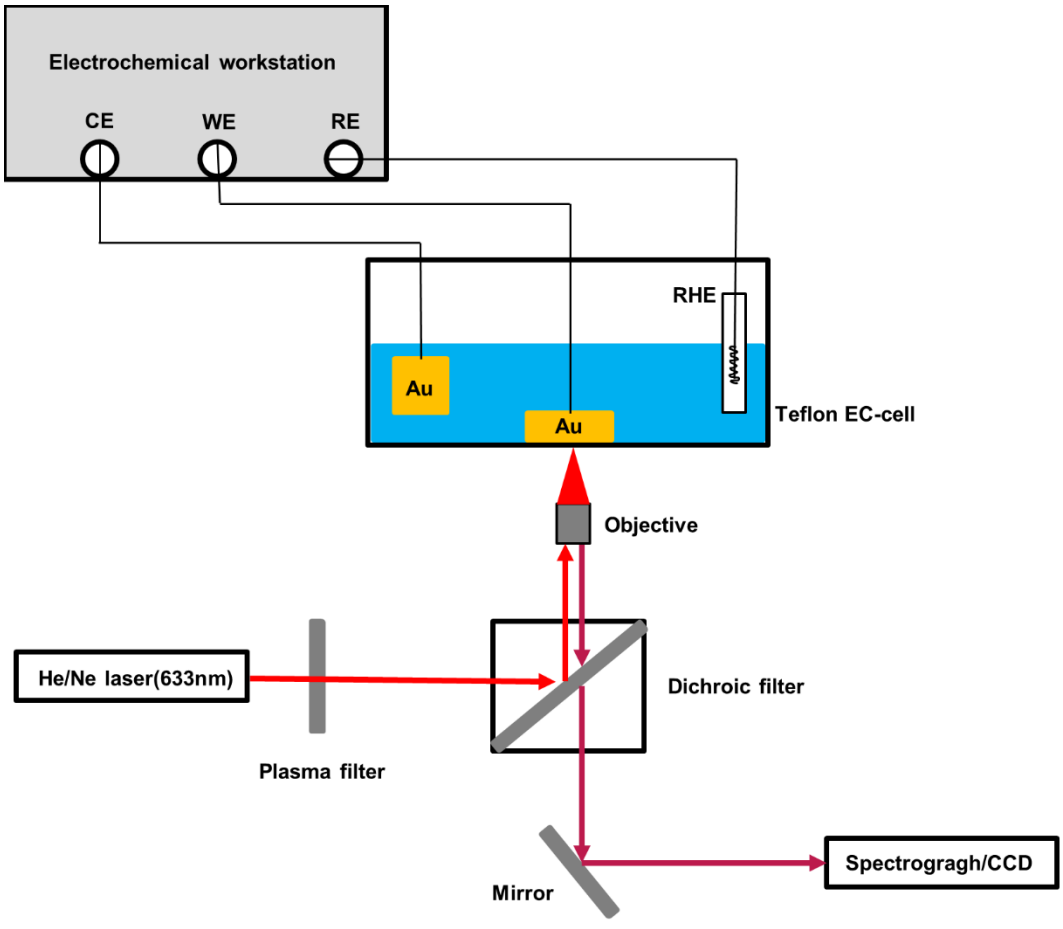

Fig. S2 Schematic diagram of electrochemical setup for in situ surface-enhanced Raman spectroscopic measurements.

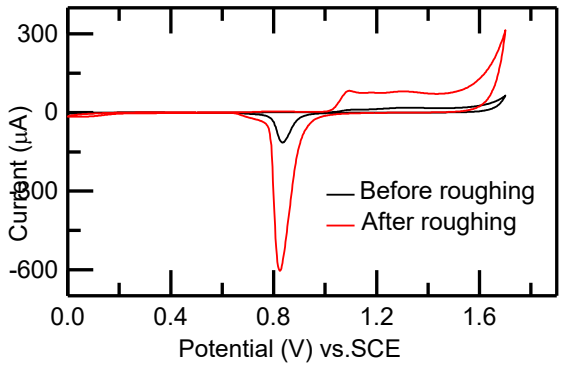

Fig. S3 Cyclic voltammogram of gold electrode at 50 mV/s in 0.1 M H_2SO_4 before and after gold surface roughing process. A successful roughing should show a significant enhanced current (at least 5 times) in a CV of roughed gold.

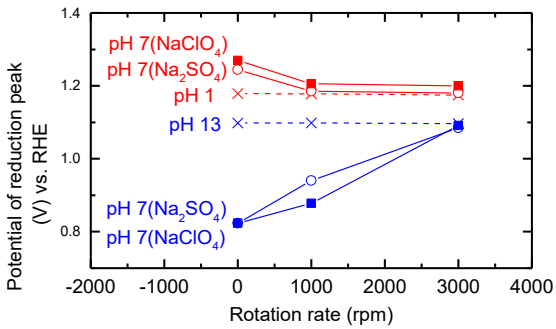

Fig. S4 The reduction potential where the α peak (red) and β peak (blue) are observed at different rotation rates. At pH 1 and pH 13 the positions of peak potential of the α and β peaks are not dependent on the rotation rate. At non rotating conditions the potential at which the α and β peaks occur has massively shifted in neutral solution compared to in the acidic and alkaline situation. However, upon rotation the potential of the α and β peak in neutral solution revert to the same position as observed in acidic and alkaline conditions. The peak potentials are obtained from Figure 3b in the main text.

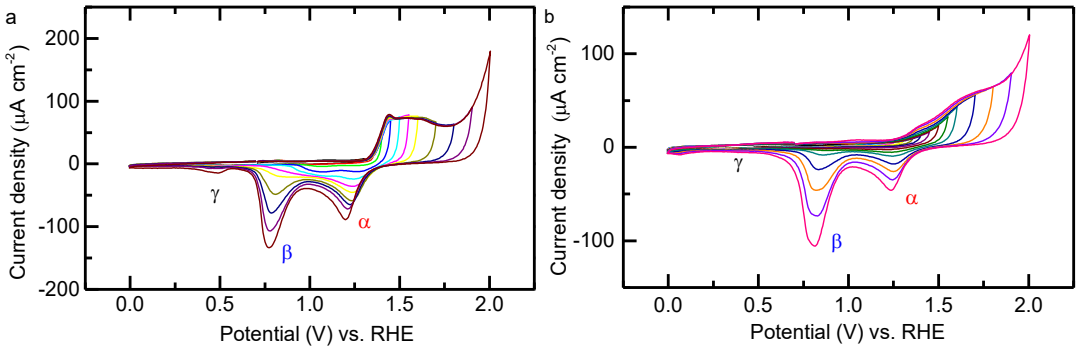

Figure S5 Cyclic voltammograms of gold at 50 mV/s with different upper potentials limits in (a) 0.1 M Na_2SO_4 or (b) 0.1 M $NaClO_4$.

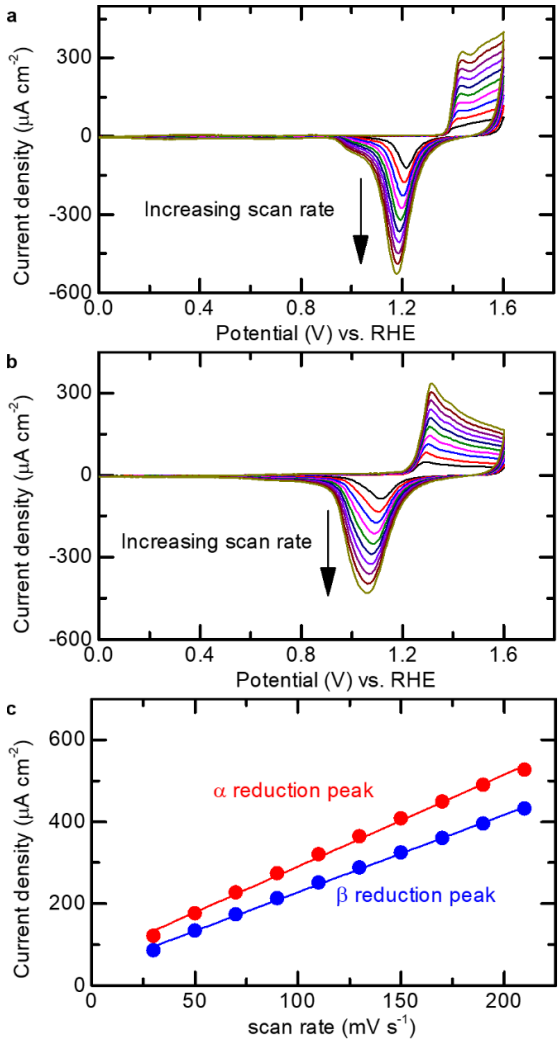

Fig. S6 CVs of gold at a range of scan rates between 30 and 210 mV/s in 0.1 M H_2SO_4 (a) or 0.1 M NaOH (b).Plot of peak currents of two oxides reduction as a function of scan rate.

Figure S6 shows the effect of scan rates to oxide reduction peaks. Because oxide reduction is an irreversible electrochemical process, both of two oxides show minor negative potential shift with increase of scan rate from 30 to 210 mV/s, as shown in Fig. S6, where α peak potential is at 1.16 ± 0.02 V and β peak potential is at 1.03 ± 0.03 V. Besides, reduction peaks was found to be linearly dependent on scan rates, not the square root of the scan rate. This reveals the redox reaction is confined to the electrode surface, i.e. no diffusion mode, which meet the characteristics of oxide reduction on the gold surface.

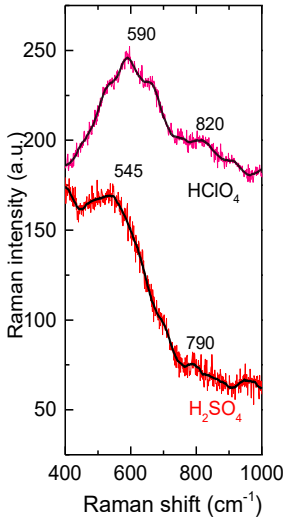

Fig. S7 In situ SERS of gold at 1.6V vs. RHE in Ar-saturated 0.1 M $HClO_4$ (pink line) and H_2SO_4 (red line) solution.. The ν(Au-O) vibration was observed at 590 cm^{-1} and the ν(O-O) vibration of Au-OOH was observed at 820 cm^{-1} in 0.1 M $HClO_4$ solution, which is consistent with previous reports in $HClO_4$ solution.[2-4] The ν(Au-O) vibration and the ν(O-O) vibration of Au-OOH have shifted to 545 cm^{-1} and 790 cm^{-1} in 0.1 M H_2SO_4 , which may be caused by adsorption of sulfate ions in H_2SO_4. Note that the ν(Au-O) vibration was reported to shift as a function of the oxidation potential.[4]

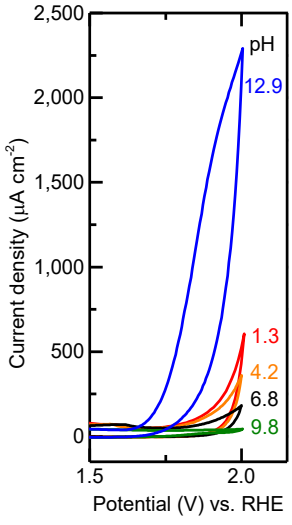

Fig. S8 Shown is the part of the CVs involving oxygen evolution, as a function of pH belonging to Figure 6a of the main text. Conditions: scan range is 0-2 V vs. RHE at 50 mv/s.

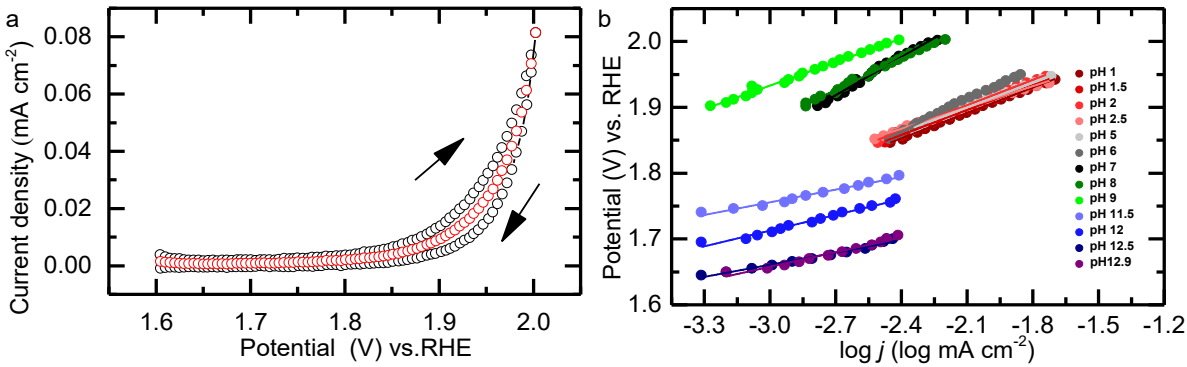

Fig. S9 a. OER activity was measured from the average (red) of the backwards (black) and forward (black) current density in a CV under steady-state conditions (1 mV s^{-1}). **b**. Tafel plot, which was obtained from the average of OER activity (red dot line in (a))

Table S1 Tafel slopes in different pH solution, which is calculated from Figure S9

pH	1	1.5	2	2.5	5	6	7	8	9	11.5	12	12.5	12.9
Tafel slope (mV/decade)	128	126	128	108	124	160	192	158	119	79	64	61	73

References

(1) Huang, Z. F.; Wang, J.; Peng, Y.; Jung, C.-Y.; Fisher, A.; Wang, X., *Adv. Energy Mater*. **2017**, *7*, 1700544.
(2) Liu, K.; Chen, T.; He, S.; Robbins, J. P.; Podkolzin, S. G.; Tian, F., *Angew. Chem. Int. Ed. Engl.* **2017**, *56*, 12952-12957.
(3) Diaz-Morales, O.; Calle-Vallejo, F.; de Munck, C.; Koper, M. T. M., *Chem. Sci.* **2013**, *4*, 2334-2343.
(4) Yeo, B. S.; Klaus, S. L.; Ross, P. N.; Mathies, R. A.; Bell, A. T., *Chemphyschem* **2010**, *11*, 1854-7

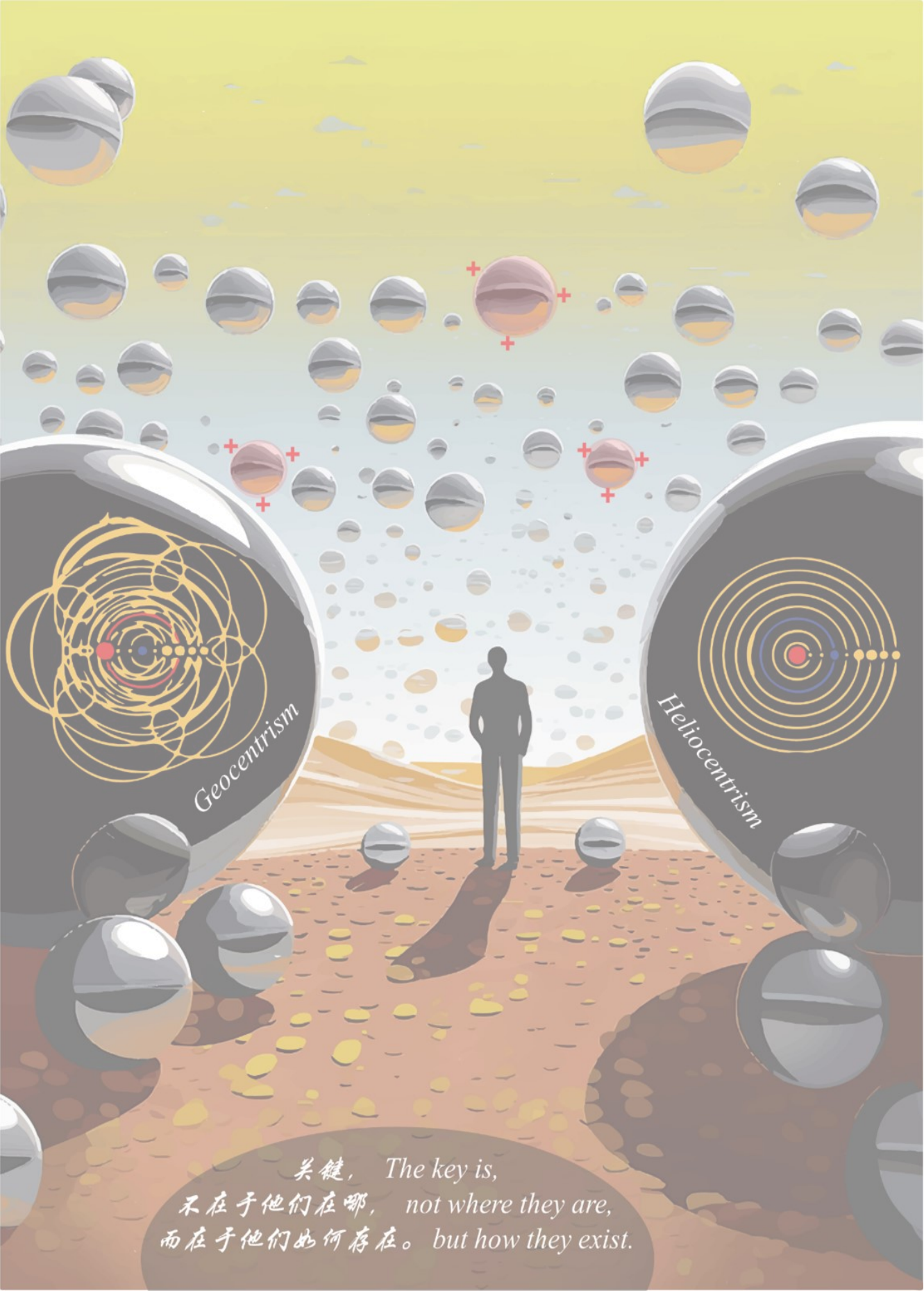

关键， The key is,
不在于他们在哪， not where they are,
而在于他们如何存在。 but how they exist.

II

Supporting Information for Chapter 3

The PDF file includes:

Materials and Methods

Supplementary Text

Figs. S1 to S16

Tables S1

Materials and Methods

General.

All glassware was thoroughly cleaned to remove impurities by overnight submersion in an aqueous 0.5 M H_2SO_4 solution mixed with 6.3 mM $KMnO_4$, followed by removal of excess $KMnO_4$ on the glassware in diluted H_2SO_4 and H_2O_2. The glassware was subsequently rinsed five times and boiled three times in Millipore MilliQ water (resistivity is 18.2 MΩ cm). Prior to each electrochemical experiment, the glassware was boiled once in MilliQ water. Alumina suspensions (1.0, 0.3, and 0.05 μm) were obtained from Buehler. Electrolyte solutions were prepared with Suprapur® (Merck) reagents and MilliQ water. Determination of the pH was done using a Hanna Instruments HI 4222 pH meter which was calibrated using IUPAC standard buffers.

Electrochemical measurements.

All electrochemical measurements were conducted with Autolab PGSTAT 12, 204 and 128N potentiostats in combination with Autolab NOVA software and carried out in conventional single compartment three–electrode glass cells at around 25 °C. A PEEK encapsulated gold electrode (A = 0.0314 cm^2, Metrohm) was used as working electrode, and a gold wire was the counter electrode, while a reversible hydrogen electrode (RHE) was employed as the reference electrode. Before a measurement, the working electrode (the PEEK encapsulated gold) was manually polished for 2 minutes with 1.0, 0.3, and then 0.05 μm alumina suspensions on Buehler cloth polishing pads, followed by sonication in MilliQ water for 10 minutes. A gold wire to be used as the counter electrode was flame annealed and rinsed with MilliQ water. The reference electrode (RHE) consisted of a Pt wire and was connected via a Luggin capillary and continuously bubbled with H_2 gas during each measurement.

The pH 1–13 solutions were obtained by mixing 0.1 M $HClO_4$, NaOH and $NaClO_4$. Unless stated otherwise, pH 1–13 represent solutions with fixed pH value comprising $HClO_4$, NaOH and $NaClO_4$ in this article and the ionic strength of the electrolyte solution was kept at 0.1 M. The solutions with different cations (Li^+, Na^+, K^+, Cs^+) and at different pH were

obtained by mixing $HClO_4$, hydroxide and perchlorate salts, shown in fig. S3. Here, in order to better compare the effects of cations to gold oxide reduction, the concentration of electrolyte solution was kept at 0.05 M rather than 0.1 M due to the low solubility of $CsClO_4$. Dissolved oxygen was removed from the solution prior to each measurements by bubbling argon (purity grade 5.0) for at least 30 min. Argon was kept flowing above the solution during all experiments.

Rotating ring–disk electrode (RRDE)

RRDE experiments were conducted using an Autolab PGSTAT 12 potentiostat and a Pine Instruments MSR rotator. All measurements were done in a custom–build glass two–compartment cell with a three–electrode setup. A gold wire was used as a counter electrode, separated from the main compartment by a glass frit. A gold disk (A=0.196 cm^2) was used in conjunction with gold ring in a Pine Instruments E6R1 ChangeDisk setup. To detect the release of Au^{3+} from the disk, the ring was set at a fixed value below the potential of oxide reduction, and higher than the onset potential of the oxygen reduction reaction (E_{ORR}) on gold. Because E_{ORR} on gold changes with pH, the E_{ring} was set at 0.6 V in 0.1 M $HClO_4$ and $NaClO_4$ and at 0.9 V in an alkaline solution.

Electrochemical quartz crystal microbalance (EQCM)

The EQCM experiments were conducted using an Autolab PGSTAT 128N potentiostat and a 5 mL Autolab EQCM cell. An Autolab gold coated quartz crystal EQCM electrode (A = 0.35 cm^2, gold layer thickness = 100 nm) was used as the working electrode and a coiled gold wire was used as the counter electrode. An RHE Luggin setup was used as the reference electrode.(*37*)

Supplementary Text

S1. Literature overview of oxide formation

In general, the oxidation of noble metals includes the two–dimensional surface processes wherein OH and O chemisorption occurs, quasi–three dimensional surface reconstruction by a place exchange between the OH and/or O species and surface metal atoms, and thickening of the oxide film in a high electrostatic field or upon long oxidation times. Historically, cathodic reduction of oxide was mainly used to determinate the oxide thickness and to investigate the different layers of oxides. For the reduction of a metal oxide ($M_2O_x + 2xH^+ + 2xe^- \rightarrow 2M + xH_2O$), the Nernst equation indicates that the reduction potential of oxide should not change on the RHE scale. However, such metal oxide reduction peaks often do show an abnormal potential shift. i.e. a non–Nernstian shift, especially when the oxidation potential increases. It is worth noting that non–Nernstian behavior is not only observed for noble metal oxides but has been extensively reported in case of many other metal oxides.(*7, 38-40*)

Explanations of the non–Nernstian behavior of the reduction of metal oxides vary substantially over literature, such as the strong effects of anions chemisorption, (*41*) a hysteresis behavior caused by the irreversible quasi–3 dimensional oxide formation(*11*), the effect of oxidation state changes, (*42, 43*) or a slow reduction process of the outer layer of a thick oxide (*21, 24*). We must point out that these above discussions are speculations and were never directly proven leading to a rather one–sided conclusion.

Non–Nernstian behavior of metal oxide reduction reactions often appear in oxide corrosion studies.(*26, 44*) This triggered the hypothesis whether the non–Nernstian behavior of the oxide reduction reaction may be directly caused by the self–reconstruction of oxides. Gold is frequently seen as the most ideal noble metal for the investigation of oxide formation. First, gold has very weak chemisorption properties so that it shows a wide double layer region, thereby avoiding the effect of co–adsorption of electrolytes during the oxide reduction process. Second, Au(+III) has been shown to be the only stable oxidation state observed in gold oxides by ex situ X–ray photoelectron spectroscopy(*22*) and in situ extended X–ray absorption fine–structure studies.(*23*) Normally only two stable forms of oxidized gold can be observed in the Pourbaix diagrams of gold, i.e. auric oxide (Au_2O_3) and gold trihydroxide ($Au(OH)_3$),(*44*) as shown in fig. S9.

In our previous research, we found that two independent forms of gold oxides, i.e α and β, are present at all pH values when the initial oxide layer forms.(*8*) The α phase is preferably formed in an acidic environment, while the β phase is preferably produced under alkaline conditions. Both phases can coexist in neutral solutions. We assigned the two oxides to Au_2O_3 (α oxide) and $Au(OH)_3$ (β oxide) by combining our in situ Surface–Enhanced Raman Spectroscopy (SERS) experiment and computational results by the Koper group.(*45*) However, all these previous studies do not answer why the oxide reduction peaks show non–Nernstian behavior.

S2 Detection of hydration shells surrounding Au^{3+} at neutral conditions by the RRDE ring

In the RRDE experiment at pH 7, when the potential is negatively scanned in order to reduce gold oxide, the consumed protons in the β oxide reduction reaction most likely do not stem from the bulk solution, but must come from the hydration shells of Au^{3+} itself. Consumed protons are not easily compensated for given that the concentration of protons at neutral conditions is low. Therefore the pH of the surface hydration shells must increase rapidly, especially at pH 7. This causes the hydration shells to obtain a negative charge at its surface:

$$Au(OH)_3 \cdots (H_2O)_n Au^{3+} + 3e^- \rightarrow Au + 3H_2O + (HO^-)_3(H_2O)_{n-3}\, Au^{3+}$$

Based on the Nernst-Planck equation, the total current distribution is a summation of a diffusion, convection and migration in a RRDE experiment.(*27, 28, 46, 47*) The ionic migration is driven by the gradient of electric filed ($\Delta E/l$) in the potential (ΔE)) over distance (l).(*27*) In the presence of an excess of supporting electrolyte, the ionic migration to the flux of electroactive species is often neglected to simplify the mass transfer conditions. (*47*) However, for many cases $\Delta E/l$ is hard to reduce and the ionic migration affect remains important in a RRDE experiment.(*28, 46*)

In RRDE experiments in a neutral solution, we observed that a positive current appears first on the ring, and is followed by a negative current ,when E_{ring} is set at higher than 0 V vs. RHE (fig. S4). Our observations are as follows:

1) The positive current is observed first and is followed by a negative current. This is independently of the lower vertex potential and scan direction set at the disk (fig. S4A-D).

2) The positive current is heavily dependent on the rotation rate (fig. S4E-F), and largely disappears at high mass transport rates (fig. S4F).

3) When change the rotation rates, the negative current detected on the ring does not change, while the positive current rapidly decreases with increasing rotation rates. While the positive current decreases, the potential at which the negative current occurs starts to shift to more positive potentials (fig. S4E).

4) Additionally, the positive current can be detected at low E_{ring} (E_{ring}> 0 V vs.RHE), which excludes the formation of most reactive oxygen species being responsible.

This reflects that the observed delay of Au^{3+} reduction is directly related by an event that apparently causes an unusual positive current on the ring. Based on these observation, we deduced that the positive current does not belong to a Faradaic current caused by an oxidation reaction, but should be assigned to a non-Faradaic current that is caused by the migration of considerably large hydration shells that accompany Au^{3+}, and largely have a negative charge due to the gold oxide reduction reaction mediated under neutral conditions. When the rotation rate increases the mass transfer of proton, the electronegativity decrease as the hydration shell is refreshed.

These hydration shells with a negatively charged surface migrate to the ring of RRDE to initially cause a non–Faradaic positive current, as shown in fig. S4. Detection of such a non–Faradaic positive current is therefore considered as a significant finger print for the presence Au^{3+} bearing a significant hydration shells at the surface of gold oxide. There are two ways to reduce the Au^{3+} cations present within these hydration shells:

1) A step–by–step reduction including shell release, shell peeling and finally Au^{3+} reduction. This process shows a delayed Au^{3+} reduction current on the ring due to an interference with the non–Faradaic caused by the shell migration and due the slow shell peeling process (fig. S4).

2) A direct reduction of Au^{3+} can be performed at a sufficiently negative ring potential (< 0 V) that is necessary to overcome the energy barrier for electron tunneling through the hydration shells (Fig. 2D)

S3 The presence of ionized Au^{3+} and hydrous Au^{3+} on the oxides surface relates to the stability of the interface double layer

Our EQCM results show that the mass loss does not start at the beginning of the oxide reduction process. Instead the mass loss takes place immediately and quickly when the potential is scanned over a particular threshold value (E_ψ). In an acidic solution (Fig. 3B), when E_+ is set below 1.5 V, the emergence of E_ψ is independent of E_α and E_β. Yet E_ψ shifts consistently with E_α once $E_+ > 1.5$ V. Our RRDE experiments show that ionized Au^{3+} exists in α oxide when $E_+ > 1.5$ V.(Fig. 2B) This suggests that the presence of Au^{3+} relates to the behavior of E_ψ as well.

It is important to note that the detected frequency changes reflect the mass change of the absorption layer, which does not only include the actual oxide layer itself, but also the rigid adsorption layer at the solid-electrolyte interface, which relates to the interface properties (viscosity, density etc.) and weight of the solvation shell and ions present therein. (*30-32*) In fig. S8, we compared the difference between the oxide mass change calculated from the overall charge transferred during the gold oxide formation, and the total mass change detected by the QCM. In an acidic solution, when ionic Au^{3+} forms on α oxide (E_+>1.5V), total mass increase is always bigger than the gold mass increase, as shown in fig. S8A. A similar phenomenon also happens in a neutral solution (fig. S8C), when hydrous Au^{3+} forms on β oxide (E_+>1.5V). Those observations clearly show that ionized Au^{3+} and hydrous Au^{3+} have the ability to fix more molecules resulting in a heavier double layer, as shown in Fig. S8B and

D. It worth to note that the extra mass change caused by hydrous Au^{3+} is much bigger than that caused by ionic Au^{3+}. This indicates hydrous Au^{3+} ions bound to β oxide has a stronger ability to bind molecule tightly in a neutral solution than ionic Au^{3+} ions bound on α oxide in an acidic solution. No significant additional mass is detected by EQCM if no Au^{3+} is present at the electrode surface. Under those conditions the mass changes detected by the EQCM fit well with the presence of the lattice oxygen atoms belonging to the stoichiometry of Au_2O_3 and $Au(OH)_3$.

According to our EQCM and RRDE experiments, the reduction of α oxide and the release of Au^{3+} start at the same time, i.e. the onset potentials of α reduction and Au^{3+} release are the same as observed by RRDE experiments (fig. S11A). However, the mass loss starts only when the scanning potential approaches E_α (fig. S5B). The change of E_ψ also follows a similar trend in neutral and alkaline solutions: E_ψ is always closer to the peak potential rather than the onset of the reduction reaction. Based on past research, oxide reduction is expected to occur via a bottom-to-top reduction process on the oxide surface.(*11*) This indicates that the bottom part of oxide should be reduced first when scanning the reduction potential over the onset potential of an oxide reduction peak. And the top part of oxide may not be reduced until the scanning potential approaches the peak potential. Therefore we deduce that the emergence of E_ψ is most likely related to the presence of Au^{3+} at the outer surface of the oxide layer. The stable structure of the double layer in the oxide–electrolyte interface will be broken due to the disappearance of Au^{3+} at the oxide surface upon reduction.

Tracing correlations between E_ψ, E_α and E_β during a CV experiment allows one to understand the role of Au^{3+}at the surface in relation to the stability of the gold oxide structure. In a neutral solution (Fig. 3C and fig. S6), when $E_+ < 1.9$ V, the existence of ionized Au^{3+} in α oxide and hydrous Au^{3+} in β oxide can be recognized on the basis of their non–Nernstian behavior at the same time. However, the EQCM data shows that E_ψ only relates to E_β and not to E_α, indicating that only hydrous Au^{3+} at β oxide are present on the surface under these conditions (fig. S6A). When E_+ is set in the range of 1.9–2.1V, the existence of two separated E_ψ values indicates that both ionized Au^{3+} at α oxide and hydrous Au^{3+} at β oxide are present on the surface (fig. S6B-D). When E_+ is set above 2.1 V, the effect of hydrous Au^{3+} to

stabilize the interface disappears (fig. S6E-F). At these conditions H_2O molecules from the hydration shells are oxidized to O_2. Unless hydration of the Au^{3+} sites is sufficiently rapid compared to the evolution of dioxygen, only ionized Au^{3+} will remain on the oxide surface.

S4 Identification of Au^{3+} saturation at the oxide surface by EQCM

As described in section S3, the E_ψ observed by EQCM experiments is a powerful indicator to reveal the presence of Au^{3+} ions at the surface of the gold oxide layer. In an acidic solution (Fig. 3B), when Au^{3+} is bound to α oxide ($E_+ > 1.5$ V), E_ψ and E_α show a consistent non–Nernstian behavior with the increase of E_+. However the consistency between E_ψ and E_α is broken when $E_+ > 2.1$ V. Here E_ψ and E_α separate upon further increase of E_+. The separation between E_ψ and E_α also appears in neutral solutions once $E_+ > 2.1$ V (Fig. 3C). Although the amount of Au^{3+} increases with E_+, there must be a maximum value for the amount of Au^{3+} that can realistically bind to the oxide surface due to the limited amount of binding sites. Further increasing E_+ will cause more Au^{3+} to be formed. Due to a lack of sufficient binding sites on the Au_2O_3 surface, these Au^{3+} ions will escape from the rigid interface into the diffusion layer.

For Au^{3+} ions binding to the oxide surface, their reduction reaction proceeds simultaneously with reduction of the oxide layer. This is illustrated by the non-Nernstian negative shift of E_α, when the amount of Au^{3+} at the surface increases. Yet, for free Au^{3+} species that have diffused into the solution, its reduction can only occur once the gold oxide layer has largely been reduced. Although free Au^{3+} produced upon the oxidation of gold shows a reversible reduction wave at a very high scan rate at an early stage of the oxide formation (fig. S10A), reduction of free Au^{3+} becomes fully irreversible when a thick oxide layer is formed. Apparently, reduction of free Au^{3+} is fully blocked by the oxide layer.

The actual reduction of free Au^{3+} occurs negatively from E_α due to Au^{3+} mass transport processes from the solution to the electrode.(*48*). Given that E_α and the reduction of free Au^{3+} are not deconvoluted, the E_α peak shifts more negatively, while E_ψ does not. After all reduction of free Au^{3+} occurring in solution is not picked up by the microbalance.

The saturation of the gold oxide layer with ionic Au^{3+} hardly appears in case of β oxide in alkaline solutions, even when very high oxidation potentials are applied. This is due to regeneration of $Au(OH)_3$ upon hydroxylation of Au^{3+} as soon as it is formed. This also explains well why E_ψ and E_β shift consistently under these conditions even at a high oxidation potentials. (Fig. 3D).

S5 Calculating the amount of Au^{3+} in α oxide based on the slope in the E_α– pH plot

When E_+ is set to higher values, Au^{3+} is formed at the oxide surface and will bind to the exposed oxide sites of α oxide (Au_2O_3) via ionic interactions. The structure of α oxide therefore must change from a fully covalent oxide (Au_2O_3) to a covalent–ionic oxide ($Au_2O_3 \cdots xAu^{3+}$), where x represents the amount of Au^{3+} per α oxide site. According to our EQCM analysis, E_ψ and E_α show a simultaneously negative shift upon an increase of E_+ when E_+ is set at or above 2.1 V. This is the result of more ionized Au^{3+} stabilizing Au_2O_3 through the formation of ionic bonds. However, when E_+ is set above 2.1 V, E_ψ and E_α will separate, indicating that ionized Au^{3+} has become saturated at the α oxide layer and free Au^{3+} migrates into the diffusion layer (see section S4). Here, we have defined that y represents the number of free Au^{3+} equivalents in solution.

When $E_+ < 2.2$ V vs. RHE, y=0 as we do not observe any separation between E_ψ and E_α in our EQCM experiments, indicating that no free Au^{3+} has formed yet. Under these conditions the α oxide reduction reaction can be expressed as

$$Au_2O_3 \cdots xAu^{3+} + 6H^+ + 3(2+x)e^- = (2+x)Au + 3H_2O \quad (1)$$

Its Nernst equation should then be formulated as:

$$\Delta E_\alpha = -0.059\left(\frac{2}{x+2}\right) \times \text{pH} \quad (2)$$

which indicates that E_α will change as a function of the pH on the RHE scale given that $\frac{2}{x+2} \neq 1$. This allows us to trace the amount of α oxide–$Au_2O_3 \cdots xAu^{3+}$ formed on the basis of the slope of $K = 0.059(\frac{x}{x+2})$ (vs. RHE) (see fig. S15). Indeed we observed that the slope of

E_α vs pH increases with E_+.(Fig. 1B) The relation between x and E_+ is shown in table S1. The amount of Au^{3+} per α oxide site increases from 0 to 0.4 before the oxygen evolution reaction (OER) commences and eventually reaches a value of 0.9 during the OER process at 2.1 V vs. RHE.

An assumption that we make here is that x does not further increase after the oxide layer has become fully saturated with Au^{3+} when $E_+ \geq 2.2$ V vs. RHE. In other words we expect $x \leq 1$, given that there are only a limited amount of sites on the surface of α oxide. It is indeed at $E_+ \geq 2.2$ V vs. RHE, where separation between E_ψ and E_α can be observed (Fig. 3 B, C). This suggests that Au^{3+} first binds to the surface of α oxide, and once the surface is fully saturated, it is lost to the double layer as free Au^{3+}.

The K value does show a slow increase below E_{OER} but rapidly increases at potentials above E_{OER} during a standard cyclic voltammetry experiment(see Fig. S15). This indicates that large amount of Au^{3+} forms at potentials above E_{OER}. It is worth noting that the increasing trend of Au^{3+} has also been directly observed in a previous metal corrosion study by a setup composed of a micro–electrochemical scanning flow cells (SFC) and inductively coupled plasma mass spectrometer (ICP–MS), where Cherevko *et. al*. found that the amount of gold cations detected is relatively minor at potentials below the onset for OER but quickly increase when the oxygen evolution reaction commences.(*26*)

S6 Transformations between ionized Au^{3+} and hydrous Au^{3+}

The complexity of the liquid–solid interface at neutral conditions is caused by the presence of both ionized Au^{3+} and hydrous Au^{3+}, and which cause different non–Nernstian shifts. Yet by carefully examining the presence of the α and β oxide peaks and their non–Nernstian shifts we can pinpoint how the oxide surface structure changes as a function of the applied reaction conditions.

First, there must be a competition between ionized Au^{3+} and hydrous Au^{3+} illustrated in fig. S12, which is dependent on the nucleophilicity of H_2O at the operating pH, and the

nucleophilicity of the oxygen sites of the metal oxide surface. When the pH is closer to 4, H^+ will inhibit the nucleophilicity of H_2O resulting in ionized Au^{3+} being formed preferably over hydrous Au^{3+}. However, when the pH is closer to 7, the formation of hydrous Au^{3+} will prevail over ionized Au^{3+}. The importance of the nucleophilicity of H_2O for the Au^{3+} hydration shell formation is shown in fig. S16. If we oxidize gold at a high oxidation potential and then directly scan in a negative direction without any stirring, the α reduction peak occurs at 1.29 V (red line in fig. S16). However, if we use MilliQ–water to rinse the oxidized gold electrode first and place the oxidized gold into a fresh 0.1 M $NaClO_4$ solution to measure a CV, we can see a significant shift with more than –0.6 V, which points to a transition from α oxide to β oxide. Furthermore, the β peaks shows a more negative shift if we increase the oxidation time to produce more Au^{3+} (see blue, purple and dark blue line in fig. S16). This illustrates that ionized Au^{3+} reduced at 1.29 V turns into hydrous Au^{3+} reduced below 0.7 V after rinsing with MilliQ–water ($\cdots Au^{3+} \xrightarrow{nH_20} \cdots (H_20)_n Au^{3+}$), as shown in the insert of fig. S16. It worth noting that the hydrous β oxide formed by MilliQ–water rinsing shows a significant more negative shift than the samples produced in 0.1 M electrolyte. This indicates that a more stable hydrous oxide is formed in MilliQ–water compared to water that is devoid of any electrolyte.

The non–covalent interactions of Au^{3+} with the oxide surface must be weak, independent whether these are ionic interactions at acidic conditions, or hydrogen bond interactions at neutral conditions. This means we can manipulate the levels of both ionized Au^{3+} and hydrous Au^{3+} by changing the rotation rate. Both the α and β peaks can still be observed when rotation rates are set below 400 rpm (see lower part in fig. S4A). Interestingly, the non–Nernstian behavior of the α and β peaks disappears when fast rotation rates are set (3000 rpm). In this latter experiment the ionized Au^{3+} and hydrous Au^{3+} species apparently dissociate from the oxide surface and are lost to the bulk solution (see fig. S13A and fig. S14A). If we increase E_+ , the β peak still will show a gradual negative shift, even at 3000 rpm (see fig. S13B and fig. S14B). When E_+ is set above E_{OER}, the mutual transformation between the α peak with ionized Au^{3+} and the β peak with hydrous Au^{3+} can be observed during the OER process by changing the rotation rate from 0 rpm to 3000 rpm.(see fig. S13C and fig. S14C). At 0 rpm

mostly α oxide is present in the cyclic voltammogram, while experiments at 3000 rpm mainly show the formation of β oxide. The water of the hydration shells is consumed during the OER process, and will lead to the transformation of hydrous Au^{3+} to ionized Au^{3+} at non rotating conditions (0 rpm) due to a local accumulation of H^{+}. Yet at a high rotation rate (3000 rpm) both the mass transport of water and protons are faster, allowing for the hydration shell structure to be refreshed timely. The mutual transformation between ionized Au^{3+} and hydrous Au^{3+} is independent of whether $NaClO_4$ or Na_2SO_4 is used as an electrolyte. (fig. S13 and fig. S14)

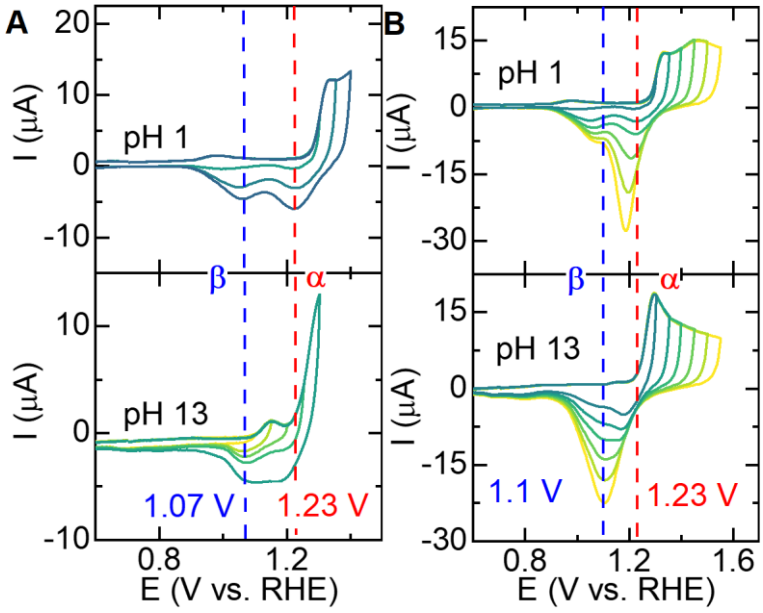

Fig. S1 Cyclic voltammograms of gold at 50 mV/s in pH 1 and 13. (**A**) E_+ was varied from 1.1–1.4 V; (**B**) E_+ was varied from 1.35–1.55 V; The red and blue dash lines represent the reduction peak potential of initial formation stage of α and β oxide, respectively.

When E+ is changed from 1.25 to 1.5, the β peak shows a minor +0.03 V shift from 1.07 to 1.1 V, which reflects the process from reversible adsorbed OH^- to a stable bulk–phase solid $Au(OH)_3$.(*8*) The minor shift of the β peak is independent of the pH, i.e. it follows Nernstian behavior. Because the values of 1.23 V for the α peak and 1.1 V for the β peak are constants providing that the potential (E_+) is kept low, they are used to represent the reduction potential non-shifted α and β oxide in our main text, respectively.

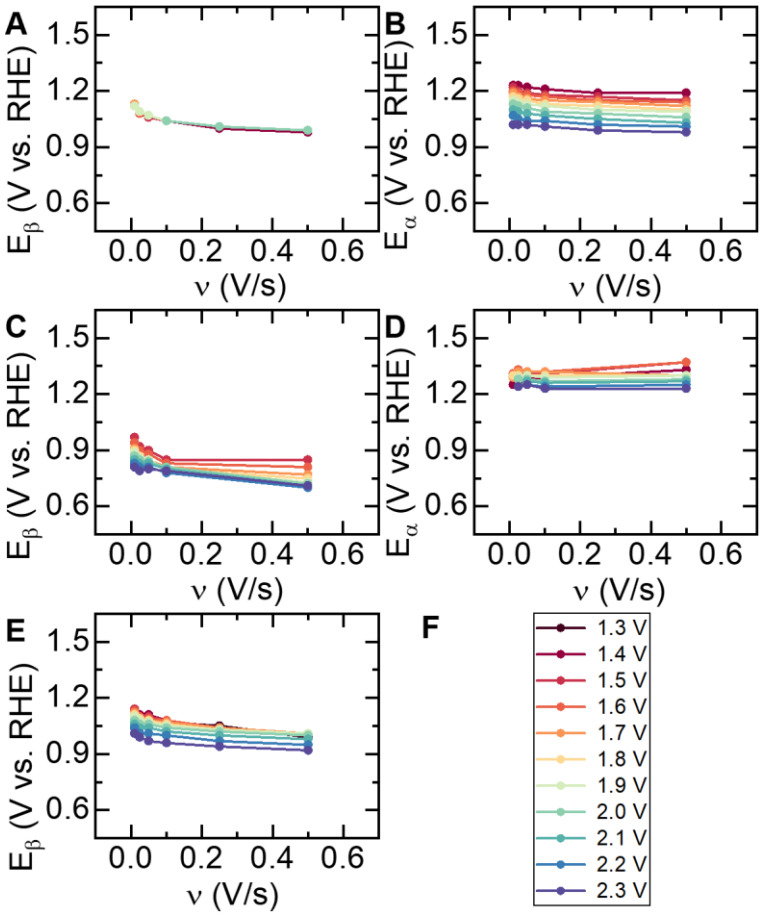

Fig. S2 The potential of the β (E_β) and α (E_α) reduction peaks with the increase of E_+ in the scan rate (ν) of 0.01-0.5 V/s in 0.1 M $HClO_4$ (**A-B**), $NaClO_4$ (**C-D**), NaOH (**E**). (**A**) E_β in 0.1 M $HClO_4$; (**B**) E_α in 0.1 M $HClO_4$; (**C**) E_β in 0.1 M $NaClO_4$; (**D**) E_α in 0.1 M $NaClO_4$; (**E**) E_β in 0.1 M NaOH; (**F**) different colorful lines shown in (**A-E**) represent the change of E_+ from 1.3V to 2.3 V on the RHE scale.

The appearance of the non–Nernstian behavior of the α and β peaks are largely consistent when the scan rate between 0.01 to 0.5 V/s, as shown in fig. S2. This indicates that the observed non–Nernstian behavior is not caused by kinetic effects. It also allows one to extrapolate the outcome to a scan rate of 0 V/s, thereby excluding any pH effects that may occur during the reduction of α and β oxide.

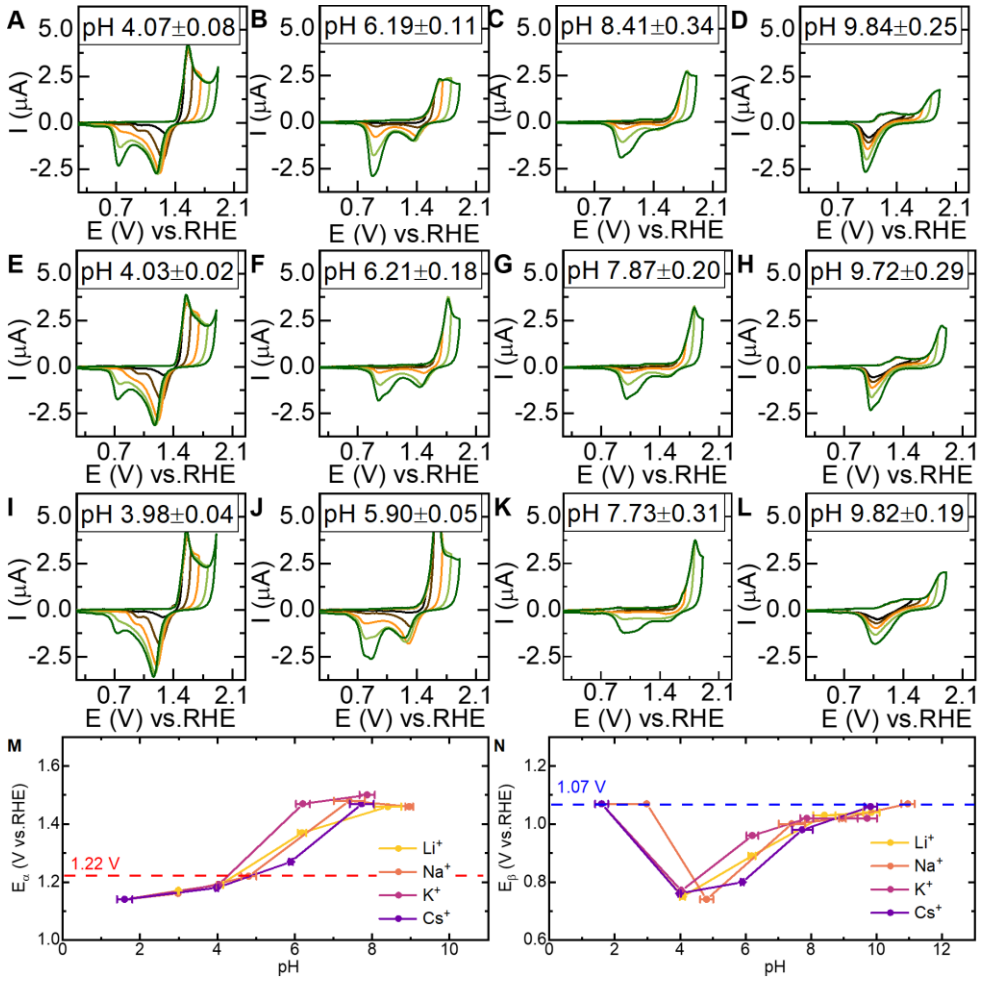

Fig. S3 Cyclic voltammograms of gold with varying E_+ in the range of 1.5–1.9 V at different pH in 0.05 M $LiClO_4$ (**A-D**), $KClO_4$ (**E-H**), $CsClO_4$ (**I-L**); (**M**) E_α of CVs (0-1.8 V vs. RHE) with changing solution pH at 0.05 M different cations and red dash line represents the reduction peak potential of initial formation stage of α oxide; (**N**) E_β of CVs (0-1.8 V vs. RHE) with changing solution pH at 0.05 M different cations and the blue dash line represent the reduction peak potential of initial formation stage of β oxide. The error represents the deviation of solution pH before and after measurements.

The non–Nernstian behavior of the β peak is most significant in neutral solutions, as shown in Fig. S3. The non–Nernstian shifts of the α and β peaks are highly consistent when we change anion (SO_4^{2-} and ClO_4^- shown in our previous work) (*8*) or the type of cation (Li^+,

Na^+, K^+, Cs^+ in Fig. S3) present in the electrolyte. We therefore can exclude electrolyte adsorption playing a major role here.

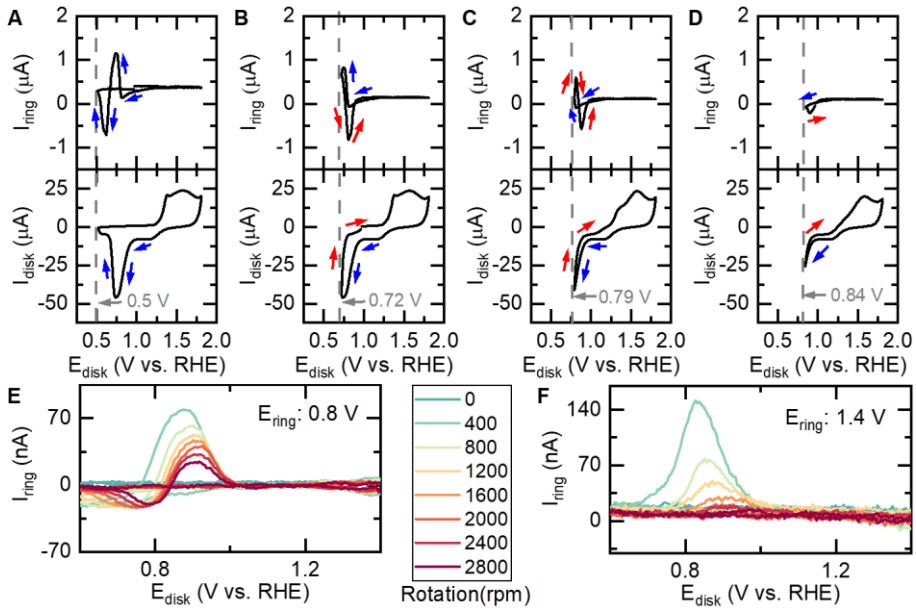

Fig. S4 (A–D) Rotating ring–disk electrode (RRDE) measurements of gold in 0.1 M $NaClO_4$ at 50 mV/s. E_{ring} is set at 0.6V, the rotation rate is 400 rpm. The blue arrow represents that the CV is negatively scanned. Red arrow represents that the CV is positively scanned. The grey dash line is to highlight $E_{–}$ in a CV. The range of E_{disk}: **(A)** 0.5–1.8 V; (**B**) 0.72–1.8 V; (**C**) 0.79–1.8 V; (**D**) 0.84–1.8 V. **(E-F)** The change of I_{ring} with various rotation rates (rpm) in RRDE measurements of gold in 0.1 M $NaClO_4$ at 50 mV/s. E_{ring} is set at 0.8 V (**E**) and 1.4 V (F), respectively.

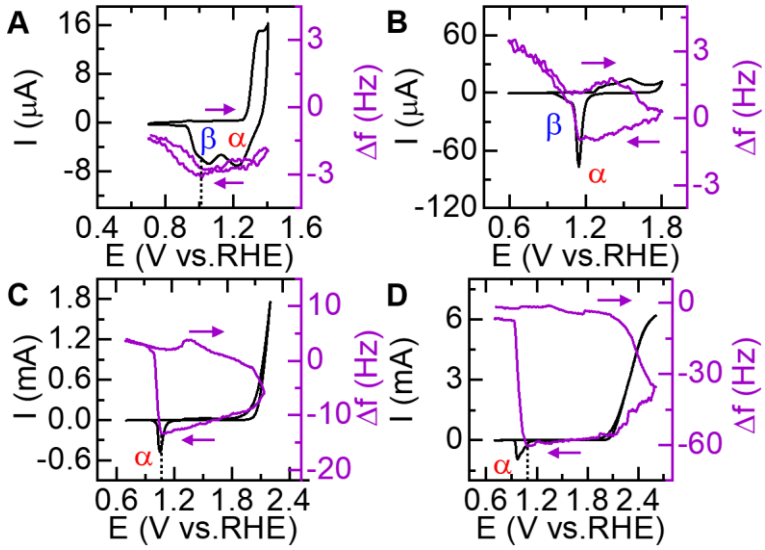

Fig. S5 Electrochemical quartz crystal microbalance measurement with a gold working electrode at 50 mV/s in 0.1 M $HClO_4$. The selected potential range is: **(A)** 0.7–1.4 V; **(B)** 0.7–1.8 V; **(C)** 0.7–2.2 V; **(D)** 0.7–2.6 V vs. RHE. The dash line shows the onset potential of mass loss (E_ψ) which reflects the potential in which the QCM signal starts to increase, i.e. mass loss, in the scanning process of a CV.

In EQCM experiments recorded in an acidic solution (Fig. 3B), the frequency change (Δf) was not observed only after the two oxides have been completely reduced, providing that E_+ is set below 1.5 V (fig. S5A)**.** When E_+ is set above 1.5 V, E_ψ immediately changes to the same potential as E_α and shifts negatively with E_α when E_+ is increased further (fig. S5B). The potential shift behavior of E_ψ will stop around 1.08 V while E_α continues to shift to more negative potentials when E_+ is set in the range of 2.1 to 2.6 V (fig. S5C–D).

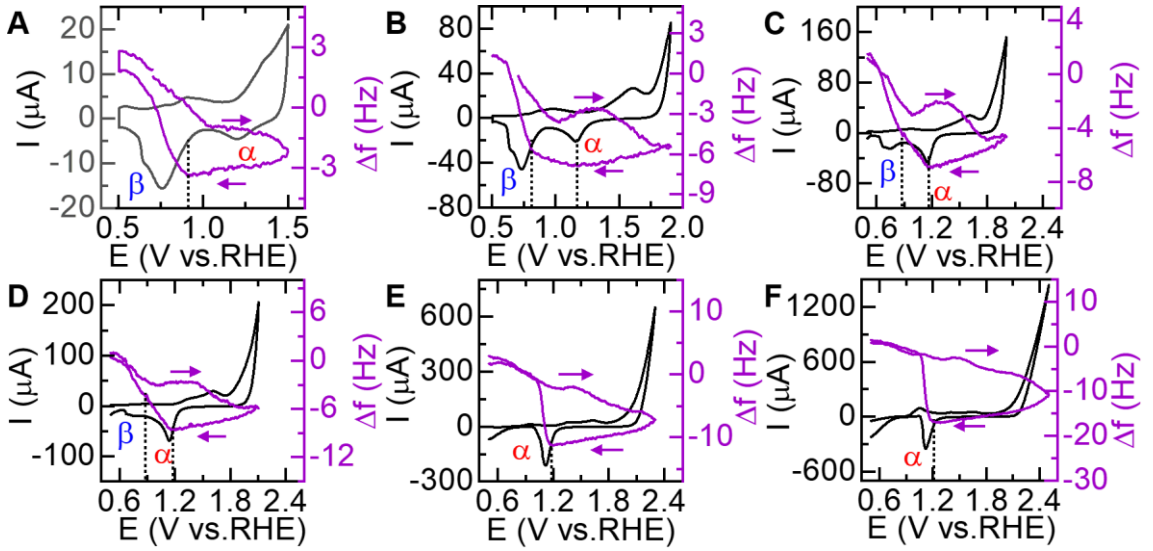

Fig. S6 Electrochemical quartz crystal microbalance measurement with a gold working electrode at 50 mV/s in 0.1 M $NaClO_4$. The potential range set is: **(A)** 0.7–1.5 V; **(B)** 0.7–1.9 V; **(C)** 0.7–2 V; **(D)** 0.7–2.1 V; **(E)** 0.7–2.3 V; **(F)** 0.7–2.5 V vs. RHE. The dash line shows the onset potential of mass loss (E_ψ) which reflect the potential in which the QCM signal starts to increase, i.e. mass loss, in the scanning process of a CV.

When the EQCM experiment is taken in a neutral solution (Fig. 3C), E_ψ appears in the first half of the β peak but shows no relationship with the α peak even though a shift of the α peak can be observed when E_+ is changed, yet kept below 1.9 V. Once E_+ is set to 1.9 V, E_ψ suddenly shifts to 1.16 V, which now coincides with E_α. From this point onwards, E_ψ and E_α shift consistently in the E_+ range of 1.9–2.1 V. Eventually E_ψ and E_α will separate gradually when E_+ is set above 2.1 V.

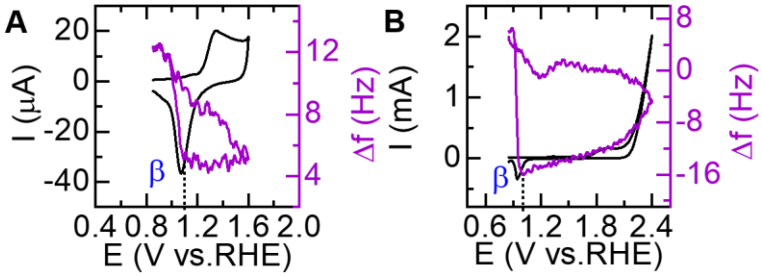

Fig. S7 Electrochemical quartz crystal microbalance measurement with a gold work electrode at 50 mV/s in 0.1 M NaOH. The potential range set is: **(A)** 0.7–1.6 V; **(B)** 0.7–2.4 V vs. RHE. The dash line shows the onset potential of mass loss (E_{ψ}) which reflect the potential in which the QCM signal starts to increase, i.e. mass loss, in the scanning process of a CV.

In an alkaline solution (Fig. 3D), E_{β} is fixed at 1.1 V providing that E_{+} is set lower than 1.7 V. E_{ψ} was found at 1.13 V unless E_{+} is set higher than 2 V. Under these conditions E_{β} and E_{ψ} will shift simultaneously with a constant potential difference of $E_{\psi} - E_{\beta} = 0.04\ V$.

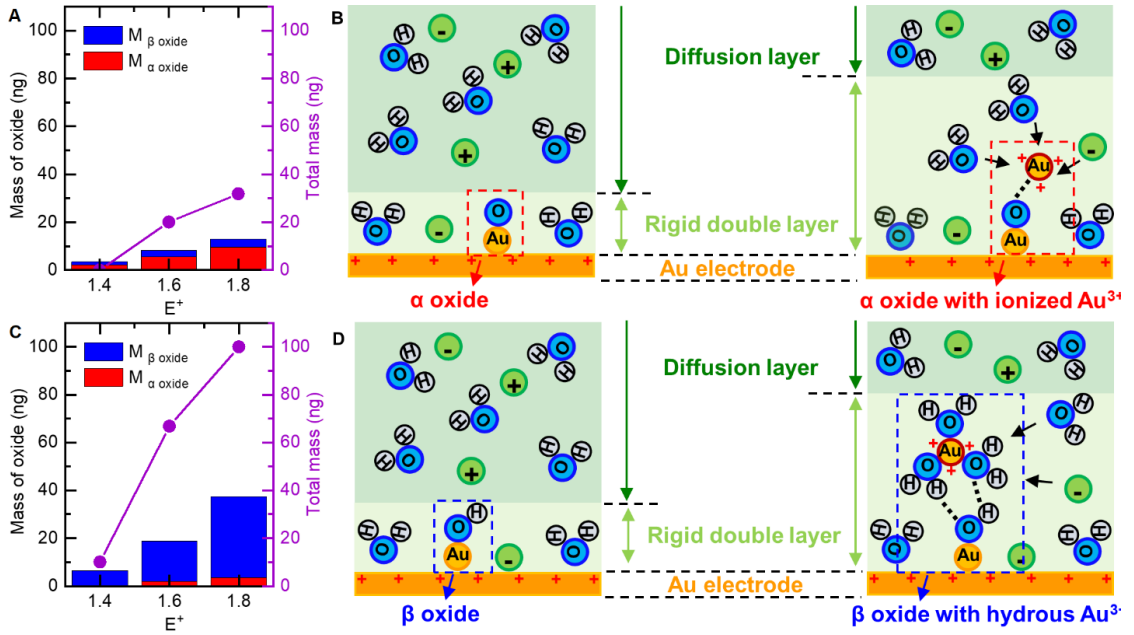

Fig. S8 Mass changes occurring during the formation of α and β oxide as a function of E_+ in 0.1 M $HClO_4$ (A) and 0.1 M $NaClO_4$ (C), and Illustrations of the proposed rigid double layer detected by EQCM at acidic (B) and neutral (D) conditions. The mass changes were calculated from the overall charge transferred during the gold oxidation (red and blue), and obtained from the frequency change detected by the microbalance (purple).The ratio of formed α and β oxide is calculated by the integrated charge of their reduction peaks. The total mass detected by the QCM was calculated from the frequency response by the Sauerbrey equation: $-\Delta f = C_f \cdot \Delta m$, for which a C_f has been determined previously as $8.54*10^7$ Hz/g/cm^2.(*37*)

The quartz crystal microbalance is a very sensitive device that can detect mass changes occurring on the electrode surface during an electrochemical reaction in the order of ng/cm^2. Not only mass changes occurring directly at the electrode surface are detected, but also due to changes occurring in the rigid part of the double layer.(*30-32*) Gold Au^{3+} ions play a massive role in the formation of a rigid double layer structure. Fig. S8A shows how the mass of the electrode changes upon formation of the gold oxide layer as a function of E_+ in 0.1 M $HClO_4$. When E_+ is set at 1.4 V, no mass changes are observed yet by the microbalance, even though

α and β oxides have already been formed. This may be related to the process of place exchange between Au and O/OH from adsorption layer at the initial oxide formation process,(*11*) where no new O/OH is fixed from bulk solution into oxide. However, when E_+ is set above 1.5 V, at which Au^{3+} cations are formed and bind onto the surface of α oxide, the total mass detected by the EQCM exceeds the amount of mass that one would expect solely by oxide removal. For this one can simply compare the mass changes expected from formation of Au_2O_3 and $Au(OH)_3$ from the charge, with the mass changes detected by EQCM. Because the EQCM can also detect mass changes into the rigid double layer,(*32, 49*) the extra mass detected by EQCM reflects that more molecules enter the rigid double layer structure from the diffusion layer. The Au^{3+} cations bound to α oxide are expected to bind more water molecules and electrolyte ions, and hold these tightly to the electrode interface resulting in these relatively large mass changes to occur. The proposed mechanism wherein this mass change occurs in an acidic solution is shown in fig. S8B.

Also in a neutral environment, the mass change detected by EQCM is significantly larger than one would expect by solely forming the oxide layer when E_+ is higher than 1.4 V. In this case the major mass changes are related to removal of β oxide rather than α oxide, as shown in fig. S8C. With increase of E_+ in 0.1 M $NaClO_4$, the Au^{3+} produced would form hydrous Au^{3+} and bind to β oxide via a hydrogen bonding network. We observed that changes in computed and detected mass changes are significantly larger at neutral conditions. That indicates that Au^{3+} ions bound to β oxide has a stronger ability to bind molecule tightly in a neutral solution than Au^{3+} ions bound to α oxide in an acidic solution. A cartoon that illustrates how these large mass changes occur in a neutral solution is shown in fig. S8D.

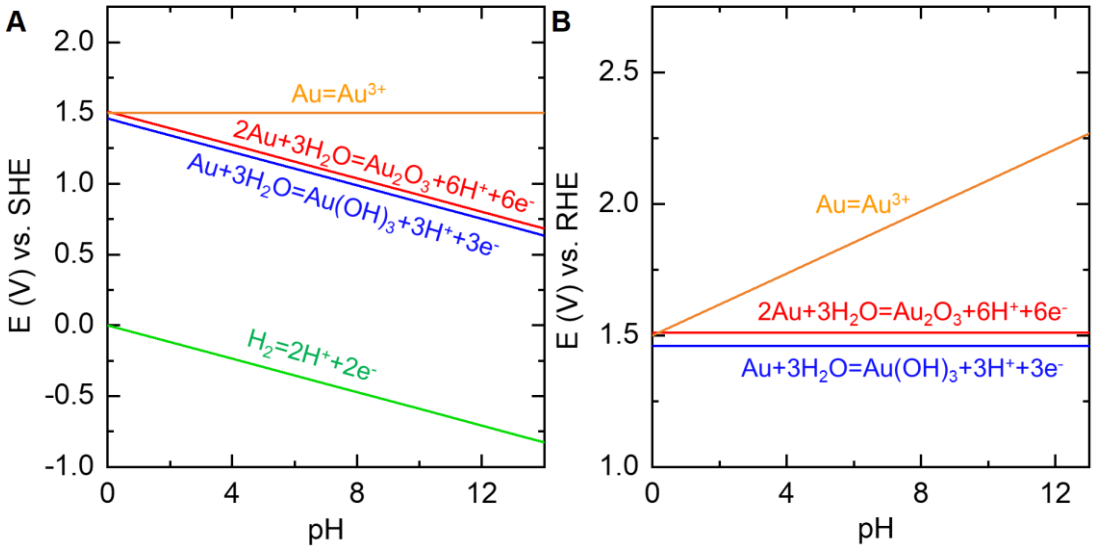

Fig. S9 (**A**)The Pourbaix diagram of gold oxidation and hydrogen oxidation on the SHE scale.(**B**) The E–pH diagram of gold oxidation on the RHE scale.

The initial stages of gold oxidation are associated with sequential formation of sub–lattices of OH or O.(*11*) Pourbaix diagrams of gold (fig. S9A) typically show two stable forms of gold oxide, i.e. Auric oxide ($2Au + 3H_2O \rightarrow Au_2O_3 + 6H^+ + 6e^-$) and Auric hydroxide ($Au + 3H_2O \rightarrow Au(OH)_3 + 3H^+ + 3e^-$).(*44*) When the number of electrons and protons are equal in a Nernst equation, the E–vs–pH plots in a Pourbaix diagram should have an identical slope ($-0.059\ V/pH$ at 25 °C), such as a reversible hydrogen reaction ($2H^+ + 2e^- \rightleftharpoons H_2$) and an ideal metal oxide reduction ($M_2O_x + 2xH^+ + 2xe^- \rightarrow 2M + xH_2O$), as shown in fig. S9A. The oxide reduction potential therefore should occur at a fixed potential independent of pH in a cyclic voltammetry (CV), when the reversible hydrogen electrode (RHE) is used as a reference potential, as shown in fig. S9B.

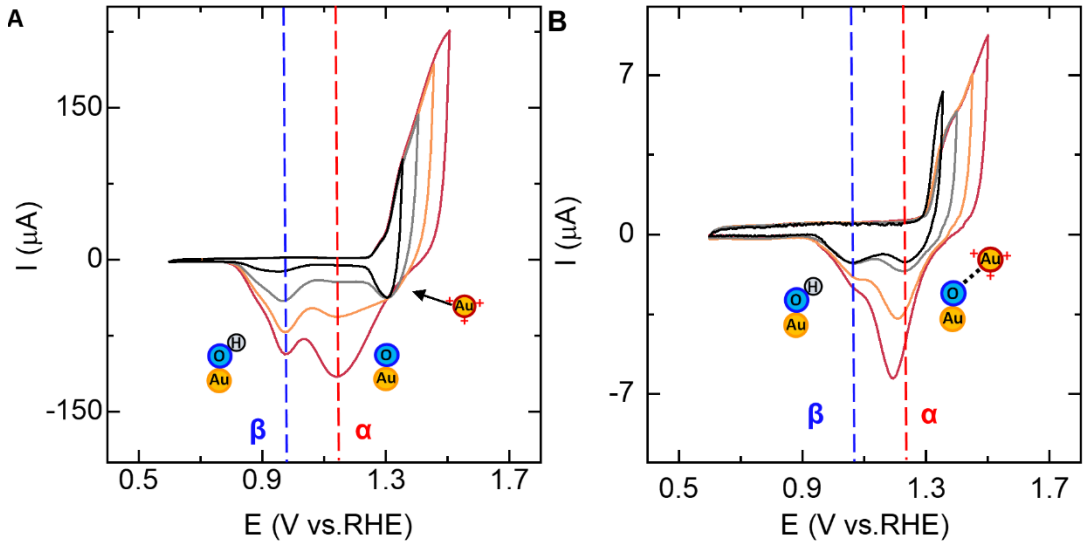

Fig. S10 Cyclic voltammograms of gold at 10 V/s **(A)** and 50 mV/s **(B)** in 0.1M $HClO_4$.

The negative shift of the α peak is caused by the formation of ionic bonds of $Au_2O_3 \cdots Au^{3+}$ that stabilize Au_2O_3. When the scan rate increases from 50 mV/s to 10 V/s, the non–Nernstian behavior will disappear and instead a reversible reduction peak appears at 1.31 V assigned to the reduction of free Au^{3+} (A, black line). Apparently it takes time for Au^{3+} to form ionic bonds with the gold surface. Reversible reduction of free Au^{3+} also appears in cyclic voltammetry experiments at high temperatures (365 K) and high (1 M) concentrations of $HClO_4$.(*35*)

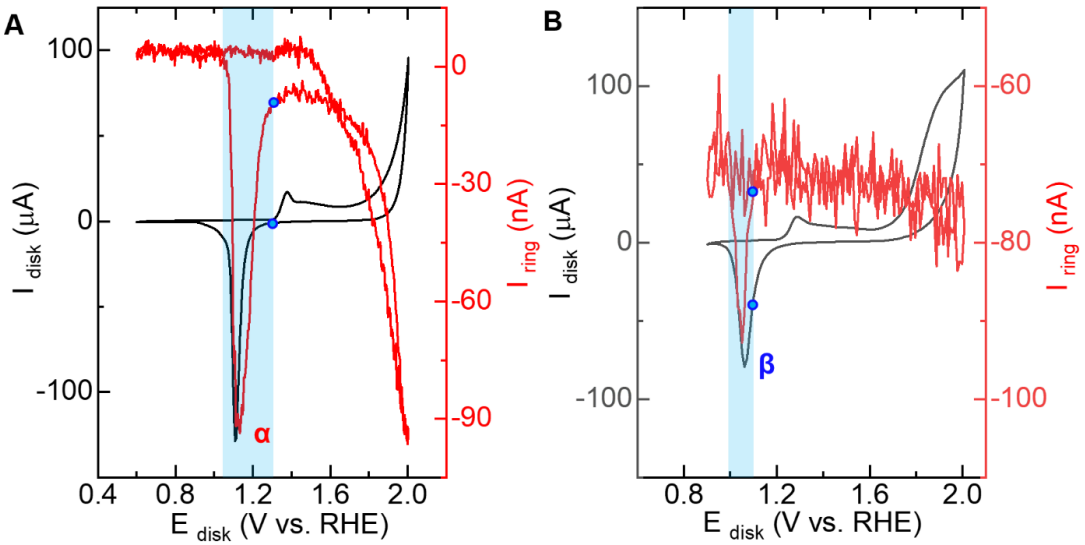

Fig. S11 Rotating ring–disk electrode measurements of gold in 0.1 M $HClO_4$ **(A)** and 0.1 M NaOH **(B)**. $Q_{Au^{3+}}$ is 220 and 24 nC in 0.1 M $HClO_4$ and NaOH, respectively. The blue dot represents the onset potential of Au^{3+}release from the disk, and the onset potential for the detection of released Au^{3+} by its reduction on the ring. The light blue window is the potential region of Au^{3+}release during the gold oxide reduction process.

The onset of Au^{3+} release from α oxide was found to occur simultaneous with the onset of the α peak, and the maximum value observed for Au^{3+} release appears in the first half of the α peak. In contrast, the onset of Au^{3+} release related to reduction of β oxide was observed at a more negative potential which is closer to the peak potential of the β oxide reduction reaction. The maximum value of Au^{3+} release appears during the second half of the β peak.

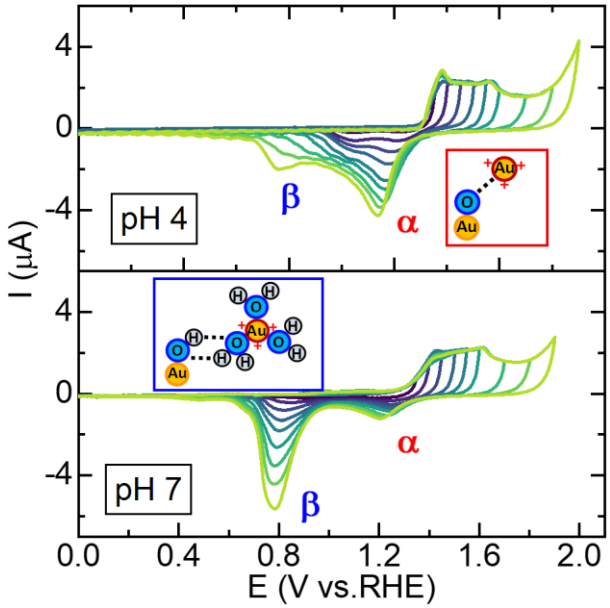

Fig. S12 Cyclic voltammograms in pH 4 and pH 7 at 50 mV/s with varying E_+. The red box shows the proposed α oxide structure leading to non-Nernstian behavior where ionic Au^{3+} binding occurs on α oxide (Au_2O_3). Theblue box shows the proposed β oxide structure leading to non-Nernstian behavior where hydrous Au^{3+} binding occurs on β oxide ($Au(OH)_3$).

Figure S12 reveals the competition between ionized Au^{3+} and hydrous Au^{3+} as a function of pH at mild pH conditions. The non–Nernstian shifts of the α peak and β peaks are caused by Au^{3+} binding to α oxide (see red box) and hydrous Au^{3+} binding to β oxide (see blue box), respectively. We have observed a small negative shift of the β peak and a clear negative shift of the α peak in a mild acidic solution (pH 4), which implies Au^{3+} prefers binding to α oxide in the form of ionized Au^{3+} over binding to β oxide in the form of hydrous Au^{3+}. When the pH of the solution increases to 7, we can observe the β peak with a clear negative shift and a much smaller negative shift of the α peak. This indicates that more stable hydration shells of Au^{3+} have formed on β oxide while less ionized Au^{3+} has appeared on α oxide. These differences of the α and β peak at pH 4 and 7 imply the existence of a competition between the ionized Au^{3+} and hydrous Au^{3+} states within these gold oxides, which is controlled by the concentration of H^+.

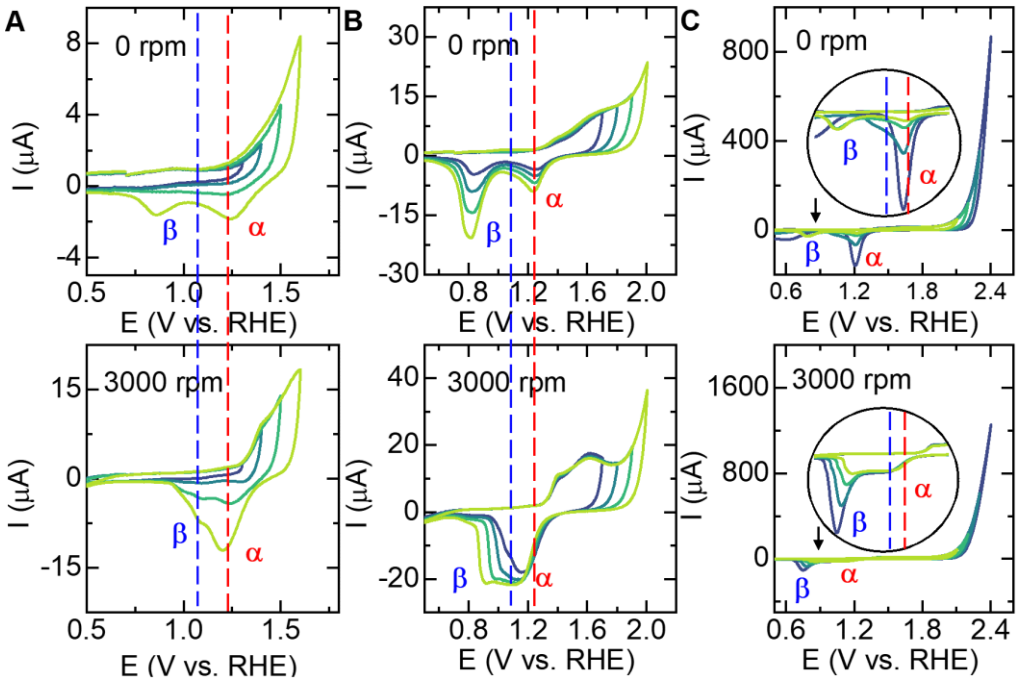

Fig. S13 Cyclic voltammograms in 0.1 M $NaClO_4$ at 50 mV/s under 0 (upper part) and 3000 (lower part) rpm. E^+ is changing from (**A**) 1.3 to 1.6 V; (**B**) 1.7–2 V; (**C**) 2.1–2.4 V. The red and blue dash lines represent the reduction peak potential of initial formation stage of α and β oxide, respectively.

The non–Nernstian behavior is caused by ionic interactions of ionized Au^{3+} on α oxide and hydrogen bonding interaction of hydrous Au^{3+} on β oxide. These two non-covalent interaction are weak. fig. S13A shows that the non–Nernstian behavior of the α and β peaks disappears at 3000 rpm when E_+ is lower than 1.6 V, indicating that the two non-covalent interactions are readily broken when a sufficiently high rotation rate is applied. Upon further increasing E_+ from 1.6 to 2 V (fig. S13B), the β peak shifts to a more negative potential even at rotation rates of 3000 rpm while the α peak appears to be less affected. That indicates that part of the hydrous Au^{3+} cannot escape from the oxide layer. If E_+ is further increased from 2 to 2.4 V (fig. S13C), and under conditions where lots of Au^{3+} are rapidly produced, the β peak disappears under non-rotating conditions while a large α peak can be observed. However the β peak increases quickly upon rotation, while the peak position of the α peak does not change at 3000 rpm. This reveals that a structure changes occur from ionic Au^{3+} to hydrous Au^{3+} upon

increase of the high rotation rate. This is most likely due to a more efficient replenishment of water, and removal of H^+ at higher rotation rates.

The phenomenon above is also observed when the electrolyte is changed from $NaClO_4$ to Na_2SO_4.(see fig. S14) This reflects that these observations are independent of the electrolyte.

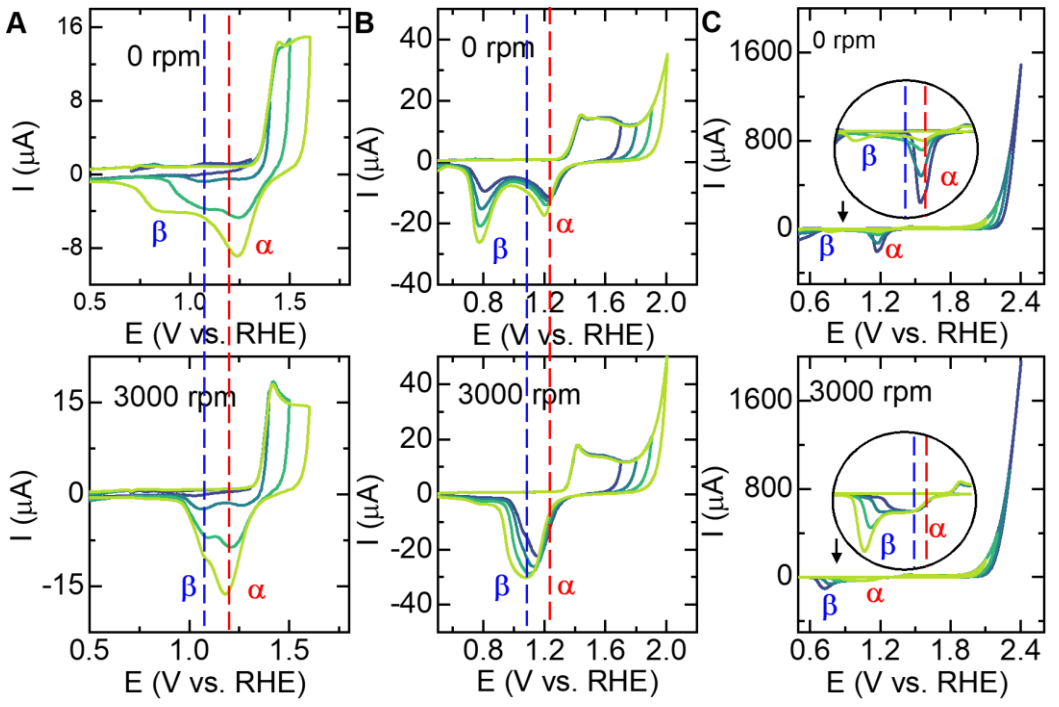

Fig. S14 Cyclic voltammograms in 0.1 M Na_2SO_4 at 50 mV/s under 0 (upper part) and 3000 (lower part) rpm. E^+ is changing from (**A**) 1.3 to 1.6 V; (**B**) 1.7–2 V; (**C**) 2.1–2.4 V. The red and blue dash lines represent the reduction peak potential of initial formation stage of α and β oxide, respectively.

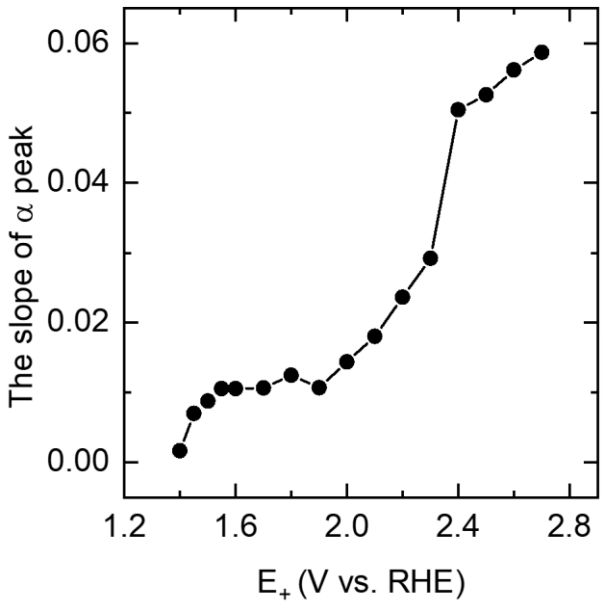

Fig. S15 The slope of the the E_{α}–vs–pH plots as a function of E_{+} obtained from cyclic voltammetry experiments on gold (calculation from the slope in Fig. 1B)

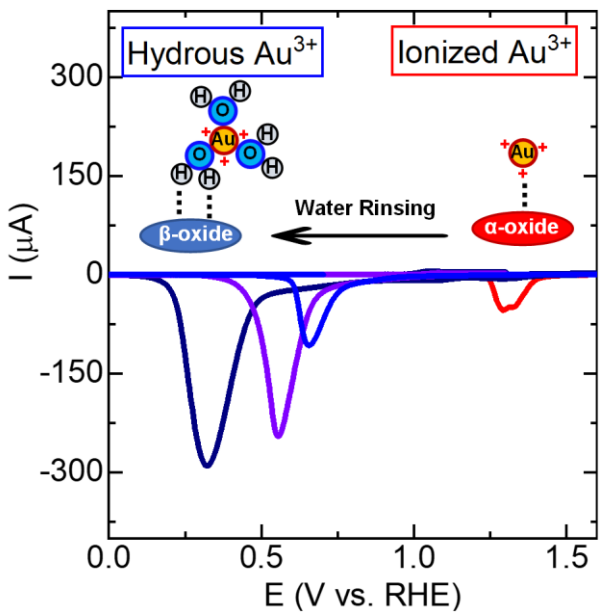

Fig. S16 The effect of Milli-Q water rinsing to position of the α and β reduction peaks of an oxidized gold at 50 mV/s in 0.1 M Na_2SO_4. The red line shows the α reduction peak of oxidized gold without rinsing; the other lines represent the β the reduction peak of oxidized

gold after MilliQ water rinsing**.** The total oxidation cycles is 2 cycles (red line), 1 cycles(blue line), 3 cycles (purple line), 5 cycles (dark blue line) in the oxidative region (1.3-2 V), respectively.

In order to further reveal the role of water replenishment to ionized Au^{3+} and hydrous Au^{3+}, we investigated the effect of rinsing with Milli-Q water on the peak potential of the oxide reduction reaction. In this experiment, the gold electrode was first scanned in the oxidative region (1.3–2 V) to form gold oxide in 0.1 M Na_2SO_4. The overall oxidation time was controlled by setting different oxidation cycles in the range of 1.3-2 V. In an control experiment wherein no rinsing occurs (red line), the oxidized gold electrode is directly reduced to obtain the α reduction peak by simple scanning negatively after formation of the oxide in the positive scan. For the other experiments the oxide was produced in the same manner, by oxidation of the gold electrode by scanning positively in the cyclic voltammogram from 1.3-2 V. The electrodes were removed from the solution and rinsed with MilliQ water by a spray bottle for 30 seconds. After rinsing the electrodes were put in a fresh 0.1 M $NaClO_4$ solution to record the peak potential of the oxide reduction reaction. Our experiment shows that the gold oxide reduction peak obtained in an experiment without rinsing by MilliQ water appears at the reduction potential expected for ionized Au^{3+} (1.29 V), while those that were rinsed with MilliQ water appear at the reduction potential of hydrous Au^{3+} (0.32-0.66 V).

Table S1 The total number of Au^{3+} (x) in an Au_2O_3 reduction process based on the slope of α peak in fig. S15

E_+	1.4	1.45	1.5	1.55	1.6	1.7	1.8	1.9	2	2.1	2.2	2.3	2.4	2.5	2.6
x	0.1	0.3	0.3	0.4	0.4	0.4	0.5	0.4	0.6	0.9	0.9	0.9	0.9	0.9	0.9
y	0	0	0	0	0	0	0	0	0	0	yes	yes	yes	yes	yes

Note: x is the number of Au^{3+} in the forms of ionic bonds ($Au_2O_3 \cdots xAu^{3+}$) in the Au_2O_3 reduction process; y shows whether free Au^{3+} exists in the diffusion layer as a result of the saturation of the α oxide with Au^{3+}.

Forms of
Electric Charge
Energy Conversion
Energy Storage
复杂背后的本质是简单。
The essence behind complexity is simplicity.

III

Supporting Information for Chapter 4

The PDF file includes:

Materials and Methods
Supplementary Text
Figs. S1 to S13

Materials and Methods

General.

All glassware used in the experiments underwent a thorough cleaning process to remove impurities. This involved submerging the glassware in an aqueous solution containing 0.5 M H_2SO_4 and 6.3 mM $KMnO_4$ overnight. The glassware was then rinsed once with MilliQ water (water with a resistivity of 18.2 MΩ cm). was used to rinse all glassware one time. Next, a mixture of diluted H_2SO_4 and H_2O_2 was added to the glassware in a beaker. This mixture was left for 30 minutes to eliminate excess $KMnO_4$ residue. The glassware underwent five rinses and three rounds of boiling in MilliQ water. Before each electrochemical experiment, the glassware was boiled once more in MilliQ water. Alumina suspensions with particle sizes of 1.0, 0.3, and 0.05 μm were sourced from Buehler. The electrolyte solutions were prepared with Suprapur® reagents from Merck and MilliQ water. pH measurements were carried out using a Hanna Instruments HI 4222 pH meter, calibrated using IUPAC standard buffers.

Electrochemical measurements.

The electrochemical measurements were conducted with approximately 25 °C using Autolab PGSTAT 12, 204 and 128N potentiostats, along with Autolab NOVA software. These measurements were performed in conventional single compartment three–electrode glass cells. The working electrode was a PEEK encapsulated gold electrode with an area of 0.0314 cm^2 (Metrohm). The counter electrode was a gold wire, and a reversible hydrogen electrode (RHE) served as the reference electrodePrior to each measurement, the working electrode was manually polished for 2 minutes using alumina suspensions of decreasing particle size, followed by sonication in MilliQ water for 10 minutes. The counter electrode's gold wire was flame annealed and rinsed with MilliQ water. The reference electrode (RHE) was constructed using a Pt wire connected via a Luggin capillary and continuously bubbled with H_2 gas during the measurements.

In the absence of particular indications, the pH values spanning from 1 to 13 were achieved by mixing perchloric acids, sodium hydroxide, and sodium perchlorate to maintain a

consistent ionic strength for different pH levels. Different types or concentrations of anions were used for solution variations. All electrochemical experiments were conducted under either saturated argon (Ar) or saturated oxygen (O_2) conditions. For the Ar experiments, dissolved O_2 was removed from the solution by bubbling argon for at least 30 minutes, and argon was maintained above the solution throughout the experiments. Similarly, for O_2 experiments, the solution was bubbled with pure O_2 for at least 30 minutes, with O_2 continuously flowing above the solution.

Electrochemical quartz crystal microbalance (EQCM)

EQCM experiments were carried out using an Autolab PGSTAT 128N potentiostat and a 5 mL Autolab EQCM cell. A gold–coated quartz crystal EQCM electrode with an area of 0.35 cm^2 and a gold layer thickness of 200 nm was used as the working electrode. A coiled gold wire served as the counter electrode. The custom–made electrochemical cell, constructed from PEEK material, had a volume of 5 mL. An RHE Luggin setup was employed as the reference electrode.(*33*)

EQCM experiments were conducted using an Autolab PGSTAT 128N potentiostat and a 5 mL Autolab EQCM cell. An Autolab gold coated quartz crystal EQCM electrode (A = 0.35 cm^2, gold layer thickness = 200 nm, the fundamental frequency of quartz crystal is 6 MHz) was used as the working electrode and a coiled gold wire was used as the counter electrode. The custom made electrochemical cell consisted of PEEK material and had a volume of 5 mL. An RHE Luggin setup was used as the reference electrode.(*33*)

Supplementary Text

S1 Understanding redox processes of X and Y: pH and electrolyte influence

In order to perform a quantitative comparison of the peak potentials associated with the redox processes X and Y, various parameters were examined in relation to the Pourbaix diagram. Specifically, the oxidation peak potentials (E_{X+}) and reduction peak potentials (E_{X-})

of the X redox couple, as well as the corresponding values for the Y redox couple (E_{Y+}) and (E_{Y-}), were plotted against pH (as depicted in Fig. 5B and Fig. 5C). An intriguing observation emerged: E_{X+} (0.31 V vs. NHE) and E_{X-} (0.19 V vs. NHE) remain constant regardless of pH, as long as pH is below 8. Contrarily, E_{Y+} and E_{Y-} exhibit a consistent shift of –59 mV/pH on the Pourbaix diagram, but only within the pH range of 8 to 13. This distinction indicates that the X redox process involves electron transfer (ET) exclusively in the pH range of 1 to 8. In contrast, the redox process of Y involves a proton coupled electron transfer (PCET) mechanism.

When the concentration of the $NaClO_4$ electrolyte was varied from 0.1 M to 0.05 M or 0.01 M, a remarkable shift towards more negative potentials was observed for X, correlating with a decreasing electrolyte concentration observed (Fig. 5A, Fig. S5 and Fig. S6). Conversely, Y displayed no shift in potential under these conditions. These findings suggest that the equilibrium potential of X is influenced by electrolyte concentration, while that of Y remains unaffected. Additional cyclic voltammetry (CV) experiments were performed on gold electrodes in both 0.1 M (Fig. S7) and 0.01 M Na_2SO_4 (Fig. S8) solutions under identical experimental conditions. These experiments further validate that the peak potentials of the X and Y redox processes as a function of pH are governed by the expressions $E_X = E_X^0 + 0\ mV/s\ (V\ vs. NHE)$ and $E_Y = E_Y^0 + 0.059\ V/s\ (V\ vs. NHE)$, respectively, regardless of whether ClO_4^- or SO_4^{2-} solutions were employed. Notably, it was observed that E_X^0 varied with electrolyte concentration (ranging from 0.01 M to 0.1 M) and the type of anions (ClO_4^-, SO_4^{2-}) while E_Y^0 exhibited no such relationship with the electrolyte composition (Fig. S9A and B). This observation strongly implies that the X redox wave should be attributed to anion adsorption/desorption events occurring at the surface. Additionally, the average current of the X redox save (I_X) is maintained at the same value in the 0.1 M and 0.05 M $NaClO_4$ solutions, but appears to decrease slightly in 0.01 M $NaClO_4$ (Fig. S9C). It is worth noting that the shifts in chemisorbed bonds of different anions (NO_3^-,ClO_4^- or SO_4^{2-}) in the potential region where X appears have been directly detected on the Au(111) surface using different in situ spectroscopy techniques (*20, 34, 35*). We therefore assign the X redox equilibrium to the chemical adsorption and desorption of anions on the Au surface.

On the other hand, the Y redox process was attributed to OH^- adsorption and desorption, especially in alkaline solutions (*36, 37*). Besides, it was found that I_Y remains independent of electrolyte concentration at pH values below 8, yet becomes sensitive to the overall electrolyte concentration at higher pH values (Fig. S9D). Consistently, the Y redox couple adheres to $E_Y = 0.8\,V - 0.059\ V/pH\ \ (V\ vs. NHE)$, remaining unaffected by the electrolyte concentration (Fig. S9B). This insight leads us to attribute the redox event Y to the chemical adsorption and desorption of hydroxide ions on the gold surface.

S2. The E_{ORR} dependence on the O_2 concentration.

In order to investigate the ORR activity, cyclic voltametry (CV) was used to investigate the potential at which the ORR occurs on polycrystalline gold in solutions of different pH. Initially, we manipulated the upper limit of the CV (E_+) to control the ocurrence of the oxygen evolution reaction within Ar–saturated 0.1 M $HClO_4$ (as shown in the top part of Fig. S10A) and 0.1 M NaOH (as illustrated in the top part of Fig. S10B). By setting E_+ above the onset potential of the oxygen evolution reaction ($onset_{OER}$), the ORR peak could be discerned during the negative scan of the CVs.

As we further elevated E_+ to increase the concentration of O_2 at the working electrode, and subsequently scanned the potential in the direction of ORR with both of Ar–saturated 0.1 M $HClO_4$ and 0.1 M NaOH, a noteworthy observation was made. The peak current of the ORR increased, yet the peak potential of the ORR (E_{ORR}) remained consistent. This behavior was observed irrespective of whether the solution was Ar–saturated (the top part of Fig. S10A and B) or O_2–saturated (the bottom part of Fig. S10A and B). Notably, in the O_2–saturated environment, the E_+ value was fixed at 1 V vs. RHE, maintained at a level lower than the potential for gold oxidation. This measure was taken to mitigate any potential interference stemming from gold oxide during the ORR.

The consistency of E_{ORR} under O_2– saturated conditions, as compared to E_{ORR} under Ar–saturated conditions, was confirmed in both 0.1 M $HClO_4$ and 0.1 M NaOH solutions. As a result of its consistency and precision on polycrystalline gold, E_{ORR} was considered to be a useful metric to monitor changes in ORR activity across the entire pH spectrum.

Furthermore, it is crucial to acknowledge that determining the precise onset potential of the ORR (onset $_{ORR}$) can be challenging due to its overlap with the potential region where the gold oxide reduction reaction occurs. This overlap is particularly pronounced in neutral and alkaline solutions. For the purposes of this manuscript, the choice was made to rely on E_{ORR} rather than onset $_{ORR}$ as the metric to track variations in ORR activity across all pH values.

S3. Surface charge calculation under saturated Ar

During the development of the mathematical model for calculating surface charge at 0.1 M $NaClO_4$, based on the EQCM system, certain definitions and simplifications were employed. These definitions are crucial for a comprehensive understanding of the calculations:

a) The electrolyte is treated as an ideal solution, maintaining a total concentration of 0.1 mol/L by mixing equimolar concentrations of $HClO_4$, $NaClO_4$, NaOH.

b) The potential region of zero charge (PRZC) marks the potential range where the frequency response recorded by EQCM remains minimum and undergoes no change. Onset $_{C^-}$ signifies the point where $-\Delta f$ begins to increase upon an decreasing applied potential. Conversely, onset $_{C^+}$ marks another transition point, where $-\Delta f$ begins to increase with an increasing applied potential.

c) When the applied potential surpasses the onset $_{C^+}$ in a CV conducted under saturated Ar, the gold surface accumulates an excess of positive charge, leading to the attraction of anions from the solution through electrostatic interactions. This potential range is referred to as the C^+ zone.

d) Conversely, when the applied potential falls below the onset $_{C^-}$, the gold surface carries an excess negative charge, resulting in the attraction of cations from the solution through electrostatic interactions. This potential range is referred to as the C^- zone.

e) The excess charge calculation solely encompasses the excess charge in the C^+ and C^- zones, while disregarding the potential influence of cation adsorption, hydrogen adsorption

and evolution at more negative potentials, oxide formation, and oxygen evolution at more positive potentials.

The range of PRZC under saturated Ar is defined based on the EQCM response. In addition:

When the pH is below 8, the X redox couple is observed in the PRZC.

When pH is 8 or higher, the Y redox couple is observed in the PRZC.

The mathematical model's development involved three key steps:

(1) The differential capacitance C under Ar in the electrical double layer (EDL) potential region:

The differential capacitance (C) in the EDL potential region can be determined using the equation:

$$C = \frac{I^{+} - I^{-}}{2 \times \nu \times A}.$$

where I^{+} and I^{-} represent the currents during positive and negative CV scans, ν is the scan rate (50 mV/s), and A is the electrode surface area (0.0314 cm^2). When the electrolyte concentration is 0.1 mol/L, C is calculated to be 18 μF/cm^2, as shown in Fig. 8A.

(2) The net Faradaic charge distribution of the redox couple in the PRZC

To quantify the chemical adsorption and desorption processes of a surface redox couple at a specific potential, the integrated oxidation and reduction charges are determined. The net integrated charge at that potential is the sum of the integrated oxidation and reduction charges as shown in Fig. S12. Mathematically:

Integrated oxidation charge (ΔQ_{X^+}) during positive CV scan: $\Delta Q_{X^+} = \frac{\int I^{+} \cdot dU}{\nu \times A}$;

Integrated reduction charge (ΔQ_{X^-}) during negative CV scan: $\Delta Q_{X^-} = -\frac{\int I^{-} \cdot dU}{\nu \times A}$;

Net integrated charge (ΔQ) at a specific potential: $\Delta Q = \Delta Q_{X^+} + \Delta Q_{X^-}$.

The calculations for the net charge of the Y redox reaction mirror those for the X redox reaction.

Where I^{+} is the current at a positive scan of a CV and I^{-} is the current at a negative scan of a CV; ν is the scan rate (50 mV/s); A is the electrode surface area (0.0314 cm^2); $\int I^{+} \cdot dU$ is the integrated area of CV at the positive scan; $\int I^{-} \cdot dU$ is the integrated area of a CV at the negative scan.

(3) The excess charge distribution in the EDL potential region.

Excess charge is calculated in the C^{+} and C^{-} zones:

Positive excess charge in C^{+} zone: $\Delta Q^{+} = \frac{C \times (E - \text{onset}_{C^{+}})}{A}$;

Negative excess charge in C^{-} zone: $\Delta Q^{-} = \frac{C \times (E - \text{onset}_{C^{-}})}{A}$;

Here, C is the capacitance (18 μF/cm^2), E represents a specific potential point in the CV, and A signifies the electrode surface area (0.0314 cm^2).

S4. Surface excess charge calculation under saturated O_2

Under O_2–saturated solutions, the oxygen reduction reaction (ORR) brings about two prominent effects on the electrical double layer (EDL) structure in comparison to conditions under saturated Ar:

(1) A changes in the potential regions for the PRZC , C^{-} and C^{+} zone:

A surface redox couple arises within the PRZC that is pinpointed by a minimum $-\Delta f$ in EQCM experiments. Under Ar conditions, anion redox reactions (X potential region) occur within the PRZC in the pH range of 1 to 8. However, redox reactions involving hydroxide (Y potential region) emerge within the PRZC when the pH exceeds 8. When the pH increases, the potential of the X redox wave shifts positively towards the potential of the Y redox wave in a cyclic voltammogram (CV). For pH values higher than 8, the X peak changes from an

electron transfer (ET) process (pH 1–8) to a proton coupled electron transfer (PCET) process similar to the Y redox reaction.

Since the X and Y regions are not discernible under O_2 conditions, it is crucial to emphasize that the characterization of the X and Y regions within this manuscript specifically pertains to their presence under Ar. It is worth highlighting that when the pH remains below 8, the width of the PRZC narrows causing the onset C^+ to shift in a negative potential. Conversely, as the pH surpasses 8, the PRZC widens with a negative potential shift of the onset C^-.

To conclude, when the pH remains below 8, the PRZC observed in O_2–saturated solutions aligns with the onset C^- observed in Ar–saturated solutions. Conversely, when the pH reaches 8 or higher, the PRZC observed in O_2–saturated solutions corresponds to the combined representation of both the X and Y regions observed under Ar–saturated solutions.

(2) A diminished capacitance in the C^- zone and an unaffected capacitance in the C^+ zone:

The ORR leads to electron consumption on the gold surface and decreasing negative excess charge within the C^- zone. Since the $-\Delta f$ increase correlates with the surface excess charge, a ratio of $-\Delta f$ change under Ar and O_2 conditions can be established (depicted in Fig. S13). This ratio serves as a corrective coefficient (K) for the capacitance under saturated O_2, expressed as $K = \frac{(\frac{-\Delta f}{\Delta E})_{O_2}}{(\frac{-\Delta f}{\Delta E})_{Ar}} = \frac{C_{O_2}}{C_{Ar}}$, where $(\frac{-\Delta f}{\Delta E})_{O_2}$ and $(\frac{-\Delta f}{\Delta E})_{Ar}$ signify the frequency change slope at specific potentials under saturated Ar and O_2, respectively. This corrective coefficient allows the determination of capacitance under saturated O_2, denoted as as $C_{O_2} = K \times C_{Ar}$. Here, C_{O_2} represents the capacitance under saturated O_2, K is the corrective coefficient, and C_{Ar} is the capacitance under saturated Ar.

Excess charge in the C^- potential region:

As K exhibits variation with changes in E wihin the C^- zone, expressed by the equation K=0.18– 0.24*E (Fig. S13B), we can calculate ΔQ as follows: $\Delta Q = K \times \frac{C \times (E - \text{onset}_{C^-})}{A}$;

Excess charge (ΔQ) in the C^+ potential region:

Since K remains at 0.8 whinin the C^+ zone, with $C_{O_2} = 0.8 \times C_{Ar}$ (Fig. S13C). we calculate ΔQ as follows: $\Delta Q = \frac{C_{O_2} \times \Delta E}{A} = \frac{0.8\, C_{Ar} \times (E - \text{onset}_{C^+})}{A}$;

Here, K represents the corrective coefficient for capacitance under O_2–saturated conditions. This comprehensive approach allows the accurate calculation of surface excess charge under saturated O_2, considering the distinctive effects introduced by ORR and changes in EDL structure.

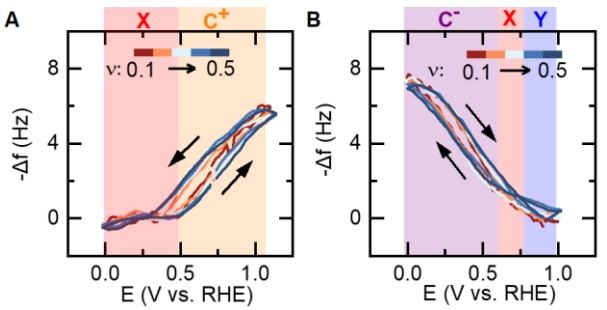

Fig. S1 Dependence of frequency change on the scan rate (ν) in 0.1 M $HClO_4$ (A) or NaOH (B). The X and Y regions indicate the potential ranges in which the X and Y redox couples can be identified in a CV, respectively. C^+ signifies the potential region of positive excess charge, while C^- represents the potential region of negative excess charge.

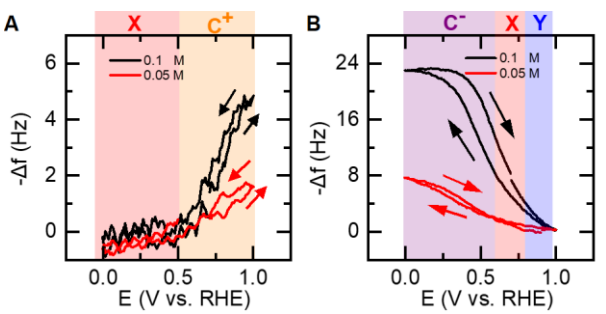

Fig. S2 Dependence of the Frequency change on the electrolyte concentration. (A) $HClO_4$ and (B) NaOH. The X and Y regions correspond to the potential regions in which the X and Y redox couples can be identified in a CV, respectively. C^+ indicates the potential region of positive excess charge, while C^- represents the potential region of negative excess

charge. Black lines and red lines correspond to measuring concentrations of electrolyte at 0.1 M and 0.05 M, respectively.

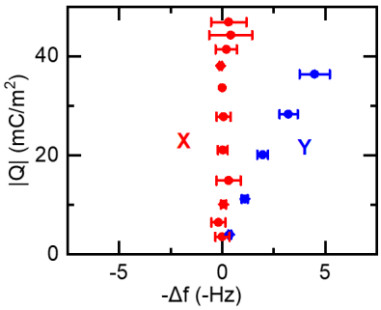

Fig. S3 Comparison of the frequency response observed by EQCM and the absolute integrated charge of the redox peaks in 0.1 M $HClO_4$ (X) and 0.1 M NaOH (Y).

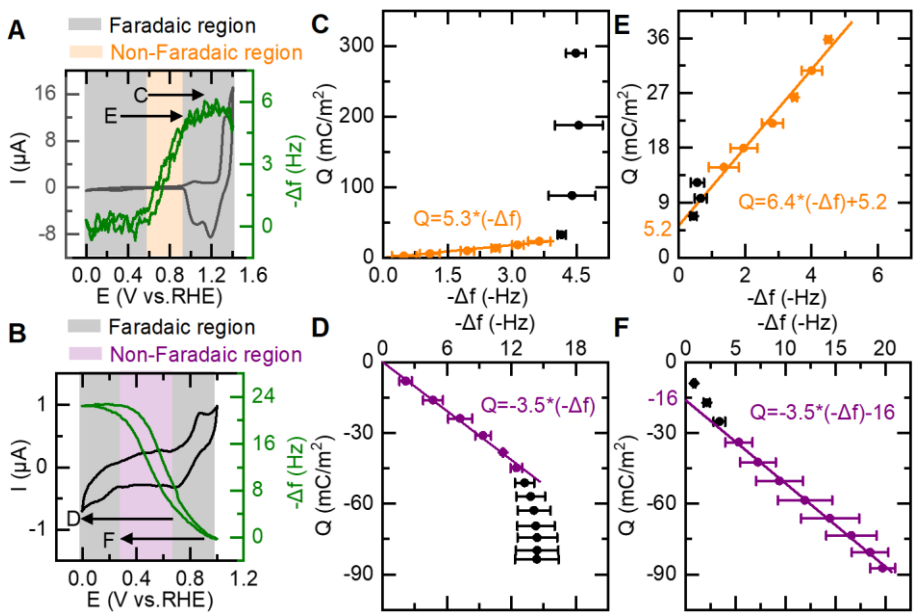

Fig. S4 EQCM measurements in different electrolyte solutions. (A) EQCM measurements conducted in 0.1 M $HClO_4$. The arrows (C, E) indicate the potential windows for charge integration (Fig. S4C and E), respectively. **(B)** EQCM measurements conducted in 0.1 M NaOH. The arrows (D, F) indicate the potential windows for charge integration (Fig. S4 D

and F). **(C)** Relationship between the integrated charge of a CV (ΔQ) and the corresponding negative frequency change (– Δf) when the applied potential transitions from the non– Faradaic region (orange part) to the Faradaic region (black part) in 0.1 M $HClO_4$. The arrow C in Fig. S4A indicates the start point and end point of the charge integration from which the relationship between ΔQ and and –Δf in Fig. S4C is determined. **(D)** Relationship between the integrated charge of a CV (ΔQ) and the corresponding negative frequency change (– Δf) when the applied potential transitions from the non– Faradaic region (purple part) to the Faradaic region (black part) in 0.1 NaOH. The arrow D in Fig. S4B indicates the start point and end point of the charge integration from which the relationship between ΔQ and–Δf in Fig. S4D is determined. **(E)** Relationship between the integrated charge of a CV (ΔQ) and the negative frequency change (– Δf) when the applied potential shifts from the Faradaic region (black part) to the non– Faradaic region (orange part) in 0.1 M $HClO_4$. The arrow E in Fig. S4A indicate the start point and end point of the charge integration from which the relationship between ΔQ and and –Δf in Fig. S4E is determined. **(F)** Relationship between the integrated charge of a CV (ΔQ) and the negative frequency change (– Δf) when the applied potential shifts from the Faradaic region (black part) to the non– Faradaic region (purple part) in 0.1 M NaOH. The arrow F in Fig. S4B indicate the start point and end point of the charge integration from which the relationship between ΔQ and–Δf in Fig. S4F is determined.

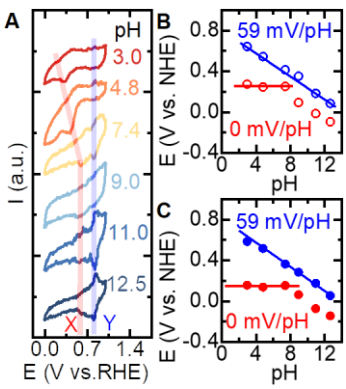

Fig. S5 pH dependence of the X and Y peaks in the electrochemical double layer region. **(A)** CVs of gold in various Ar– saturated pH solutions at a scan rate of 50 mV/s. **(B)** Pourbaix

diagram of X^+ (E_{X+}) and Y^+ (E_{Y+}) redox peaks in the positive scan of CVs of gold. **(C)** Pourbaix diagram of X^- (E_{X-}) and Y^- (E_{Y-}) redox peaks in the negative scan of CVs of gold. The concentration of ClO_4^- is maintained at 0.05 mol/L.

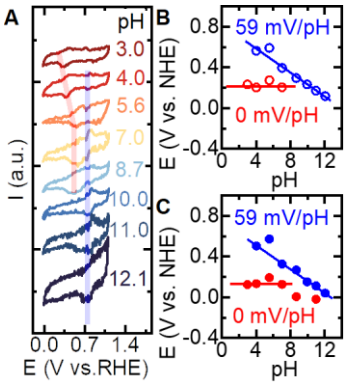

Fig. S6 pH dependence of the X and Y redox peaks in the electrochemical double layer region under diluted conditions. (A) CVs of gold in various Ar– saturated pH solutions at a scan rate of 50 mV/s. **(B)** Pourbaix diagram of X^+ (E_{X+}) and Y^+ (E_{Y+}) redox peaks in the positive scan of CVs of gold. **(C)** Pourbaix diagram of X^- (E_{X-}) and Y^- (E_{Y-}) redox peaks in the negative scan of CVs of gold. The concentration of ClO_4^- is maintained at 0.01 mol/L.

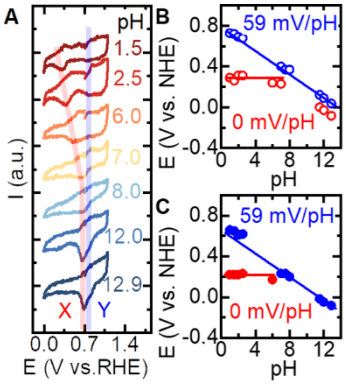

Fig. S7 pH dependence of the X and Y peaks in the electrochemical double layer region in sulfate solutions. (A) CVs of gold in various Ar– saturated pH solutions at a scan rate of 50 mV/s. **(B)** Pourbaix diagram of X^+ (E_{X+}) and Y^+ (E_{Y+}) redox peaks in the positive scan of

CVs of gold. **(C)** Pourbaix diagram of X^- (E_{X^-}) and Y^- (E_{Y^-}) redox peaks in the negative scan of CVs of gold. The concentration of SO_4^{2-} is maintained at 0.1 mol/L.

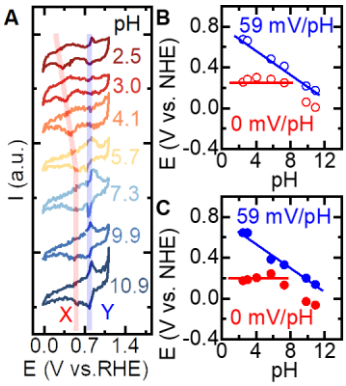

Fig. S8 X and Y redox peaks in the electrochemical double layer region under diluted conditions. (A) CVs of gold in different Ar– saturated pH solutions at a scan rate of 50 mV/s. **(B)** Pourbaix diagram of X^+ (E_{X^+}) and Y^+ (E_{Y^+}) redox peaks in the positive scan of CVs of gold. **(C)** Pourbaix diagram of X^- (E_{X^-}) and Y^- (E_{Y^-}) redox peaks in the negative scan of CVs of gold. The concentration of SO_4^{2-} is maintained at 0.01 mol/L.

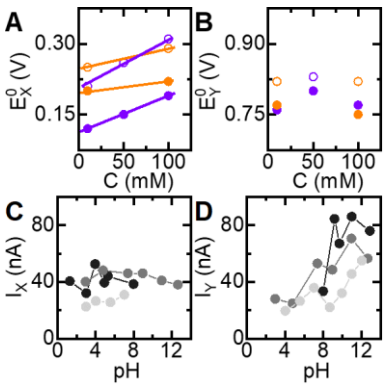

Fig. S9 Effect of electrolyte concentration on the potential and current of X and Y peaks. (A) The $E_{X^+}^0$ (open circle) at the positive scan and $E_{X^-}^0$ (solid circle) at the negative scan of CV in different concentrations of ClO_4^- (violet) and SO_4^{2-} (orange) [$E_X = E_X^0 - 0\ mV/s\ (V\ vs. NHE)$]. **(B)** The $E_{Y^+}^0$ (open circle) at positive scan and $E_{Y^-}^0$ (solid circle) at negative scan in different concentrations of ClO_4^- (violet) and SO_4^{2-} (orange) [$E_Y = E_Y^0 -$

$0.059\ V/s\ (V\ vs. NHE)$]. **(C)** The average peak current I_X ($I_X = \frac{I_{X^+} - I_{X^-}}{2}$) in the concentration of 0.1 M (black), 0.05 M (dark grey), and 0.01 M (light grey) of ClO_4^-. **(D)**The average peak current I_Y ($I_Y = \frac{I_{Y^+} - I_{Y^-}}{2}$) in the concentrations of 0.1 M (black), 0.05 M (dark grey), and 0.01 M (light grey) of ClO_4^-.

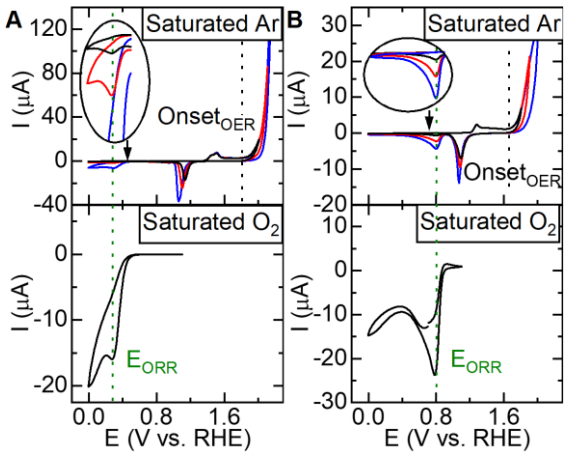

Fig. S10 CVs of gold in Ar–saturated (top) and O_2–saturated (bottom) 0.1 M $HClO_4$ (A) and 0.1 M NaOH (B) at 50 mV/s. Black and olive dotted lines represent the onset potential of the oxygen evolution reaction ($Onset_{OER}$) and the peak potential of the oxygen reduction reaction (E_{ORR}), respectively.

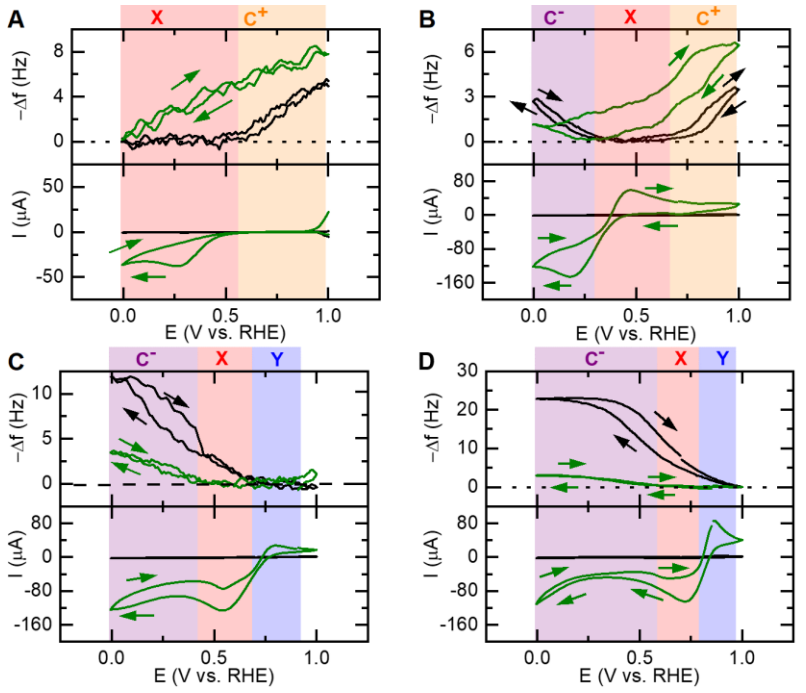

Fig. S11 EQCM measurements in Ar–saturated (black line) and O_2–saturated (green line) solutions at pH solutions. pH 1 **(A)**, pH 4 **(B)**, pH10 **(C)**, pH 13 **(D)**. X and Y regions represent the potential regions in where X and Y redox couples can be detected in a CV under saturated Ar, respectively. C^+ signifies the potential region of positive excess charge, while C^- represents the potential region of negative excess charge.

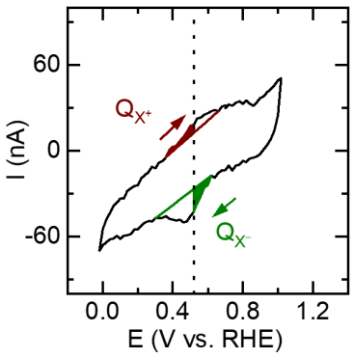

Fig. S12 Intergrated charge of X redox couple in a CV at pH 5 under saturated Ar. Integrated charge of X adsorption at positive scan is $Q_{X^+} = \frac{\int I^+ \cdot dU}{v \times A}$, where $\int I^+ \cdot dU$ represents the integral area of X at positive scan (dark red part). Integrated charge of X desorption at the

negative scan is $Q_{X^-} = -\frac{\int I^- \cdot dU}{\nu \times A}$, where $\int I^- \cdot dU$ represents the integral area of X at negative scan (dark green part). ν is the scan rate, and A is the surface area of gold electrode.

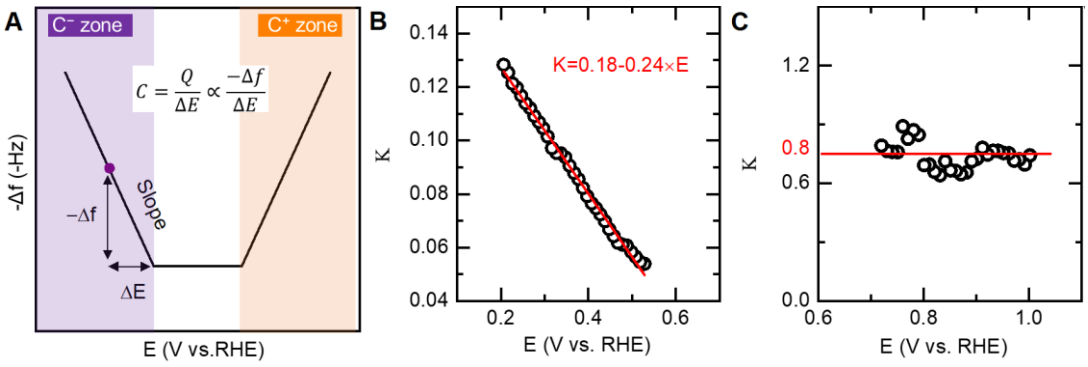

Fig. S13 Corrective coefficient (K) of the capacitance under O_2. (A) Graph that illustrates how the capacitance is calculated at each potential utilizign the frequency response in EQCM. Given that frequency changes in EQCM are directly propotional to surface charge, the slope of these frequency changes is linked to capacitance through the equation $C = \frac{\Delta Q}{\Delta E} \propto \frac{-\Delta f}{\Delta E}$. The corrective coefficient (K) is defined as the ratio of $(\frac{-\Delta f}{\Delta E})_{O_2}$ under O_2 to $(\frac{-\Delta f}{\Delta E})_{Ar}$ under Ar at each applied potential (E). This relationship is represented by $K = \frac{(\frac{-\Delta f}{\Delta E})_{O_2}}{(\frac{-\Delta f}{\Delta E})_{Ar}} = \frac{C_{O_2}}{C_{Ar}}$. **(B)** The K of capacitance under O_2 in the C^- zone. A linear relationship between K and E is observed in the C^- zone, with the equation K=0.18– 0.24× E. This indicates that the capacitance under O_2 is diminished in the C^- zone comparing with that under Ar. **(C)** The K of capacitance under O_2 in the C^+ zone. K is of roughly 0.8 is found indepedent of the potential indicating that the ratio of capacitance under O_2 and capacitance under Ar is constant.

Samenvatting

Sinds het gebruik van voltammetrische technieken is uitgebreid van het oorspronkelijke gebruik van kwikelektroden naar een breed scala aan elektrodematerialen, is moderne voltammetrie geëvolueerd tot een onmisbare techniek. Het biedt waardevolle inzichten in de elektrochemische eigenschappen en gedrag van materialen, en heeft daarom een grote impact gehad op verschillende vakgebieden zoals materiaalkunde, energieopslag, corrosiestudies en sensorontwikkeling. In een voltammogram is de juiste interpretatie van de stroomrespons buitengewoon cruciaal wanneer er een potentiaal wordt aangelegd door de potentiostaat, maar dit is niet altijd eenvoudig te ontrafelen. Historisch gezien was goud het middelpunt in sommige van de eerste publicaties in de elektrochemische oppervlaktewetenschap, met name in de studies van Frumkin, Butler, Browden en Rideal, die gelijktijdig plaatsvonden met het initiële onderzoek naar kwik. De kennis die is opgedaan door de interpretatie van het elektrochemische gedrag van goud heeft een diepgaande invloed gehad op veel moderne wetenschappelijke gebieden.

In dit proefschrift onderzochten we de relatie tussen het type oxide en de activiteit van de zuurstofevolutiereactie (OER) door in-situ Raman- en voltammetriemetingen te combineren (**Hoofdstuk 2**). We onderzochten het gedrag van de oxide-reductiepieken met behulp van roterende ring-disk-elektrode (RRDE) en elektrochemische kwartskristalmicrobalans (EQCM), waarbij belangrijke details van de structurele reconstructie van goudoxides werden onthuld (**Hoofdstuk 3**). Daarnaast evalueerden we de verdeling van oppervlakteladingen in aanwezigheid van chemische adsorptiegebeurtenissen en zelfs tijdens het zuurstofreductiereactie (ORR) katalytische proces met behulp van EQCM (**Hoofdstuk 4**). In dit hoofdstuk is het primaire doel om de bevindingen die in dit proefschrift worden beschreven samen te vatten en enkele inzichten uit onze bevindingen te delen.

De dubbele reductiepieken die worden waargenomen bij goudoxides duiden op de reductie van verschillende soorten oxiden, in plaats van reductie van de zogenaamde binnenste en buitenste oxidelagen.

Experimenteel onderzoek van oxidevorming in de elektrochemie gaat terug tot de jaren 1930. De introductie van de "charge-curve" methode, werd oorspronkelijk toegepast door Bowden en Rideal voor het meten van de dubbellaagcapaciteit van Hg. Significante vooruitgang werd geboekt door Will en Knorr in de jaren 1960, die onze kennis van elektrochemische oppervlakteprocessen bij edelmetalen verbeterden door gebruik te maken van potentiostaten. Deze methode, een uitbreiding van de potential-sweep benadering (d.w.z. voltammetrie) werd al gebruikt in polarografie bij DME, en bood een nieuwe mogelijkheid om interfaciale processen bij edelmetalen te verkennen. Deze nieuwe instrumentatie maakte het mogelijk elektrochemische experimenten te doen, waarbij de potentiaal gecontroleerd kon worden, iets wat cruciaal is voor het bestuderen van de vorming van anodische oxidefilms op metalen.

Bij het onderzoek naar de vorming en de reductie van oxidelagen hebben elektrochemici verbanden gelegd tussen verschillende reductiepieken en afzonderlijke oxidelagen. Deze denkwijze vindt zijn oorsprong in Shibata's bevindingen over de reductie van dikke Pt-oxidefilms, waar hij onderscheid maakte tussen de quasi-2D oxidefilm (α-toestand) en de dikke oxide (β-toestand) gedurende een potentiaalverlaging. Shibata stelde voor dat het dikke (β) oxide zich zou bevinden tussen het bulkmetaal en een laag nieuw afgezette metaalatomen aan de buitenkant van het resterende β-oxide.

Burke en Roche introduceerden een alternatief model dat bekend staat als het hydrous oxide-model. Volgens dit Burke-model bestaat een dikke metaaloxide uit een binnenste monolaag (compact en anhydrous) en een buitenste oxide laag (verspreid en hydrous). In het hydrous oxide-model wordt de binnenste oxide laag eerst gereduceerd, gevolgd door de buitenste oxide lagen. Hoewel deze artikelen geen direct experimenteel bewijs bevatten dat reductie van de verschillende oxide lagen koppelt aan de reductiepieken, legden ze de basis voor verder onderzoek. Dit omvatte een breder scala aan materialen waarbij verschillende oxide lagen onderzocht werden door de reductiepieken te volgen. Als direct gevolg daarvan zijn voltammetrische gegevens ten onrechte beschouwd als een handig middel om onderscheid te kunnen maken tussen de binnenste anhydrous oxide laag en de buitenste hydrous oxide laag.

In **hoofdstuk 2** richtte onze studie zich op de analyse van de reductiepieken van goudoxide over het gehele pH-bereik, waarbij een aanzienlijk gebrek in het bestaande hydrous oxide-model aan het licht kwam. Ten eerste bleek dat de O_2-reductiepiek vaak verkeerd toegekend is aan een oxide-reductiepiek in de gebruikelijke literatuur, wat leidt tot serieuze misinterpretaties bij de analyse van de structuur van oxide lagen. Hoewel het duidelijk is dat goudoxides binnenste en buitenste componenten hebben, is de cruciale vraag die tot nu toe niet is beantwoord of de elektrochemische reductie van deze binnenste en buitenste componenten verantwoordelijk is voor de waarneming van meerdere goudoxide-reductiepieken in het voltammogram.

Daarom voerden we een diepgaander onderzoek uit naar de reductiechemie van goudoxide, waarbij we gebruik maakten van een combinatie van cyclische voltammetrie en oppervlakte-versterkte Raman-spectroscopie. Uiteindelijk bevestigden we de aanwezigheid van twee verschillende soorten oxiden (α-oxide en β-oxide). Deze classificatie van oxiden werd vastgesteld door systematische het reductiegedrag van het goudoxide in kaart te brengen in combinatie met in situ oppervlakte-versterkte Raman-spectroscopie (SERS). Daarnaast onderzochten we de relatie tussen de OER-activiteit en het type aanwezige oxide, en ontdekten dat beide oxiden cruciaal zijn voor de OER, maar dat OER katalyze op beide oppervlakken plaats vindt via verschillende reactiepaden. Hierdoor heeft deze ontdekking aanzienlijk bijgedragen aan ons begrip van hoe de OER-activiteit op goud aanzienlijk varieert afhankelijk van de pH-waarde.

De anomalieën in potentiaalverschuivingen die worden waargenomen bij de reductiepieken van goudoxide worden niet veroorzaakt door mysterieuze ion-effecten uit het elektrolyt; in plaats daarvan weerspiegelen deze nauwkeurig de manier waarop goudoxides zelfreconstructieprocessen ondergaan.

Op dit moment is ons begrip van de metaaloxide-structuur op atomaire schaal grotendeels gebaseerd op ex situ spectroscopische technieken in vacuüm en berekeningen op goed gedefinieerde en sterk symmetrische metaaloppervlakken. Tijdens katalyse leiden corrosie en reconstructie van het metaaloxideoppervlak echter tot de vorming van amorfe

structuren. Deze amorfe structuren verschillen aanzienlijk van de oorspronkelijke goed gedefinieerde kristallijne materialen die in vacuüm en door berekeningen zijn bestudeerd. Op dit moment weet de wetenschap maar heel weinig over de atomaire structuur van echte metaaloxidekatalysatoren, vooral aan het grensvlak tussen de vloeistof and de vaste stof waar elektrokatalyse plaatsvindt. Daarom wordt de verandering van de structuur van amorfe oxiden tijdens een katalytisch proces beschouwd als een van de meest uitdagende wetenschappelijke vraagstukken.

In **Hoofdstuk 2** hebben we het traditionele hydrous model gecorrigeerd, dat ten onrechte verschillende reductiepieken van goudoxide beschouwde als het reductieproces van afzonderlijke oxide lagen. De verstoring van dat model heeft ons aangespoord om de werkelijke onderliggende redenen achter potentiaalverschuivingen van goudoxide reductie pieken, die niet de regels van de wet van Nernst volgen in detail te bestuderen. Dit is cruciaal omdat veel interpretaties van dergelijke potentiaalverschuivingen van oxide reductiepieken zijn gebaseerd op misinterpretaties met betrekking tot het hydrous model. Om deze redenen presenteren we onze bevindingen in **Hoofdstuk 3**.

In **Hoofdstuk 3** hebben we de intrigerende chemie achter dit "niet-Nernstiaanse gedrag" verkend, dat wordt gekenmerkt door abnormale potentieverschuivingen in de oxide-reductiepieken van CV's. Onze verkenning werd vergemakkelijkt door gebruik te maken van geavanceerde in situ-technieken, waaronder de roterende ring-disk-elektrode (RRDE) en de elektrochemische kwartskristalmicrobalans (EQCM). Met behulp van deze instrumenten konden we diep ingaan op de complexiteiten van de amorfe oxide-structuur onder realistische katalytische condities. Zo konden we bijvoorbeeld het moment van detectie van Au^{3+} in het oxide-reductieproces aanwijzen door de reductiestroom van Au^{3+} op de ring te observeren tijdens een RRDE-experiment. Door het moment van massaverlies op EQCM te onderzoeken, kregen we inzicht in de rol van deze Au^{3+}-ionen bij het stabiliseren van het grensvlak tussen oxiden en oplossingen. Uiteindelijk bleken de gegevens van verschillende technieken met elkaar verbonden te zijn, waarbij het kon worden geconcludeerd dat Au^{3+}-kationen een cruciale rol spelen in de chemie van goudoxide. Ze vormen bindingen met nucleofielen

aanwezig binnen de amorfe goudoxide-laag en de elektrolytoplossing, en bepalen zo de interacties aan de vaste-vloeistofgrensvlak.

In deze studie leggen we een belangrijke schakel tussen niet-Nernstiaanse piekverschuivingen, en de interacties die Au^{3+} aangaat op het grensvlak tussen goudoxide en de vloeistoffase, maakt het mogelijk conclusies te trekken over de dynamische evolutie van oxidestructuren door het volgen van deze niet-Nernstiaanse gedragingen van goudoxide-reductie. Dit toont aan dat het mogelijk is om structurele veranderingen veroorzaakt door metaal kationen binnen amorfe metaaloxiden te traceren door het onderzoeken van niet-Nernstiaanse gedragingen van oxiden. Het laat zien dat in metaaloxiden de manier waarop metalen binnen oxiden binden (ionische binding, covalente binding of waterstofbinding) cruciaal is voor het begrijpen van de dynamische gedrag van amorfe oxidelagen.

Het is mogelijk om de verdeling van de oppervlaktelading tijdens chemische adsorptie/desorptie en katalytische processen te verkennen door gebruik te maken van EQCM.

Geïnspireerd door het werk in de twee voorafgaande hoofdstukken (die gericht waren op het potentiaalbereik waarin oxiden aanwezig zijn op het goudoppervalk), ligt de focus van **Hoofdstuk 4** op de relatief negatieve potentialen waar geen oxiden aanwezig zijn, specifiek het elektrochemische dubbellaag-gebied. Hier werd een nieuw onderzoek vanaf de basis opgebouwd om het elektrochemisch gedrag in het dubbellagengebied op goud te begrijpen. Zo kwam **Hoofdstuk 4** tot stand.

Onze oorspronkelijke kennis van de structuur van de elektrische dubbellaag komt voort uit oppervlaktespanningsmetingen aan kwik, waar de potentiaal van nul lading (PZC) wordt aangewezen als die potentiaal dat overeenkomt met de maximale oppervlaktespanning op een elektrocapillaire curve. Variaties in de elektrode ladingsdichtheid zullen een herverdeling van ionen veroorzaken, resulterend in niet-Faradische stromen die kunnen worden waargenomen met behulp van voltammetrie. Omdat er een correlatie is tussen de landingsdichtheid en niet-Faradaische stroom, zijn we in staat om de ladingsdichtheid op de elektrode te onderzoeken via de stroomrespons zonder daarbij oppervlaktespanningsmetingen hoeven uit te voeren.

Deze correlatie is cruciaal voor vaste elektroden, aangezien oppervlaktespanningsmetingen onmogelijk zijn op vaste materialen. Daarom hebben elektrochemische capaciteitsmetingen, berekend uit de stroomresponsen in een voltammogram, een cruciale rol gespeeld bij het begrijpen van de elektrochemische grensvlakstructuur op het elektrodeoppervlak, met name voor vaste elektroden.

De aanwezigheid van Faradaische stromen als gevolg van de chemische adsorptie/desorptie van ionen vormt echter een uitdaging voor de nauwkeurigheid van capaciteitsmetingen, aangezien dergelijke chemische processen vaak voorkomen bij vaste elektroden. Hoewel talrijke gemodificeerde Gouy-Chapman-Stern (GCS) modellen adsorptie en desorptie processen meenemen in het bespreken van de dubbellaagstructuur, moet worden benadrukt dat we nog steeds geen precies begrip hebben van hoe de ladingsdichtheid op het electrodeoppervlak precies wordt opgebouwd in aanwezigheid van chemische adsorptie/desorptie. Het gebruik van de EQCM kan nieuwe inzichten bieden in ons begrip van elektrochemische grensvlakken. Het potentiële gebruik van QCM als massasensor werd voor het eerst gedemonstreerd door Sauerbrey in 1959. Nomura en Okuhara breidden de toepasbaarheid van QCM uit naar op vloeistof gebaseerde systemen in hun publicatie uit 1982, wat het begin markeerde van de ontwikkeling van EQCM voor het vakgebied van grensvlak elektrochemie. Aanvankelijk werden QCM's voornamelijk gebruikt om dunne filmafzetting te monitoren en zo de filmdikte te reguleren. De initiële toepassing van EQCM-metingen is geworteld op basis van de correlatie tussen de Faradaische lading en de massaverandering gedurendej elektrochemische depositie reacties. Echter, voortschrijdend onderzoek heeft onthuld dat EQCM ook de elektrostatische aantrekking van zowel ionen als kationen kan detecteren. Deze inspanningen hebben ons onderzoek naar de verdeling van de ladingsdichtheid op het goudoppervlak geïnspireerd.

In **Hoofdstuk 4** introduceren we het gebruik van EQCM als een innovatieve benadering om de ladingsdichtheid te onderscheiden en kwantificeren. De EQCM maakt gebruik van de oscillatiefrequentie van een kwartskristal als een gevoelige indicator voor massa-veranderingen op een goud elektrode. gebruik te maken van de frequentieresponsveranderingen van het kwartskristal op de elektrostatische aantrekking van

vrije ladingen, kan deze methode een middel bieden om de gebieden met een positieve en een negatieve overschot lading te identificeren. Door een vergelijking van de frequentierespons, die is bepaald door de EQCM, en de capaciteit, die is vastgelegd door cyclische voltammetrie, kunnen we de ladingsdichtheid van het elektrodeoppervlak en de Faradaische lading in het hele pH-bereik schatten. Bovendien, door de correlatie tussen de overschot vrije lading en de frequentierespons te onderzoeken, hebben we oppervlakteladingdistributiediagrammen geconstrueerd voor zowel Ar- als O_2-verzadigde oplossingen. Deze diagrammen beogen visueel weer te geven hoe de oppervlakteladingdsdichtheid kan fluctueren bij specifieke pH-niveaus en aangelegde potentiaal voor en tijdens katalyse.

De experimentele resultaten zijn fascinerend omdat we door deze studie niet alleen inzicht hebben gekregen in de verdeling van de verschillende oppervlakteladingen (oppervlakteladingsdichtheid en de lading geconsumeerd in absorptie/desorptieprocessen) in aanwezigheid van chemische adsorptie zonder interferentie van Faradaische stromen, maar ook hebben ontdekt dat deze methode om de distributie van oppervlakteladingsdichtheid te testen mogelijk blijft, zelfs tijdens het zuurstofreductieproces.

De ontdekkingen beschreven in dit proefschrift benadrukken de noodzaak voor verder diepgaand onderzoek. Ten eerste werd het Burke-model met betrekking tot verschillende oxide-lagen voorgesteld op basis van de oxidatiereductiegedragingen van verschillende nobele metalen. **Hoofdstuk 2** onthult onnauwkeurigheden bij het toepassen van het Burke-model op goud, wat een onderzoek naar de toepasbaarheid er van op andere metalen noodzakelijk maakt. Ten tweede opent de beperkte invloed van elektrolytische ionen op de reductiegedragingen van goudoxiden mogelijkheden om de relatie tussen niet-Nernstiaanse gedragingen en veranderingen in de oxide-structuur te verkennen (**Hoofdstuk 3**). Ten derde geeft ons werk significante verschillen aan in het elektrodeoppervlak die plaatsvinden gedurende zowel de zuurstofevolutie als de reductie reacties op goud. Daarom is het begrijpen van de veranderingen in de elektrodestructuur cruciaal voor het kunnen verklaren van de relatieve hoge overpotentiaal die nodig is voor het uitvoeren van deze reacties (**Hoofdstuk 2-4**). Tot slot toont **Hoofdstuk 4** aan dat EQCM kan worden gebruikt om de elektrodeoppervlakteladingsdichtheid op goud te onderzoeken tijdens ORR. Dit opent de

intrigerende mogelijkheid om de elektrodeoppervlakteladingsdichtheid op verschillende materialen en gedurende verschillende elektrochemische reactieprocessen te onderzoeken. Daarnaast hebben deze drie eerder genoemde hoofdstukken ons geïnspireerd om meer complexe vragen te heroverwegen over hoe we de verbinding begrijpen tussen de aangebrachte potentiaal en de stroom in voltammetrie. Bijvoorbeeld, hoe interpreteren we veranderingen in de vorm van redox-pieken over verschillende tijdschalen, zoals meettijd? Hoe identificeren we nauwkeurig de ruimtelijke positie van de actieve deeltjes in verschillende homogene en heterogene processen gedurende voltammetrie? En waarom nemen we soms een discrepantie waar tussen oxidatie- en reductieladingen in voltammetrie?

总结

伏安法技术起源于最初的汞电极，逐渐扩展到了各种固体材料的广泛应用，如今已经发展成为一项不可或缺的技术。它为材料的电化学性质和行为提供了有价值的见解，因此在材料科学、能量存储、腐蚀研究和传感器开发等多个领域都产生了深远的影响。在伏安图中，当电位仪改变工作电极上的电位时，对电流响应进行正确解释变得尤为关键。在早期与电化学相关的表面科学著作中，金电极的研究曾是焦点之一，特别是在 Frumkin、Butler、Browden 和 Rideal 等学者的研究中，这些研究与最初对汞的研究同时期进行着。因为黄金是最早用于固体电极研究的材料之一，因此对金电极的电化学行为的解释为许多现代科学领域奠定了基础。

在本论文中，我们通过结合原位拉曼和伏安法测量（**第 2 章**），探究了氧化物类型与氧化还原活性之间的关系。通过利用 RRDE 和 EQCM，我们深入研究了氧化物还原峰的行为，从一个新的角度揭示了金氧化物结构重构的规律（**第 3 章**）。此外，我们使用 EQCM 评估了在化学吸附存在时和在催化氧气还原过程中表面电荷的分布（**第 4 章**）。在本章中，主要的目标是总结本论文中描述的发现，以及这些发现如何改变对黄金伏安行为的解释。

分离的氧化还原峰表明存在不同类型的氧化物，并不能反映内外层的不同。

在电化学历史中，对于氧化物形成的实验探索可以追溯到上世纪 30 年代。"电荷曲线" 方法最初由 Bowden 和 Rideal 引入，用于测量 Hg 的双电层电容，而在上世纪 30 年代初，Frumkin 和 Butler 等人独立地将其应用于铂和金的电化学过程的研究。在上世纪 60 年代，Will 和 Knorr 取得了重大进展，通过使用恒电位仪深化了我们对贵金属电化学表面过程的理解。这种方法是电位扫描方法（即伏安法）的延伸，在当时早已被应用于滴汞电极（DME）的极谱法中。这一方法为探索贵金属界面过程提供了新的途径。受电化学仪器进步影响，精准可控的电位技术的应用保障了研究金属阳极氧化膜的形成过程的准确性。与气相氧化方法或采用控制电流的氧化方法相比，这种方法在观察氧化膜形成过程方面具有明显的优势。

在氧化层形成和还原的研究中，早年的电化学家们将不同的氧化物还原峰与不同氧化层之间建立了关联。这种关联最早可以追溯到 Shibata 对厚层的铂氧化膜还原行为的解读，他在负电位扫描过程中区分了准二维氧化膜（α状态）和厚氧化膜（β状态）。Shibata 提出，厚氧化膜（β状态）将位于金属块和残余β氧化膜外表面新沉积金属原子层之间，而那些新沉积的金属原子层则被认为来源于α状态氧化膜的还原。

然而，Burke 和 Roche 提出了一种替代模型，被称为水合氧化物模型。根据 Burke 模型，厚金属氧化物包括内部单分子层（紧密且无水的）和外部氧化物层（疏松且水合的）。在水合氧化物模型中，内部氧化物层总是首先被还原，然后是外部氧化物层。尽管这些论文缺乏直接的实验证据来连接氧化物层与不同还原峰，但由于这种模型的存在，使得人们可以通过追溯还原峰的行为来探索各种材料的不同氧化物层，因此该模型开始更广泛地用于研究不同氧化层行为。因此，这种因为错误地将伏安法数据视为区分内部无水氧化物层和外部水合氧化物层的行为，曾一度被视为研究不同氧化层的便利手段。

在**第二章**中，我们深入研究了金氧化物在整个 pH 范围内的还原峰，揭示了现有水合氧化物模型的一个重大缺陷。首先，氧气还原峰在早年的许多文献中经常被误认为氧化物还原峰，导致对氧化层结构分析的不准确。虽然氧化物必然存在具有内层和外层，但关键问题是：氧化物层与不同还原峰之间是否存在必要的逻辑联系？

于是，我们通过采用循环伏安法和表面增强拉曼光谱的结合，对金氧化物进行了更深入的研究。最终，我们确认了两种明显依赖于 pH 的氧化物的存在。α氧化物主要出现在低 pH 环境中，而β氧化物则在高 pH 环境中占主导地位。通过对金氧化物还原行为的系统追踪和原位表面增强拉曼光谱（SERS）的表征，我们确认了这两种不同氧化物的存在。进一步的研究还表明，这两种氧化物对氧气析出反应（OER）至关重要，它们会导致不同的 OER 途径。我们的研究表明，存在两种 OER 机制：一种通过α氧化物介导的质子耦合电子转移（PCET）步骤进行水分裂，另一种机制是通过 $Au(OH)_3$（β氧化物）的去质子形式介导，其中电子和质子转移是分离的。这种 pH 有关的氧化物的准确识别为我们全面了解金属氧化物在不同 pH 范围内的

OER 机制提供了不同的视角。此外，基于这一发现，我们得以理解了在不同溶液 pH 环境下 OER 活性会发生变化的原因。

氧化物还原峰异常电位漂移：是氧化物结构自我重构过程的反映，而非电解质中难以理解的离子效应。

目前，我们对金属氧化物结构的原子尺度的理解主要依赖于真空中进行的异位光谱技术和对定义明确、高度对称的金属表面的计算。然而，在催化过程中，金属氧化物表面的腐蚀和重构导致了无定形结构的形成。这些结构与在真空和计算中研究的结构简单的单晶界面有着明显的不同。目前，科学界对金属氧化物催化剂的真实的原子结构知之甚少，尤其是在发生电催化的固液界面的原子结构。因此，无定形氧化物在催化过程中的结构变化是一直被认为是最具挑战性的科学问题之一。

在**第二章**中，我们修正了传统的水合模型，该模型错误地将不同的金氧化物还原峰视为来自不同氧化层的还原过程。这一模型的纠正促使我们开始重新考虑氧化物的非能斯特行为（即氧化物还原峰的异常电位漂移）背后真正的原因。这种重新思考的重要性在于，过去对氧化物非能斯特行为的许多解释都建立在与水合模型相关的误解基础上。基于这些原因，我们有了我们**第三章**中科学发现。

在**第三章**中，我们探讨了伏安曲线中氧化物还原峰的异常电位移动，即“非能斯特行为”。我们采用了包括 RRDE 和 EQCM 在内的原位技术，这些工具使我们能够深入探讨无定形氧化物结构在真实催化环境中的复杂性。我们展示了，在氧化条件下，Au^{3+}阳离子不断在无定形金氧化物中形成，并且这是造成先前未能理解的非能斯特电位移动等现象的主要原因。Au^{3+}阳离子在金氧化物的结构变化中发挥了关键作用，它们与存在于无定形金氧化物层和电解质溶液中的亲核试剂形成不同的键，从而在固液界面上主导了这种相互作用。此外，我们展示了这些裸露的阳离子位点不仅在固液界面的结构中发挥着关键作用，而且还积极参与了催化水氧化反应。

在这项研究中，我们介绍了金属非共价态（离子和水合金属阳离子）与共价氧化物之间的重要联系。这种逻辑联系发现的意义在于，使我们可以通过追踪氧化物还原的非能斯特行为，得以追踪金属离子在无定形金属氧化物中引起的结构变化。这提醒我们，在金属氧化物中，金属的键合模型（离子键、共价键或氢键）对于理解氧化物结构的演变至关重要。

探索表面电荷分布在化学吸附/解吸和催化过程中是可能的。

受到前两章的工作启发（重点关注于氧化物存在的高电位区间），我将注意力转向相对负的电位范围，即没有氧化物存在的电化学双层电位区间。我们从头开始，以了解过去关于金在双层区域的电化学行为，于是**第四章**应运而生。

我们对界面上电化学双层结构的最初理解来自对汞的表面张力测量，其中零电位（PZC）被确定为在电毛细曲线上具有最大表面张力的电位。表面剩余电荷的变化会引起离子的重新分布，导致在伏安图中可观察到的非法拉第电流。由于剩余电荷与非法拉第电流之间存在逻辑联系，因此允许我们通过电流响应而无需表面张力测量来研究过量电荷。这种关联对于固体电极至关重要，因为在固体材料上不可能进行表面张力测量。因此，对于固体电极而言，从伏安图中电流响应计算得到的电化学电容测量在理解电极表面的电化学界面结构方面发挥了至关重要的作用。

然而，由于离子的化学吸附/解吸过程经常发生在固体电极，这些化学过程导致的法拉第电流的存在对电容测量的准确性构成了严峻的挑战。虽然许多改进的 GCS 模型通过整合涉及电子转移的吸附/解吸来讨论电双层结构，但必须强调的一点是，我们仍然缺乏对在化学吸附/解吸存在的情况下剩余电荷的分布的准确理解。

石英晶体微天平（QCM）作为一种质量传感器的潜在用途最早是由 Sauerbrey 于 1959 年首次证明的。Nomura 和 Okuhara 在他们 1982 年的论文中将 QCM 的适用性扩展到基于液体的系统，从而推动了 EQCM 在界面电化学领域的发展。最初，QCM 主要用作薄膜沉积的监测器以控制膜厚度。EQCM 测量背后的最初应用根植于涉及电化学沉积的法拉第电荷和质量变化之间存在关联。然而，越来越多的研究表明，EQCM 还可以检测到离子和阳离子的静电吸附。这些

努力激发了我们对金表面过量电荷分布的研究，这主要是通过伏安法和 EQCM 测量的结合来完成。

在**第四章**中，我们介绍了使用 EQCM 作为一种创新方法来识别和量化电极表面剩余的自由电荷的分布。EQCM 利用石英晶体的振荡频率作为对金电极上质量变化的敏感指标。通过利用石英晶体对自由电荷的静电吸引的频率响应，这种方法可能提供了一种识别存在正剩余电荷和负剩余电荷的电位区域的手段。通过比较 EQCM 记录的频率响应和循环伏安法记录的电容，我们可以估算整个 pH 范围内过量自由电荷和法拉第电荷的量。此外，通过检查剩余自由电荷和频率响应之间的相关性，我们构建了 Ar 和 O_2 饱和溶液的剩余自由电荷分布图。这些图表旨在直观地展示剩余电荷在特定 pH 水平和催化前后的不同电位下如何波动的。

实验结果是令人兴奋的，因为通过这项研究，我们不仅对在化学吸附中表面电荷（剩余电荷和成键电荷）的分布有了深入了解，而且令人惊讶地发现是，即使在氧还原过程中，这种测试过量电荷分布的方法仍然有效。

我们论文中的发现激发了我们对更深入的研究伏安行为的渴望。首先，Burke 模型涉及不同氧化层是基于各种贵金属的氧化物还原行为提出的。**第二章**揭示了将 Burke 模型应用于金时的不准确性，我们仍然需要检查该模型对其他金属的适用性。其次，电解质离子对金氧化物还原行为的相对有限影响为探索非能斯特行为与氧化物结构变化之间的关系开辟了途径（**第三章**）。这个发现引发我们思考了一个更有趣的问题：当电解质离子在更复杂的金属氧化物中也对非能斯特行为产生影响时，那些存在于氧化物中的金属阳离子如何发挥作用呢？第三，我们的工作表明了氧在金上的氧化还原过程的界面环境存在显著差异。因此，理解这些电极结构变化对于解释这些反应的高过电位变得至关重要（**第 2-4 章**）。最后，第四章表明 EQCM 可以用于探索 ORR 期间金上的富余自由电荷。这又引发了一个有趣的可能性，即在各种材料和不同电化学反应过程中调查富余自由电荷。

此外，我们前面提到的这三章启发我们重新思考在伏安法中如何理解应用电位和电流之间的关系的更复杂的问题。例如，我们如何解释不同时间尺度（如测量时间）下氧化还原峰形状

的变化？我们如何精确地识别伏安法中不同均相和异相过程中活性物种的空间分布？为什么我们有时在伏安法中观察到氧化和还原电荷之间是不平衡的呢？

CURRICULUM VITAE

Shengxiang Yang was born in Yunnan, China in July 1990. He earned his bachelor's degree in Environmental Engineering from Lanzhou University in 2013. His research focused on "The Influence of Sewage Irrigation on Maize Plants". During his undergraduate studies, he received the "Innovative Style Scholarship" (Reward for Outstanding Performance in the Art, Sport or Research) and the "Second-class Scholarship" from Lanzhou University.

In 2014, he relocated to Xuzhou, where he commenced his research on "Effective Nitrate-Ammonia Simultaneous Electroreduction into Nitrogen in Different Electrode Reactor Configurations" as a master's student in Environmental Engineering at China University of Mining and Technology, under the supervision of Prof. Lizhang Wang. Throughout his master's studies, he was honored with the "First-class Scholarship" from 2014 to 2016. Additionally, he received the "Master of innovation scholarship" (Reward for Outstanding Researcher) and the "National Scholarship" (Top 2%) at 2016.

In September 2017, he embarked on his doctoral journey as a PhD candidate in the research group of Dr. Dennis Hetterscheid. During his PhD, he conducted research in the labs of the Metals in Catalysis, Biomimetics & Inorganic Materials (MCBIM) and the Catalysis and Surface Chemistry (CASC) research groups. The results of the studies, included in this thesis, were presented as oral presentations at the 2020 Netherlands Catalysis and Chemistry Conference (NCCC) and the 2023 Kroese-Duijsters Symposium. Furthermore, he participated in or presented some of his research work as posters at the NCCC (2019, 2021), the Chemistry as Innovative Science (CHAINS, online) conference (2020), the Reedijk Symposium (2018, 2019, 2020, 2023) and the Holland Research School of Molecular Chemistry (HRSMC) Symposium (2017, 2018, 2019).

During his PhD, he attended various schools and courses, including "Catalysis: An Integrated Approach" organized by the Netherlands Institute for Catalysis Research, HRSMC courses such as "Physical Methods in Inorganic Chemistry", "High Impact Writing", as well as "the Scientific Conduct" course provided by the Graduate School of Leiden University. He also participated in the summer school course "Electrochemical Approaches to Chemical Synthesis"

organized by the International Center for Advanced Studies of Energy Conversion and the graduate school course “Effective Communication and Scientific Conduct” organized by Leiden University. Additionally, during his PhD, he supervised a BSc student (Bañó Gómez Javier).

Published:

1. **Yang, S**.; Hetterscheid, D. G. H., Redefinition of the active species and the mechanism of the oxygen evolution reaction on gold oxide. *ACS Catal.* **2020,** *10*, 12582-12589.

2. **Yang, S.**; Wang, L.; Jiao, X.; Li, P., Electrochemical Reduction of Nitrate on Different Cu-Zn Oxide Composite Cathodes. *Int. J. Electrochem. Sci.* **2017,** *12*, 4370-4383.

3. **Yang, S.**, Wang, L., Wu, B., Zhang, B., Li, Z. Electrochemical oxidation of phenol on AC/SnO_2-Sb particle electrodes. *Chem. Industry Eng. Prog.*, **2016**, 35 (4): 1230-1236.

4. Wang, L.; **Yang, S.**; Wu, B.; Li, P.; Li, Z.; Zhao, Y., The influence of anode materials on the kinetics toward electrochemical oxidation of phenol. *Electrochim. Acta* **2016,** *206*, 270-277.

5. Wang, L.; **Yang, S.**; Wu, B.; Li, Z.; Li, P.; Zhao, Y., A comparative study for electrochemical oxidation of aromatic compounds in the absence and in the presence of granular activated carbon (GAC). *Int. J. Electrochem. Sci.* **2016,** *11*, 2284-2296.

6. Kong, Y.; Wang, L. Z.; **Yang, S**.; Zhao, P., Preparation and Electro-catalytic Mechanisms for Nitrate Ion Reduction of $Ti_{(100-\delta)}Cu_{\delta}$($\delta$=0.02, 0.09, 0.28, 1.39, 5.65) Cathodes. *Chemical Journal of Chinese Universities-Chinese* **2018,** *39*, 132-140.

7. Wang, L.; Zhao, Y.; **Yang, S.**; Wu, B.; Li, P.; Zhao, Y., Employment of TiO_2/AC as particulate electrode for efficient phenol oxidation. *Int. J. Electrochem. Sci.* **2016,** *11*, 2401-2407.

8. Wang, L.; Kong, Y.; Wei, D.; **Yang, S.**; Chen, Q.; Kong, Y.; Li, P.; Ting, Y. ; Ong, C. N., Toward the quantitative evaluation of an activated carbon particle electrode performance in a packed-bed system. *Chemelectrochem* **2017,** *4*, 2464-2468.

9. Wang, L.; Kong, Y.; Jiang, J.; Wei, D.; Li, P.; **Yang, S.**; Ting, Y., Optimal wastewater treatment using a packed-bed electrode reactor (PBER): From laboratory experiments to industrial-scale approaches. *Chemical Engineering Journal* **2018,** *334*, 707-713.

10. Li, Z. N.; Wang, L. Z.; Zhao, Y.; Li, P.; **Yang, S.**, Effect of Sodium Dodecyl Sulfate (SDS) on Electro-Catalytic Performances of IrO_2-Ta_2O_5/SnO_2-Sb-MnO_2/Ti Electrode. *Rare Metal Materials and Engineering* **2017,** *46*, 2963-2968.

Under review:

1. Yang, S.; Hetterscheid, D. G. H., Tracing the dynamic structural changes occurring in amorphous metal oxides during catalysis through mapping of non-Nernstian behavior.

Manuscript in preparation:

1. Yang, S.; Hetterscheid, D. G. H., Exploring the excess free charge distribution under catalytic conditions using a quartz crystal microbalance methodology.

2. Yang, S.; Peng L.; Hetterscheid, D. G. H., Electrochemial quartz crystal microbalance (EQCM) study recognize non-Faradaic from Faradaic behavior in the electrode-driven electrochemical process.

ACKNOWLEDGMENT

First, I want to express my gratitude to the China Scholarship Council (CSC) for their financial support though grant number 201706420073. This support has been instrumental in my academic journey.

I extend my heartfelt thanks to Dr. Dennis Hetterscheid for offering me a PhD position in his group and for his guidance over the past years. Dennis, thank you for allowing me the freedom to explore electrochemistry and for instilling in me to a scientific mindset in every discussion. I will miss our brainstorming sessions, and your insightful questions have helped me grow.

I also wish to thank Prof. Dr. M.T.M. Koper for his invaluable discussions and feedback on my thesis chapters, which have significantly enhanced its quality. Additionally, I am grateful for the feedback from group members and the enjoyable outing organized by the Metals in Catalysis, Biomimetics & Inorganic Materials (MCBIM) and the Catalysis and Surface Chemistry (CASC) research groups.

A special thanks goes to my fellow "Minions" for their support and enjoyable company. Konstantin, Koen, Martijn, Silvia, Nicole, Michiel, Bas, Daan, Andrey, Kyra, Dana, Ross, Jan, Phebe, Sjoerd, Marleen, Yidan, and Charlotte, your contributions to our scientific discussions and the relaxed working environment you all fostered are truly appreciated.

I am thankful to my friends in Leiden—Chengyu, Weizhe, Xuequan, Mengjie, Mingchuan, Diyu, Chunmiao, Ye, Yurong, Chen, Yi, Chenguang, Deyi, Xiaoting, Zhiqin, Linfan, Jinwen, Wanbin, Fen, Lin, Liyan, Juan, and Furong—for the wonderful moments we shared. Meeting my promoters, colleagues, and friends in the Netherlands has been a joy, and I am sure my time here will be among my most cherished memories.

Finally, I wish to extend my heartfelt appreciation to my family for their steadfast support. Despite they may not fully understand my work, their belief in and support for me have been unwavering .

Shengxiang

In Leiden, April, 2024